Catalytic Reforming of Methane

in the Presence of CO_2 and H_2O

at High Pressure

Zur Erlangung des akademischen Grades eines
DOKTORS DER NATURWISSENSCHAFTEN
(Dr. rer. nat.)

Fakultät für Chemie und Biowissenschaften
Karlsruher Institut für Technologie (KIT) - Universitätsbereich
genehmigte

DISSERTATION

von
Dipl.-Ing. Thomas Luc Roussière

aus
Nantes (France)

Dekan: Prof. Dr. Martin Bastmeyer

Referent: Prof. Dr. Olaf Deutschmann

Korreferent: Prof. Dr. Jan-Dierk Grunwaldt

Tag der mündlichen Prüfung: 24. Oktober 2013

Abstract

Exploiting the greenhouse gas CO_2 as raw material could be more advantageous than its long-term storage. For instance, CO_2 can be used on large scale for the production of CO-rich syngas with a H_2/CO ratio of unity. Such a syngas can be used for the synthesis of commodity chemicals like aldehydes and ketones obtained through carbonylation of alkenes in hydroformulation and can be produced by CO_2 reforming of methane. The actual CO_2 reforming processes are conducted at low pressure (below ca. 7 bar), which is not suitable if the upstream as well as the downstream processes are operated at high pressures (typically the case in petrochemical platforms).

The investigations conducted in this study consist of the development of active catalysts as well as a process concept for the valorization of CO_2 within the CO_2 reforming of methane under high pressure (21 bar) in order to achieve a CO-rich syngas with a H_2/CO ratio of one.

Simulations of reforming equilibria highlights the fact that water is always produced in the CO_2 reforming of methane; therefore, CO_2 reforming is conducted with addition of the amount of water produced at the thermodynamic reforming equilibrium to enable coke gasification on the catalyst with water.

The use of high pressures above 10 bar, high temperatures above 1173 K (900°C), and high partial pressure of methane leads to significant impact of the gas-phase reactions and the formation of coke precursors, like ethylene. The addition of more than 30 vol.% H_2 in the feed stream can significantly limit the formation rate of coke precursors whereas the addition of water shows no particular influence on coke-precursor formation rates.

Various Pt-based catalysts are studied with regard to the dependence of activity and stability in steam reforming with various zirconia supports. The Pt/ZrO_2 catalyst exhibits strong deactivation under steam reforming due to a fast decrease of its specific surface area. The modification of the support of this Pt/ZrO_2 with silica is likely to form Pt particles embedded in silica, resulting in a low activity in steam reforming. On the other hand, the performance of a Pt-based catalyst supported on ZrO_2, which is modified with 10 wt.% La_2O_3 and 6 wt.%

CeO_2, exhibits an enhanced stability and activity when used close to the thermodynamic equilibrium of steam reforming of methane under 21 bar and at 1123 K (850°C).
In a kinetic study, this Pt-based catalyst, tested in steam reforming in the absence as well as in the presence of CO_2, shows that at 1023 K (750°C), atmospheric pressure, and a GHSV (Gas Hourly Space Velocity) above 33000 h^{-1} the activation of methane is performed with steam while CO_2 reacts with H_2 and/or methane. In addition, the TOFs (Turn Over Frequency) of methane conversions are found to be higher as the steam content in the feed increases, while the TOFs of CO_2 conversions increase as a higher CO_2 content in the feed is used. Furthermore, the TOFs of methane conversions are always superior to the TOFs of CO_2 conversions.

The Ni-based spinel catalyst prepared by molten-salt impregnation of hydrotalcite-like carrier with the stoichiometry of Mg spinel (Mg/Al=1/2) exhibits, after final calcination at 1223 K (950°C) for 4 h, the formation of mixed oxides, (Ni/Mg)O and $(Ni/Mg)Al_2O_4$, with a relatively high specific surface area (42 $m^2.g^{-1}$). After preformation in reducing atmosphere above 1073 K (800°C), Ni nanoparticles highly dispersed on $MgAl_2O_4$ are produced. This preformation step is found to be very sensitive to the presence of 10 vol.% H_2O or 5 vol.% CO_2, which inhibits the preformation mechanism. Compared to the samples prepared by precipitation and spray drying, the molten-salt impregnation performed by using a hydrotalcite-like carrier displays a much higher specific surface area and a much smaller crystallite size of both mixed oxides (< 20 nm). In CO_2 reforming of methane with addition of 10 vol.% H_2O at 1223 K (950°C) and 21 bar, the molten-salt-impregnated catalyst with a corundum prebed can achieve stable performances with CH_4 and CO_2 conversions 3-4 % below the thermodynamic equilibrium of reforming after a long preformation using the H_2 test protocol. In comparison, the use of the H_2O test protocol leads to the inhibition of the catalyst preformation, and performances are far from thermodynamic equilibrium, with methane conversions below 40%.

The performance of Ni hexaaluminate as catalyst in CO_2 reforming strongly depends on the choice of the mirror plane cation as well as the degree of substitution of Al^{3+} with Ni^{2+} in the hexaaluminate lattice. In addition, moderate calcination of hexaaluminate samples at 1473 K (1200°C) permits retention of the high specific surface area of 15 $m^2.g^{-1}$ necessary for the stabilization of the metallic Ni nanoparticles. Only Sr,Ni and Ba,Ni hexaaluminates are highly active, while the Ni loading should be kept below the sensitivity threshold of y=0.25 in $SrNi_yAl_{12-y}O_{19-\delta}$ and in $BaNi_yAl_{12-y}O_{19-\delta}$ to maintain the high dispersion of metallic Ni nanoparticles that exhibits highly stable performances under CO_2 reforming of methane at 1123 K (850°C) and moderate pressure (11 bar) for 10 h.

Kurzzusammenfassung

Die Verwendung von CO_2, anstelle von CO_2 Speicherung, könnte eine langfristige Lösung sein. Zum Beispiel könnte CO_2 in großem Umfang verwendet werden, um CO-reiches Synthesegas mit einem H_2/CO Verhältnis von eins herzustellen. Solch ein Synthesegas findet Anwendung in der Oxosynthese zur Herstellung von Aldehyden und Ketonen aus Alkenen. Die Herstellung von Synthesegas erfolgt durch das CO_2 Reformieren von Methan in Synthesegas mit einem H_2/CO Verhältnis von eins. Heutezutage erfolgt das CO_2 Reformieren unter niedrigen Drücken (< 7 bar), was ungünstig für die Downstream Prozesse ist, die meistens deutliche höhere Drücke benötigen (wie in Petrochemieverbünden).

Die Untersuchungen, die im Rahmen dieser Arbeit durchgefürt wurden, beschäftigen sich mit der Entwicklung aktiver Katalysatoren sowie eines Prozesses für das Reformieren von CH_4 mit CO_2 unter höherem Druck (21 bar) zur Hestellung eines Synthesegases mit einem H_2/CO Verhältnis von eins.

Thermodynamische Gleichgewichtsimulationen zeigen, dass Wasser immer im Gleichgewicht vorhanden ist. Weil Wasser die Koksvergasung beschleunigt, wird eine kleine Menge Wasser der Feedversorgung zudosiert, um mögliche Koksablagerungen, besonders am Anfang des Katalysatorbettes, zu vergasen.

Unter hohen Drücken (> 10 bar), hohen Temperaturen und hohen Partialdrücken an Methan finden Gasphasen-Reaktionen statt und die Bildung von Koksprekursoren wie Ethylen konnte festgestellt werden. Dadurch wird das Verkokungsrisiko deutlich erhöht. Die Zugabe von mehr als 30 vol.% H_2 zu der Feedversorgung begrenzt deutlich den Einfluss der Gasphasenreaktionen während die Wasserzugabe fast keinen Einfluss auf diese Reaktionen hat.

Verschiedene Pt-Katalysatoren wurden untersucht um die Aktivität und Stabilität unter Dampfreformierungsbedingungen von verschiedenen Trägern basierend auf Zirkonoxid zu bestimmen. Der Pt/ZrO_2 Katalysator zeigt unter Dampfreformierungsbedingungen eine starke Deaktivierung durch Verlust an spezifischer Oberfläche. Die Modifikation von Pt/ZrO_2 mit SiO_2 erzeugt wahrscheinlich eingebettete Pt Partikel, die nicht aktiv in der Dampfreformierung sind. Andererseits kann Pt/ZrO_2 mit 10 wt.% La_2O_3 und einer Dotierung mit

6 wt.% CeO_2 modifiziert werden. Solche Zirkonoxid Modifikation zeigt eine hohe Stabilität und Aktivität nahe am Dampfreformierungsgleichgewicht bei 1123 K (850°C) und hohem Druck (21 bar).
Kinetische Untersuchungen wurden an diesem Katalysator unter Dampfreformierung mit und ohne CO_2 bei 1023-1173 K (750-900°C) und bei Atmosphärendruck durchgeführt. Mit einem GHSV ("Gas Hourly Space Velocity") von 33000 h^{-1} und bei 1023 K (750°C) erfolgt die Methanaktivierung durch H_2O, während CO_2 entweder mit H_2 und/oder CH_4 reagiert.

Ein Ni-basierter Spinellkatalysator synthetisiert über Schmelzimprägnierung von hydrotalkitähnlicher Struktur mit einem Mg/Al Verhältnis von 1/2 zeigt eine spezifische Oberfläche von 42 $m^2.g^{-1}$ nach Kalzinirung bei 1223 K (950°C) während 4 h auf. Die Röntgendiffraktometrieanalyse beweist die Bildung von Mischoxiden, (Ni/Mg)O und $(Ni/Mg)Al_2O_4$, nach dieser Kalzinierung. Die Vorformierung, durchgeführt unter reduktiver Atmosphäre, führt bei über 1073 K (800°C) zur Bildung von hochdispersen Ni-Nanopartikeln auf $MgAl_2O_4$. Die Präsenz von H_2O und/oder CO_2 in der reduktiven Atmosphäre behindert deutlich den Vorformierungsmechanismus. Im Vergleich zu den Katalysatoren präpariert durch Fällung oder Sprühen zeigt ein Katalysator, der durch Schmelzimprägnierung hergestellt wurde, sowohl eine höhere spezifische Oberfläche als auch eine feinere Kristallitgröße der Mischoxide (< 20 nm). Für das CO_2 Reformieren durchgeführt mit Hilfe des Wasserstofftestprotokols unter 21 bar bei 1223 K (950°C) und Zugabe von 10 vol.% H_2O liegen die Umsätze mit dem schmelzimprägnierten Katalysator und einer Korund-Verschüttung ca. 3-4 % unter dem thermodynamischen Gleichgewicht. Das Wassertestprotokoll zeigt im Vergleich eine langsame Vorformierung, und die Methanumsätze liegen weit unter dem thermodynamischen Gleichgewicht bei max ca. 40%.

Die Leistungen von Ni-Hexaaluminaten in CO_2 Reformierung hängen stark von dem Zwischenebenekation sowie dem Substitutionsgrad von Al^{3+} durch Ni^{2+} im Hexaaluminatsgitter ab. Die Kalzinierung von Proben bei einer angemessen Temperatur von 1473 K (1200°C) erlaubt es eine spezifische Oberfläche von ca. 15 $m^2.g^{-1}$ zu erreichen. Solche eine hohe Oberfläche wird benötigt um die Ni-Nanopartikel gegen Sintern zu stabilisieren. Nur Sr,Ni und Ba,Ni Hexaaluminate sind hoch aktiv, während nur ein kleiner Substitutionsgrad (y=0.25 in $SrNi_yAl_{12-y}O_{19-\delta}$ oder $BaNi_yAl_{12-y}O_{19-\delta}$) von Al^{3+} durch Ni^{2+} ausreicht um hochdisperse Ni-Nanopartikel zu erzeugen, die aktiv und stabil in der CO_2 Reformierung bei 1123 K (850°C) und mittlererem Druck (11 bar) über 10 h sind.

To my family

Acknowledgements

I would like to acknowledge my supervisor at hte AG, Dr. Stephan A. Schunk, for the chance he gave me to work on this very interesting theme, his help and tips through the different steps to success. I would like to thank also my supervisor at Karlsruhe Institute of Technology (KIT), Prof. Olaf Deutschmann, for his scientific support and the friendly discussions.

Furthermore, I am grateful to the whole hte team for the great team work, atmosphere, German speaking/writing experience and especially to:

- Guido Wasserschaff for sharing his scientific experience as well as mentoring my technical work; Virginie Zöller for the professional work and support on the different setups, and finally Harry Kaiser for the test prototype that was already built when I started my PhD thesis.
- Dr. Sven Titlbach for the strong scientific background that he taught me on XRD analysis and crystallography.
- my supervisors in the synthesis laboratory, Andreas Strasser and Simon Holz, for their strong support. In addition, I acknowledge the help and improvement suggestions provided by Michael Bartz, Robert Müller, David Jakobi, Karl Spielhaupter during my project; this is without forgetting the help of the liner filling team and especially Sebastian Mittler and Hendrik Erdmann.
- the analysis department of hte AG and particularly Tamara Gabriel, Stefanie Wagner and Oliver Laus for the support they arranged on X-ray diffraction and fluorescence, BET, DSC, STA-TG.
- Dr. Stefan Kallus for his precious help and experience he gave me to record the different patents.
- Oliver Püttmann for the physical validation of the screening setup.
- Gerard Bollmann, Timo Emmert, Toni Pfennig as students during their Bachelor Theses, Davide Barbera during his internship for the additional knowledge, and support they brought to the project.
- Korwin Schelkle for his Master Thesis and further discussions.

I would also like to thank the Arbeitskreis Deutschmann at KIT and especially Lea Kahle and Karla Herrera Delgado for their contributions to the project, Denise Chan and Kathrin Schäfer for the dispersion measurements. Finally, I am grateful to Dr. Radian Popescu for the TEM measurements at KIT.

I am very proud and at least as much grateful for the BASF support that I got during these three years, particularly from Dr. Andrian Milanov and Dr. Ekkehard Schwab. Furthermore, I appreciate the fact that my work has been authorized for publication. Finally, I am also thankful for the support of the BASF analytical department, especially Dr G. Cox for the additional high-quality measurements made for the project and my PhD thesis.

I am also grateful to the other project partners:

- from Universität Leipzig, Prof. Roger Gläser, Juliane Titus, Bettina Stolze, Dr. Andreas Peters, for their fast, efficient, meaningful work on testing.
- from the Linde Group, Dr. Axel Behrens, Dr. Nicole Schödel, Stefan Hoffmann, for the feedback on promising patented materials.
- from TU München, Prof. Johannes A. Lercher, Dr. Andreas Jentys, Linus Schulz, for testing further samples, SEM pictures, and additional XRD measurements.

I owe a special thanks to Halgard Staesche for her advice, which helped me improving the quality of this thesis.

I would like to thank my buddy Eko Prasetyo for the interesting scientific discussions but also for the nice distractions to chill out during the long days at work.

I am grateful for the financial support of my project, the DryRef project, from the German Federal Ministry of Economics and Technology (FKZ 0327856A).

Finally, I would like to thank my parents and my brother Maxime for their support during the hard times. Last but not least, I am especially grateful to my beloved friend, Sandra, for her great support throughout my PhD thesis.

Until you try, you don't know what you can't do.

Henry James

Contents

Nomenclature

*	catalyst adsorption site
°C	degree Celsius
β	broadening at full width at half maximum or at integer breadth [-]
γ	surface tension of Hg [mN.m^{-1}]
ΔH_{298}	enthalpy of reaction at 298 K [kJ.mol^{-1}]
ΔH_j	enthalpy change of the reaction or adsorption of compound i at a temperature T [J.mol^{-1}]
$\Delta_R G_i$	free enthalpy of the reaction i [J.mol^{-1}]
ε_P	porosity of the material [-]
η	effectiveness factor [-]
θ	incident angle of the X-ray beam [rad]
θ'	contact angle [rad or °]
θ_0	angular position of the peak maximum [rad]
θ_A	degree of coverage of the reactant A on the catalyst surface [-]
λ	wavelength of X-ray beam or of photon (in Planck's equation) [m]
$\nu_{i,j}$	algebraic stoichiometric coefficient of the compound k for the reaction i [-]
τ	tortuosity [-]
ϕ	Thiele modulus [-]
Å	Ångström
ATR	AutoThermal Reforming
a.u.	arbitrary unit
bar	absolute pressure equal to 10^5 Pa
BET	Brunauer-Emmet-Teller
c	speed of light [m.s^{-1}]
c'	constant from BET equation including heat of adsorption and condensation [-]
C^*	concentration of free adsorption site on the catalyst surface [mol.m^{-3}]
C_A	concentration of A [mol.m^{-3}]
C_A^*	concentration of A adsorbed on the adsorption site * [mol.m^{-3}]
$C_{A,S}$	concentration of A at the surface [mol.m^{-3}]
$C_{f,i}^{out}$	specific correction factor of compound i [-]
$C_{P,i}^{out}$	specific heat capacity of compound i [J.mol^{-1}.K^{-1}]
CPOX	Catalytic Partial OXidation
CTEM	Conventional Transmission Electron Microscopy
d	distance between the spacing between diffraction planes [m]
dr	thickness of spherical shell for mass balance [m]
D	diffusion coefficient of A [m^2.s^{-1}]
D	dispersion [-]
D_0	initial dispersion [-]
D_{eq}	dispersion at infinite time [-]
D_e	effective diffusion coefficient of A [m^2.s^{-1}]

DEN	denominator of the reaction rate equations [-]
DryRef	CO_2 reforming or dry reforming
DSC	Differential Scanning Calorimetry
DTA	Differential Thermal Analysis
E	Energy of photon [J]
E_A	activation energy [J.mol^{-1}]
$E_{a,i}$	activation energy of the reaction i [J.mol^{-1}]
$E_{A,eff}$	observed activation energy related to r_{eff} [J.mol^{-1}]
$E_{A,true}$	activation energy at surface condition [J.mol^{-1}]
fcc	face-centered cubic
FID	Flame Ionization Detector
FWHM	Full Width at Half Maximum
GC	Gas Chromatography
GHSV	Gas Hourly Space Velocity
h	hour
h'	Planck's constant [J.s]
HAADF	High-Angle Annular Dark-Field
HGFM	High Gas Flow Meter
HRTEM	High Resolution Transmission Electron Microscopy
j	diffusion flux of A per area (three dimensional case) [mol.m^{-2}.s^{-1}]
j_r	diffusion flux of A per area on a shell of radius r (one dimensional case) [mol.m^{-2}.s^{-1}]
k	effective rate constant [mol.s^{-1}
k'	effective rate constant [mol.s^{-1}.Pa^{-1}]
k"	general rate constant
k_0	rate constant of sintering [s^{-1}]
k_1	rate constant of reaction 1 (WGS) under T [kmol.kg cat^{-1}.h^{-1}]
k_2	rate constant of reaction 2 (Steam Reforming) under T [kmol.bar$^{-0.5}$.kg cat^{-1}.h^{-1}]
k_3	rate constant of reaction 2 (Steam Reforming, with S/C=2) under T [kmol.bar$^{-0.5}$.kg cat^{-1}.h^{-1}]
k_{1,T_r}	rate constant of reaction 1 (WGS) under T_r [kmol.kg cat^{-1}.h^{-1}]
k_{2,T_r}	rate constant of reaction 2 (Steam Reforming) under T_r [kmol.bar$^{-0.5}$.kg cat^{-1}.h^{-1}]
k_{3,T_r}	rate constant of reaction 2 (Steam Reforming, with S/C=2) under T_r [kmol.bar$^{-0.5}$.kg cat^{-1}.h^{-1}]
k_A	rate constant coefficient of consumption of A [(mol$^{1-n_A}$.m$^{3.n_A}$.s^{-1}]
k_{eff}	kinetic rate coefficient of the observed reaction rate for first order reaction [m^3.s^{-1}]
$k_{Scherrer}$	constant for Scherrer equation [-]
K	constant [-]
K_A	equilibrium constant from the law of mass action [bar^{-1}]
K_i	equilibrium constant from the law of mass action of reaction i=2 or 3 [bar^2], for i=1 [-] according to Xu and Froment
K_j^0	coefficient of adsorption at temperature T_r for j=CH_4, H_2O, CO, H_2 [bar^{-1}]
K_j	coefficient of adsorption at temperature T for j=CH_4, H_2O, CO, H_2 [bar^{-1}]
K_{H_2O}	coefficient of adsorption at temperature T for H_2O [-]
$K_{H_2O}^0$	coefficient of adsorption at temperature T_r for H_2O [-]
kJ	kilojoule
kmol	kilomole
KIT	Karlsruhe Institute of Technology
kV	kilovolt
l	liter
L_{hkl}	particle size in the perpendicular direction to the (hkl) - Miller index - plane [m]
LBD	Loose Bulk Density [g.ml^{-1}]
LOI	Loss On Ignition [-]
m	meter
m	order/random coefficient [-]

mA	milliampere
mbar	millibar
$m_{cat.}$	mass of catalyst [kg]
$\dot{m}_C$	coke precursor molar rate [g.s^{-1}]
$M_{C,i}$	molar mass of compound i [g.mol^{-1}]
MFC	Mass Flow Controller
min	minute
ml	milliliter
mN	millinewton
MP	MagnetoPlumbite
MS	Mass Spectrometry
MSCR	Mixed Steam-CO_2-Reforming
n_A	partial order of reaction with respect to reactant A if A reacts with itself or decomposes, or overall order of reaction [-]
n	integer [-]
p_k	partial pressure of k [bar]
P_0	saturation pressure [bar]
P_i	partial pressure of i [bar]
ppmw	particle per million by weight
P	applied pressure in BET equation [bar]
P'	applied pressure in Washburn equation [Pa]
PAH	polycyclic aromatic hydrocarbons
PBG	Pressure Build-up Gas
PGM	Platinum Group Metal
PHG	Pressure Hold Gas
POX	Partial OXidation
ppm	particle per million
PSA	Pressure Swing Adsorption
r	radius of spherical shell [m]
r_A	consumption rate of A [mol.m^{-3}.s]
r_{eff}	efficient reaction rate [mol.m^{-3}.s]
r_P	radius of pore [mm]
r_S	reaction rate that would be obtained at surface conditions [mol.s^{-1}]
R	constant of the ideal gas [J.mol^{-1}.K^{-1}]
R	radius of catalyst particle [m]
rad	radian
Rec_i	percentage of i recovered in the product stream [-]
RDS	Rate-Determining Step
RIR	Reference Intensity Ratio
sccm	standard cubic centimeters per minute
SEM	Scanning Electron Microscopy
SMR	Steam Methane Reforming
SPARG	Sulfur PAssivated ReforminG
SMR	Steam Methane Reforming
S/C	Steam-to-Carbon ratio [-]
SEM	Scanning Electron Microscopy
STA	Simultaneous Thermal Analysis
STEM	Scanning Transmission Electron Microscopy
STY_i	Space-Time Yield of product i [mol.m^3.s^{-1}]
t	time [s]
T	temperature [K]
$T_{Huettig}$	temperature of Hüttig [K]

T_{Tamman}	temperature of Tamman [K]
T_r	reference temperature in Xu and Froment model [K]
TCD	Thermal Conductivity Detector
TEM	Transmission Electron Microscopy
TG	ThermoGravimetry
TOF_i	TurnOver Frequency of compound i [h^{-1}]
TPD	Temperature-Programmed Desorption
TPO	Temperature-Programmed Oxidation
TPR	Temperature-Programmed Reduction
V	absorbed gas volume [m^3]
$V_{cat.}$	volume of catalyst [m^3]
V_m	molar volume [22.4 $l.mol^{-1}$]
V_M	volume of the monolayer [m^3]
$\dot{V}_i^{in}$	molar flow rate of i in feed stream [$mol.s^{-1}$]
$\dot{V}^{out}$	volumetric flow rate of product stream corrected [$m^3.s^{-1}$]
$\dot{V}^{out}$,	volumetric flow rate of product stream uncorrected [$m^3.s^{-1}$]
$\dot{V}_i^{out}$	molar flow rate of i in the product stream [$mol.s^{-1}$]
vol.%	volume percent
X_i	conversion of compound i [-]
XRD	X-Ray Diffraction
XRF	X-Ray Fluorescence
wt.%	weight percent
WTY	Weight-Time Yield of compound i [$mol.s^{-1}.kg^{-1}$]
YAG	Yttrium Aluminum Garnet
YSZ	Yttria-Stabilized Zirconia

Part I

Introduction and motivation

The most important greenhouse gas arising from anthropogenic activities is CO_2 [1], and its emissions increased significantly over the past years, reaching in 2010 over 30 Gt (Gigatons) of CO_2 [2]. In order to minimize the impact of the greenhouse gas CO_2, it can be used where it is produced on a large scale, like in fossil fuel power plants and also in ammonia synthesis. Indeed, both of these sources produce large amounts of CO_2 that can be sequestered for storage [3;4] or used as raw chemical [5;6].

The large storage capacity of CO_2 can help neutralizing the CO_2 emission for a few decades, with a current CO_2 storage capacity estimated around 1000-20000 Gt [7]; however, CO_2 storage is limited by the energetic waste required for CO_2 capture and compression [8]. In addition, CO_2 storage may become unsafe and risky in the long term due to potential leaks [9]. Application of CO_2 on a large scale as a raw material is, therefore, more attractive than CO_2 storage.

Reforming of methane with CO_2 can be a potential application on a large scale, as shown in Fig. 1. Indeed, CO_2 reforming of methane can produce a syngas with a theoretical H_2/CO ratio of one, which is lower than the H_2/CO ratio delivered by partial oxidation, steam reforming, or autothermal reforming of methane, which typically achieve only H_2/CO ratios of 1.7 [10]. Such a syngas with a rich CO content offers the possibility to produce syngas stoichiometries suitable for processes such as the direct synthesis of aldehydes and alcohols with the oxo-synthesis [11;12] or olefin/gasoline synthesis by Fischer-Tropsch synthesis [12–14].

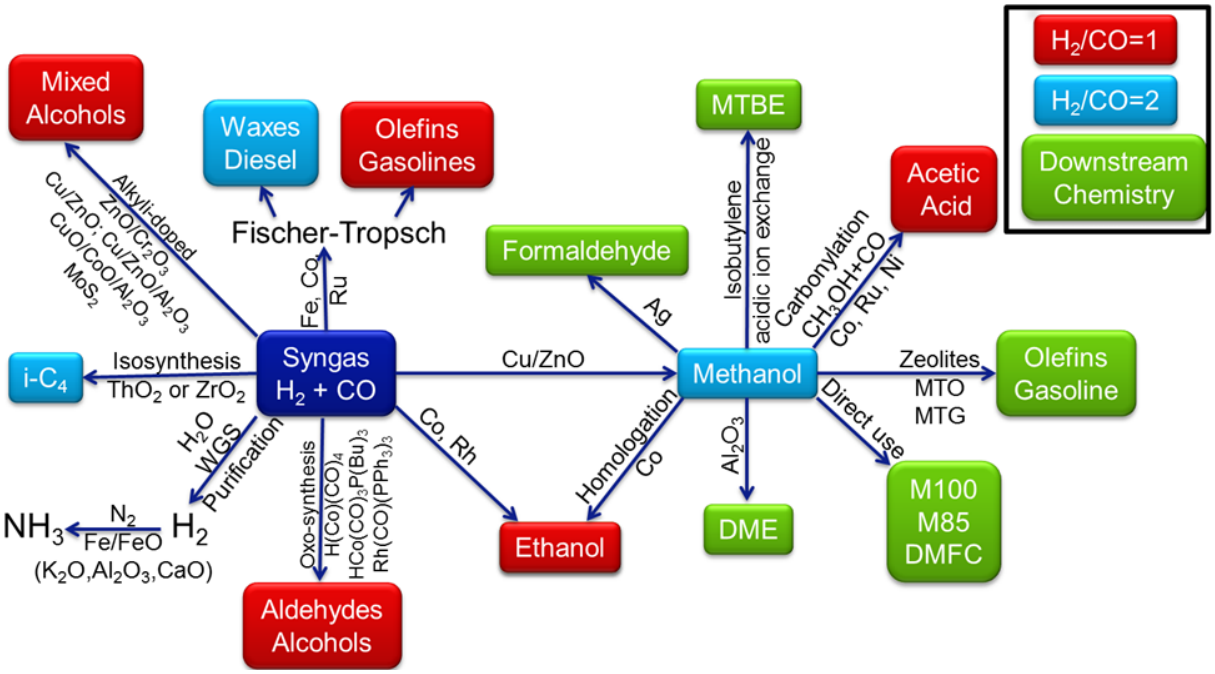

Figure 1: Use of syngas in chemical industry (taken from [15]);DME, DiMethyl Ether; DMFC, Direct-Methanol Fuel Cell; i-C_4, isobutane; M85, mixture of 15% methanol in benzine; M100, pure methanol; MTBE, Methyl Tertiary-Butyl Ether

CO_2 reforming of methane is well established at low pressure (1-7 bar)[16–20], but this process suffers from an inherent drawback because upstream and downstream processes operate preferentially at high pressures. Therefore, CO_2 reforming of methane conducted at high pressure for the production of syngas with a H_2/CO ratio of one is promising due to its easy integration in downstream platform technologies.

The addition of water, even in small amounts in CO_2 reforming, can help adjusting the H_2/CO ratio through the water gas shift reaction. Moreover, water addition can enhance the gasification rate of carbonaceous species on the catalyst surface. If water is added, the process is described as mixed-steam CO_2 reforming.

Commercial methane reforming processes are conducted at high temperature to enhance reforming reaction rates and syngas yields because of a shift in equilibrium due to the reforming reaction of methane with steam and CO_2 being highly endothermic. Typically, a temperature range of 773-1223 K (500-950°C)[21] and a pressure between 20-40 bar are applied in industrial steam reforming processes[21]. In the case of mixed-steam CO_2 reforming of methane, only temperatures above 973 K (700°C) are realistic to avoid disproportionation of CO in the CO-rich syngas, which results in carbon deposits. The use of such high temperatures implies that gas-phase reactions, in addition to catalytic reactions, may occur due to the methane decomposition[22;23] and further coupling, resulting in the formation of coke precursors like ethylene. As a result, the catalyst as well as the reactor concept should be adapted to achieve high catalytic performances in reforming despite of the impact of gas-phase reactions.

The reforming catalysts can be produced with active metals including noble metals[24–28] and transition metals[29–35]. Noble metals have an enhanced coke resistivity in comparison to transition metals. However, the high price and the low availability of noble metals[10] limit their applications and do not facilitate scale up of such catalysts for industrial purposes. Typically, nickel is used to substitute noble metals in reforming processes; however, nickel is known to be prone to coking because carbon can dissolve in the Ni surface layer[36]. Minimizing coke deposition on metallic Ni particles and catalyst support is necessary for commercial mixed-steam CO_2 reforming of methane.

The investigations conducted in this study consist of the development of active masses as well as a process concept for the valorization of CO_2 within the process of methane CO_2 reforming under high pressure (21 bar) and relevant commercial operating conditions in order to achieve a syngas with a H_2/CO ratio of one.

The major challenge that must be faced in mixed-steam CO_2 reforming of methane is coking, particularly with Ni-based catalysts. The coke selectivity on such Ni-based catalysts is believed to be suppressed by using small Ni nanoparticles[37;38], whereas large Ni nanoparticles exhibit enhanced selectivity of coke

formation[39–41]. Therefore, the synthesis of highly dispersed and stable metallic Ni nanoparticles can be an attractive solution for the development of stable and active catalysts for the target process.

Based on this work assumption, the following concept is used for the production of such highly dispersed and stable metallic Ni nanoparticles for their application in high temperature mixed-steam CO_2 reforming of methane. A carrier material is used to disperse Ni on an atomic scale, for instance by dissolving Ni in a solid solution, like the (Ni/Mg)O solid solution[42;43], or by dissolving Ni in a material lattice like perovskites[44;45] or hexaaluminates[46;47]. Due to the high dispersion of Ni^{2+} in the carrier material, the subsequent reduction is expected to lead to an enhanced dispersion of metallic Ni nanoparticles[47]. Finally, the highly dispersed Ni nanoparticles as well as the catalyst support should be thermally stable and especially stable against sintering. Indeed, sintering leads to the formation of large Ni particles that are likely to undergo coking[39–41].

Four different subjects are highlighted in the framework of this PhD thesis to design catalysts for the mixed-steam CO_2 reforming of methane under high pressure and at high temperature.

- First, the impact of the gas-phase reactions is evaluated over a wide range of industrially relevant temperatures for methane reforming in the presence of steam as well as CO_2.
- Second, Pt-based catalysts with various zirconia supports are developed to generate kinetic data and highlight a possible mechanism of mixed-steam CO_2 reforming over Pt-based catalyst.
- Third, an unconventional preparation of Ni-based spinel catalysts prepared with hydrotalcite-like clay is benchmarked against typical preparation routes for their application in mixed-steam CO_2 reforming at high pressure.
- Fourth, Ni hexaaluminate design of experiments for their application in CO_2 reforming is performed in a small-scale unit at moderate pressure, and the formation of highly stable and dispersed Ni nanoparticles is investigated.

Part II

Theoretical concepts

1 Reforming technologies

Production of hydrogen and syngas can be achieved by numerous processes using large variety of feedstocks, such as liquid and gaseous hydrocarbons, alcohols, carbohydrates[48], by-products of third processes like glycerol in the production of biodiesel[49], and even solid feedstock like coal[50] or biomass[51]. The following equations represent the most common reactions involving methane and heavier hydrocarbons (C_mH_n) used on a technical scale[48]:

- Steam reforming:

$$CH_4 + H_2O \rightleftharpoons CO + 3\ H_2 \tag{1.1}$$
$$C_mH_n + m\ H_2O \rightleftharpoons m\ CO + (m + n/2)\ H_2 \tag{1.2}$$

- Partial oxidation

$$CH_4 + 1/2\ O_2 \rightleftharpoons CO + 2\ H_2 \tag{1.3}$$
$$C_mH_n + m/2\ O_2 \rightleftharpoons m\ CO + (n/2)\ H_2 \tag{1.4}$$

- Autothermal reforming or oxidative steam reforming

$$CH_4 + 1/4\ O_2 + 1/2\ H_2O \rightleftharpoons CO + 5/2\ H_2 \tag{1.5}$$
$$C_mH_n + m/4\ O_2 + m/2\ H_2O \rightleftharpoons m\ CO + (m/2 + n/2)\ H_2 \tag{1.6}$$

- Gasification of carbon (coal, coke)

$$C + H_2O \rightleftharpoons CO + H_2 \tag{1.7}$$
$$C + O_2 \rightleftharpoons CO_2 \tag{1.8}$$
$$C + 1/2\ O_2 \rightleftharpoons CO \tag{1.9}$$
$$C + CO_2 \rightleftharpoons 2\ CO \tag{1.10}$$

- Water Gas Shift (WGS) or Reverse Water Gas Shift (RWGS)

$$CO + H_2O \rightleftharpoons CO_2 + H_2 \tag{1.11}$$

The WGS/RWGS equilibrium 1.11 is always involved in reforming processes. Most of these reactions occur on specific catalysts at given operating conditions.

1.1 Reforming processes

A broad variety of reforming processes has been developed to fit also a large range of requirements needed in downstream processes for commodity chemicals. In this study, I will restrict the description of the reforming processes to stationary applications. For these applications, two categories are identifiable with regard to the desired products.
First, the production of pure H_2 from syngas with a high H_2/CO ratio (over 2.5-3) with a subsequent shift of the equilibrium to H_2 and CO_2 is used mainly for ammonia production. Second, the production of syngas with a low H_2/CO ratio (lower than 2-2.5) is further used to synthesize gas-to-liquids products, methanol, phosgene, acetic acid, and products from oxosynthesis[13].

1.1.1 Steam reforming

This reforming process is well-known and used since the 30s for hydrocarbon reforming[52]. This reforming application produces a syngas with a H_2/CO ratio in the range of about 2.2 to 4.8[48] depending on the feed composition. Steam reforming is often conducted with natural gas, which is available worldwide, relatively cheap, and in large quantities[53–55]; however, heavier hydrocarbons like naphtha are also used but hydrocarbons with a higher boiling point than naphtha have not reached the commercial stage yet[52]. For instance, Steam Methane Reforming (SMR) proceeds in two steps, the reforming reaction (Eq. 1.1), which is strongly endothermic (206 kJ.mol^{-1}), and the WGS (Eq. 1.11), which is slightly exothermic (-41 kJ.mol^{-1}). Before using natural gas, desulfurization of natural gas must be achieved to avoid catalyst poisoning (see section 2.5). The sulfur content in fuel streams is usually kept under 1 ppmw (particle per million by weight)[10].
The following equations represent a set of possible reactions with their respective enthalpy at 298 K under steam-reforming conditions:

- Steam Methane Reforming (SMR - Eq. 1.1)

$$CH_4 + H_2O \rightarrow CO + 3\ H_2 \qquad \Delta H_{298} = 205.9\ kJ.mol^{-1}$$

- Water Gas Shift (WGS - Eq. 1.11)

$$CO + H_2O \rightarrow CO_2 + H_2 \qquad \Delta H_{298} = -41\ kJ.mol^{-1}$$

- Boudouard reaction (Eq. 1.10)

$$2\ CO \rightarrow CO_2 + C \qquad \Delta H_{298} = -172.4\ kJ.mol^{-1}$$

- Coke gasification (Eq. 1.7)

$$C + H_2O \rightarrow CO + H_2 \qquad \Delta H_{298} = +131.3\ kJ.mol^{-1}$$

- Methane cracking

$$CH_4 \rightarrow C + 2\ H_2 \qquad \Delta H_{298} = +74.6\ kJ.mol^{-1} \tag{1.12}$$

- CO oxidation

$$CO + 1/2\ O_2 \rightarrow CO_2 \qquad \Delta H_{298} = -283\ kJ.mol^{-1} \tag{1.13}$$

A simplified steam reforming scheme is presented in Fig. 1.1.

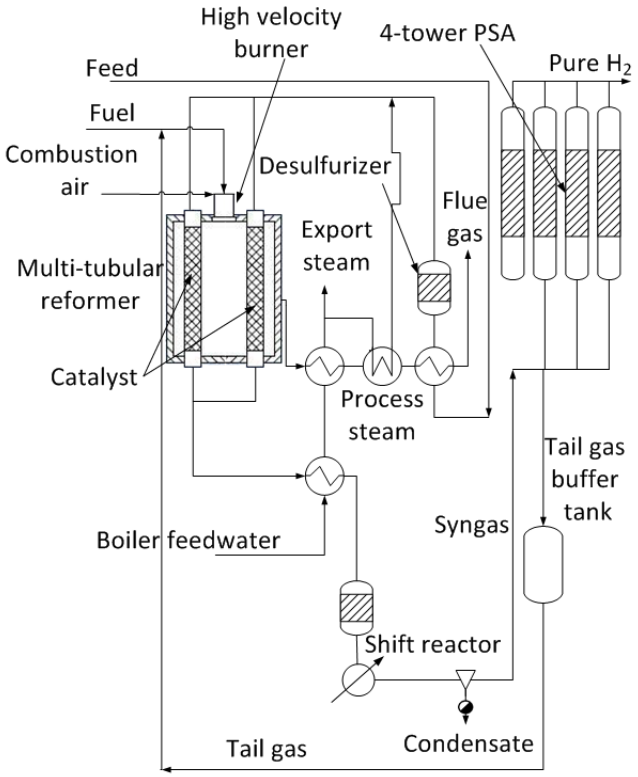

Figure 1.1: Simplified flow sheet of industrial-scale steam reforming of hydrocarbons (taken from[56])

Part of the hydrocarbon feed is burnt with air to heat up the reformer, and the recovered heat at the reformer outlet is used for steam production and feed preheating. The hydrocarbon feed must first be desulfurized and preheated before entering the catalyst reformer tubes. The preheated feed passes through the catalytic bed in a multi-tubular reformer reactor. Usually steam reforming is performed at around 773-1173 K (500-900°C), above 20 bar, and with a steam-to-carbon ratio of around 2.5-3 to ensure coke-free operations[10]. If maximum hydrogen production is desired, the reformer outlet undergoes first the WGS reaction to maximize the hydrogen production. The hydrogen is then purified to above 99.95% purity by

getting rid of steam and CO_2 through condensation and Pressure Swing Adsorption (PSA)[57;58], respectively. Instead of PSA for CO_2 recovery, a permeable reactor membrane can be used[59;60]. The tail gas after PSA is used to enrich the fuel and provide further energy to heat up the reformer.
Most of the hydrogen is used to synthesize ammonia for the production of fertilizers, but for the past few years, the growing attractiveness of fuel cells has also lit up its application in electrochemical systems.

1.1.2 Partial Oxidation (POX) and Catalytic Partial Oxidation (CPOX)

In contrast to endothermic steam reforming, POX and CPOX are exothermic. The reaction enthalpy of methane POX (Eq. 1.3) is equal to $\Delta H_{298} = -35.9\ kJ.mol^{-1}$, and the syngas produced has a H_2/CO ratio close to 2, which is attractive for several chemical syntheses like direct methanol synthesis[12] or Fischer-Tropsch synthesis[13;14].
Conducted mainly over a temperature range of 1423-1773 K (1150-1500°C) and a pressure range of 25-80 bar[61], the homogeneous POX still requires an additional heat management equipment. The high pressure and pure oxygen required by the economics of the downstream processes are responsible for the primary costs[62]. Further costs are expected for post treatments, separation of acid gases, and treatment of coke and soot[61].
The advantage of CPOX over POX is that it includes a heterogeneous catalyst and, therefore, requires lower temperatures; however, CPOX is still at the stage of catalyst development[14]. The reaction pathway for POX and CPOX is not completely understood[61;63]. For POX, all carbon-carbon bonds are destroyed, resulting in the formation of CO and H_2; after complete hydrocarbon destruction, H_2O and CO_2 can be formed by using the oxygen surplus[63]; however, other results have shown that the formation of H_2O and CO_2 stems from the primary reactions[63;64]. For CPOX a similar reaction pathway has been observed: catalytic partial oxidation of methane dominates on the upstream of the catalytic bed, whereas WGS and steam reforming take place on the downstream part of the catalytic bed[65]. CPOX is particularly adapted for mobile applications like in fuel cells[66] due to its simplicity and possibility of small-scale applications.
Commercially, three types of partial oxidation processes are established, representing worldwide more than 320 operating plants[63]:

- the Texaco process used only natural gas as feedstock and changed to liquid hydrocarbons only after the process of steam reforming of natural gas became available[63],
- the Shell process used heavy oils from the beginning[63],
- the Lurgi process used the broadest range of feedstock including gasification of tars, oils, and slurries formed as by-products of fixed bed gasification[63].

The reactor design of POX and CPOX is presented as a scheme in Fig. 1.2. The POX reactor simply comprises two zones, first the flame part where the hydrocarbons, oxygen, and possibly low amounts of steam react together and second a heat exchanger that recovers the heat excess after the reaction. The

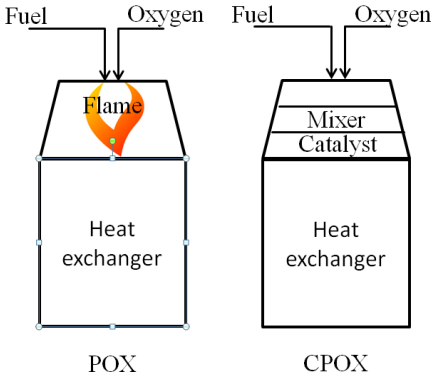

Figure 1.2: Reactor designs for POX and CPOX (taken from[61])

CPOX reactor design is similar to POX, but the flame part is replaced by a mixer before the catalytic bed to homogenize the mixture and avoid coke deposits.
Depending on the downstream processes, the syngas can be directly used after clean-up or first shifted to another equilibrium to obtain the desired H_2/CO ratio.
The CPOX and POX processes will not be retained to benchmark the performance of the process developed in this thesis due to the fundamental differences in process design (e.g. presence of flame, very high temperature,...).

1.1.3 Autothermal reforming (ATR)

ATR is another alternative technology using both steam reforming and partial oxidation in which the resulting overall reaction enthalpy is closer to zero than for either CPOX or steam reforming. In order to achieve an overall enthalpy close to zero, the workflow has to be delicately balanced between the exothermic partial oxidation and the endothermic steam reforming. The ATR is usually performed between 1173-1773 K (900-1500°C) in the range of 1-80 bar[61]. The H_2/CO ratio produced can vary depending on the amount of steam, oxygen, and fuel used in the feed and is usually close to 2, which makes it attractive for methanol and Fischer-Tropsch synthesis[10]. The process flexibility with regard to feed composition (e.g. hydrocarbons, steam-to-carbon ratio) and operating conditions (e.g. pressure 30-40 bar) are the reasons for its attractiveness[10]. For instance, the ATR process is often used after a steam reformer (primary reformer) and used as "secondary reformer", which corresponds to the actual standard technique in the production of ammonia synthesis gas[10].
Because a robust burner, mixer, and significant heat exchange requirements, like in steam reforming or POX, are no longer necessary for ATR, low-cost and compact reactors can be built[61], for instance for fuel-cell applications[67;68]. Nevertheless, the process remains dependent on expensive pure oxygen at high pressure.
Different reactor designs exist, the two-step ATR process that uses the CPOX reactor design with a steam feed after the partial oxidation reactions, the one-step process that combines both steps in a fluidized bed like Exxon does, or with H_2O and O_2 in the feed stream for a "secondary reformer"[52].

Like POX and CPOX, the ATR process will not be used to benchmark the performance of our process due to the fundamental differences in process design.

1.1.4 Gasification of coal and biomass

Coal's share of the global energy mix will overtake oil in 2017[69], showing how attractive and strategically important coal feedstocks are. For syngas or energy production, gasification of coal and biomass such as wood is also of interest. Three different sectors for gasification products are identifiable[70]:

- syngas with variable H_2/CO ratios for various syntheses: ammonia, gas-to-liquids products, and methanol;
- methanation for the synthetic natural gas production;
- power generation by combustion of products in gas turbines.

This list excludes combustion as it mainly produces CO_2 and H_2O, which do not have leftover heat energy.

Gasification processes allow processing of any hydrocarbon feedstock, gas feedstock, as well as petroleum coke, and the H_2/CO ratio is variable depending on the carbon source, but also carbon-to-oxygen and steam-to-carbon ratios that are used in the feed. This high flexibility can explain the large number of operating gasifiers. There were a total of 366 gasifiers, producing about 42700 MW in 2007[70].

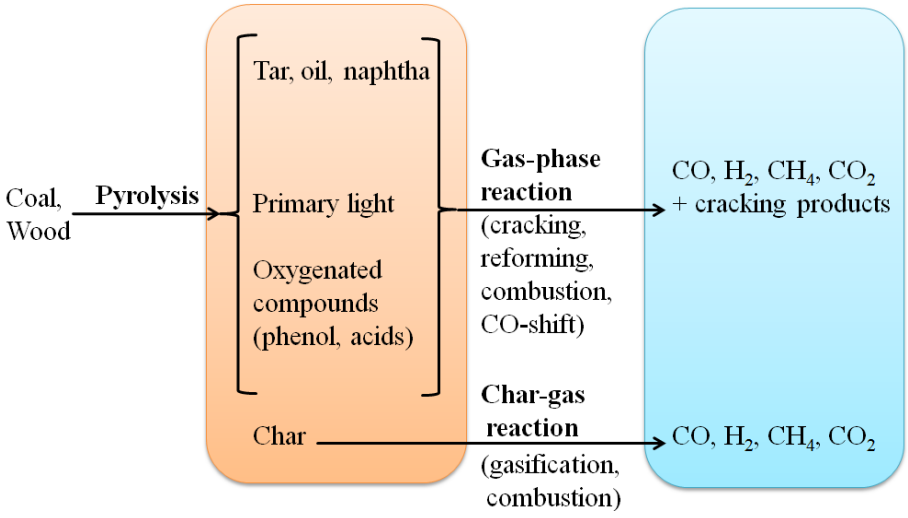

Figure 1.3: Schematic reactions of coal and wood gasification (taken from[71])

The gasification of solid feedstock is a complex chemical process that involves both homogeneous and heterogeneous reactions coupled with heat and mass transfer. This gasification process generally includes evaporation of moisture followed by pyrolysis of coal and subsequent gas-phase reactions as well as heterogeneous reactions of char with gaseous compounds[70]. From all of these steps, the char gasification is

the rate-controlling process and is performed at high temperatures (1073-2073 K, 800-1800°C). The corresponding reaction scheme is given in Fig. 1.3. For all gasification processes, post treatment of product gas that includes several steps is required to remove sulfur compounds, inert gases, and acids [70;71](HCN, organic acids, unsaturated, and heavy hydrocarbons).

Due to the large amount of gasification processes [72], they can be classified as described in Tab. 1.1, and the different reactors are presented in Fig. 1.4.

Classification criteria	Variable	Classification criteria	Variable
Type of gasification reactor (Fig.1.4)	moving fixed bed fluidized bed entrained flow molten bath	Type of solid feed	coal wood, biomass solid waste materials petroleum-derived residue
Gasifying medium	air oxygen steam steam/air steam/oxygen hydrogen	Heat supply for gasification reactions	internal external
Particle size of solid feedstock	fine medium corse	Operating pressure	atmospheric elevated
Condition of gasification residue to be removed	dry ash in non-slagging operation slag in slagging operation	Application of product gas	residue fuel gas syngas synthetic natural gas

Table 1.1: Classification of gasification processes (taken from [71])

In a moving bed (non-slagging counter current), granular or lump fuel is introduced at the top of the reactor while the gasifying medium is blown from the bottom. The outgoing ashes heat the gas inlet before the outlet, and the syngas exit heats up the feed, resulting in an excellent energy efficiency of the process [73]. Due to long residence times of the moving particles inside the bed , a high carbon conversion is reached [71;73].

The gas velocities used in the fluidized bed reactor are high enough to allow the catalyst bed to be fluidized. This bed is constituted of small particles (about 1 mm) mixed as if used in a perfectly mixed reactor [74]. Furthermore, this process requires a heat recovery system for a better energy efficiency [71].

In the entrained flow reactor, gas and carbonaceous feed move in the same direction. Because of short residence times of a few seconds, the feed particles used should be very small (typically <100 μm) and elevated temperatures as high as 1773 K (1500°C) are necessary to achieve sufficient carbon conversion [73;75].

The molten-bath reactor uses a melt made of molten slag, metal, or salt, and the gasifying medium is injected into it [72]. The slag is used as a heat-transfer medium [71].

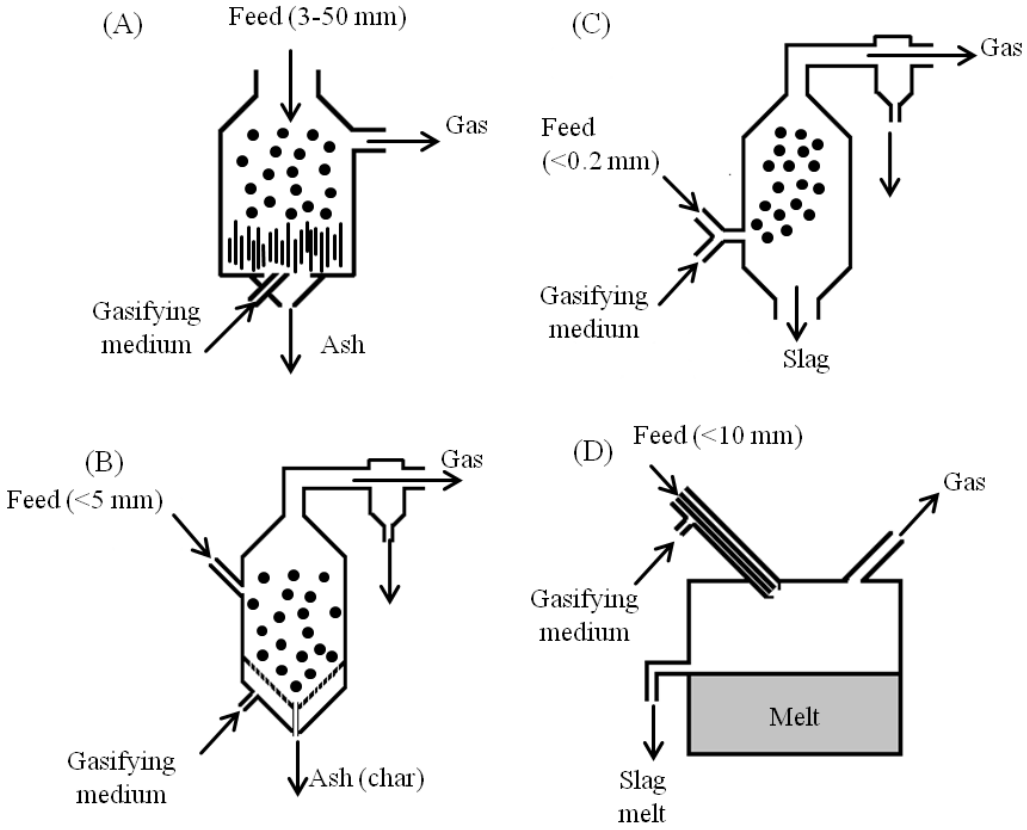

Figure 1.4: The 4 types of gasifier reactors (taken from[71]), (A) moving bed (non-slagging counter current), (B) fluidized bed, (C) entrained flow, (D) molten bath.

The different feedstocks should also be characterized because the feed properties must meet the requirements of the chosen process. First, the molar ratios (hydrogen/carbon and oxygen/carbon) are of interest since they determine the composition of the syngas. Solid carbonaceous feedstocks also have different properties such as moisture content, ash content, volatile matter (oil, tar, gas, phenol compounds), residual char after pyrolysis, caking behavior, reactivity, and particle-size distribution that influence the gasification process[71].

Environmental matters depend on the process. With regards to air emissions, sulfur compounds (H_2S, COS and CS_2), NOx, and NH_3 should be removed before they exit the reactor, and with regards to waste water obtained from low temperature raw gas (moving bed), it should also be treated with conventional wastewater purification methods to remove tar and phenol products[70;71].

1.1.5 CO_2 reforming and mixed-steam CO_2 reforming (MSCR)

Since CO_2 is available in steam reformer exhausts, its recycling or further use of CO_2 becomes interesting. CO_2 can be used in reforming either as a substitute of steam in pure CO_2 reforming, which is also known as dry reforming, or as an additional complement in mixed-steam CO_2 reforming (also called combined-steam CO_2 reforming). The major drawbacks of the pure CO_2 reforming of methane is that

it is 40 kJ more endothermic (Eq. 1.14) than steam reforming and that the higher carbon concentration favors coke deposition.

$$CH_4 + CO_2 \rightarrow 2\,CO + 2\,H_2 \qquad \Delta H_{298} = +246\,kJ.mol^{-1} \tag{1.14}$$

However, the major advantage is that the H_2/CO ratio can be decreased to below one due to the RWGS, allowing production of CO-rich syngas. The addition of steam in the feed has several advantages: it helps controlling the H_2/CO ratio required for the downstream processes and avoids coke deposition or at least limits it.

The flow chart of the MSCR, based on Fig. 1.1, is simplified and presented in Fig. 1.5.

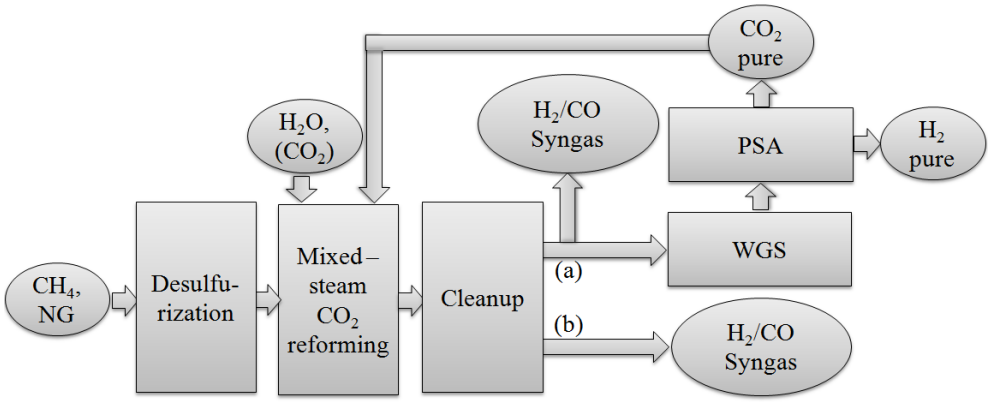

Figure 1.5: Simplified flow chart of mixed-steam CO_2 reforming. NG, natural gas; solution (a), production of CO-rich syngas and pure H_2; solution (b), production of CO-rich syngas

The feedstock is first desulfurized up to less than about 1 ppmw[10]. Then the steam and CO_2 are mixed and preheated in the convective part the reformer, and then reformed at high temperatures in the reformer reactor heated by combustion of natural gas with air. At the reactor outlet, the heat is recovered and the hydrocarbons that did not react are removed. Afterwards two different production alternatives exist: the production of (a) a syngas with a low H_2/CO ratio and pure hydrogen including a recycling step or (b) simply low-H_2/CO-ratio syngas. The first alternative is obviously more expensive due to an additional step to shift the equilibrium to increase the CO_2 conversions and to separate CO_2 by the pressure swing adsorption. According to the requirements of syngas from (b), a PSA step can be added to remove CO_2 that can be recycled.

1.1.5.1 Sulfur-PAssivated ReforminG (SPARG) process

The sulfur-passivated reforming developed by Haldor Tops∅e operates at high carbon concentrations and favorable thermodynamic coke-formation conditions (see Fig 1.11 of this part (II)). The process benefits from controlling the amount of hydrogen sulfide in the feed stream that block the carbon nucleation sites on the catalyst through chemisorption of H_2S on the step sites of metallic Ni particles[21;76;77]. The "ensemble control", described by Rostrup-Nielsen[19], explains thanks to density-functional-theory

calculations how the thermodynamic influence can be partially "overcome". It has been also shown that potassium and gold act in the same way, that is, by chemisorption on step sites[21].

Figure 1.6 shows the simplified process flow diagram. The feed and the reformer are heated by combustion of fuel and tail gas with air. CO_2 is added to the feed, while steam addition allows better control of coking and flexibility in adjusting the syngas composition to H_2/CO ratios between 0.7 and 1.9[20]. Such

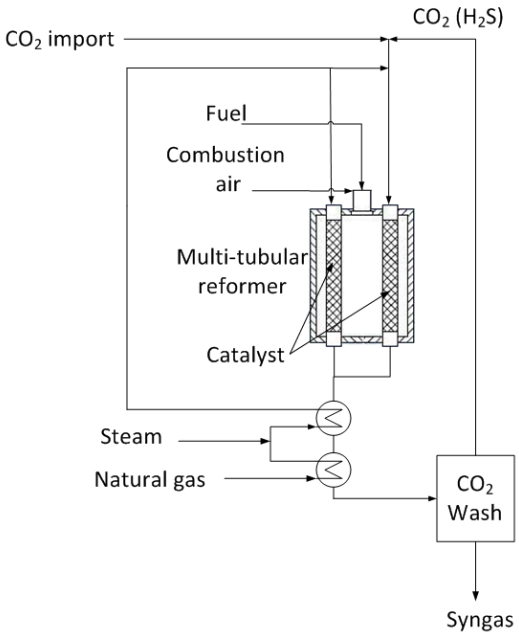

Figure 1.6: Simplified SPARG process flow diagram (taken from[20])

a process can be used to prepare CO-rich syngas for the synthesis of the acetic acid, dimethyl ether and oxoalcohols[78], or for the direct reduction of iron ore[79] that cannot be achieved by conventional steam reforming.

1.1.5.2 Calcor process

CO-rich syngas can also be produced by the Calcor process (Fig 1.7). This process works at low pressure and high temperature with a desulfurized feed.

The desulfurized feed and CO_2 are heated up and sprayed through a high velocity burner to provide the heat for the highly endothermic reaction. The flame is fed by a fuel (usually hydrocarbons from the feed) and tail gas from CO purification. Syngas can be then compressed and CO filtered off through membrane processes as in the Economy Calcor process described in Fig. 1.7. Otherwise, an alternative is suggested, that is, the Standard Calcor process[18], which directly produces a syngas with a low H_2/CO syngas after purification with CO_2 recycling.

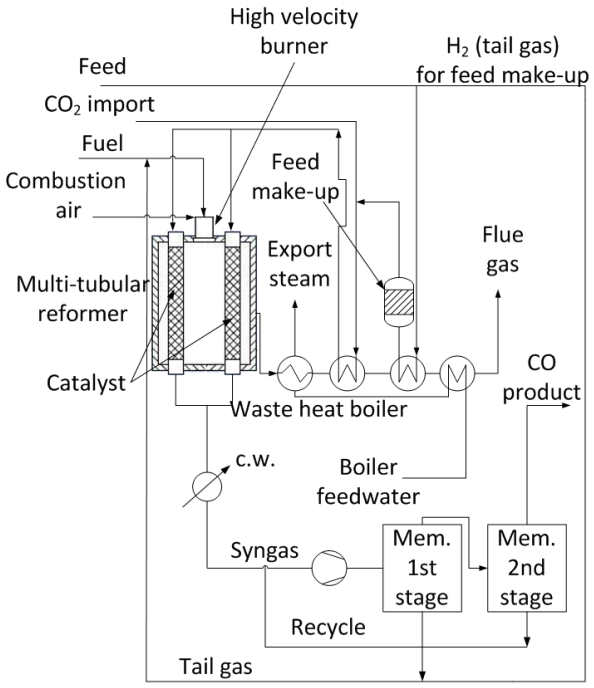

Figure 1.7: Simplified Economy Calcor flow sheet diagram (taken from [18], c.w., cooling water; Mem., Membrane)

1.2 Reforming thermodynamics

For conception and optimization of processes, thermodynamic reforming equilibria should be calculated. The influence of temperature, pressure, and feed composition will be discussed because of their influence on the thermodynamic equilibria. The calculations of this section have been performed with the help of DETCHEM^{EQUIL}; this freeware [80] is available online from Deutschmann's group at the Karlsruhe Institute of Technology (KIT). This computational tool determines equilibrium gas-phase compositions based on Gibbs free enthalpy minimization. Further calculations were made with the CH_4, H_2O, CO, CO_2, and H_2 species on the basis of three types of reforming of methane by using stoichiometric amounts of reactants in the feed (Tab. 1.2): steam reforming, CO_2 reforming (or dry reforming), and mixed-steam reforming, and reactions at 1123 K (850 °C) and 21 bar. The choice of pressure and temperature is based on our test conditions.

Conditions	Pressure	Temperature	Composition	
SMR	21 bar	1123 K (850°C)	CH_4/H_2O=1/1	SMR
CO_2 reforming of methane	21 bar	1123 K (850°C)	CH_4/CO_2=1/1	CH_4-DryRef
Mixed-steam CO_2 of methane	21 bar	1123 K (850°C)	$CH_4/H_2O/CO_2$=1/1/1	CH_4-MSCR

Table 1.2: Standard conditions used for the simulations of reforming equilibria

1.2.1 Effect of pressure on reforming equilibria

Pressure is known to have a major influence on the conversions of methane and CO_2 in reforming reactions, where 4 mol of products are made of 2 mol of reactants. As Le Chatelier's principle states, increasing the pressure favors the side of the equilibrium with the least number of gaseous molecules.

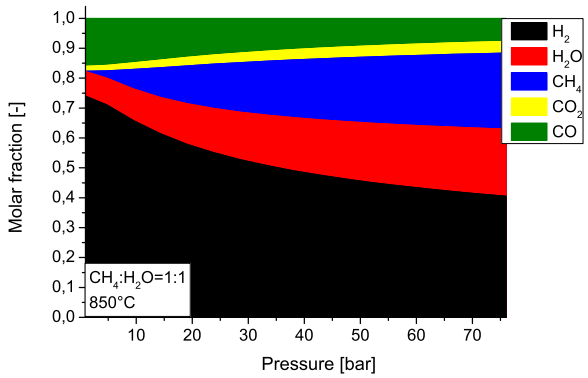

(a) Molar fractions at SMR equilibrium

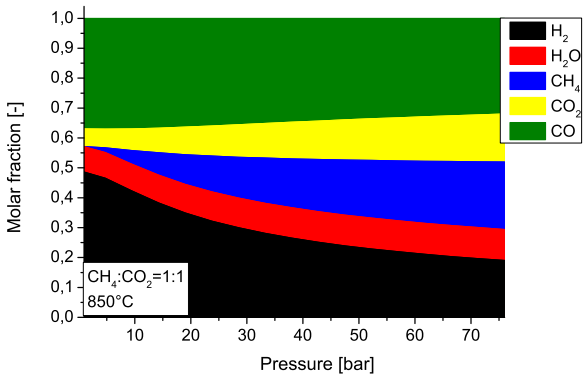

(b) Molar fractions at CH_4-DryRef equilibirum

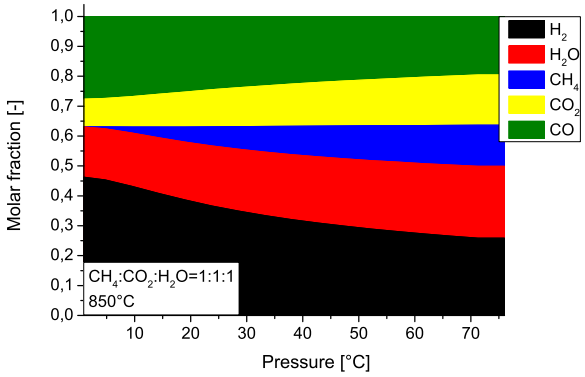

(c) Molar fractions of CH_4-MSCR equilibrium

Figure 1.8: Effect of pressure on thermodynamic equilibria of reforming reactions of methane

In Fig. 1.8, the pressure effect can be seen. Independent of the reforming conditions and pressure, steam and CO_2 are observed under thermodynamic conditions even if they are not present initially in the feed. The presence of steam even at reforming equilibrium could be used to our advantage by lowering the severity of the operating conditions of CO_2 reforming without significant modification of the syngas composition produced by addition of little amount of water to the feed (about 10-20 vol.%). Indeed, the presence of steam could enhance carbon gasification. The H_2/CO ratio decreases with a higher pressure except for steam reforming.

In addition to the conversions, the coke deposition is also affected by a pressure increase. This matter will be further discussed in section 1.2.4.

1.2.2 Effect of temperature on reforming equilibria

Le Chatelier's principle also states that raising the temperature favors endothermic reactions, like steam and CO_2 reforming, but also the RWGS. In Fig. 1.9, the temperature effects are presented.

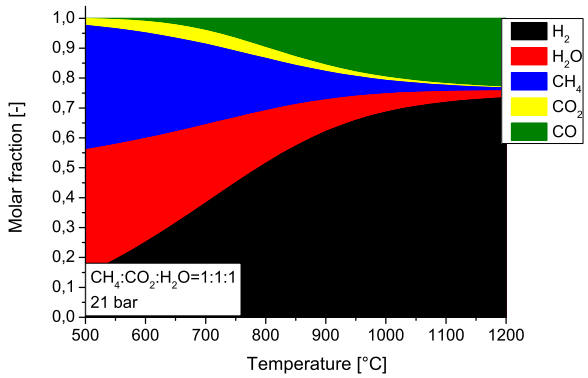

(a) Molar fractions at SMR equilibrium

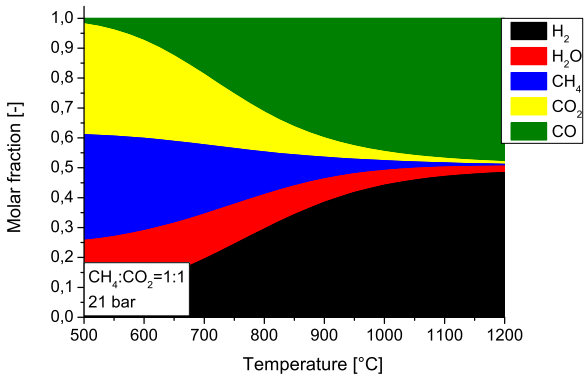

(b) Molar fractions of CH_4-DryRef equilibrium

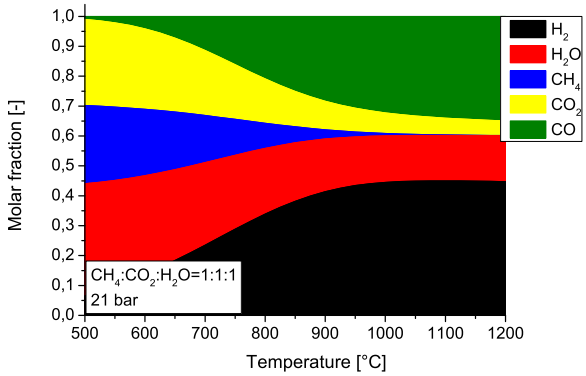

(c) Molar fractions of CH_4-MSCR equilibrium

Figure 1.9: Effect of temperature on thermodynamic equilibria of reforming reactions of methane

As expected at higher temperatures, the amount of syngas produced increases up to almost complete conversion of methane.

In a typical temperature range that is the most probable for reforming to be performed (1073-1273 K - 800-1000°C), steam and CO_2 are always observable in non-negligible concentrations. Independent from temperature and reforming process, steam remains at the reforming equilibrium and could be used to lower the severity of operating conditions of CO_2 reforming as mentioned in the previous section.

In addition to the conversions, coke deposition is also affected by higher temperatures, which favors methane cracking and limits the Boudouard reaction; see section 1.2.4.

1.2.3 Effect of feed composition on reforming equilibria

The variation of feed composition may also help to create milder operating conditions or to improve efficiency of the overall process. In Fig. 1.10, the influence of varying the feed composition is studied.

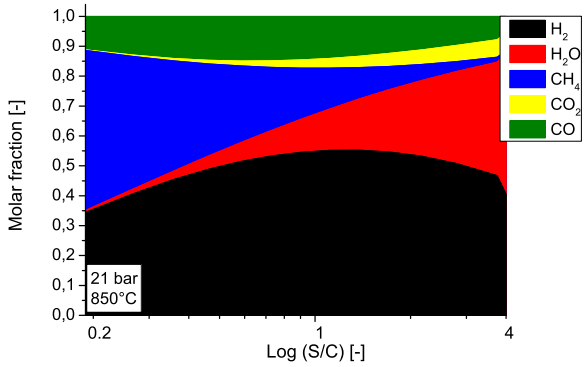

(a) Molar fractions at SMR equilibrium

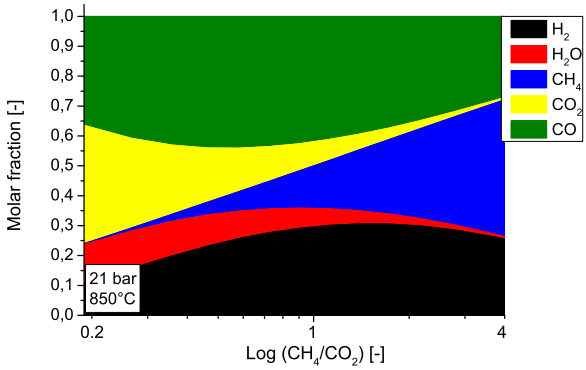

(b) Molar fractions of CH_4-DryRef equilibrium

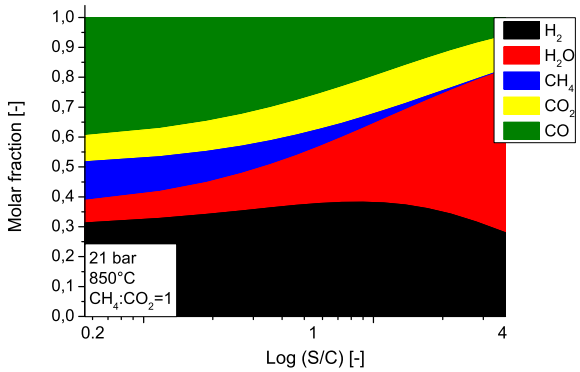

(c) Molar fractions of CH_4-MSCR equilibrium

Figure 1.10: Effect of feed composition on thermodynamic equilibria of reforming reactions of methane

The simulations show that for steam-to-carbon and CH_4/CO_2 ratios close to one, the presence of steam and CO_2 is confirmed at thermodynamic equilibria. As mentioned before, the addition of a small amount of steam in CO_2 reforming would have a minor influence on the quality of the syngas produced. Furthermore, this would result in milder operating conditions.

For methane reforming with steam, CO_2, or both, the steam-to-carbon and CH_4/CO_2 ratios have a major influence on the product concentrations and may help to reach almost full conversion of the reactant that is not present in excess.

The feed composition also has a strong influence on coke deposition as detailed in the following section 1.2.4.

1.2.4 Thermodynamic equilibrium of coke formation in reforming

In addition to conversions and H_2/CO ratio, coke deposition is also a factor of interest that must be considered for coke-free operations over time. Methane cracking is more likely to occur at high temperatures and high partial pressures of methane, while the shift of the Boudouard reaction to coke and CO_2 is more likely to happen at lower temperatures and low H_2/CO ratios[36]. The feed content also plays a major role in the coke-deposition probability. The S/C and CO_2/CH_4 ratios should be kept as high as possible to avoid coke deposition and achieve higher conversions, but in practice it leads also to higher operation costs because of a low syngas concentration in the product gas[81].

At a given temperature and for a given hydrocarbon, carbon formation is expected to occur under a critical threshold of S/C and/or CH_4/CO_2 ratios[21]. This observation illustrates the carbon formation principle on a Ni-based catalyst: carbon formation occurs if the gas shows an affinity for carbon after the thermodynamic equilibrium (SMR and WGS) is reached[82]. Rostrup-Nielsen et al.[16;21;83] investigated different catalysts and defined a thermodynamic limit for carbon formation on Fig. 1.11. The pressure has been fixed at 25.5 bar as well as the Ni particle size at 250 nm; simulation at different molar ratios of CH_4/CO_2 and H_2O/CH_4 have been performed. Thanks to this model, it is possible to evaluate the coking risk expected at defined operating conditions for instance for the Ni-based catalysts A and B. Particularly attractive are catalyst C (noble metal-based) and sulfur-passivation[77;84](catalyst D) that allow coke-free operations even if coke formation is thermodynamically favored on the chosen Ni-based catalyst.

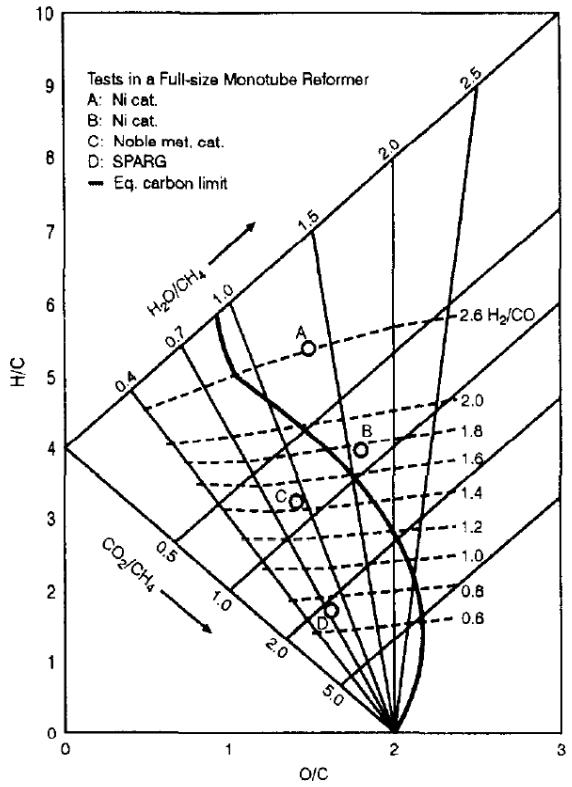

Figure 1.11: Carbon limit diagram at 25.5 bar (adapted from[21]) for Ni paricle size of 250 nm. The ratios are molar. (cat, catalyst; met., metal; Eq. equilibrium) (Copyright Elsevier)

1.3 Commercial catalyst review

For about a century, when the first industrial steam-reforming processes were started, the number as well as the varieties of studied and commercialized catalysts has increased steadily. Fig. 1.12 illustrates this trend from the 50s up to now.

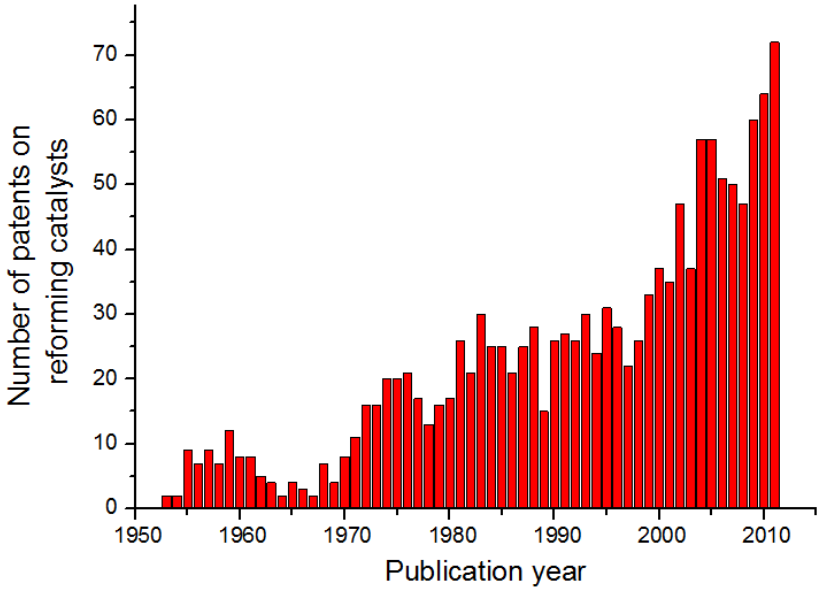

Figure 1.12: Recorded patents for reforming catalysts using the PatBase Express search engine

At the beginning of reforming history, only noble metal-based catalysts have been studied and patented, followed by other non-precious metals like Ni. Then new supports were developed to reduce the acidity of pure alumina carrier, and later catalyst promotion has been introduced in reforming as well as bimetallic catalysts, for instance, alkali promotion of Ni on magnesia-alumina or Pt-Re bimetallic catalysts for naphtha reforming.

The extensive studies on reforming processes have led to a wide variety of different catalytic technologies. In Tab. 1.4, few commercial steam-reforming catalyst compositions with the corresponding feedstock used for their reforming applications are listed.

For mixed-steam CO_2 reforming with a low steam content, no commercial catalysts are at this time available on the market even if a few patents and articles have been published (see section 3.3.1 of this part (II)).

Manufacturer	Trade Name	Feedstock	NiO [wt.%]	Promoter [wt.%]	Carrier [wt.%]	SiO_2 [wt.%]
Haldor Tops∅e	R-67-7H	NG to Naphtha	>12	-	$MgAl_2O_4$ (bal.)	<0.2
	AR-301	NG to light HC	>30	K_2O (2-5)	$MgAl_2O_4$ (bal.)	-
	RK-202	Naphtha	>15	K_2O (>1)	$MgAl_2O_4$ (bal.)	<0.2
Johnson Matthey	23-4	Naphtha, NG light HC	18	-	Al_2O_3 (balance)	<0.1
	57-4	NG, light HC	18	-	$CaAl_2O_4$ (bal.)	<0.1
	46-6Q	Naphtha	16	-	$CaAl_2O_4$ (bal.)	0.5
Süd Chemie	G90	NG	14	-	$CaAl_{12}O_{19}$ (bal.)	-
	G91	NG, LPG	18	K_2O (1.6)	$CaAl_{22}O_{33}$ (bal.)	-
	C11-NK	Naphtha	25	K_2O (8.5)	$CaAl_2O_4$ (bal.)	-
United Catalysts	NGR-615-K	Naphtha	15-20	K_2O (1.5-8)	Al_2O_3 (bal.)	<0.2
BASF	SG9301	NG	16.5	MgO (6) ReO (3)	Al_2O_3 (bal.)	<0.1
	G1-50	Naphtha	20	MgO (11) CaO (16) K_2O (7)	Al_2O_3 (bal.)	14

Table 1.4: Few commercial steam-reforming catalysts and their compositions (taken from[10])(NG, natural gas; HC, hydrocarbons; LPG, liquefied petroleum gas, bal., balance)

1.4 Kinetics and mechanisms

For a better comprehensive model, knowledge of reforming mechanism and kinetics are of great help. Kinetics of steam reforming of methane have been extensively studied since the 90s[85;86] and due to a large amount of different attractive catalysts identified so far are still widely investigated[87–94]. In addition, CO_2 reforming[31;95–99], sometimes combined with steam reforming[100;101], is also currently examined.

The different kinetic models that will be discussed are presented in the Tab. 1.5.

For CO_2 reforming of methane, Gokon et al.[95] discussed different catalytic models and showed that Langmuir-Hinshelwood model (see section 2.3.1) gave the best fits for reforming reactions between 873 and 973 K (600-700°C) on Ru/Al_2O_3 catalyst supported on Ni-Cr-Al metallic foam absorber with a CO_2/CH_4 ratio between 0.3 and 3 at 1 bar and a Gas Hourly Space Velocity (GHSV) range of 8500-25500h^{-1}.
For steam reforming more kinetic studies are available. Rostrup-Nielsen et al.[21] as well as Trimm and Önsan[102] have described the kinetics based on the Langmuir-Hinshelwood expression rates published by Xu and Froment[86] already in 1989. The intrinsic reaction rates of Xu and Froment[86] have been derived for the steam reforming of methane, accompanied by WGS on a $Ni/MgAl_2O_4$, which is a usual steam-reforming catalyst. A thermodynamic analysis helped in reducing the number of possible mechanisms. Twenty-one sets with three rate equations have been retained and subjected to model discrimination

Authors	Catalyst	Process	Temperature	Pressure	Equation rate	Form of kinetics
Xu and Froment[86]	$Ni/MgAl_2O_4$	SRM	673-1000 K (400-727°C)	30 bar	$\frac{\frac{k_2}{p_{H_2}^{2.5}}\left(p_{CH_4}p_{H_2O}-\frac{p_{H_2O}^3 p_{CO}}{K_2}\right)}{(1+K_{CO}p_{CO}+K_{H_2}p_{H_2}+K_{CH_4}p_{CH_4}+\frac{K_{H_2O}p_{H_2O}}{p_{H_2}})^2}$	LH
Rostrup-Nielsen et al.[21]	$Ni/MgAl_2O_4$	SRM	773-1073 K (500-800°C)	1-35 bar	"	LH
Trimm and Önsan[102]	Ni/MgO	SRM	583-823 K (310-550°C)	1-30 bar	"	LH
Wei and Iglesia[103–107]	Ni/MgO and	SMR with	823-1023 K (550-750°C)	1-5 bar	"	Elementary steps
	Ru, Ir, Rh and Pt/ZrO_2	CO_2	823-1023 K (550-750°C)	1-5 bar	"	
Gokon et al.[95]	Ru/Al_2O_3 on metallic foams	CO_2 reforming	873-1023 K (600-750°C)	1 bar	$1.17.10^4$.exp(-83.498/RT) $mol.dm^{-3}.s^{-1}$ K_{CO2}=$3.11.10^{-3}$.exp(49.220/RT) bar^{-1} K_{CH4}=0.653.exp(16.054/RT) bar^{-1}	LH

Table 1.5: Comparison of kinetic studies; LH, Langmuir Hinshelwood

and parameter estimation. The parameter estimations in the best model are statistically significant and thermodynamically consistent. The developed model has been determined for a temperature range of 673-1000 K (400-727°C) in a pressure on the order of 30 bar.
According to Xu and Froment[86], the most significant reactions are listed in Tab. 1.6.

Reaction number i	Reaction
1	$CO + H_2O \rightleftharpoons CO_2 + H_2$
2	$CH_4 + H_2O \rightleftharpoons CO + 3H_2$
3	$CH_4 + 2H_2O \rightleftharpoons CO_2 + 4H_2$

Table 1.6: Reactions considered in steam reforming of methane

The three equilibria and their associated kinetics are expressed as follow:

$$r_1 = \frac{\frac{k_1}{p_{H_2}}\left(p_{CO}p_{H_2O} - \frac{p_{H_2O}p_{CO_2}}{K_1}\right)}{DEN^2} \tag{1.15}$$

$$r_2 = \frac{\frac{k_2}{p_{H_2}^{2,5}}\left(p_{CH_4}p_{H_2O} - \frac{p_{H_2O}^3 p_{CO}}{K_2}\right)}{DEN^2} \tag{1.16}$$

$$r_3 = \frac{\frac{k_3}{p_{H_2}^{3,5}}\left(p_{CH_4}p_{H_2O}^2 - \frac{p_{H_2O}^4 p_{CO_2}}{K_3}\right)}{DEN^2} \tag{1.17}$$

And DEN is calculated with the following expression:

$$DEN = 1 + K_{CO}p_{CO} + K_{H_2}p_{H_2} + K_{CH_4}p_{CH_4} + \frac{K_{H_2O}p_{H_2O}}{p_{H_2}} \tag{1.18}$$

where

- k_i, the rate constant, is calculated by: $k_i = k_{i,T_r}.\exp\left[\frac{E_{a,i}}{R}\left(\frac{1}{T_r} - \frac{1}{T}\right)\right]$, with i the reaction number equal to 1, 2, or 3, and

k_{i,T_r}	the constant rate of reaction i at the temperature T_r in kmol.bar$^{-0.5}$.(kg cat.h)$^{-1}$ for k_2 and k_3, and k_1 kmol.(kg cat.h)$^{-1}$
$E_{a,i}$	the activation energy of the reaction i in J.mol^{-1}
R	the constant of the ideal gas in J.mol^{-1}.K^{-1}
T and T_r	respectively the temperature of the mixture and the reference temperature in K.

- K_i, is the equilibrium constant obtained from the law of mass action of the reaction i and calculated by using the relation $K_i = \exp\left(\frac{\Delta_R G_i}{R.T}\right) = \prod_{k=1}^{4} p_k^{\nu_{i,j}}$, where p_k is the partial pressure of component k in bar, $\nu_{i,j}$ the algebraic stoichiometric coefficient, and $\Delta_R G_i$ is the free enthalpy of the reaction i in J.mol^{-1}.

- p_{CH_4}, p_{H_2O}, p_{CO}, p_{CO_2} and p_{H_2} are partial pressures in bar.

- r_1, r_2 and r_3 are the reaction rate in kmol.(kg cat.h)$^{-1}$
- K_j, is the adsorption constant of j (for CH_4, H_2O, CO and H_2) at a temperature T, which is calculated from $K_j = K_j^0.\exp\left[\frac{\Delta H_j}{R}\left(\frac{1}{T_r}-\frac{1}{T}\right)\right]$, with:

K_j^0	coefficient of adsorption of j at the temperature T_r in bar^{-1}, except K_{H_2O} that is dimensionless
ΔH_j	enthalpy change of the reaction or adsorption j in J.mol^{-1}.

Simulations are then performed to optimize temperature profiles, temperature, pressure, GHSV, catalyst shape, and so on. Thanks to the kinetic data evaluated[86], the simulations yield, with the knowledge of the catalyst pore network, to the effectiveness factor η of the reactions[108] (see section 2.2), which helps to optimize the operating conditions for cost-effective operations. Further investigations are required to understand why the catalyst deactivates. Isotopic studies combined with kinetic investigations lead to precious mechanistic information. Wei and Iglesia have shown[103–107] for steam and CO_2 reforming over Ni- and noble metal-based catalysts that the stable CH_4 decomposes sequentially by H-subtraction up to chemisorbed carbon (C^*). This adsorbed carbon reacts then with steam or CO_2. The first step of methane decomposition has been identified as the rate-determining step (RDS)[21]. That can be justified by the high stability of methane, which owns a strong C-H bond, exhibiting an average enthalpy change in the gas phase of 416 kJ.mol^{-1} [10]. Mechanism can be written as described in Eqs. 1.19-1.28.

$$CH_4 + 2\,^* \longleftrightarrow CH_3^* + H^* \tag{1.19}$$
$$CH_3^* + ^* \longleftrightarrow CH_2^* + H^* \tag{1.20}$$
$$CH_2^* + ^* \longleftrightarrow CH^* + H^* \tag{1.21}$$
$$CH^* + ^* \longleftrightarrow C^* + H^* \tag{1.22}$$
$$H_2O + 2\,^* \longleftrightarrow OH^* + H^* \tag{1.23}$$
$$CO_2 + 2\,^* \longleftrightarrow CO^* + O^* \tag{1.24}$$
$$OH^* + ^* \longleftrightarrow H^* + O^* \tag{1.25}$$
$$C^* + O^* \longleftrightarrow CO^* + ^* \tag{1.26}$$
$$CO^* \longleftrightarrow CO + ^* \tag{1.27}$$
$$2\,H^* \longleftrightarrow H_2 + 2\,^* \tag{1.28}$$

The first step, RDS, occurs on active metal such as Ni, Pt, or Ir. Wei and Iglesia have shown that the RDS occurs faster on noble metals than on Ni[107]. In addition, this mechanistic approach helps to understand how coke or carbon deposition takes place on the catalyst. The coke/carbon removal can be achieved by steam in steam reforming or probably by CO_2 in CO_2 reforming. That means that coke/carbon formation can be avoided when the coking rates are slower than the gasification rate[36]. Sometimes a distinction is made between coke and carbon. The difference between coke and carbon is somewhat arbitrary[109]: usually disproportionation of CO gives carbon whereas coke originates from methane cracking.
A high partial pressure of methane provokes faster coking rates[110;111] and lack of CO_2 or H_2O to gasify C^* leads to coke deposition. Furthermore, too low H_2/CO ratios also lead to carbon formation through

the Boudouard reaction[36], especially in CO_2 reforming at high pressures[112].

1.5 Reactor design and development

The selection of a reactor design depends on the choice of reforming. In the case of mixed-steam CO_2 reforming, the technology would be analogue to steam reforming due to the high endothermicity of the reaction, in comparison with POX (and also CPOX) and ATR reformers, where an exothermic and an almost athermal overall reaction take place, respectively.

In order to optimize the use of a heterogeneous catalyst, a broad variety of reactor types has been designed due to the large variety of possible process specifications. But commonly cheap, reliable, and continuously working reactors are preferred for industrial purposes. That is why fixed bed reactors and fluidized bed reactors are used in the majority of industrial reactors[113;114] instead of batches or semi-batches that cannot work continuously.

1.5.1 Fixed bed reactor

The simplest reactor used in most reforming processes is the fixed bed reactor. It consists of a simple tube filled with catalyst particles. The design of these particles is carefully chosen to limit the pressure drop, maximize the specific area of the catalyst, and facilitate mass and heat transfer through the whole catalytic bed. The active material filled into the tube is located in the isothermal zone in the simplest case or it is filled beyond the lower and/or upper limit of the isothermal zone, while the fluid flows through the fixed catalytic bed.
For highly endothermic reactions, like steam reforming, mixed-steam CO_2 reforming, or highly exothermic reactions, like partial oxidations, the reactor diameter should be reduced to limit the temperature gradient within the catalytic bed[115]. If a high GHSV needs to be used a multitube reactor is preferentially used to improve heat exchange and limit radial temperature gradients[116]. Energy for/from the chemical reaction is introduced/removed to maintain a constant temperature within all the catalyst particles. In addition, all the tubes of a multitube reactor should have the same pressure drop and the same amount of catalyst in order to limit the temperature gradient and subsequent ageing of catalyst as well as tube material[113;117].

1.5.2 Development of reactor design

Much effort is put into the development of a reformer design to improve its efficiency. In the case of hydrogen production, new approaches are used to achieve the same performance at milder operating conditions, improve reactor mass and heat transfer as well as reduce CO_2 emissions[10].

Pd-based membranes for selective separation of H_2 have been extensively investigated to improve methane conversion and hydrogen purity[59;118;119]. However, this concept suffers from the relatively high price of Pd and possible membrane degradation by carbon and acidic gases[120]. Other issues concern the CO_2 sorption by limestone or dolomite[10] to shift the reforming equilibrium. For this technique, efforts are concentrated on improving the CO_2-sorbent materials and stability over the cycles.

Another development possibility for reforming can be the use of other energies. For instance, use of solar energy to heat up the reformer instead of methane combustion. It has been claimed that solar reformers can save 40% of the fuel[10].

1.6 Cost-effective operations

Optimal design of reforming processes are simulated to meet the best cost-efficient operations. Major initial capital costs are engaged in:

- Multi-tubular reactors
- Heat exchangers required for heat management
- Separation units (e.g. PSA)

Furthermore, several operation costs should not be neglected, among them:

- Shutdown/start-up for maintenance
- Utilities especially to heat the unit
- Ecological footprint, depending on the local legislation (e.g. carbon tax)

In addition, during the planing phase, GHSV, temperature, and pressure of the process should be adapted to the environment and requirements of downstream processes to limit costs by minimizing utility duties by using for instance a low steam-to-carbon ratio[81;121], low heat flux, and low outlet temperature at the reformer[121]. Furthermore, utilization of a prereformer[121] and/or limited footprint with CO_2 recycling can reduce the net CO_2 emissions up to 67% in comparison to standard steam reforming[122]. All these factors can improve the profitability due to lower investment and operation costs.

2 Heterogeneously catalyzed gas-phase reactions

Already introduced by Berzelius[123] in 1836, catalysis has been correctly described thanks to the definition of a catalyst by Ostwald (1895)[124]: "a catalyst accelerates a chemical reaction without affecting the position of equilibrium". The two main domains of catalysis are heterogeneous and homogeneous catalysis. In the case of catalyzed reforming processes, only heterogeneous catalysis is involved since the feed is gaseous or liquid and the catalyst a solid material. Heterogeneous catalytic processes (Fig. 2.1) are usually characterized by absorption of the reactant(s) on the catalyst surface on which the reaction takes place to form the product(s); finally, the catalyst is "regenerated" to its initial state by desorption of the product(s).

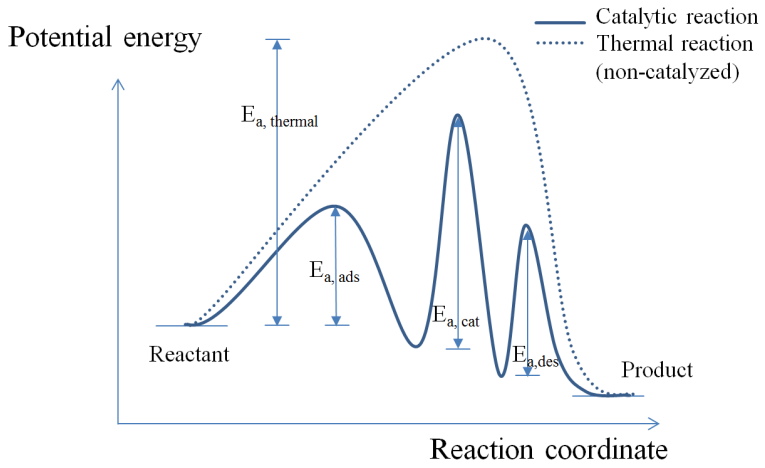

Figure 2.1: Pathway of catalyzed and non-catalyzed reactions (E_a, activation energy; $E_{a,ads}$, activation energy of adsorption; $E_{a,cat}$, activation energy of the catalytic reaction; $E_{a,des}$, activation energy of desorption; $E_{a,thermal}$, activation energy of thermal reaction)

The energy barrier of a thermal reaction on a catalyst is consequently decreased, which opens up new reaction pathways.

2.1 Molecular processes of heterogeneously catalyzed reactions

Heterogeneous catalytic reactions involve purely physical as well as purely chemical steps, and in the simplest case a catalytic reaction on a porous catalyst occurs in the following order (Fig. 2.2):

1. Diffusion of the reactant(s) into the boundary layer to the catalyst surface

2. Diffusion of the reactant(s) through the pores
3. Adsorption of the reactant(s) on the inner pore surface
4. Chemical reaction on the catalyst surface
5. Desorption of the product(s) from the catalyst surface
6. Diffusion of the product(s) out of the pores
7. Diffusion of the product(s) through the boundary layer to the gas phase

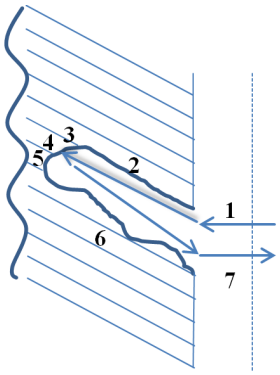

Figure 2.2: The 7 steps of the catalyzed reaction pathway (adapted from [125]).

Depending on transport and reaction rates, the effective reaction rate r_{eff}, observed during the catalytic reaction, follows three different regimes:

- kinetic limitation, when the reaction rate is slow in comparison with the diffusion rates in the gas film and the pores,
- diffusion limitation in pores, when the diffusion rate in pores is slow compared with the diffusion rate in the gas film and the kinetic reaction rate,
- diffusion limitation in the gas film, when the diffusion rate in the gas film is slow compared with the kinetic reaction rate and the diffusion rate in pores.

Ideally, the resistance effect of diffusion limitations in the gas film and pores is reduced as much as possible to maximize r_{eff}.

2.2 Mass-transfer effects

The materials used in heterogeneous catalysis are only rarely non-porous. Indeed, porous materials with a large active area are preferred to improve the catalyst performance. Due to this porosity, the elementary steps of the microkinetic model described in Fig. 2.2 must be taken into account. The use of the effectiveness factor η, which describes the ratio of the reaction rate observed on a porous material particle to

the reaction rate that would be obtained at surface conditions r_S (without any diffusion or film limitation) allows the quantification of the effect of mass-transfer limitations.

In order to find an analytic expression for η, a mass balance is assumed on a catalyst particle of radius R from the catalytic bed across a spherical shell of thickness dr (Fig. 2.3):

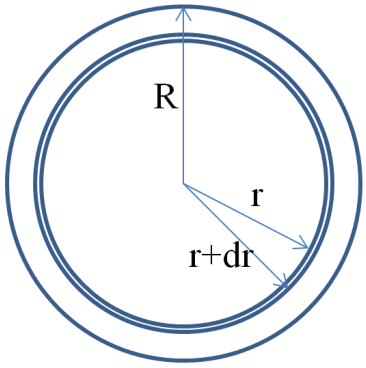

Figure 2.3: Mass balance on a spherical shell of thickness dr

The mass balance can be literally described as the number of moles of A entering the shell less the number of moles A leaving the shell, which is equal to the molar consumption/production of A in this shell. The consumption/production of A is the result of the chemical reaction. Assuming the general power law expression (Eq. 2.1) for the consumption rate r_A of reactant A:

$$r_A = k_A.C_A^{n_A} \tag{2.1}$$

where:

- k_A is the rate constant coefficient of consumption of A expressed in $(\text{mol.m}^{-3})^{1-n_A}.\text{s}^{-1}$
- C_A the concentration of A in mol.m^{-3}
- n_A the order of reaction with respect to reactant A [dimensionless]

Mathematically, the equation can be written as:

$$4.\pi.(r+dr)^2.j_{r+dr} - 4.\pi.r^2.j_r = 4.\pi.r^2.dr.k_A.C_A^{n_A} \tag{2.2}$$

where j_r and j_{r+dr} are, respectively, the diffusion flux of A through the sphere of radius r and r+dr in $\text{mol.m}^{-2}.\text{s}^{-1}$.
j is expressed by Fick's law of diffusion and defined by Eq. 2.3, where C_A is the spatial concentration:

$$j = D_e.\nabla C_A \tag{2.3}$$

where D_e, the effective diffusion coefficient expressed in $\text{m}^2.\text{s}^{-1}$, is expressed as a function of:

- D, diffusion coefficient of A in the considered catalyst particle [$m^2.s^{-1}$]
- ε_P, the porosity of the catalyst particle [-]
- τ, the tortuosity [-]

and its expression is:

$$D_e = \frac{D.\varepsilon_P}{\tau} \tag{2.4}$$

In case of one-dimensional radial diffusion, the diffusion flux j_r, on the sphere of radius r, is expressed by Eq. 2.5.

$$j_r = D_e.\frac{dC_A}{dr} \tag{2.5}$$

Performing a Taylor development on $\left.\frac{dC_A}{dr}\right|_{r+dr}$, it is easy to obtain after rearrangements[126]:

$$\frac{d^2C_A}{dr^2} + \frac{2}{r}\frac{dC_A}{dr} = \frac{k_A.C_A^{n_A}}{D_e} \tag{2.6}$$

Considering the boundary conditions at the particle surface (r=R), the concentration of A equals the concentration at the surface (C_A=$C_{A,S}$), whereas in the middle of the catalyst particle (r=0), $\frac{dC_A}{dr}$ is equal to zero as a result of the symmetry of the concentration profile in the spherical catalyst particle.
Using the following dimensionless numbers and their boundary conditions derived from the previous quoted boundary conditions[126]:

$$f = \frac{C_A}{C_{A,S}} \tag{2.7}$$

$$x = \frac{r}{R} \tag{2.8}$$

a general differential equation is obtained:

$$\frac{d^2f}{dx^2} + \frac{2}{x}\frac{df}{dx} = \phi^2.f^{n_A} \tag{2.9}$$

where ϕ, called the Thiele modulus, is the only parameter of the differential equation and is equal to:

$$\phi = R\sqrt{\frac{k_A.C_{A,S}^{n_A-1}}{D_e}} \tag{2.10}$$

The solution of this differential equation is:

$$f(x) = \frac{\sinh(\phi x)}{x.\sinh(\phi)} \tag{2.11}$$

The expression for the reaction rate observed r_{eff} and the reaction rate at surface conditions is given by Eqs. 2.12 and 2.13, respectively. The reaction rate observed is equal to the amount of A diffusing through

the catalyst particle surface.

$$r_{eff} = 4\pi.R^2.D_e.\frac{C_{A,S}}{R}\left.\frac{df}{dx}\right|_{x=1} \tag{2.12}$$

$$r_S = \frac{4}{3}\pi.R^3.k_A.C_{A,S} \tag{2.13}$$

It is now possible to mathematically express η:

$$\eta = \frac{r_{eff}}{r_S} = \frac{3}{\phi}.\left(\frac{1}{\tanh(\phi)} - \frac{1}{\phi}\right) \tag{2.14}$$

It is also particularly interesting to note that η depends only on R, the radius of the catalyst particle.

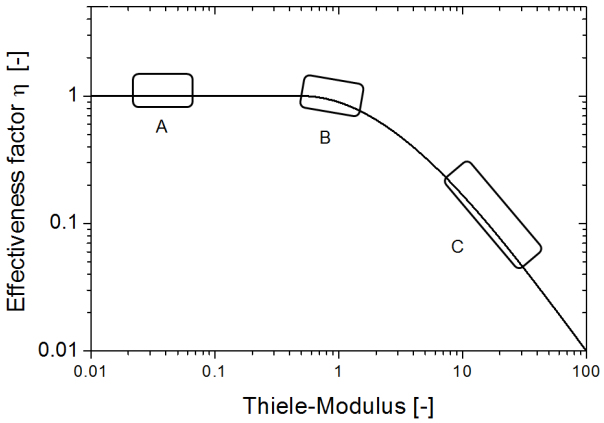

Figure 2.4: Effectiveness factor vs Thiele modulus (A, kinetic control; B and C mass-transfer control) (taken from [126;127])

When plotting the effectiveness factor vs the Thiele modulus, three different regimes are identifiable [128] (Fig. 2.4):

- the kinetic control (A). With small values of the Thiele modulus, the interior surface of the catalyst is completely accessible for the starting material.
- the regime of pore diffusion (mass-transfer control) (B). With a Thiele modulus value of about one, this regime is preferred for technical operations.
- the regime of transport limitation (mass-transfer control) (C). At higher values of the Thiele modulus, the reaction is limited by the diffusion in the boundary layer, which means that the starting material reacts on the outer surface of the catalyst because the diffusion through the pores is too slow.

Furthermore, depending on the kind of identified regime, the expression of $\ln(k_{eff})$ for a first order reaction (n_A=1) plotted against 1/T would provide access to the observed activation energy $E_{A,eff}$ from an Arrhenius diagram, with k_{eff} being the rate constant of the observed reaction rate.

- the kinetic control (A), with ϕ<0.3, yields equal reaction rates r_{eff}=r_S and thus η=1 and $E_{A,eff}$=$E_{A,true}$ where $E_{A,eff}$ and $E_{A,true}$ are the observed activation energies with respect to r_{eff} and at surface conditions, respectively.

- mass-transfer control in pore diffusion (B), with 0.3<ϕ<3 and η=k_{eff}/$k_{A,S}$ $\approx 1/\phi$, k_{eff} is now described by k_{eff}=$\frac{k_{A,S}}{\phi}$=$\frac{1}{R}\sqrt{D_e.k_{A,S}}$, and thus:

$$ln\, k_{eff} = -ln\, R + \frac{1}{2}.ln\, D_e + \frac{1}{2}.ln\, k_0 - \frac{E_A}{2RT} \tag{2.15}$$

  This linear equation of ln(k_{eff}) as a function of 1/T yields the observed activation energy: $E_{A,eff}$=$E_{A,true}$/2

- mass-transfer control in transport limitation (fluid/solid) (C), with ϕ >3, shows ϕ <<1 and thus $E_{A,eff}$ is close to zero.

This is summarized in Fig. 2.5.

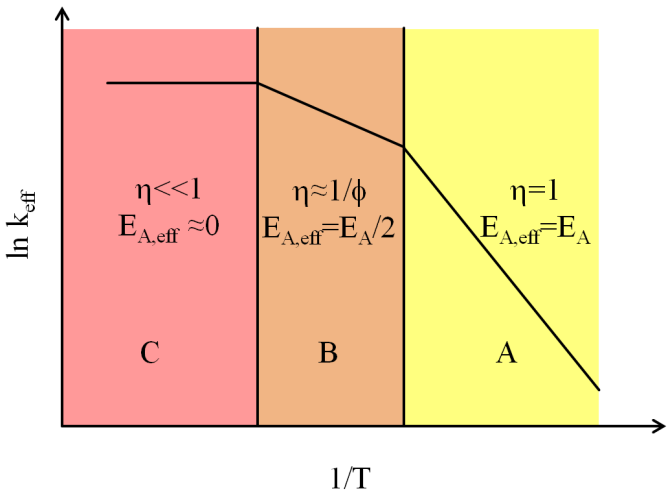

Figure 2.5: Arrhenius plot showing the observed expression of activation energy $E_{a,eff}$ and the corresponding values of the Thiele modulus depending on the mass-transfer regime (A, kinetic control; B, pore diffusion in mass-transfer control; C, gas/solid mass-transfer control).

2.3 Microkinetics and mechanisms in heterogeneous catalysis

In order to determine kinetics of the reactions on the catalyst, the adsorption step preceding the reaction and the desorption step following the chemical reaction needs to be modeled using chemical reaction. This mechanistic approach known as microkinetics considers also the important adsorption/desorption steps in heterogeneous catalysis. Two different kinds of adsorption exist[129]: chemisorption representing the chemical reaction between the catalyst surface and the adsorbate, which results in the formation of a bond, and physisorption resulting only from weaker Van der Waals forces. In the heterogeneous-catalysis mechanism, chemisorption is involved and occurs preferentially on active sites.

The description of the chemisorption on the catalyst surface is achieved with a correlation between the quantity of adsorbed molecules of reactant A and the pressure P_A of the reactant A at a constant temperature. Langmuir adsorption isotherms correspond to the simplest model, assuming that:

- the catalyst surface is ideally homogeneous
- maximum coverage is obtained with a monolayer
- there is no interaction between the adsorbed molecules.

Considering θ_A, the degree of coverage of the reactant A is defined as the ratio of number of adsorbed molecules on the surface to the number of adsorbed molecules on a monolayer on the surface. Adsorption of A can be written as in Eq. 2.16.

$$A + ^* \rightleftharpoons A^* \tag{2.16}$$

The corresponding law of mass action gives Eq. 2.17:

$$K_A = \frac{C_A^*}{C^*.P_A} \tag{2.17}$$

where P^A, C^*, and C_A^* are, respectively, the partial pressure of A in the gas phase, the concentration of free adsorption sites on the catalyst surface, and the molar concentration adsorbed on the catalyst surface. For a monolayer applies:

$$C_A^* = \theta_A \tag{2.18}$$

$$C^* = (1 - \theta_A) \tag{2.19}$$

Combining Eqs. 2.18 and 2.19 with the expression of K_A (Eq. 2.17) gives after recombination the expression of the degree for coverage with A (Eq. 2.20):

$$\theta_A = \frac{K_A.P_A}{1 + K_A.P_A} \tag{2.20}$$

Considering the following reaction (Eq. 2.21)

$$A \rightleftharpoons P \tag{2.21}$$

where A adsorbed without dissociation and P is the product after desorption, the reaction rate r_{eff}, which is proportional to the number of chemisorbed molecules of A, can be expressed as follows [125] (Eq. 2.22):

$$r_{eff} = \frac{k.K_A.P_A}{1 + K_A.P_A} \tag{2.22}$$

This simple case with a single reactant can be extrapolated to a system of two reactants, A and B, that react to form product P. Mixed adsorption of A and B, which compete to adsorbed on free sites, can be

modeled thanks to the fact that the number of free sites is now 1-θ_A-θ_B. The degree of coverage of A (Eq. 2.23) and B (Eq. 2.24) are:

$$\theta_A = \frac{K_A.P_A}{1 + K_A.P_A + K_B.P_B} \tag{2.23}$$

$$\theta_B = \frac{K_B.P_B}{1 + K_A.P_A + K_B.P_B} \tag{2.24}$$

A special case should not be forgotten, that is, dissociative adsorption of hydrogen or more generally A_2 [130]. Its associated equation is:

$$\frac{1}{2}A_2 + ^* \rightleftharpoons A^* \tag{2.25}$$

From that equation results the degree of coverage:

$$\theta_A = \frac{K_A\sqrt{P_A}}{1 + K_A\sqrt{P_A}} \tag{2.26}$$

In order to design reactors, knowledge of reaction kinetics is required. The most often used model for gas-phase reactions is the power law type (Eq. 2.28), for instance for Eq. 2.27:

$$A + B \rightleftharpoons C \tag{2.27}$$

and will have the following effective reaction rate:

$$r_{eff} = k".P_A^{\alpha}.P_B^{\beta}.P_C^{\gamma} \tag{2.28}$$

Here, k" is the rate constant, P_i the partial pressure relative to i, and α, β, γ the reaction partial orders, respectively, with regard to A, B, C. The sum of these partial orders is equal to n, the overall order of the reaction. γ is usually equal to 0, but in heterogeneous catalysis the desorption of C may interfere with the reaction rate, and the partial order of the product would not be equal to zero. The effective reaction rate can be generalized for heterogeneous catalysis applications [125;130]:

$$r_{eff} = \frac{(kinetic\ term).(driving\ force)}{(resistance\ term)^m} \tag{2.29}$$

The exponent m is usually equal to 1 or 2 depending on the number of catalytic centers involved in the RDS. Since bimolecular processes are prevailing in heterogeneous catalysis, bimolecular models will be developed in the following subsections.

2.3.1 Langmuir-Hinshelwood mechanism

In the Langmuir-Hinshelwood model [125] (Fig. 2.6), the reactant species A and B are assumed to be first adsorbed on the surface and then, after chemisorption, to react to form the product P that will desorb after the reaction.

Figure 2.6: Elementary steps according to the Langmuir-Hinshelwood mechanism (adapted from [130;131])

In practice, all steps can be a rate-determining step; here, the chemical reaction between A* and B* was chosen as the rate-determining step. A simplified rate Eq. 2.30 obtained by first considering the relationship for mixed adsorption:

$$r_{eff} = k\theta_A\theta_B = \frac{kK_AP_AK_BP_B}{(1+K_AP_A+K_BP_B)^2} \tag{2.30}$$

To simplify and determine the constants involved in this general rate equation, different boundary cases can be taken into account:

- weak adsorptions of A and B, means $K_A \ll 1$ and $K_B \ll 1$:

$$r_{eff} = kK_AP_AK_BP_B \tag{2.31}$$

- adsorption A weaker than B, $K_A \ll K_B$:

$$r_{eff} = \frac{kK_AP_AK_BP_B}{(1+K_BP_B)^2} \tag{2.32}$$

- with a constant partial pressure of B, increasing the pressure of A leads to a simpler equation rate:

$$r_{eff} = \frac{kK_BP_B}{K_AP_A} \tag{2.33}$$

2.3.2 Eley-Rideal mechanism

In this model [125] (Fig. 2.7), which was found to be more often valid, only A is chemisorbed on the catalyst surface and then reacts directly with B in the gas phase to form product P.

Based on a Langmuir adsorption isotherm, the following equation is obtained [125] for a RDS corresponding to the reaction of A* with B:

$$r_{eff} = k'P_B\theta_A = k'P_B\frac{K_AP_A}{1+K_AP_A} \tag{2.34}$$

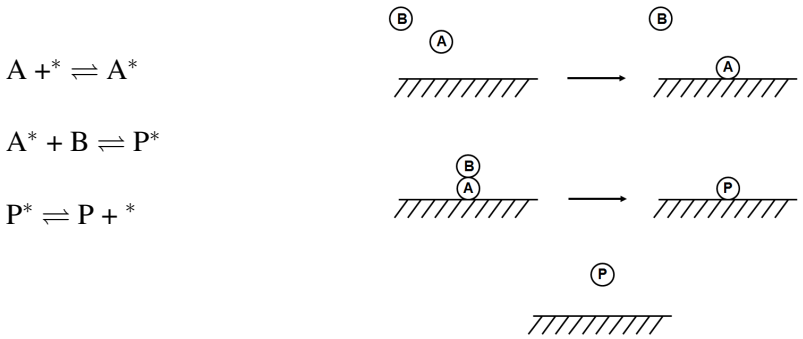

Figure 2.7: Elementary steps according to the Eley-Rideal mechanism (adapted from [130;131])

In this case, it is interesting to take a closer look at the boundary cases:

- Constant pressure of B and decrease of partial pressure of A leads to a decrease of the reaction rate similar to the Langmuir-Hinshelwood mechanism for mixed adsorption of A and B with a rate-determining step of the chemical reaction.
- Constant pressure of A and an increase in the partial pressure of B leads to an increase of reaction rate. This is precisely the opposite case in comparison to the Langmuir-Hinshelwood mechanism for mixed adsorption of A and B with a rate-determining step of the chemical reaction. This can be used to differentiate both mechanisms.

2.4 Catalyst deactivation

Catalysts are designed to maintain a high activity over time; however, activity loss is always observed for catalytic processes over variable timescales, from seconds up to years. Understanding these catalyst deactivation phenomena is important. Indeed, the catalyst price is generally relatively high and the down-time needed for catalyst treatment or replacement is an expensive task due to waste of time and thus capital investment in the industrial catalytic processes [132]. Different types of deactivation phenomena are already known [36;113;125;132] and can be sorted into: catalyst fouling, thermal degradation, and sintering, volatilization of active components and poisoning. Catalyst deactivation can influence conversions and/or selectivity differently, which is why different models for deactivation should be considered [125;132;133].

2.4.1 Catalyst fouling and coking

As described in the macrokinetics section, the activity of a catalyst is proportional to the catalyst's active surface area via the degree of coverage with reactants. Fouling concepts describe the loss of the specific surface required for a high catalyst activity. For instance in reforming processes, carbon deposits are likely to be produced and block active sites or/and the catalyst pores that are responsible for a high active surface. Some examples of carbon deposits are presented in Tab. 2.1.
In the case of reforming processes, all these types of carbon deposits can be involved.

Type	Origin	Temperature of formation	C:H	Gasification
C_α	atomic carbon adsorbed on surfaces	>473 K (200°C)	α	easy
C_β	polymeric amorphous film	>573 K (300°C)	≈ 8	possible
Whisker	whisker carbon usually with a metal particle	>573 K (300°C)	≈ 8	reasonably easy
Carbide surface	metal carbides deposited on non-catalytic or catalytic surfaces, often from gas-phase intermediates	>573 K (300°C)	≈ 50	reasonably easy
Gas-phase	formed in gas phase	>773 K (500°C)	≈ 8	difficult
Graphite		>1273 K (1000°C)	high	difficult

Table 2.1: Coking types and their origins (taken from [132])

- C_α is formed from CO or hydrocarbon. Ideally, C_α should be gasified and form methane or CO, but if coking occurs it forms C_β and subsequently graphitic and amorphous carbon[36]. C_α can also dissolve in Ni and form filaments or whisker. Ni carbides may also be formed[134;135].
- Whisker carbon is a filamentous carbon with a Ni crystallite at the end[136]. It does not block active sites (for example, on Ni), but grows very rapidly between catalyst particles thus crushing them and finally plugging the reactor within seconds or minutes.
- Carbides may form on the active compound (like Ni). Nickel carbide Ni_2C is known to be a potential support for the growth of graphene[137], but Ni_2C is reported to be unstable under steam-reforming conditions[135].
- Carbonaceous species may stem from the gas-phase reactions of hydrocarbons at high temperature[22]. For instance in reforming processes, hydrocarbons tend to decompose to alkanes, olefins, and up to highly aromatics by radical mechanism at high temperatures[36;138;139].
- Graphite or graphene result from dehydrogenation and/or polymerization of hydrocarbons[36] and might be found already on Ni at 773 K (500°C)[36].

The deactivation rate strongly depends on operating conditions and particularly temperature and gas composition. Fundamentally, carbon formation is an equilibrium between the rate of carbon formation and gasification. For instance, catalyst supports are chosen in order to maximize the gasification rate to avoid coking. In Fig. 2.8, the reaction pathways of carbon deposit formation and gasification are illustrated for steam reforming on Ni-based catalyst.

The mechanism of coke formation is complex and proceeds differently depending on operating conditions; however, a general mechanism model could be drawn from Bartholomew's work[36], Deutschmann's group[139] as well as Billaud's group work[138], as is shown in Fig. 2.9. First, olefins are formed by pyrolysis and then couple to a Brønsted acid site; these coupling products condensate and undergo cyclization to form benzene derivatives. These benzene products polymerize then to polynuclear aromatic hydrocarbons and finally form coke.

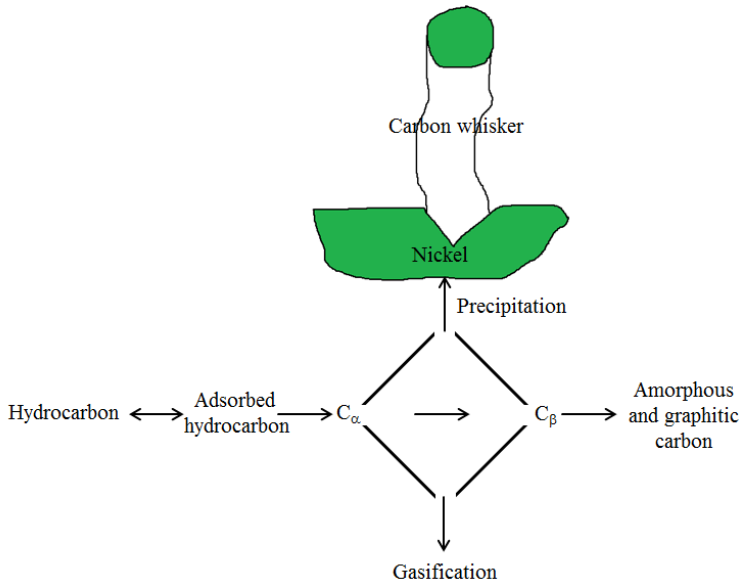

Figure 2.8: Schematic drawing of carbon deposition in steam reforming over Ni-based catalyst (adapted from [134;140])

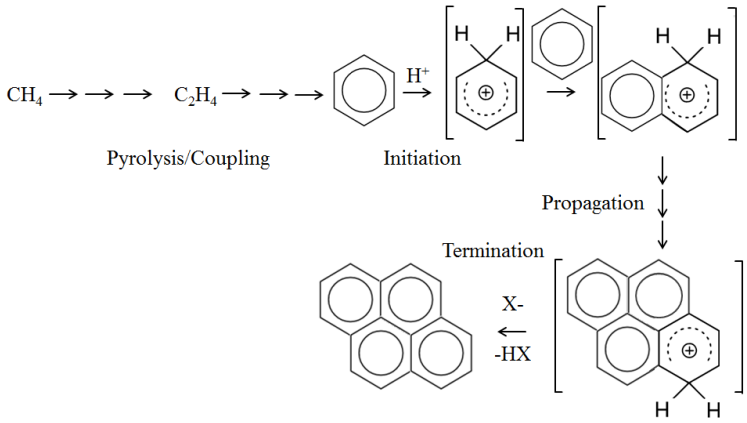

Figure 2.9: General coke formation mechanism starting from methane pyrolysis and coupling, followed by cyclization and polymerization up to polycyclic aromatic hydrocarbons before termination of the polymerization (adapted from [36;138;139])

2.4.2 Thermal degradation and sintering

High temperatures applied to the catalyst to achieve a higher activity can enhance thermal deactivation. The major process involved in thermal deactivation is sintering, which lowers the active surface area, metal surface area, and/or pore volume [36]. In addition to temperature, the gas-phase composition [109] can also promote sintering, for instance, a CO-rich gas phase may also favor metal particle agglomeration through carbonyl transport via the gas phase [141]. Sintering effects are generally irreversible or difficult to reverse, which is why it should be prevented.

In case of a single phase, the sintering mechanism is described as follows: around the Huettig temperature

(Eq. 2.35), the atoms near the defects exhibit a first significant mobility, and then around the Tamman temperature (Eq. 2.36) the atoms of the bulk become increasingly mobile, up to the melting point. Semi-empirical relationships for these temperatures are given by Mouljin et al.[142] (Eqs. 2.35 and 2.36).

$$T_{Huettig} = 0.3\,T_{melt} \quad (T\ in\ K) \tag{2.35}$$

$$T_{Tamman} = 0.5\,T_{melt} \quad (T\ in\ K) \tag{2.36}$$

Trimm[143] and Baker et al.[144] reviewed sintering of carriers. Single-phase oxide carriers can sinter through the following processes[36]:

- solid-state diffusion,
- surface diffusion,
- condensation/evaporation of volatile atoms or molecules,
- grain-boundary diffusion,
- phase transformations.

Some other factors like the alkali-metal presence or the steam atmosphere are known to be detrimental to the thermal stability of the carriers[132]. However, use of baria or lanthana as surface-area stabilizer have been suggested[132]. These stabilizers form either a surface coating[145] or lead to insertion of stabilizers at anion vacancies[146].

The sintering process of metal particles in the case of supported catalysts used to be described by a simple power law (Eq. 2.37), where D is the dispersion at time t, D_0 the initial dispersion, k_0 the rate constant, and n an order between 3 and 13[147–149].

$$-\frac{d(D/D_0)}{dt} = k_0 \left(\frac{D}{D_0}\right)^n \tag{2.37}$$

However, this model has been proven to be defective since over a certain period of time the surface area should reach zero[36]. Fuentes[150] and Bartholomew and co-workers[36;151] presented another model (Eq. 2.38), with a second term added to correct for this fault.

$$-\frac{d(D/D_0)}{dt} = k_0 \left(\frac{D}{D_0} - \frac{D_{eq}}{D_0}\right)^m \tag{2.38}$$

m is an order[36] equal to 1 or 2, D is the dispersion, D_0 the initial dispersion, and D_{eq} the dispersion at infinite time. Bartholomew also reported for m=2 the sintering rate of Pt, Ni, and Ag catalysts supported on alumina[152]. He showed that even if the vaporization of Pt on heating is higher than Ni, on alumina, Pt sinters faster than Ni; this observation has been explained by a possible higher metal-support interaction.

Thermal ageing can also result from phase transformations. For instance, a phase transition from γ-alumina to α-alumina, occurring around 873-1073 K (600-1000°C), decreases drastically the specific surface area of the support from about 250 $m^2.g^{-1}$ to circa 1 $m^2.g^{-1}$ [113].

Like thermal degradation and sintering, the loss of activity by volatilization of active compounds is irreversible. Indeed, certain compounds like MoO_3, P_2O_5, and Bi_2O_3 have a sublimation point that is particularly low, while other compounds like Ni may form volatile compounds like nickel tetracarbonyl ($Ni(CO)_4$) or nickel chloride ($NiCl_2$) if the feed is rich in CO or chlorine [36;113;125].

2.5 Catalyst poisoning

Strong interactions between active sites and third compounds alter the activity. Poisoning can occur by strong chemisorption or formation of surface complexes [36;153] even if reactivation of sites is considerable when chemisorption is relatively weak [113]. The chemical species can be classified into four different categories [36], which are shown in Tab. 2.2.

Chemical Type	Examples	Type of interaction with metals
Group VA, VIA elements	P, S, Sb, Se	through s- and p-orbitals; shielded structures are less toxic
Group VIIA elements	F ,Cl ,Br ,I	through s- and p-orbitals; formation of volatile halides
Toxic heavy metals and ions	As, Bi, Pb, Sn	occupy d-orbitals; may form alloys
Molecules that adsorb with multiple bonds	benzene, acetylene	chemisorption through multiple bonds and back bonding

Table 2.2: Classes of poisons according to their chemical nature (taken from [36])

The most common poisoning occurring in reforming processes is the sulfur poisoning due to the presence of sulfur compounds in hydrocarbon feedstocks. Metallic Ni particles react with sulfur to form the stable and inactive Ni sulfide. Indeed, the feedstock used almost always has at least a low concentration of sulfur compounds; this is why most of industrial reforming processes are located downstream from a desulfurization plant.

Apart from the challenges that poisoning represents, selective poisoning has useful applications. For instance, sulfur may be used in small quantities to poison carbon-formation sites located on Ni particles to prevent coke formation and allow operations with a very high carbon content in the feed (like in the SPARG process [19]).

2.6 Promotion of catalytic performance

Catalytic promoters are a third group of elements that improve the activity, the selectivity, or the stability of the catalyst. For reforming catalysts, promotion is used to reduce coking risk. Rostrup-Nielsen et

al.[82;154] have presented three different ways to improve catalyst performance with regard to coking at steady state:

- enhance the adsorption of steam or CO_2. For instance, kinetic experiments have shown that steam adsorption is promoted by "active" magnesia and alkali[82].
- enhance the rates of the surface reaction. Isotope exchange experiments have shown that the performance of catalysts with added magnesia is improved[154]. The "ensemble-control" effect observed is due to enhanced steam adsorption coupled with spill-over of OH species to the nickel surface.
- decrease the activation rate of hydrocarbons. For instance, magnesia but also calcium oxide neutralize the acidic sites of the catalyst[10] that catalyze hydrocarbon cracking and polymerization reactions[82;155].

The "ensemble-control" already described for the SPARG process (see section 1.1.5.1 of this part (II)) is the reason for improved performance. Indeed, coking is a dynamic process resulting from a "too low" gasification rate in comparison with the carbon-deposition rate. These three ways of promotion only aim at gasifying the adsorbed carbon species.
Apart from catalytic promoters, bimetallic catalysts are also of interest. The concept is similar to alloying; different active metals are used to combine their properties to enhance the performance and stability of the catalyst's active particles. For the broad variety of bimetallic catalysts used in reforming studies, three categories are clearly identifiable:

- bimetallic catalysts with two noble metals like Pt-Re[156;157]. This catalyst category is used for special applications due to the high price of the noble metals and possible difficulty of recycling both noble metals; an example is reforming of heavy hydrocarbons under high severity conditions,
- bimetallic catalysts made of a non-noble metal doped with a noble metal. This catalyst class is widely studied for reforming cases[158–160]. Most of the reported bimetallic catalysts are made of Ni-Pt alloys[161–166] for reforming,
- bimetallic catalysts free of noble metals. This category is the most attractive due to the lower price of the raw materials. In literature studies, Ni is often alloyed with Co[167–171] or more rarely with Fe[172].

Obviously, this concept is applicable to trimetallic and multimetallic catalysts[173;174].

2.7 Preparation of heterogeneous catalysts

Catalysts are the heart of chemical processes in industrial plants, and for this reason they should be very carefully prepared to fulfill all their specific requirements that can be listed as:

- cheap catalyst materials and preparation,
- reproducibility of the catalyst preparation even on larger scales,
- strong mechanical, chemical, and thermal strength,
- high activity and selectivity especially at low temperatures,
- high life expectancy, very low deactivation rate.

With this in mind, catalyst preparation should be studied and optimized prior to experiments.

A broad variety of catalyst preparation methods exists. Most of the industrial catalysts are prepared by simple techniques like precipitation or impregnation and are divided into two classes: bulk and supported catalysts.
In their simplest form, bulk catalysts are active masses, like alloys or glasses, and so called because of the composition being identical in the bulk and on the surface of the catalyst. Common bulk materials are prepared by precipitation for instance.
On the other hand, many catalysts consist of active component(s) deposited on high-surface-area carriers. The carrier can be chosen as a bulk material where active component(s) can be deposited on the outer surface area of the support, thus forming a supported catalyst.

2.7.1 Precipitation and coprecipitation

Precipitation consists of the formation of a phase-separated solid from a homogeneous solution[175]. The formation of a solid stems from a supersaturation of a homogeneous solution. Precipitation and crystallization can be confused with each other; however, crystallization is a phenomenon that involves low supersaturation, whereas precipitation is induced by introduction of an agent that starts the chemical reaction or reduces the solubility[175]. Precipitation is very often used for the preparation of the catalyst support.
If more than one component is needed, precipitation of all components occurs simultaneously and is called coprecipitation. This method is also often used to prepare catalysts like Ni/Al_2O_3 or $Ni/MgAl_2O_4$.
The precipitation usually occurs as presented in the following scheme (Fig. 2.10).
The metal solution is brought into contact with the precipitating agent. The precipitated solid is aged, filtered, and dried. The filtration and drying steps may be replaced by spray drying. The dried precursors undergo calcination and then shaping or vice versa.
The process of precipitation is presented in Fig. 2.11 and occurs in two stages, first the nucleation and then the growth.
Nucleation takes place as soon as the precursor concentration increases over the nucleation threshold and as long as the concentration remains over this critical concentration. As soon as nuclei are formed their

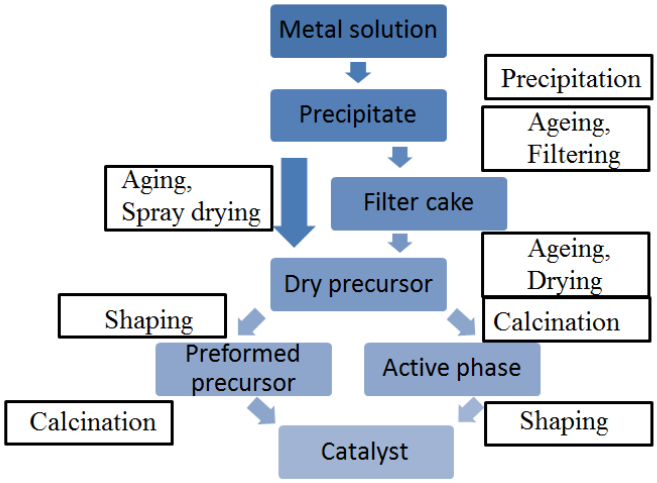

Figure 2.10: Workflow of catalyst preparation by precipitation (taken from [175])

growth occurs until the precursor concentration falls below the equilibrium concentration. The three different regimes of particle growth can be identified as:

- (I) the solution remains unchanged and nothing happens,
- (II) nucleation regime: mainly nuclei formation occurs,
- (III) growth regime: only particle growth takes place.

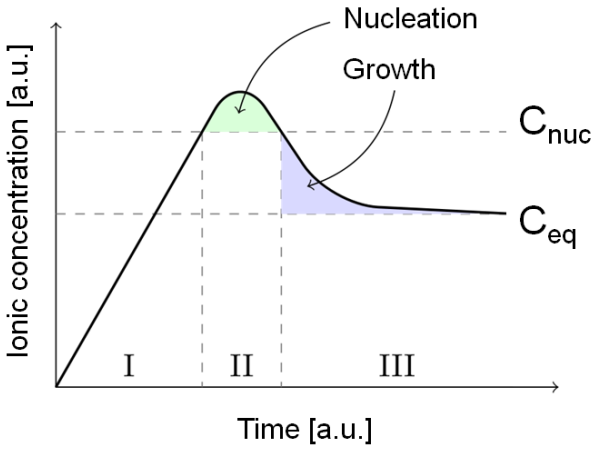

Figure 2.11: Crystal concentration depending on precipitation time (taken from public domain image via Wikipedia Creative Commons). C_{nuc},nucleation treshold; C_{eq}, equilibrium concentration

This process description has its limits because of the complex nucleus formation [175]. In addition, attrition or agglomeration of precipitated particles is possible depending on the operating conditions. The possible pathways have been discussed by Horn and Rieger [176] and Auer and Frenkel [177].

Typically, precipitation is industrially performed in a continuously stirred tank reactor. The process requires a highly automated process to be able to control temperature, pH, concentration, and residence time in precipitation vessel of the precipitate as shown in Fig. 2.12.

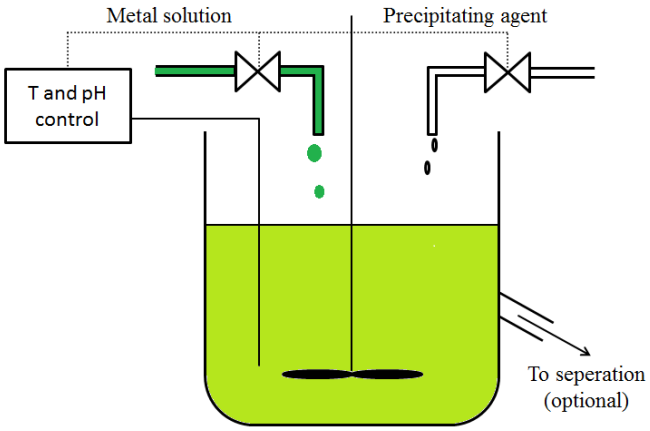

Figure 2.12: Schematic drawing of a precipitation unit (taken from [175])

The properties of the final product can be influenced in many ways. Starting with the raw materials, nitrates of metal precursors and ammonia or sodium carbonate are preferred as precipitation agents because they decompose to volatile compounds [175]. The concentration of ions is also kept relatively high to increase space-time yields and reduce plant investment [175]. For economic reasons, water is the preferred solvent in comparison to the much more expensive organic solvents.
Temperature is an extremely sensitive parameter for the nucleation rate. It is hard to predict how it will influence a specific precipitation, and for this reason an optimal temperature should be determined experimentally [175]. Control of the pH value is also crucial for supersaturation control (at least for hydroxide precipitates). Finally, ageing of the precipitate can strongly influence the properties of the final product because the particle size increases through Ostwald ripening or recrystallization of different phases or amorphous precipitates to a crystalline material [175].

2.7.2 Impregnation

The other widely used technique for solid-catalyst preparation is the deposition of one or more active components on a high-surface-area material. The goal of such a synthesis is to highly disperse component particles over the high-surface-area material surface and stabilize them against sintering [178]. The preparation of supported catalysts includes two stages: first, the deposition of dispersed particles on the active component precursor and second, the transformation of this precursor to its final state, that is, mainly metal oxides for catalytic reforming. The deposition techniques involve mainly aqueous solutions but may also be deposited from the gas phase.
Different types of "humid" impregnation methods can be used depending on the quantity of solvent involved in the impregnation step. If the total pore volume of the support is noted V_p, the incipient wetness

impregnation corresponds to an impregnation with a volume V_p of precursor solution, so that no solvent remains outside the pore of the support after impregnation. Such an impregnation takes a few seconds. On the other hand, diffusional or wet impregnation may last for a few hours and involves a support to be placed in the solvent to which the precursor solution (active compound dissolved in solvent) is added and then dried to remove the solvent. This technique should be used only if the interactions between precursor and carrier are sufficient[178].

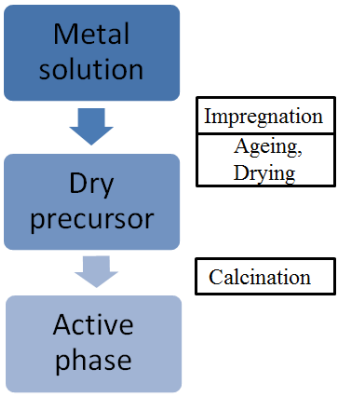

Figure 2.13: Workflow of catalyst preparation by impregnation

The synthesis steps involved in the preparation of impregnated catalysts are presented in the simplified scheme shown in Fig. 2.13. In comparison with precipitation, the synthesis of supported catalysts is much simpler. After calcination, the catalyst is dried if solvent traces remain on the solid catalyst and then calcined.

The essential parameters for an optimized impregnation are the electrostatic interactions between the metal complex and the support, the solution pH, and the type of ligand used.

The point of zero charge of the oxide support is essential to initiate the electrostatic interaction between the metal complex and the support. Two techniques have been developed to regulate the point of zero charge: changing the temperature of the impregnated solution[178] and selective doping of the surface with different types of ions[179].

The pH value is important because it influences the desired ion-support interaction[178]. The pH value of the solution determines the sign of the surface charge and thus the opposite sign has to be chosen for the complex (that is formed by the ion to be fixed on the support) to obtain an electrostatic interaction between support surface and complex. In addition, the pH influences the nuclearity of the complex (e.g. mononuclear MoO_4^{2-} and $Mo_8O_{26}^{4-}$)[180]; however, it is worth to mention that the pH value is difficult to control[181].

The type of ligand influences also the metal complex-support interaction by its charge or the nature of the ligand (bi-, tridentate...) for instance[178].

2.7.3 Formation of the final catalyst

Before loading the reactor with a catalyst, catalyst formation should be finalized. Typical examples are the calcination and reduction steps for reforming catalysts.
During the formation of the final catalyst, two factors must be considered: the metal dispersion and the precursor-support interaction [182].
The fundamental reactions involved during calcination and reduction are the solid-state diffusion-controlled and the interface-controlled reactions [182]. The first consists of the diffusion of one chemical species through the bulk. A typical example is the formation of a $NiAl_2O_4$ spinel with diffusion of NiO through γ-Al_2O_3 support during calcination. On the other hand, interface-controlled reactions proceed at the solid-liquid interface with a reactant and is kinetically limited by the interfacial process [182]. This can be illustrated by the reduction of oxides, like Ni^{2+} in NiO to metallic Ni.
Before their use most catalysts are calcined; this step consists of a thermal decomposition of the catalyst precursors into oxides under an oxidizing atmosphere like air. Depending on the final compounds expected the handling can be performed with different gases (nitrogen, oxygen, steam, reducing atmosphere, etc...) or under vacuum. Calcination is usually necessary to obtain an interaction between the support and precursors and reach an improved thermal stability [182]. An enhanced control of this interaction can be achieved by optimizing the choice of the precursors to achieve higher dispersion, formation of the new compound, or solid solution. Finally, the temperature and surrounding atmosphere have an important influence by affecting the lattice defects in solids and thus the interdiffusion in oxides. That is why, for instance, these two parameters are crucial for the formation of defect structures like spinel and perovskites [182].

The last step before catalyst testing is usually the reduction of active metal oxide. The understanding of catalyst activation by reduction is essential to find a compromise between an acceptable duration of activation and high activity [182].

Reduction of the bulk catalyst can be interpreted by means of the nucleation model or the contracting sphere model [183]. Assuming a spherical oxide particle being reduced directly to metal in an H_2 stream and a nucleation-controlled regime (nucleation rate much slower than growth rate), the reduction starts after an induction period when oxygen ions are removed from the metal oxides [183]. Following this oxygen withdrawal, defects are created and when a critical value is reached the lattice rearranges and metal or suboxide nuclei are formed [184]. As long as enough reducing agent is present, these nuclei grow. Their growth rate increases continuously due to a growing interface between "metallic nuclei" and the oxide inside the bulk. When the growing nuclei come into contact, they form a coating layer and the reduction rate decreases. This mechanism occurs until the reducible oxide is completely reduced [183].
For supported-catalyst reduction, the support plays the role of a dispersing agent [183]. If the reduction occurs on a homogeneously dispersed surface, the interactions between the support and the reducible

species may strongly influence the reducibility. Moreover, their reduction may proceed as individual metal ions or clusters[183].

In a solid solution, Lemaitre[185] showed that the process follows the model of contracting spheres like bulk catalysts. However, the interfacial area where the reaction occurs is constant and the reduction rate decreases because of depletion of reducible species[183].

2.8 Catalyst characterization methods

In order to understand and develop the catalysts and their supports, numerous physical and chemical properties must be characterized to obtain a better understanding of the catalyst functions and maybe link the catalyst properties to the activity, selectivity, and/or deactivation. Iterative approaches in catalyst development are performed to enhance the specific catalytic features, which can be identified by adapted characterization methods[186].

2.8.1 X-Ray Diffractometry (XRD)

For heterogeneous catalyst characterization, X-ray diffraction is one of the major techniques of analysis[187]. This non-destructive analytical method is based on the observation of a scattered intensity of a X-ray beam hitting the sample as function of the incident and scattered angle as described in Fig. 2.14. In case of XRD, the Cu K_α monochromatic radiations are often used. The incoming beam from the left side hits the sample with an angle θ and a part of the radiation is reflected and analyzed. In most cases the produced spherical waves after reflection generate destructive interference, while in the case of the Bragg's law (Eq. 2.39), the waves create constructive interference in a few specific directions and produce a reflection spot on the X-ray diffraction patterns. The uniqueness of each phase diffraction pattern helps to identify the presence of characteristic crystalline phases in the specimen.

$$2d \sin\theta = n\lambda \tag{2.39}$$

Here, d is the distance between the diffraction planes, θ is the incident angle of the X-ray beam, n is an integer, and λ is the wavelength of the X-ray beam.
The qualitative phase identification is performed on the basis of 2θ values and reflex intensities and compared with different databases, the most often being the Powder Diffraction File (PDF) distributed by the International Center for Diffraction Data (ICDD)[187].
The phase quantification can be achieved with different methods. Reference Intensity Ratio (RIR) methods and Rietveld methods are two of these methods using input of single-crystal data.
The Rietveld analysis is based on a routine that fits with iterations the single-crystal data to the measured XRD patterns. In addition, the Rietveld method uses refinement features that help identifying for instance variation in site occupancy or solid solutions[188]. The principle of the RIR method is similar

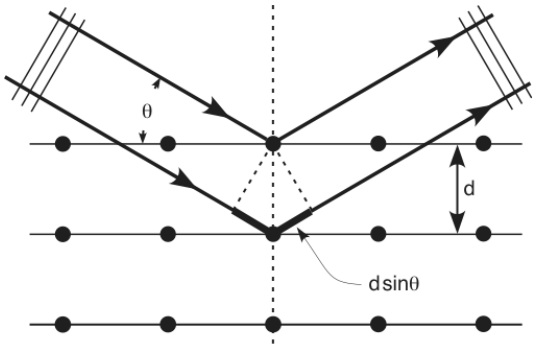

Figure 2.14: Scheme of Bragg's law (taken from public domain image via Wikipedia Creative Commons)

to the qualitative phase identification and close to internal standard methods. The ratio of intensities of the reflex from a 50:50 mixture of corundum with the pure phase to pure corundum is calculated and compared with the measured XRD pattern for quantification of phases present in the analyzed sample[188].

The particle size of crystallites can be estimated from XRD patterns with the Scherrer equation (Eq. 2.40). Assuming that lattice defects in the particles are negligible and considering X-ray reflections on N lattice planes with d_{hkl} spacing, the crystallite thickness L_{hkl} in the perpendicular direction of the diffraction plane (hkl) can be obtained[189] according to the Scherrer equation[190] by :

$$L_{hkl} = \frac{k_{Scherrer}\lambda}{\beta \cos\theta_0} \tag{2.40}$$

where λ is the wavelength of the Cu K_α radiation; θ_0 is the angular position of the peak maximum in radians; β, expressed in radians, can be chosen as the broadening at full width at half maximum (FWHM) or as integral breadth, which is the total area under the profile line divided by the line intensity at maximum[189;190]. The latter definition of β has been demonstrated to be more fundamental[191], and finally $k_{Scherrer}$ is a constant that can be set equal to 1, but equal to 0.9 if β is used as FWHM.

2.8.2 X-Ray Fluorescence (XRF)

The use of fluorescence is widely used for elemental analysis. In XRF applications, it consists of exposing samples to high energy X-rays, which have the potential to expel low energy electron(s). Because after this ionization the resulting electronic structure is unstable, the electrons from higher orbitals move to lower orbitals to minimize their energies. This rearrangement emits radiation that is specific for each atom allowing determination of atoms and their quantification, which is necessary for elemental analysis. This physical mechanism is presented in Fig. 2.15.

The characterization of the electronic reorganization around the atom is possible due to limited electronic mechanisms that are of K_α, K_β, or L_α type, representing L→K, M→K, or M→L transitions, respectively. A fluorescent photon resulting from this transition emits a characteristic energy equal to the difference

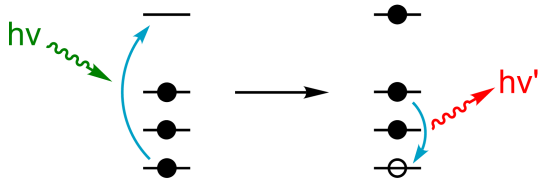

Figure 2.15: Physics of XRF in a schematic representation (taken from public domain image via Wikipedia Creative Commons)

between its final and initial state. The associated wavelength is given by the Planck equation (Eq. 2.41):

$$\lambda = \frac{h'.c}{E} \tag{2.41}$$

where λ is the wavelength of the radiation , h' the Planck's constant (h'=6.62617.10^{-34} J.s), c the speed of light, and E the energy of the photon.
Identification of the fluorescent radiation can be achieved either by sorting the wavelengths of the radiation or the energies of the photons and is called wavelength-dispersive analysis or energy-dispersive analysis, respectively.

2.8.3 Surface area and porosity

The physical properties of a catalyst can be summarized in three different categories [192]

- morphology: surface topology and steric conditions,
- porosity: pore volume in catalyst particle,
- texture: pore structures of the particle (pore size, pore size distribution, and pore shapes).

There is also a pore-size differentiation: pores larger than 25 nm are called macropores, pores smaller than 2 nm micropores, and in-between mesopores.
The pore-size distribution of macropores and mesopores is usually determined by mercury porosimetry. The macropores are of major importance for the diffusion limitation in the catalyst and its life expectancy. The micropores and mesopores have also their importance for activity because they are responsible for the high specific surface area. The texture of micropores and mesopores are determined by adsorption of gases at low pressure like N_2-physisorption.

2.8.3.1 Mercury porosimetry

Based on the volume of mercury entering the pores under pressure, the mercury porosimetry can determine the volume of larger pores. By increasing the hydrostatic pressure, mercury enters the pores in a decreasing order of width. The measurement of the pore size r_P in millimeter under the applied pressure P' is based on the Washburn equation [192] (Eq. 2.42):

$$r_P = -\frac{2\gamma}{P'}\cos\theta' \tag{2.42}$$

where P' is the applied pressure in Pa; γ the surface tension of mercury, usually taken to be equal to 485 mN.m^{-1} for pure mercury; and θ' the contact angle equal to 140° if no suitable information is available. This method remains the standard method for the investigation of macropores. Modern equipment with a pressure range from 0.003 to 4080 MPa can measure pore radii from 200 µm down to 1.8 nm if the sample allows using such high pressures[193]. Deviation in the use of this method can be observed because the pores are not exactly cylindrical as assumed[113].

2.8.3.2 N_2 physisorption

The distribution of smaller pores is measured by adsorption of gas, generally N_2. The quantity of gas needed to form a monolayer, according to the Brunauer-Emmett-Teller (BET) method[194], which is measured by volumetric or gravimetric methods[113], gives the specific surface area of the specimen. The volume adsorbed is plotted against P/P_0, the pressure ratio of the pressure P and the saturation pressure P_0. Monolayer adsorptions obtained at low pressure are governed by the Langmuir equation (Eq. 2.43):

$$\frac{V}{V_M} = \frac{K(P/P_0)}{1+K(P/P_0)} \tag{2.43}$$

with V_M the volume of the monolayer, K a constant. This formula is valid when P/P_0 is between 0.05 and 0.35[130] . Brunauer, Emmert, and Teller[194] formulated the following Eq. 2.44 for higher P/P_0 ratios for multilayer adsorption:

$$\frac{V}{V_M} = \frac{c'P}{[P-P_0][1+(c'-1)P/P_0]} \tag{2.44}$$

where c' is a constant that includes the heat of adsorption and condensation. The linearization of this equation leads to:

$$\frac{P}{V(P_0-P)} = \frac{1}{V_M c'} + \frac{(c'-1)}{V_M c'}(P/P_0) \tag{2.45}$$

The slope and the ordinate intersection allows to determine the values of c' and also V_M[192], which are directly linked to the specific surface area expressed in m^2.g^{-1}.

2.8.4 Gas chemisorption for dispersion measurements

Selective chemisorption is widely used to characterize metal catalysts[189]. It is particularly attractive to quantify the active surface of supported metal catalysts such as Pt, Pd, Rh, Ni, and Cu[195;196]. Based on the active-surface-area quantification, the metal dispersion is calculated as the ratio of the total number of metal atoms on the metal surface accessible to the adsorbate species to the total amount of metal amount in the sample[189]. The dispersion measurements are often conducted with H_2 or CO as adsorbate gas[197;198] by gas desorption methods like Temperature-Programmed Desorption (TPD), which gives the amount and type of adsorbed species and the bond energies between adsorbate and surface[199]. Due to diffusion and readsorption, the experimental results can differ slightly.

Mainly two types of measurements are performed, either at ultra-high vacuum or atmospheric pressure[200].

The choice of the adsorbate gas should be made so that the chemisorption on the metal is irreversible or weakly reversible and a minimal adsorption takes place on the support. The ratio of adsorbate gas to metal site has to be known to quantify the number of metal atoms accessible by the adsorbate gas. In the case of H_2 chemisorption, the H/Metal ratio is usually equal to one because H_2 adsorbs dissociatively on the metal surface. However, this ratio can be higher than one for example for zeolite-supported catalyst [189]. In case of CO chemisorption, various CO/Metal ratios can be expected due to different chemisorption types: dissociatively (CO/Metal$\geq$2) or associatively in a linear, bridged, or capped manner (see Fig. 2.16). The relative proportion of these forms does not depend only on pressure and temperature but also on the metal particle size [201] .

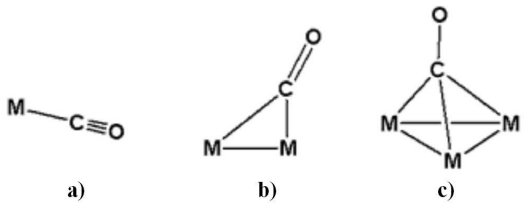

Figure 2.16: Most important types of bonding of CO on metal; a) linear; b), bridged; c) capped (taken from public domain image via Wikipedia Creative Commons)

For these reasons, the operating conditions of the gas chemisorption have to be chosen carefully. Moreover, the use of different adsorbates would improve the consistency of the results and avoid risk of artifacts [189]. Finally, the average particle size can be calculated thanks to the determination of the active area. This result can be then compared with the value obtained from the Scherrer equation (see Eq. 2.40).

2.8.5 Temperature-Programmed Reduction/Oxidation (TPR/TPO)

Thermal analysis is widely used in catalysis because of their economics and simplicity [183]. The technique consists of measuring the response (e.g. mass difference or energy release/adsorption) resulting from the temperature change of a solid specimen. Dynamic methods mostly use a constant temperature ramp. Among these measurements, Differential Scanning Calorimetry (DSC), Differential Thermal Analysis (DTA), and ThermoGravimetry (TG) belong to the standard techniques [202;203].

The DSC analysis technique describes the heat variations required to heat up the sample at a constant rate. The variation of heat shows at which temperature phase transitions take place and if these are exothermic or endothermic thanks to simultaneous comparison with a standard inert material. This analysis helps to choose the conditions for calcination. Indeed, highly endothermic or exothermic reactions may occur on the catalyst particles and produce non-homogeneous calcined particles within a batch.

Thermogravimetry aims to determine the mass increase or mass loss of a sample depending on gas mixture, temperature, and pressure applied. When performed together with DSC, the technique is usually called STA-TG (Simultaneous Thermal Analysis-ThermoGravimetry).

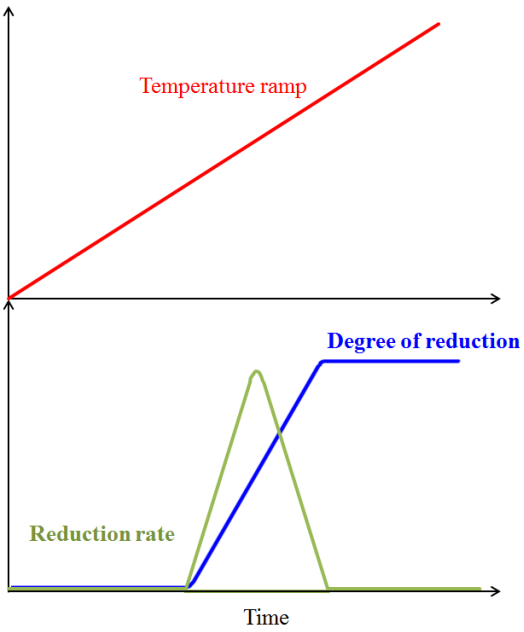

Figure 2.17: Scheme of time dependence of reduction rate and degree of reduction (adapted from [183])

These thermoanalytical techniques are used to understand the surface reactivities and gas-solid interactions. In TPR and TPO, the solid catalyst is exposed, respectively, to reducing or oxidizing atmospheres while the temperature is increased. The reducing atmosphere is typically H_2 or CO diluted in an inert gas and for an oxidizing atmosphere air is usually used. During the reduction/oxidation, the outlet mixture is analyzed to quantify the amount of reducing/oxidizing agent. For instance, the time dependence of the reduction is presented in Fig. 2.17.

The reduction of bulk materials, solid solutions containing reducible species as well as supported reducible species have been described in section 2.7.3 of this part (II).

2.8.6 Techniques in electron microscopy

The images produced by electron microscope techniques help understanding the morphology and structure of catalysts within a range of micrometers down to the atomic scale. The scheme in Fig. 2.18 shows the signals generated by an incoming electron beam. The wide variety of signals makes it possible to use a whole spectrum of instrumental methods for the characterization of the geometric, compositional, and electronic structure of the catalyst[204].

Even if a broad variety of electron microscope measurements exists for the structural characterization of surfaces, only direct methods can provide real information on local inhomogeneities such as defects, steps, and terraces[205]. The method consists of beaming electrons onto the specimen surface to produce an overall contrast due to differential absorption of photons or particles (amplitude contrast) or diffraction phenomena (phase contrast)[206]. Based on these principles, the obtained image allows to obtain phase and structural information, as well as element composition and distribution. The application of electron microscopy is limited to the complexity of image interpretation or constraints on the specimen

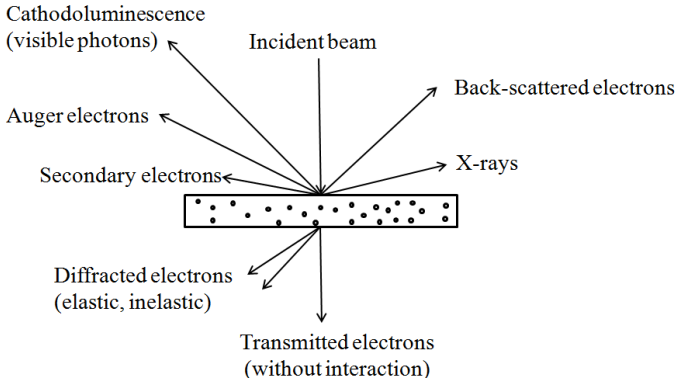

Figure 2.18: Signals generated from an incident electron beam on a specimen showing the large variety of applicable electron microscope techniques (taken from [204])

preparation and the environment in the microscope [206].

Transmission Electron Microscopy (TEM) is the imaging of an electron beam passing through a very thin specimen where it interacts with the specimen in the object plane (Fig. 2.19). The transmitted electromagnetic beam goes through a converging lens, producing a 2D diffraction pattern in the lens' focal plane, and the recombination of the diffracted beams occurs in the image plane [204]. The excitation variation of a series of projection lenses allows to observe either a magnified image or a diffraction pattern on a detection device [204].

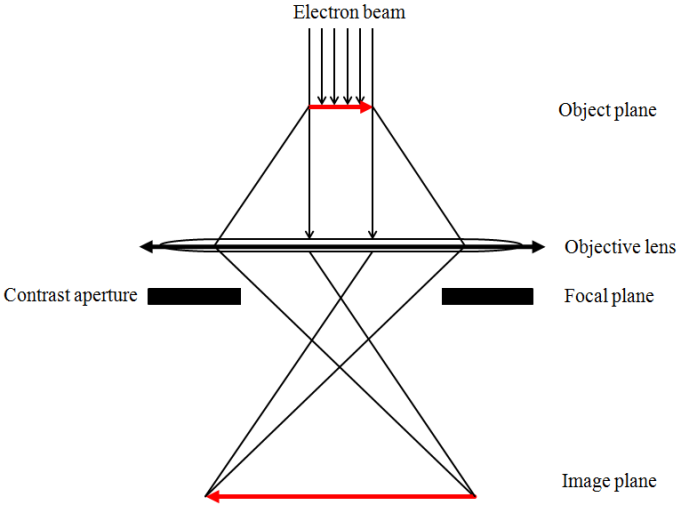

Figure 2.19: Scheme of image formation in a TEM (taken from [207])

The conventional TEM (CTEM) and the high-resolution TEM (HRTEM) are TEMs operating in two modes [204].

The image contrast within CTEM is performed by the aperture that should eliminate the diffracted beams. Darker fields are generated either due to diffraction or mass-thickness effects. The mode of imaging can be bright field (BF) if all diffracted electrons are eliminated by aperture or Dark Field (DF) if only

diffracted electrons are selected with aperture and the central beam is excluded[204]. For instance, if detection of the presence of a small metal particle (2-3 nm) is desired for low magnification bright-field imaging is preferred[204;206]
HRTEM uses several diffracted beams that interfere with the axially transmitted beam to form the image-producing contrast that reflects the relative phases of the various beams[204]. This imaging mode is preferred to determine the atomic structure of the particles.

Another mode of electron microscopy is Scanning Transmission Electron Microscopy (STEM), where a small spot formed from a convergent beam is raster-scanned over the specimen while detecting electrons that are transmitted or scattered[204]. Another advantage of STEM is the number of techniques that can be used for imaging (see Fig. 2.20). STEM also has a relatively low signal-to-noise ratio thanks to the intense electron probe giving images of very small particles on the subnanometer scale[204].

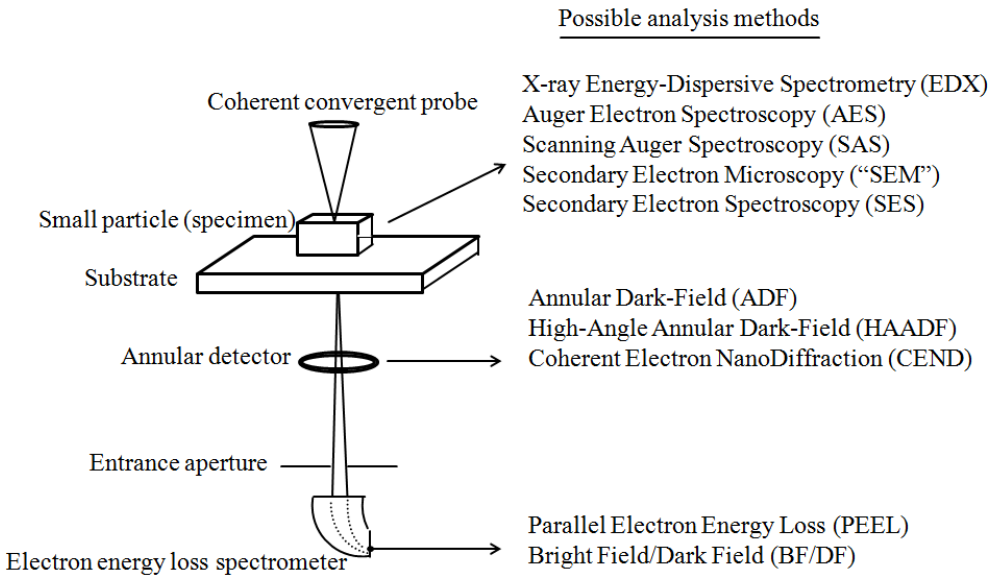

Figure 2.20: Scheme of image formation in a STEM with associated analysis methods (taken from[208])

Of particular interest is High-Angle Annular Dark-Field (HAADF) imaging, which uses an annular ring that collects the electrons scattered at high angles to form the image while the transmitted beam can be further analyzed in an electron spectrometer for simultaneous elemental analysis[204;209].

Scanning Electron Microscopy (SEM) produces an image by scanning it with a focused electron beam. The difference to TEM and SEM is that the SEM sample does not need to be very thin because transmission is not used[210]. The topographical images are obtained from back-scattered primary or low-energy secondary electrons[206]. Energy-dispersive X-ray spectroscopes are often used to identify and perform quantification of elements[206]. This technique is based on the X-ray fluorescence (see section 2.8.2 of this part (II)).

2.9 Further characterizations for catalyst tests

2.9.1 Gas Chromatography (GC)

Chromatography is a well-known technique used for phase separations in preparatory synthesis; however, it is also applied to characterization. The technique is based on the separation of phases or compounds through an adsorption column due to the affinity of the mobile phase (the fluid to be analyzed) and the immobile phase (filling material in the column). After separation of the gases of the specimen, their respective concentrations are measured by means of different detectors: thermal conductivity detector (TCD) or flame ionization detector (FID), the first being non-destructive can be used before FID, which is destructive.

The different constituents exhibit characteristic retention times, and the area under the chromatogram at a defined retention time is proportional to the concentration of the compound expected at this retention time. The calibration measurements are made with a characteristic gas composition, which provides a standard and the possibility to calculate precisely the composition of the desired specimen.

2.9.2 Gas-flow measurement

The mass-flow meter measures the quantity of fluid going through it during a defined period of time. The first technique is based on the twisting effect of flow on elongated parts in the flow direction moving within the cross section of the pipe.

The second technique is used in the setups described in this thesis. A gas is split and only a small amount of the gas in a parallel circuit undergoes a heat flux in upstream. The temperature of gas is measured downstream, while the temperature differential that generates a proportional change in the resistance of the sensor winding is measured and compared to the calibration, thus indicating the real flow.

3 Catalytic reforming at high temperatures

At high temperatures, the catalyst performance has been shown to often result from complex heterogeneous, homogeneous, and radical mechanisms coupled with mass and heat transfer[211]. Such complexes favor the broadening of reaction pathways and thus decrease selectivities of desired products. In addition, the catalyst itself has to endure harsh operational conditions that require special material features like high thermal stability and mechanical strength.

3.1 Challenges of catalytic reforming at high temperatures

The detailed mechanisms of reforming in catalytic partial oxidation[211–213] and CO_2 reforming of methane[28;214] have been studied by the Deutschmann's group.
In addition to the well-known catalytic reforming reaction occurring on the catalysts, gas-phase reactions are involved in CO_2 reforming at high temperatures even if small amounts of H_2O are added to the feed stream[22]. Indeed, methane decomposition occurs, leading to the formation of olefins, aromatics, and coke[22]. These results will be presented and discussed in the following parts of this thesis.
Beside gas-phase reactions, high temperatures are also challenging for catalyst stability, especially due to:

- decrease of catalytic specific area,
- sintering of active particles (e.g. Ni, Pt...) leading to larger particles and smaller active areas in addition to coking[38;215],
- favoring the fatigue of all materials including reactor materials.

3.2 Solutions for catalytic reforming at high temperatures

First of all, process temperatures should be kept as low as possible for economical reasons due to elevated costs of materials required for high-temperature operations in multi-tubular reformers, utility prices, significant sintering effects, material fatigue, and loss of specific area.
The choice of catalyst, like in every catalytic process, is of major importance. The type of active metal can be first chosen taking in consideration costs and sintering temperature. For the active metal of catalysts, two different categories exist: the expensive noble metal (e.g. for reforming: Ir, Rh, Ru, Pt) with

a slightly higher sintering temperature compared to the inexpensive non-noble metals (e.g. Co, Cu, Fe, Ni). For economical reasons, the cheaper materials are favored while noble metals are used in small-scale units, for instance in three-way catalytic converters[216;217] but also in fuel-cell reformers[218;219]. Sintering effects of these active-metal particles can be delayed using appropriate support materials where small and well-dispersed active-metal particles with strong metal-support interactions can be generated[134]. This is easily achieved when particle size of the active metal is kept in the nanometer range, for instance small particles of Ni on MgO-Al_2O_3[38;215]. For that reason, the catalyst support material should be chosen meticulously.

3.3 Catalytic reforming review for high-temperature purposes

A large amount of catalytic materials has been tested up to now on different merging applications like CPOX or CO_2 reforming in fuel cells or methane combustion. The experience gain from these fields of applications but also from other more atypical like solid-state lasers[220] (e.g. YAG) or ionic conductors[221] (e.g. hexaaluminates), helps finding new catalysts for the mixed-steam CO_2 reforming under high pressure. Moreover, experience with mixed-steam CO_2 reforming with a few of these catalytic materials has been reported in the literature[215;222–226], giving a partial benchmarking of the different materials.

Few supports are already known for high-temperature applications like spinels in reforming[10], hexaaluminates in catalytic combustion of methane and catalytic partial oxidation[227;228] , α-alumina in catalytic partial oxidation of methane[10], and perovskites for high-temperature fuel cells[229]. The Yttrium Aluminum Garnets (YAG)[220;227], zirconia[230], and molybdenum carbide[14;231–235] are also quoted in the reforming literature and should fulfill the requirements of high-temperature supports due to their high melting points over 2173 K (1900°C).

3.3.1 Attractive catalytic systems known in mixed-steam CO_2 reforming

Platinum Group Metal (PGM)-based catalysts are known in addition to their price to have a very low intrinsic coking affinity and high activity in comparison with non-noble metals for steam reforming (e.g. Ni/ZrO_2 and Pt/ZrO_2[230]) and CO_2 reforming (e.g. Ni/ZrO_2 and Pt/ZrO_2[29]). Based on this knowledge, it is much simpler to develop and produce a benchmark catalyst necessary to compare PGM-based catalysts with non-noble-metal-based catalyst performances. In the case of Pt-based catalysts, the aim is to synthesize highly dispersed Pt-particles over a support able to stabilize such nanoparticles. A wide range of readily available support materials can be selected for this task, like α- and γ-alumina, ZrO_2, or TiO_2. These supports can even be modified by promoters like silica, lanthanum, or ceria for zirconia stabilization to improve the catalyst's stability and activity in the reforming of methane.

Up to now only the Ni-on-$MgAl_2O_4$ system has been extensively investigated for mixed-steam CO_2 reforming. Yoon's group has studied extensively mixed-steam CO_2 reforming on Ni over $MgAl_2O_4$[215;222;223],

and promotion through CeO_2-ZrO_2 has been further investigated by Jun et al.[224;225]. Lately, they have patented this catalytic system[226] for reaction temperatures between 1073-1273 K (800-1000°C), at pressures from 0.5 up to 20 bar, with a $CH_4/H_2O/CO_2$ ratio in the range of 1/1-2/0.3-0.6, and a GHSV from 1000 up to 500000 h^{-1}.

3.3.2 Other potentially attractive catalytic systems for CO_2 reforming applications

Other carrier matrices, quoted in this chapter to have a high stability potential, may be applicable for mixed-steam CO_2 reforming.

3.3.2.1 Hexaaluminates

Hexaaluminates have a high potential due to a high thermal stability in hydrocarbon combustion[236–239]. In addition, Al^{3+} could be substituted with active metals (e.g. Ni, Co, Fe) within the crystal structure to obtain after reduction well-dispersed active Ni^0-nanoparticles[46;240;241]. Ni-hexaaluminates have been also used in the partial oxidation of hydrocarbons[46;47;242] as well as in CO_2 reforming of methane[243–246]. For instance in CO_2 reforming of methane, $La_{0.8}Pr_{0.2}NiAl_{11}O_{19}$ exhibits high and stable CH_4 and CO_2 conversions of 89% and 95%, respectively, at atmospheric pressure, 1023 K (750°C), 0.2 g of catalyst with an input flow rate of 30 $ml.min^{-1}$; finally after 300 h only 0.75 g of coke per gram of catalyst was found[247].

3.3.2.2 Perovskites

Perovskite-like catalysts of formula ABO_3, with A as large trivalent cation and B as small cation that can be partially substituted by an active metal, could also have an attractive potential by dispersing active metals within its lattice. However, reduction of active metals leads to structural collapse[25;248] because of too many defects within the perovskite lattice; the structures found after reduction are mainly Ruddlesden-Popper phases ($(AO)(ABO_3)_n$), where n is an integer). A large variety of perovskites has already been tested for the CO_2 reforming reaction by Valderrama and co-workers[25;249;250] and Sierra Gallego et al.[248;251;252]. Both groups have worked on $LaNiO_3$ with a perovskite-like structure and Sr, Ce, Pr, Co, and Mg promotion, but no proof of extreme stability has been reported. Hayakawa et al.[253] also have tested Ba-, Ca-, Sr-titanate perovskite-like catalysts partially substituted with Ni with similar activity and stability as Ni/MgO but not as good as hexaaluminates without noble-metal-containing perovskite. Recently, Pavlova and co-workers[254] have presented a perovskite-based catalyst $PrFe_{0.65}Ru_{0.05}Ni_{0.3}\ O_3$, which worked without coking at 1073 K (800°C) and a GHSV of 22 $l.h^{-1}.g^{-1}$ catalyst with a stable methane conversion of 90%. The perovskite-like structure can be formed with a large amount of compounds, leading to unconventional new materials like $NdCoO_3$; Choudhary et al. have tested it under CO_2 reforming and mixed-steam CO_2 reforming conditions[255;256], after which reduction of the catalyst

led to formation of Co on Nd_2O_3. Under CO_2 reforming conditions, this catalyst converted stably, over 60 h at 1123 K (850°C), atmospheric pressure, and 20000 $ml.h^{-1}.g^{-1}$, 92% and 96% of methane and CO_2 conversion, respectively, and after 15 h no coke formation was detected. The authors also published an overview of other catalysts including Ru on alumina, showing that $NdCoO_3$ showed high performance and the best stability among all other compared catalysts[255].

3.3.2.3 Molybdenum carbides

York and co-workers have assessed for more than a decade already the potential of molybdenum carbides substituted with Ni in CO_2 reforming reactions[231–235]. Ni-modified Mo_2C is found to be active in CO_2 reforming of methane but also in partial oxidation and steam reforming[231]. For CO_2 reforming of methane, these carbides are active, operating without carbon deposits and comparable with noble metals[231] even at 12 bar[232]. This comparison is also true for steam reforming and partial oxidation of methane[234]. High pressure favors the stability of these carbides[233]; however, Mo_2C can be oxidized to MoO_2 and is found to deactivate faster with oxygen than with steam or CO_2[233]. Based on this knowledge, the operating stability is governed by a controlled reduction/oxidizing balance pinpointed by Zhang et al.[257].

Part III

Experimental part

1 Reforming test units

The different synthesized catalysts are tested by the means of four different setups (Tab. 1.1). Two large-scale units operating at 21 bar and 1123-1223 K (850-950°C) and other small-scale units, one screening unit operating at 1 bar and 1123-1223 K (850-950°C) with 16-fold reactors in addition to a differential reactor working at 11 bar and 1073-1123 K (800-850°C).

Scale	Unit type	Pressure	Catalyst amount	Number of reactors	Temperature range used
Large	Prototype	21 bar	20 ml	1	1123-1223 K (850-950°C)
Large	Screening unit	21 bar	20 ml	6	1123-1173 K (850-900°C)
Small	Screening unit	1 bar	0.125-1 ml	16	1023-1173 K (750-900°C)
Small	Differential reactor	11 bar	20 mg	1	1073-1123 K (800-850°C)

Table 1.1: Overview of the different units used for the evaluation of catalyst performances at high temperature

1.1 Reactor concept

Because of the high temperature as well as the high plugging risk with carbon deposits, the reactor is made of a high temperature alloy. This alloy material contains active metals (e.g. Co, Ni,...); for this reason an inner ceramic tube, made of α-alumina, is installed. The design of the reactor concept is presented in Fig. 1.1.

In the primary ceramic tube, a frit made of α-alumina is placed on a smaller secondary ceramic tube from the bottom. The ceramic assembly is inserted into a metal tube to ensure that the entire gas feed flows through the catalytic bed. On the reactor bottom, small holes ensure a steady gas flow and no pressure gradient that could cause the primary ceramic tube to break. A nitrogen flush is added at the top of the reactor to ensure an inert atmosphere between metal and ceramic tube.

First, the ceramic tubes and frit assemblies are put together and then inserted into the metal tubes. The reactor is filled vertically with 2 cm of steatite balls and then about 20 ml of catalyst, which are supported by the frit. The catalyst amount is measured with a measuring glass cylinder, packed by knocking on the cylinder walls 5 times on every side and on the bottom and finally the exact volume and mass are noted. The reactor liners are filled and packed at a precise height to keep the catalyst in the desired hot zone.

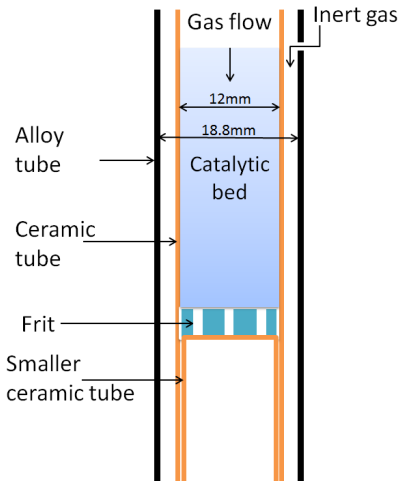

Figure 1.1: Design of the reactor concept

When necessary, an additional corundum prebed is added to reduce the residence time of the gas in the reactor front bed.

1.2 High-pressure experimental setups

Catalyst performance is evaluated in two setups that can perform the reforming reactions of methane with steam and CO_2 at high pressure and temperature levels typically used in reforming plants.
A single reactor (prototype) and a screening unit consisting of six-fold reactors are used for the assessment of catalyst performance. The experimental setups are based on a similar technology, and product streams are analyzed by Gas Chromatography (GC) and a gas flow meter. Both of the plants are used at 21 bar within a temperature range of 1123-1273 K (850-1000°C); the GHSV is kept constant at 3800 h^{-1}.

1.2.1 Prototype unit

The prototype unit is set up to simulate the behavior of a syngas-production pilot plant. A simplified scheme of the setup is presented in Fig. 1.2. The feed rack is made of a High-Performance-Liquid-Chromatography (HPLC) pump with a preparative pump head; on the other hand, gases are delivered by Mass-Flow Controllers (MFC) that measure and control the delivered gas flows.
The feed is then heated up in an evaporator from room temperature up to 473 K (200°C). The feed passes then through the reactor and is heated up by a furnace; pressure is then built up to 21 bar thanks to a pressure-controlled valve located at the bottom of the reactor. The upper reactor end is held at 473 K (200°C) in a secondary oven while at the reactor bottom the temperature of the secondary oven is set at 453 K (180°C). In the downstream section, the product stream is quenched, with the pressure-hold gas (N_2) at atmospheric pressure. The flow is then measured with a Hot-Gas Flow Meter (HGFM). The water is then separated in a condenser before the exhaust, and a small amount of product stream gas is injected into the GC.

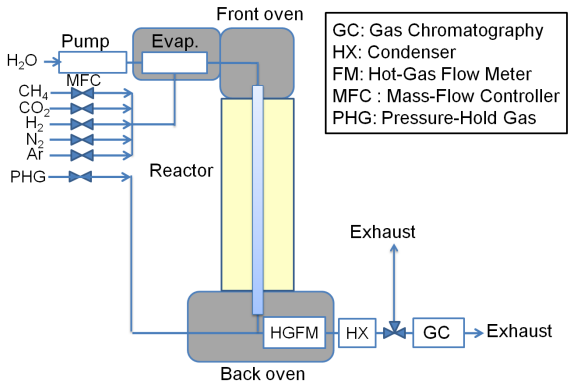

Figure 1.2: Scheme of single reactor test unit. The grey areas are kept at about 473 K (200°C) and the yellow area at reaction temperature (1123-1223 K - 850-950°C).

Due to the possibility of reactor blockage and subsequent pressure increase, the setup is programmed for automatic shutdown if the pressure increases over 29 bar. In this case, feed streams are shut down, the pressure-controller opens the valve completely, the temperature is set to room temperature, and only nitrogen flows through the setup and flushes the reactor.

1.2.2 Six-fold screening unit

The screening setup is built based on the same basis as the single reactor setup and is presented in Figs. 1.3 and 1.4. Specifications are adapted to deliver gas through six positions plus a bypass. 14 secondary ovens are used as seen in Fig. 1.3. There are six three-zone ovens and each is associated with two secondary ovens, plus the upper left one is used to heat the gas-distribution manifold and the bypass position, while the lower left one is used for heating the "bottom" of the bypass, the multi-position valve, and HGFM.

Figure 1.3: Screening test unit

After the evaporator, the feed temperature is kept constant at 473 K (200°C), and the feed stream is divided up to feed the 6 reactor positions plus the bypass equally. The gas distribution is achieved on the basis of adapted pressure restrictions controlling the head pressure to be at a constant level. A safety valve is also included in this part to directly feed the stream excess to the exhaust if the head pressure rises over a defined pressure. In case one or more reactors plug, the excess of the feed stream is first measured and then sent straight to the exhaust. This allows the gas streams to keep flowing through the unplugged reactors and to keep the bypass at steady operating conditions, even if one or more reactors are plugged. The pressure within every position is kept constant by a pressure-control process that includes nitrogen quenching of product streams by Pressure-Build-up Gas (PBG), and pressure is held constant by using nitrogen in Pressure Hold Gas (PHG)[258]. After the reactors and the bypass, the pressure is lowered to about atmospheric pressure, the steam is condensed, and then the product stream is analyzed by GC. The outstream distribution is performed by a multi-position valve that directs only one position to the analytic rack and the rest to the exhaust. After reaction and characterization, all streams are directed to a plate heat exchanger to get rid of water before the exhaust.

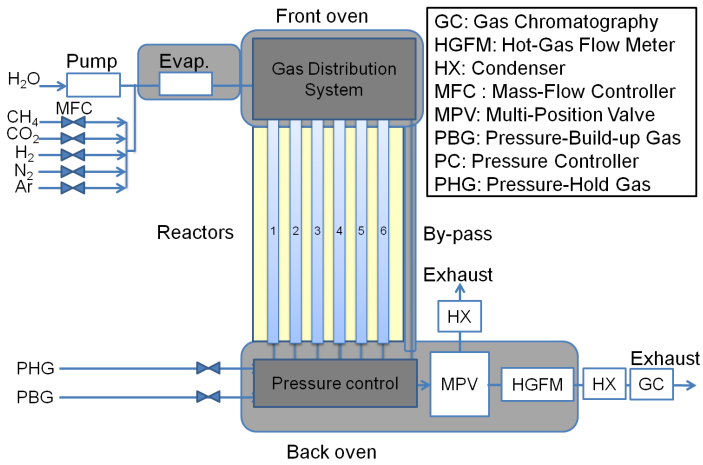

Figure 1.4: Scheme of six-fold screening unit. The grey areas are kept at about 473 K (200°C), and the yellow area at reaction temperature (1123-1223 K - 850-950°C).

1.2.3 Software and hardware supports

In order to control the setups, different software platforms are used at hte AG. myhte is the database used to record and link synthesized samples, process data, and evaluations including calculations. hte control on the other hand is used to monitor the different parameters such as temperatures, flows, pressures,... Both platforms were developed internally by hte AG. In addition, EZChrom Elite (Agilent Technologies) is used to control the GC and analyze its measurements.

The complexity of the screening unit is monitored by an improved interface managed by the Zenon platform. The interface also allows to use a remote controller for MFC calibration, for instance.

In a similar way to for catalyst preparation, every task performed is described in a electronic laboratory

journal (E-WorkBook-2011 from IDBS®). This includes the following steps depending on the flow range of the chosen MFC: setup modifications, calibrations, reactor-filling data, catalytic bed properties, starting procedures, test protocols, and operating conditions.

1.3 Low-pressure experimental setup

For the kinetic studies, a screening setup unit made of 16-fold reactors is presented in Fig. 1.5 and operated at atmospheric pressure. The reactors are grouped four by four in different ovens. This allows to perform tests at different temperatures. The mass of the catalyst can be varied up to 1 ml with a split of 315-500 µm. The flow is held constant at 1067 sccm; however, light variations are possible due to the different pressure drop in the different catalytic bed. The setup works similarly to the screening setup operating at high pressure shown in Fig. 1.4 (section 1.2.2 of this part (III)).

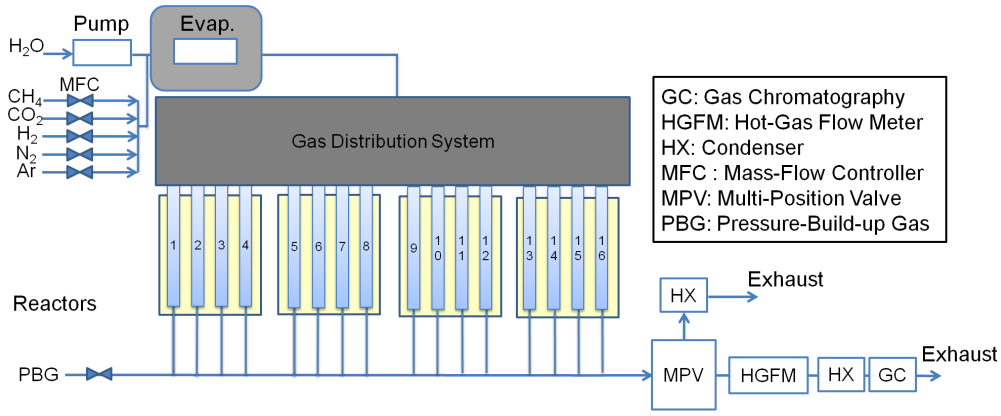

Figure 1.5: Screening unit with 16-fold small-scale reactors at atmospheric pressure. Grey areas are kept at about 473 K (200°C) and the yellow area at reaction temperature (1023-1173 K - 750-900°C).

For the kinetic measurements, the influence of temperature is studied at different temperatures (1023, 1073, 1123, 1173 K - 750, 800, 850, and 900°C, respectively), the influence of GHSV is studied by varying the volume of the catalyst (0.1, 0.2, and 1 ml of catalyst), and for the fourth reactor, 1 ml of corundum is used to explore the gas-phase reactions.

1.4 Recycling setup

The content of this section consists of the reuse of the experimental part of a published article about Ni hexaaluminates[241] during this PhD thesis.

In collaboration with the Technische Universität München, test reactions are performed in recycling reactor (Fig. 1.6). The setup for the measurements operates at 11 bar and 1123 K (850°C) in closed loop. This means that the product stream is reused as gas inlet while the inlet stream is shut down.

20 mg of catalyst (500-710 µm) is diluted with 80 mg of SiC of the same size. The mixture is placed in a tube made of alumina with a 6 mm inner and 7 mm outer diameter. This tube is sealed to be gas proof, so that no gas contact occurs with the stainless steel tube, which prevents a possible breach of the ceramic tube. The catalytic bed is first flushed with N_2, heated up to 1073 K (800°C), and reduced with 20% H_2 in N_2 for 2 h at atmospheric pressure in a single pass mode like in a typical reactor. After this, the reactor is flushed with N_2 still at atmospheric pressure and the loop is closed. At t=0, the reactant mixture, a stoichiometric quantity of CH_4 and CO_2, is added to the closed loop where the pressure reached 11 bar. The reaction is conducted in closed loop during 10 h at 11 bar with a CH_4/CO_2 ratio of one and N_2 as an internal standard.

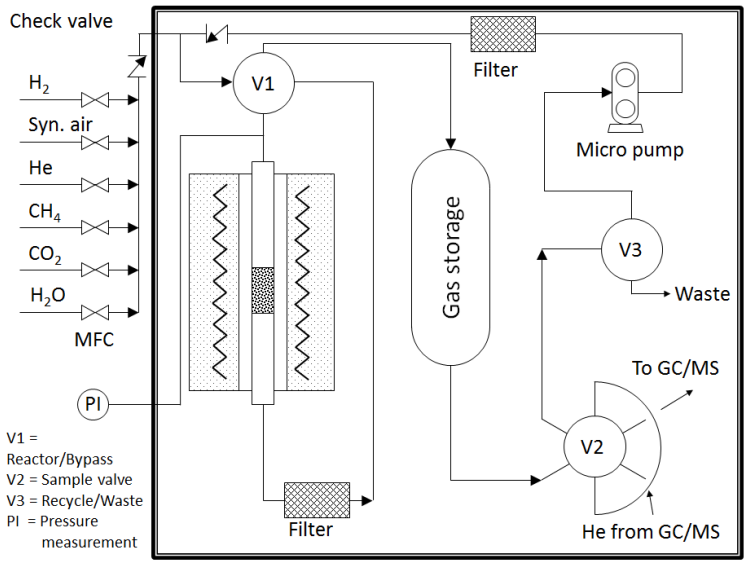

Figure 1.6: Design of recycling reactor (or differential reactor) (taken from[241])

The product gas is analyzed by a coupled GC/GC-mass spectrometry (MS) system of Shimdadzu equipped with a HP-PlotQ (0.53 mm x 30 m) and a molecular-sieve (0.54 mm x 30 m) column to separate the different components before MS/GC analysis (FID, TCD, and Quadropole MS as detectors).

2 Calculations

The following calculations are included in an algorithm to determine the molar rates and conversions. Depending on the setup, there are minor changes; however, principles are the same.

2.1 Volumetric flows and molar flow rates

Before performing any calculations, knowledge of flows and molar rates are required. Firstly, the raw data given by the MFC need to be corrected by using a specific factor $C_{f,i}$ for gas i because every compound has its own conductivity. $C_{f,i}$ is calculated from the heat capacity of gas i, $C_{P,i}$:

$$C_{f,i} = \frac{C_{P,N_2}}{C_{P,i}} \tag{2.1}$$

The specific heat capacities $C_{P,i}$ and $C_{f,i}$ as well as the molar mass are listed in Tab. 2.1.

i	Gas	Molar weight [g.mol^{-1}]	$C_{P,i}$ at 1 bar and 453 K (180°C) [J.(mol.K)$^{-1}$]	$C_{f,i}$ [-]
1	Ar	39.95	20.82	1.414
2	CH_4	16.04	44.29	0.665
3	CO	28.01	29.58	0.995
4	CO_2	44.01	43.22	0.681
5	H_2	2.02	29.21	1.008
6	H_2O	18.02	35.36	0.833
7	N_2	28.01	29.44	1.000

Table 2.1: Gases and their properties

This allows to obtain the corrected outlet flow $\dot{V}^{out}$ calculated from the flow $\dot{V}^{out'}$, measured by each HGFM after the reactor, and the molar fractions x_i^{out} in the HGFM relative to compound i. The molar fractions x_i^{out} in the product stream are calculated through the integration of the chromatograms. These areas are proportionally correlated to the concentration in the product stream that is measured in the HGFM and thus the following corrected flow can be calculated:

$$\dot{V}^{out} = \frac{\dot{V}^{out'}}{\sum_{i=1} \left(x_i^{out} / C_{f,i} \right)} \tag{2.2}$$

The outlet molar flow rates $\dot{V}_i^{out}$ are obtained by the following equation:

$$\dot{V}_i^{out} = \frac{\dot{V}^{out}.x_i^{out}}{V_m} \tag{2.3}$$

where V_m i the molar volume (22.4 l.mol^{-1}).
The inlet molar flow rates $\dot{V}_i^{in}$ are calculated directly from the valve position of the MFC and converted into real flows thanks to the respective calibration curves.

2.2 Conversions and H_2/CO ratio

The conversion calculations are based on the previous evaluation of molar flows entering the reactor and leaving it. Assuming no accumulation of gas in the reactor, it can be stated, based on the mass balance of compound i in the reactor, that the gas flow of compound i leaving the reactor is the result of the amount entering minus the amount of i converted/plus the amount of i produced. The corresponding equations for the conversions of methane X_{CH_4}, carbon dioxide X_{CO_2}, and of water X_{H_2O} are defined as:

$$X_{CH_4} = \frac{\dot{V}_{CH_4}^{in} - \dot{V}_{CH_4}^{out}}{\dot{V}_{CH_4}^{in}} \tag{2.4}$$

$$X_{CO_2} = \frac{\dot{V}_{CO_2}^{in} - \dot{V}_{CO_2}^{out}}{\dot{V}_{CO_2}^{in}} \tag{2.5}$$

$$X_{H_2O} = \frac{\dot{V}_{H_2O}^{in} - \dot{V}_{H_2O}^{out}}{\dot{V}_{H_2O}^{in}} \tag{2.6}$$

Obviously, no conversion of H_2O or CO_2 is achieved if they are not present in the feed stream.
The ratio of H_2/CO is defined by the ratio of the molar flow of H_2 and CO in the product stream:

$$H_2/CO = \frac{\dot{V}_{H_2}^{out}}{\dot{V}_{CO}^{out}} \tag{2.7}$$

2.3 Balances

Balances are of great importance because they allow to verify the assumption of no accumulation in the reactor. Indeed, reactor plugging or coking lead to an accumulation of gas or carbon atoms in the reactor, which would invalidate this assumption.
In addition, it is possible that a leak appears in the setup. For this reason, Ar is used as internal standard to detect possible malfunctions of the unit. For Ar, since it is inert, the balance or the recovery Rec_{Ar} is defined as the percentage of Ar recovered at the output:

$$Rec_{Ar} = \frac{\dot{V}_{Ar}^{out}}{\dot{V}_{Ar}^{in}} \tag{2.8}$$

Furthermore, the coking tendency is evaluated also by an atomic carbon balance and the following expression of the carbon recovery Rec_C.

$$Rec_C = \frac{\dot{V}_{CH_4}^{out} + \dot{V}_{CO}^{out} + \dot{V}_{CO_2}^{out}}{\dot{V}_{CH_4}^{in} + \dot{V}_{CO}^{in} + \dot{V}_{CO_2}^{in}} \tag{2.9}$$

In the same way the balance of atomic H Rec_H and O Rec_O are calculated:

$$Rec_H = \frac{4.\dot{V}_{CH_4}^{out} + 2.\dot{V}_{H_2O}^{out} + 2.\dot{V}_{H_2}^{out}}{4.\dot{V}_{CH_4}^{in} + 2.\dot{V}_{H_2O}^{in} + 2.\dot{V}_{H_2}^{in}} \tag{2.10}$$

$$Rec_O = \frac{\dot{V}_{CO}^{out} + 2.\dot{V}_{CO_2}^{out} + \dot{V}_{H_2O}^{out}}{\dot{V}_{CO}^{in} + 2.\dot{V}_{CO_2}^{in} + \dot{V}_{H_2O}^{in}} \tag{2.11}$$

All these calculations are currently not used, but helpful for interpretation of results, especially if something goes wrong in the setup.

2.4 Space-Time Yield (STY), Weight-Time Yield (WTY), Turnover Frequency (TOF)

The STY and WTY are proportional to the molar flow rates of the desired products, as the analytic expressions show:

$$STY_i = \frac{molar\ rate\ of\ i\ consumption}{V_{cat.}} = \frac{mol.s^{-1}}{m^3\ cat.} \tag{2.12}$$

$$WTY_i = \frac{molar\ rate\ of\ i\ consumption}{m_{cat.}} = \frac{mol.s^{-1}}{kg\ cat.} \tag{2.13}$$

where $V_{cat.}$ and $m_{cat.}$ are the volume and the mass of the catalyst respectively.
TOF of i can also be used to compare performances. It describes the specific activity of a catalytic center for the consumption of i and is equal to:

$$TOF_i = \frac{molar\ rate\ of\ i\ consumption}{mole\ of\ active\ centers} = \frac{mol.s^{-1}}{mol} \tag{2.14}$$

Further parameters can be also used for comparison and optimization of performances. In this study, these parameters are found to be the most representative and relevant for the characterization of the catalysts and exploring gas-phase reactions.

Part IV

Gas-phase reactions over "inert" materials

Prior to catalytic testing, the properties of the test units need to be evaluated in order to understand the impact of gas-phase reactions and their influence on the catalyst performance to improve reactor design by limiting coke formation. For this investigation, different reactor configurations, including non-catalytic and catalytic cases, are studied under a typical range of operating reforming conditions. The goal is to understand the relation between the gas-phase reactions and the catalytic reactions in the different parts of the reactor (prebed, top and bottom of the bed as well as post-bed), and then to make a choice on the operating reforming conditions for the catalysts in a performance test.
For these reasons, the gas-phase reactions have been studied at hte AG by using the screening plant, and the results have been simulated in Deutschmann's group at Karlsruhe Institute of Technology (KIT).

1 Gas-phase reactions and coke precursors: State of the art

Reforming of hydrocarbons with a high carbon content in the feed stream is a risky task due to homogeneous and heterogeneous reactions leading to coke formation followed by reactor plugging. The heterogeneous reactions leading to coke deposits on the catalyst surface are well known and have been extensively studied[21;36;259].

Among the heterogeneous reactions leading to coke deposits, methane cracking ($CH_4 \rightleftharpoons C_{(s)}+2\ H_2$) and the Boudouard reaction ($2\ CO \rightleftharpoons CO_2+C_{(s)}$) are prevailing. The catalysts can handle these reactions as long as the coke gasifying rates are higher than the coking rates[36], that is, if coke is not stable under thermodynamic equilibrium.

Among homogeneous gas-phase reactions leading to coke precursor formation or coke deposition, the investigations dealing with reforming conditions are limited. Nevertheless, homogeneous gas-phase reactions can benefit from previous studies dealing with similar subjects, such as oxidative coupling of hydrocarbons under partial oxidation[260–262] and methane pyrolysis[138] or chemical vapor deposition studies[139;263]. Coke deposition of methane from homogeneous reactions proceeds by stepwise dehydrogenation and a free-radical mechanism, resulting in the formation of ethane, ethylene, and heavier hydrocarbons[264]. Of particular influence are the temperature, residence time, the hydrocarbon (particularly the H/C atomic ratio) used in the feed, and the pressure[138]. Indeed, high temperature and high partial pressure of hydrocarbon species favor hydrocarbon pyrolysis and thermal coupling, while longer residence times result in higher concentrations of coupled products. This is even more emphasized if the hydrocarbon used in the feed stream has a low H/C atomic ratio.

For methane partial oxidation, Chen and co-workers[261] as well as Zanthoff and Baerns[262] have successfully simulated oxidative coupling of methane, showing that ethane and ethylene formation originates from methane coupling via a methyl radical and pyrolytic chain reactions. Furthermore, ethylene is found to stem from pyrolysis rather than oxidative dehydrogenation of ethane[261]. The effect of pressure in the total pressure range of 2-9 bar at about 800-1100 K (527-827°C) is reported to be minor[262]. Higher hydocarbons than methane were studied by Kaltschmitt et al.[260], who reported thermal cracking of isooctane into C_3-C_4 olefins at their reactor inlet of the catalytic partial oxidation reactor. Moreover, ethylene and acetylene have been found especially in the fuel-rich regime. These precursors lead to the

formation of benzene and subsequently polycyclic aromatic hydrocarbons (PAHs)[36;138;265], which are very likely to adsorb strongly or even chemisorb on solids and start polymerizing to coke (C_nH_m)[36;266]. Due to their high stability, PAH compounds are very likely to grow as long as no termination occurs[36]. The best way to avoid coking is then to avoid the formation of such PAHs through gas-phase reactions. Chemical vapor deposition of carbon has been investigated by Norinaga et al.[139;263]. They used coke precursors such as ethylene, acetylene, and propylene, and studied the reaction pathways leading to PAHs. 1,3-butadiene, vinylacetylene, and propylene have been found to be important intermediates to produce PAHs[139]. The further developments of this mechanism have consisted of improving the reactions following PAH formation; however, this has only led to minor improvement of the agreement between model and experimental results[263].

The higher the H_2 partial pressure, the lower is the formation of coke[132]; indeed, H_2 is involved in reaction balances leading to olefins, benzene, and PAHs. Moreover, coke on the support is partially removed probably via H_2 spillover from the metal[132;267;268] leading to methanation. Becker et al.[264] have investigated homogeneous gas-phase reactions with an α-alumina deposition tube and found that at around 1273 K (1000°C) H_2 inhibits coke formation from methane pyrolysis by formation of C-H surface complexes that block the free active sites. For instance, benzene chemisorption is completely inhibited only at high H_2 partial pressures (but not that of acetylene chemisorption[264]). More recently, the inhibition effect has been confirmed with C_2-C_6 hydrocarbons[269].

The homogeneous gas-phase mechanism of PAH formation is complex but relatively well understood. What follows the formation of naphtalene, anthracene, and pyrene is still not very clear[263] because the radical mechanisms and the surface reactions create a plethora of products. Moreover, the homogeneous mechanisms of the gas-phase reactions need to be coupled with existing reaction mechanisms for heterogeneous catalysts to completely simulate the reforming reactions.

2 Test design for the study of gas-phase reactions

Before starting the screening program, the influence of the reactor design is investigated. The test designs aimed to map the overall operating conditions to optimize reactor configuration and later achieve a more detailed interpretation of catalyst test results.

2.1 Test programs

The tests are performed in order to compare the influence of the gas feed on the gas-phase reactions taking place in each reactor. The optimized procedure is then repeated for the startup of catalyst tests.

Before starting a test protocol, the setup is flushed with nitrogen. Pressure is built up to 21 bar with a constant feed stream of 1.23 $l.min^{-1}$ (at standard pressure and temperature) per position, corresponding to the desired GHSV, and the same flow is applied downstream of the reactor to quench the product stream. A pressure test is done, and potential leaks are fixed. When the setup is considered gas proof, a flow balance is made based on the equality of the feed stream and the product stream. If more than 97% of the volumetric flow rate entering the setup is recovered at the output, the setup is considered gas proof. It is satisfactory, if the flows of each position of the screening setup is found equal to the average flow of 1.23 $l.min^{-1}$ (at standard conditions) with a relative error of less than 3%. Temperatures are then increased up to 473 K (200°C) upstream, 453 K (180°C) downstream, and 5 vol.% of nitrogen is substituted with Ar. The gas distribution is then measured with the GC and the mass flow meter in downstream, which measures for each position the amount of Ar recovered. The temperature is then increased to 1123 K (850°C) with a heating rate of 25 $K.min^{-1}$. The first set of feed composition is finally stepped against N_2.
Due to the large variety of operating conditions that can be applied with this setup, two different test programs are used and called H_2 test protocol and H_2O test protocol. Furthermore, four different designs have been studied as shown in Fig. 2.1.
The "non-catalytic case", simulated by reactor configurations (a) and (b), are used to test the reactor concept. The "catalytic case" is represented by reactor configurations (c) and (d), which simulate an "inert" catalytic bed.

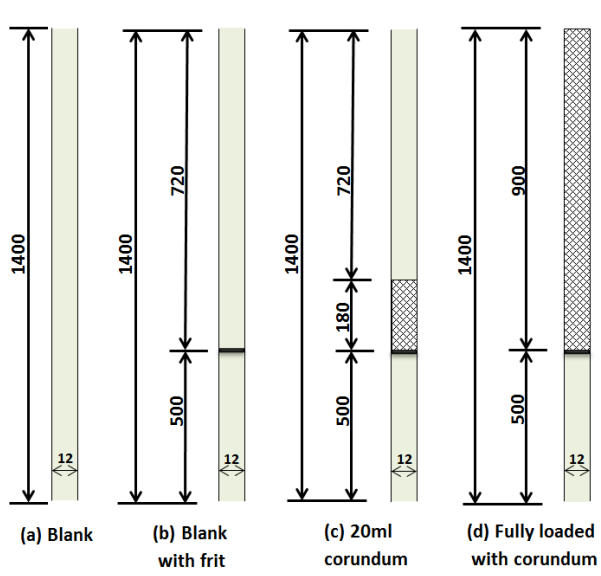

(a) Design of reactors for blind activity measurements (adapted from[22]), (a) and (b) ("non-catalytic case") and (c) and (d) ("catalytic case") ; length in mm

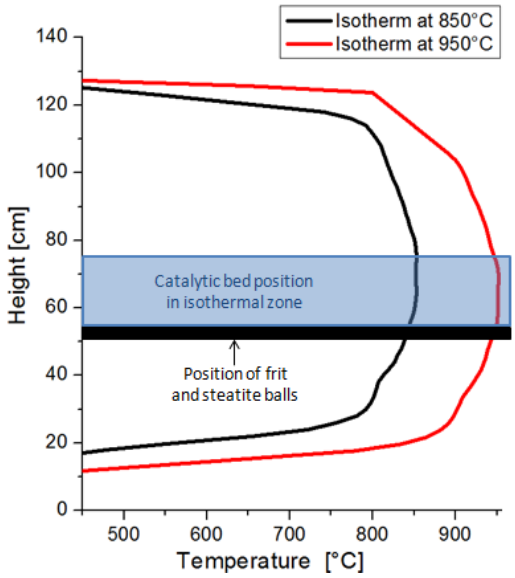

(b) Temperature measurement at 1123-1223 K (850-950°C) and position of the isothermal zone within the reactor in screening unit reactor

Figure 2.1: Overview of reactor designs for blind activity measurements and evaluation of gas-phase-reaction impact

The blank reactor (a) simply contains an empty ceramic tube. The second reactor (b) has a primary ceramic tube and a frit supported on the secondary ceramic tube.
Reactor (c) is in addition filled with 20 ml of the "inert" material. For this role, α-alumina split (500-1000 µm) similar to catalyst-split size is chosen. Finally, the reactor (d) is loaded like (c) but with 90 ml corundum, including a "prebed" that decreases the residence time of gaseous molecules in the front bed.

Two sets of reactors are used, the first set for the H_2 test protocol and the second for H_2O test protocol, which allows to increase the severity up to possible reactor plugging for each test protocol.
For both of these test protocols, conversions are calculated as well as molar rates of hydrocarbons heavier than methane from methane pyrolysis/coupling. The sum of mass formation rates of the coke precursors (ethane, ethylene, propane, propylene, butane, etc...) is also calculated:

$$\dot{m}_C = \sum_i \dot{V}_i^{out} . M_{C,i} \tag{2.1}$$

for i compounds resulting from methane coupling.

2.1.1 H_2 test protocol

The H_2 test protocol is conducted first because it is proven to limit coking[264;269;270]. Indeed, due to the stability of the measurements every test condition is held about three hours before moving forward to the next step of the test protocol presented in Tab. 2.1. The operation starts from high H_2 concentra-

tions, which is decreased down to very low concentrations. In addition, between each feed change, the temperatures of 1123, 1173, and 1223 K (850, 900, and 950°C, respectively) are tested.

#	Temperature [K]	CH_4 [vol.%]	CO_2 [vol.%]	H_2 [vol.%]	Ar in feed [vol.%]
1	1123, 1173, 1223	27.5	27.5	40	5
2	1123, 1173, 1223	32.5	32.5	30	5
3	1123, 1173, 1223	37.5	37.5	20	5
4	1123, 1173, 1223	42.5	42.5	10	5

Table 2.1: Feed composition and reactor temperature for the H_2 test protocol

The protocol follows the general principle used for all further studies, that is, startup under low severity up to high severity operating conditions.

2.1.2 H_2O test protocol

This test protocol is a minor variation of the H_2 test protocol. It starts with steam reforming conditions ($CH_4/H_2O/Ar/N_2$ = 47.5/47.5/5/0 (vol.%)). According to the steam reforming conditions, CO_2 is introduced at a CH_4/CO_2 ratio of one, which is maintained until the end of the protocol. The amount of methane and carbon dioxide is increased simultaneously, while the steam content is decreased as it can be seen in Tab. 2.2. The phases are held at least 4 h to reach a stable performance. During phase transition a particular care is taken to guarantee a smooth increase of the carbon fraction and avoid a sudden increase of carbon that might provoke coke build up. Therefore, phase transitions are always made stepwise.

#	Temperature [K]	CH_4 [vol.%]	CO_2 [vol.%]	H_2O [vol.%]	Ar in feed [vol.%]
1	1123, 1173	47.5	-	47.5	5
2	1123, 1173	27.5	27.5	40	5
3	1123, 1173	32.5	32.5	30	5
4	1123, 1173	37.5	37.5	20	5
5	1123, 1173	42.5	42.5	10	5

Table 2.2: Feed composition and reactor temperature for the H_2O test protocol

The test program is performed first at 1123 K (850°C) under steam-reforming conditions (phase 1), then CO_2 is added with a CO_2/CH_4 ratio of one, and then the CO_2 concentration is increased keeping a CO_2/CH_4 ratio of one while the H_2O content is decreased down to 10 vol.% ($CH_4/H_2O/CO_2/Ar$ = 42.5/10/42.5/5(vol.%)). This program is finally repeated at 1173 K (900°C).

3 Results and discussion of the reactor configurations

Both test protocols are tested until reactor plugging is observed. For the H_2 test protocol, the test is also made under pure CO_2-reforming conditions ($CH_4/CO_2/Ar$ = 42.5/42.5/5(vol.%)) at 1123 K (850°C); however, a vivid coking has been observed and unfortunately no satisfying measurements has been achieved. For the H_2O test protocol, the last satisfying measurements are performed with the same feed composition $CH_4/H_2O/CO_2/Ar$ = 42.5/10/42.5/5(vol.%) but only up to 1173 K (900°C) because reactor plugging is observed with the H_2O test protocol at 1223 K (950°C).

3.1 Results of the H_2 test protocol

As already reported[264;269;270], addition of H_2 to the feed stream limits the influence of methane pyrolysis through gas-phase reactions. This is proven experimentally by the high stability of the measurements.

3.1.1 Influence of the reactor configuration on CH_4 and CO_2 conversions

The influence of H_2 concentration in the feed stream as well as temperature on CO_2 conversions and then CH_4 conversions are investigated using the four reactor configurations. The CO_2 conversions are presented in Fig. 3.1.

In the non-catalytic case, reactor configurations (a) and (b) exhibit very similar CO_2 conversions. The temperature and the H_2 concentration in the feed stream show a significant influence on the CO_2 conversions. Higher temperature as well as higher H_2 concentration in the feed stream favor CO_2 conversion with up to 40% conversions at 1223 K (950°C) and 40 vol.% H_2 in the feed stream.

In the catalytic case, configurations (c) and (d) exhibit a relatively similar behavior of CO_2 conversions, which are more sensitive to the concentration of H_2 in the feed; however, much higher CO_2 conversions are achieved. Reactor configuration (c) shows a sensitivity to temperature increase similar to non-catalytic case, whereas the influence of the concentration of H_2 in the feed stream is much higher than in the non-catalytic case. With the presence of the corundum prebed (reactor configuration (d)), CO_2 conversions are enhanced at similar temperature and similar H_2 concentration in the feed stream in com-

parison with the reactor configuration (c).

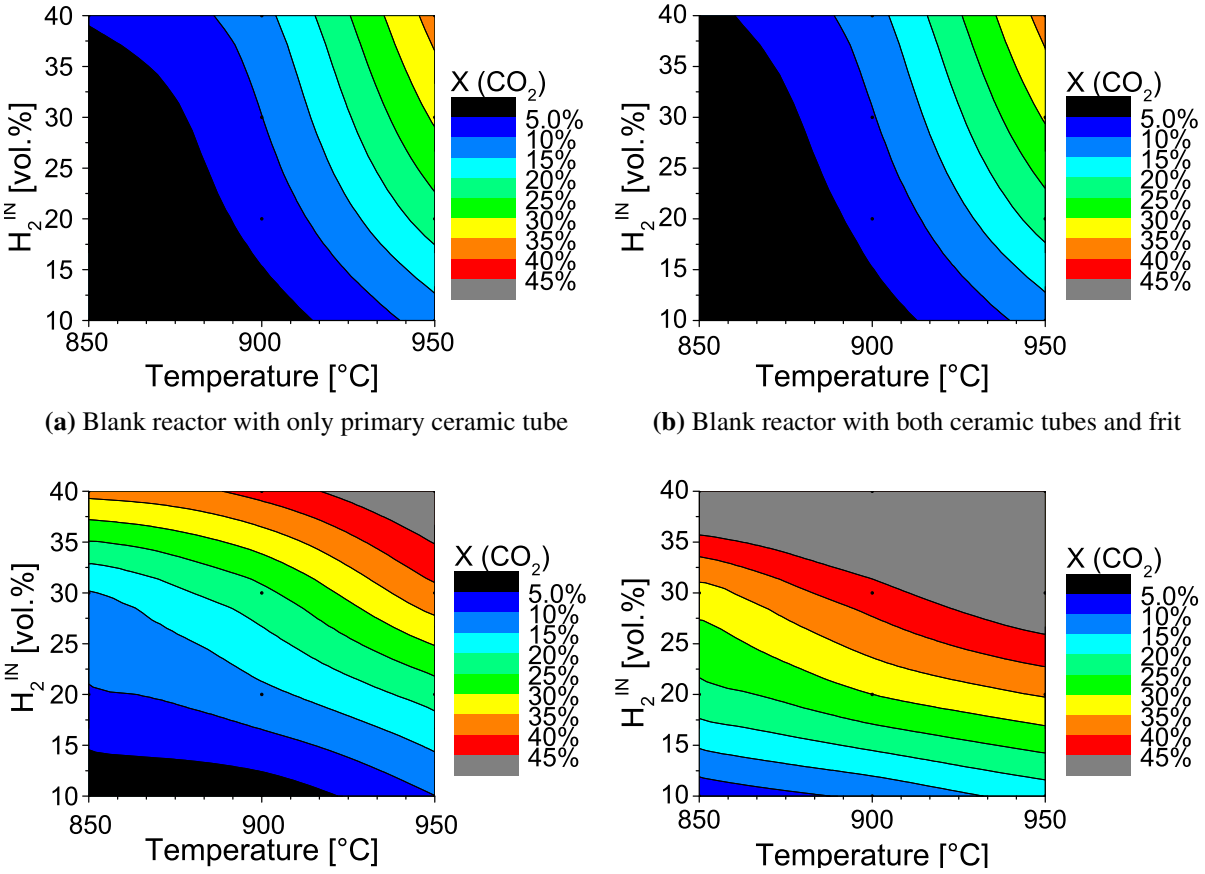

(a) Blank reactor with only primary ceramic tube

(b) Blank reactor with both ceramic tubes and frit

(c) Reactor concept used with 20 ml corundum

(d) Reactor concept fully loaded with corundum

Figure 3.1: CO_2 conversions observed using the different reactor configurations and the H_2 test protocol in the temperature range 1123-1223 K (850-950°C)

In the non-catalytic case, beside very low specific surface area of corundum (less than 0.1 $m^2.g^{-1}$), the inner surface of the reactor tube becomes active in RWGS when the temperature is higher than 1173 K (900°C) and the H_2 concentration in the feed stream is higher than 20 vol.%.

In the catalytic case, if 20 ml of corundum split is used (configuration (c)) only a volume of H_2 of less than 15% in the feed stream and a temperature below 1123 K (850°C) is allowed for a low RWGS activity. The impact of the RWGS reaction impact is not negligible in all other cases. The use of the corundum prebed, like in configuration (d), increases the influence of the RWGS reaction so that the impact is almost independent from temperature and depends only on the H_2 concentration in the feed stream. Indeed, the corundum surface is so "large" that the thermodynamic equilibrium of the RWGS reaction is almost always reached.

The presence of H_2 and CO_2 leads to a significant impact of RWGS especially at high partial pressure of H_2 but also, to a lesser extent, at high temperature. Particularly at lower temperatures, there is a risk that the high CO concentration disproportionates into CO_2 and carbon through the Boudouard reaction[36;271].

For the methane conversions, the effect of temperature and H_2 concentration in the feed stream can be seen in Fig. 3.2. For all reactor configurations, methane conversions are similar and very low with a maximum of 7% at 1223 K (950°C) and 10 vol.% H_2 in the feed stream. Below a temperature of 1183 K (910°C) or above a H_2 concentration in the feed stream of 20 vol.%, at most 1% methane is converted. The use of a corundum prebed (configuration (d)) appears to slightly increase the methane conversions to 2% (absolute).

It is interesting to note that the steam formed by the RWGS reaction does not enhance steam reforming of methane. For this reason, methane conversions at high temperature and low H_2 concentration in the feed stream come from the prevailing methane cracking or pyrolysis[36;264;269]. Despite of the presence of acidic sites on alumina[268;272], methane conversions are not significantly promoted. As it has been explained, gas-phase reactions including methane pyrolysis and coupling should be avoided to limit the coke-precursor formation rates.

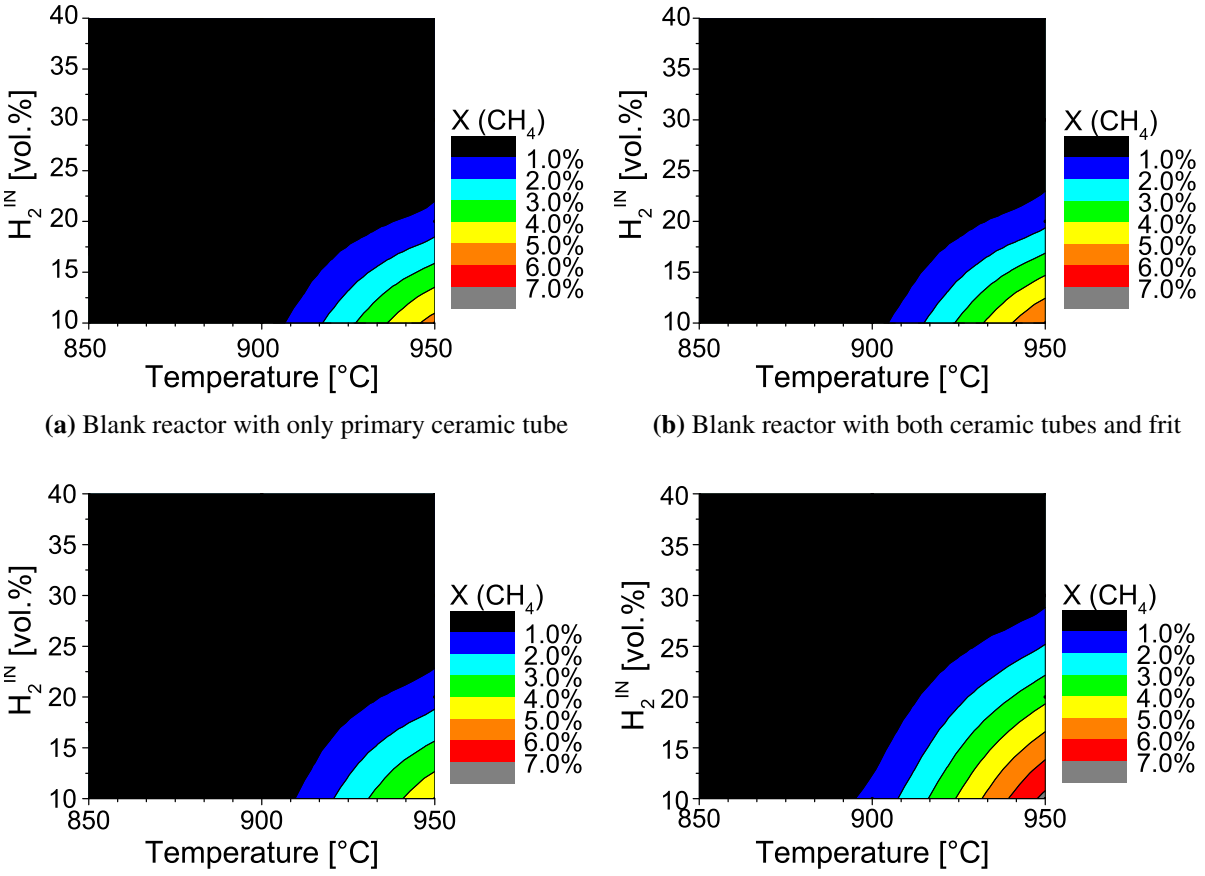

(a) Blank reactor with only primary ceramic tube

(b) Blank reactor with both ceramic tubes and frit

(c) Reactor concept used with 20 ml corundum

(d) Reactor concept fully loaded with corundum

Figure 3.2: CH_4 conversions observed with the different reactor configurations and the H_2 test protocol in the temperature range 1123-1223 K (850-950°C)

At high temperature and low H_2 concentration in the feed stream, the impact of methane decomposition should be considered, whereas RWGS should be considered at high H_2 concentration in the feed stream

and also at high temperature.

3.1.2 Influence of the reactor configuration on formation rate of coke precursors

Small alkanes, other than methane, and olefins are formed during the H_2 test protocol. These are called coke precursors because of their higher selectivity toward coke formation in comparison to methane. Their quantification is performed in the FID detector of the GC, allowing to detect concentrations down to 5 ppm.

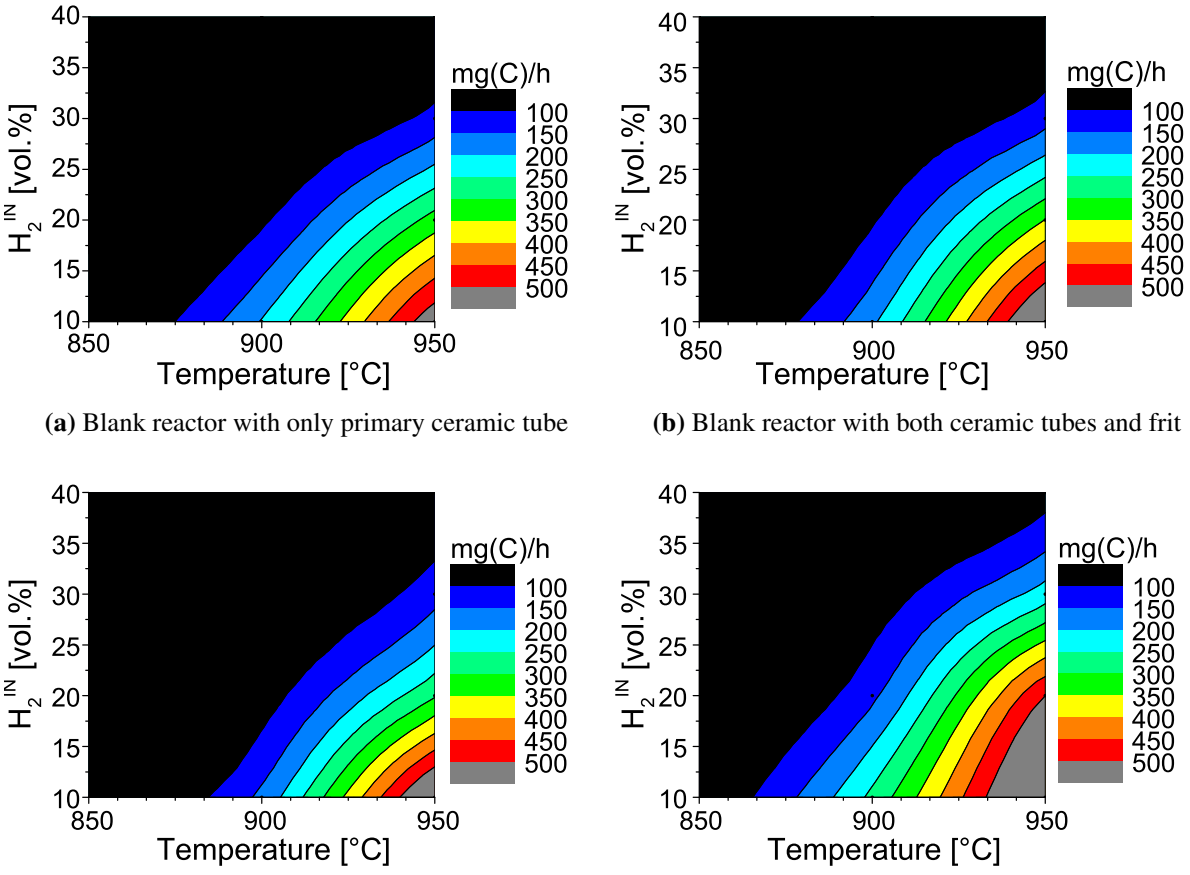

(a) Blank reactor with only primary ceramic tube

(b) Blank reactor with both ceramic tubes and frit

(c) Reactor concept used with 20 ml corundum

(d) Reactor concept fully loaded with corundum

Figure 3.3: Sum of mass formation rates of coke precursors observed using the different reactor configurations and the H_2 test protocol in the temperature range 1123-1223 K (850-950°C)

An overview of coke-precursor formation rates and specific molar formation rate depending on temperature and partial pressure of H_2 are presented in Figs. 3.3 and 3.4, respectively.

Reactor configurations (a), (b), and (c) exhibit similar concentrations of coke precursors. The reactor configuration (d) with a prebed exhibits, however, a slightly higher concentration of coke precursors.

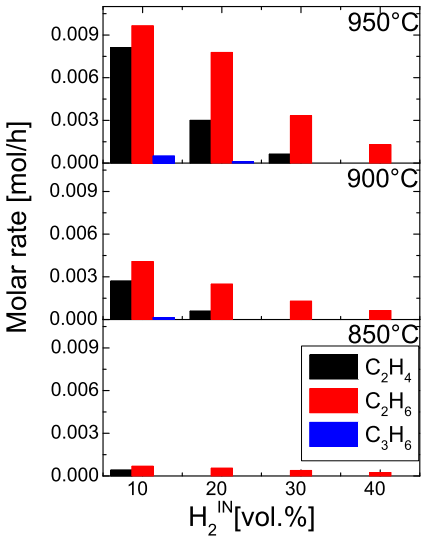

(a) Blank reactor with only primary ceramic tube

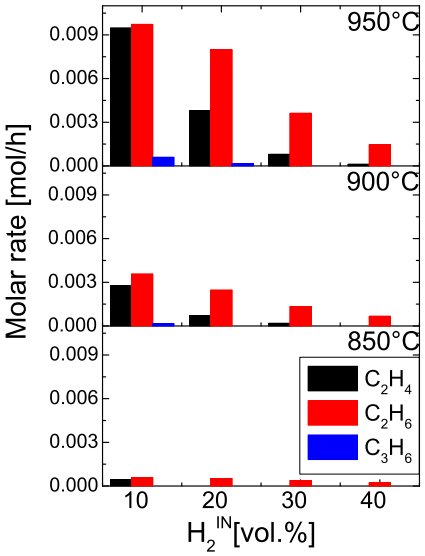

(b) Blank reactor with both ceramic tubes and frit

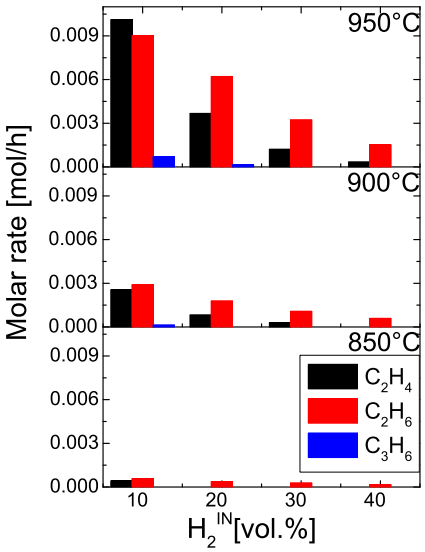

(c) Reactor concept used with 20 ml corundum

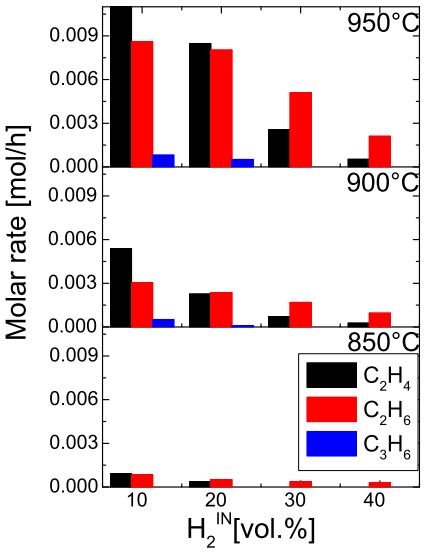

(d) Reactor concept fully loaded with corundum

Figure 3.4: Molar coke-precursor formation rates (C_2H_4,C_2H_6,C_3H_6) observed using the different reactor configurations and the H_2 test protocol in the temperature range 1123-1223 K (850-950°C)

The presence of ethylene, ethane, and propylene is observed. Ethane appears first at 1123 K (850°C), a significant ethylene formation rate is then found above circa 1173 K (900°C) and at a H_2 concentration in the feed stream of less than circa 30 vol.%. Finally, propylene could be identified above 1173 K (900°C) and at a lower H_2 concentration in the feed stream than for ethylene formation.
The formation of coke precursors occurs through gas-phase reactions starting from methane pyrolysis [138;263;273;274]. Indeed, CH_4 conversions previously observed in Fig. 3.2 can be compared with Fig. 3.3. This comparison emphasizes that, as CH_4 conversions increase, the coke-precursor concentrations also increase. This confirms that methane is converted mainly to coke precursors by means of pyrolysis/coupling.

As the temperature is increased above 1173 K (900°C), the impact of the gas-phase reactions forming coke precursors becomes significant especially below a H_2 concentration in the feed stream of 15 vol %. The use of a prebed, like in configuration (d), and a low H_2 concentration in feed stream seems to increase the C_2H_4/C_2H_6 ratio, which results in an increased coking risk. Indeed, ethane is more stable than ethylene, which can react faster to coke [138]. Furthermore, it can be speculated that the "acidic" sites on alumina increase the methane cracking rate and thus the rate of ethylene formation [10;82].

3.2 Results of the H_2O test protocol

The measurements obtained with the H_2O test protocol are less stable compared to those obtained by the H_2 test protocol, probably due to coking. Moreover, as coking takes place in the reactor, other catalytic reactions are catalyzed at high temperature over carbon, leading to unstable operations. For this reason, the accuracy of the measurements is limited when using the H_2O test protocol.

3.2.1 Influence of the reactor configuration on CH_4 and CO_2 conversions

The conversions observed showed two different trends (Fig. 3.5), one in the non-catalytic case ((a) and (b)), and another for the catalytic case with corundum split ((c) and (d)).

In the non-catalytic case, the conversions are mostly negligible at 1123 K (850°C), while at 1173 K (900°C), the CH_4 and CO_2 conversions become significant.
In the catalytic case, corundum appears to facilitate the conversions of CH_4 and CO_2 at 1123 K (850°C) and relatively high H_2O concentrations in the feed stream. At 1173 K (900°C), only constant methane conversions of 5-10% are observed for all H_2O concentrations in feed stream.

The complexity of the measurements caused by coke deposits allows only to draw conclusions with regard to the case (non-catalytic or catalytic).
In the non-catalytic case, the impact on the reactions becomes significant above 1173 K (900°C) and consequently on methane conversions probably due to methane decomposition.

In the catalytic case, high conversions of methane and carbon dioxide are achieved at 1123 K (850°C) probably due to the presence of acidic sites on corundum that might enhance methane decomposition, while the CO_2 conversions observed may come from the reaction of CO_2 with carbon to CO or with H_2 through RWGS. CO_2 reforming of methane might be also possible.

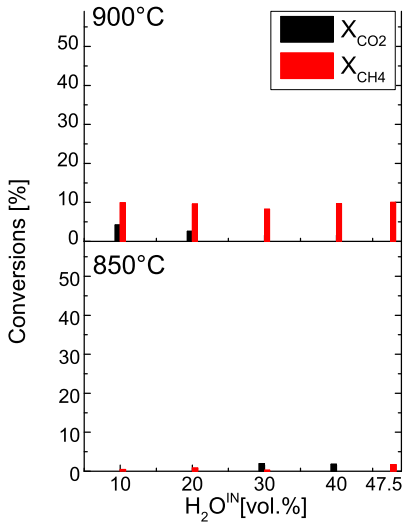

(a) Blank reactor with only primary ceramic tube

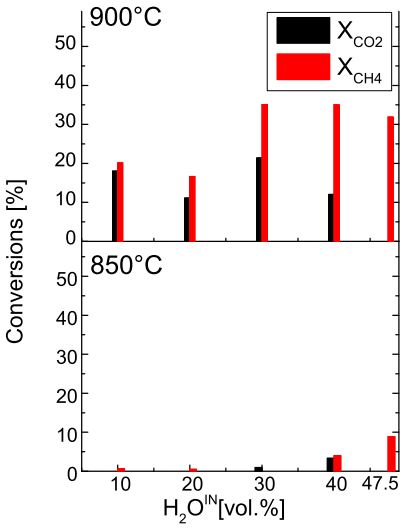

(b) Blank reactor with both ceramic tubes and frit

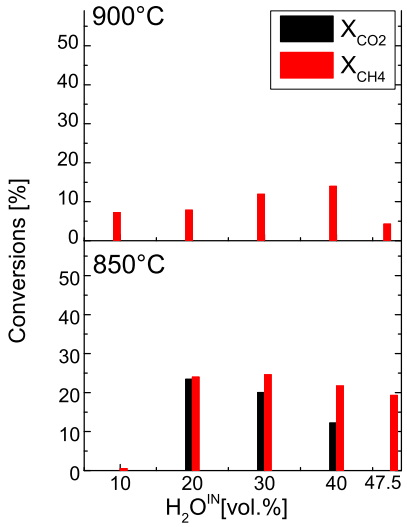

(c) Reactor concept used with 20 ml corundum

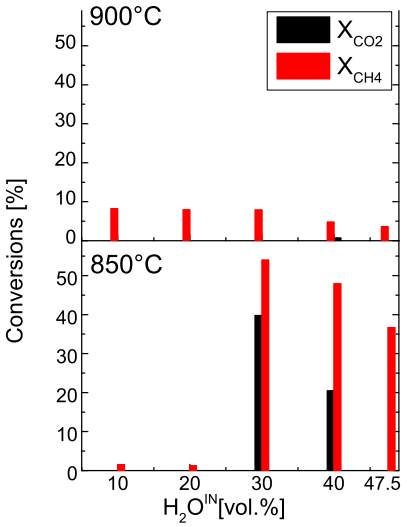

(d) Reactor concept fully loaded with corundum

Figure 3.5: Conversions of CO_2 and CH_4 observed using the different reactor configurations and the H_2O test protocol at 1123 K and 1173 K (850 and 900°C, respectively)

It can be speculated that coking occurs during the test protocol at various rates depending on the methane partial pressure. At the beginning, coking takes place; when the "inert" catalyst is covered with coke, methane or/and products from methane decomposition products can be dehydrogenated and increase the

amount of coke up to reactor plugging.

3.2.2 Influence of the reactor configuration on formation rate of coke precursors

An overview of the coke precursor formation rates is presented in Fig. 3.6 and clearly shows that much higher coke-precursor formation rates are achieved at higher temperatures in the non-catalytic case as well as in the catalytic case. In addition, the higher the concentration of CH_4 in the feed stream, the higher are the coke-precursor formation rates.

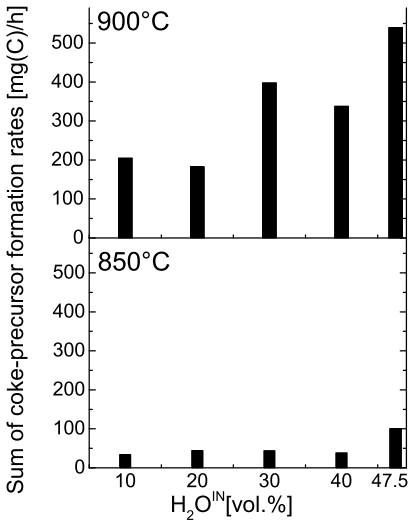

(a) Blank reactor with only primary ceramic tube

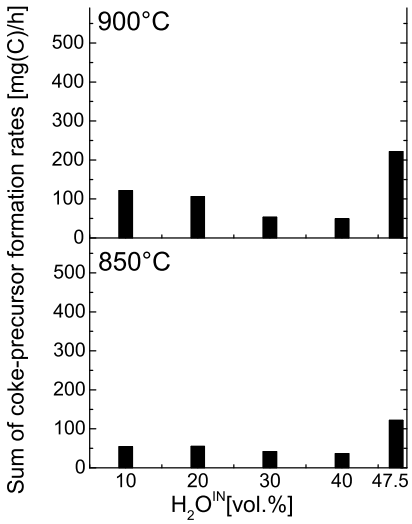

(b) Blank reactor with both ceramic tubes and frit

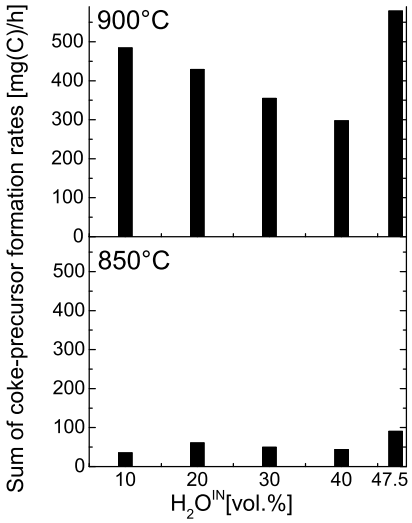

(c) Reactor concept used with 20 ml corundum

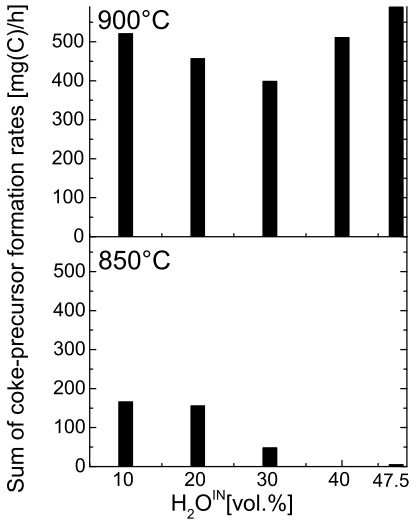

(d) Reactor concept fully loaded with corundum

Figure 3.6: Molar coke-precursor formation rates observed using the different reactor configurations and the H_2O test protocol at 1123 K and 1173 K (850 and 900°C, respectively)

The comparison of the previous results of CH_4 and CO_2 conversions (Fig. 3.5) and the coke-precursor formation rate (Fig. 3.6) shows that generally high coke-precursor formation rates are observed when CO_2 conversions are not measured. The influence of H_2O concentration in the feed stream is not clear.

Higher temperatures favor methane decomposition[275]; therefore, higher coke-precursor rates of formation are observed. In addition, the higher partial pressure of methane also increases the formation rates of coke precursors, as reported by Billaud and Baronnet[138].
An important point may result from the comparison of CO_2 conversions and coke precursor formation rate. Indeed, CO_2 conversions appear to minimize the coke-precursor rate of formation. This is very likely to occur by reverse CO disproportionation.

The coke-precursor formation rates are further detailed in Fig. 3.7. For the H_2O test protocol, coke precursors up to butane and butene can be identified in the product stream for all four reactor configurations.

In the non-catalytic case, the reactor configuration (a) exhibits particularly high formation rates of heavy coke precursors like butene and butane at 1173 K (900°C). The reactor configuration (b) shows the same performance at 1123 K (850°C) but much lower coke-precursor formation rates at 1173 K (900°C).
In the catalytic case, the reactor configurations (c) and (d) exhibit behavior similar to (b) but with much higher coke-precursors formation rates, especially for ethylene, at 1173 K (900°C).

The presence of heavier coke precursors like butene or butane results from the methane pyrolysis and coupling, which is not inhibited by the presence of H_2O in the feed stream. Reactor configuration (a) appears to produce high coke-precursor rates probably because the residence time of methane and its decomposition products at high temperature is longer than in the other reactor configurations.

Performing the H_2O test protocol at 1123 K (850°C) allows to minimize the impact of gas-phase reactions and particularly methane pyrolysis and coupling. At 1173 K (900°C), the impact of the coke-precursor formation rates are significant and must be taken into account. The influence of steam on the impact of gas-phase reactions is still not clear.

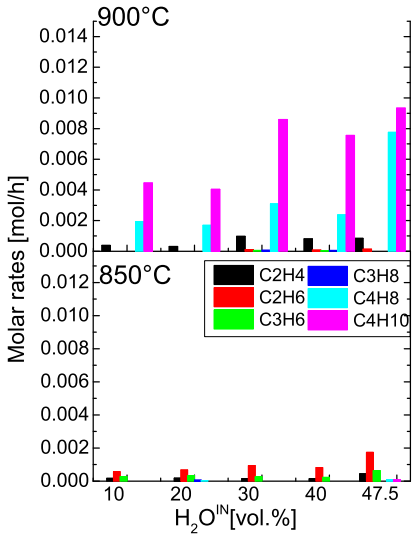

(a) Blank reactor with only primary ceramic tube

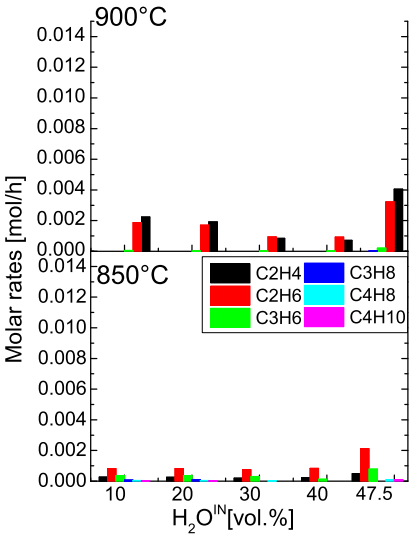

(b) Blank reactor with both ceramic tubes and frit

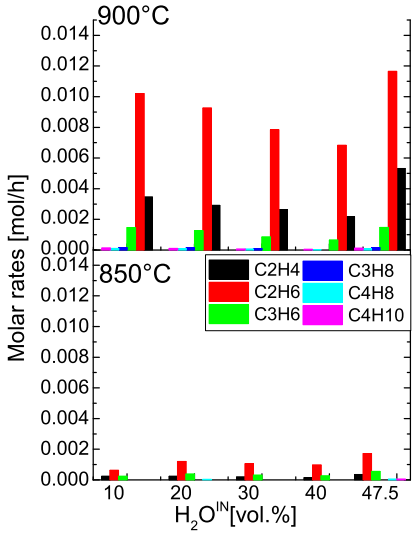

(c) Reactor concept used with 20 ml corundum

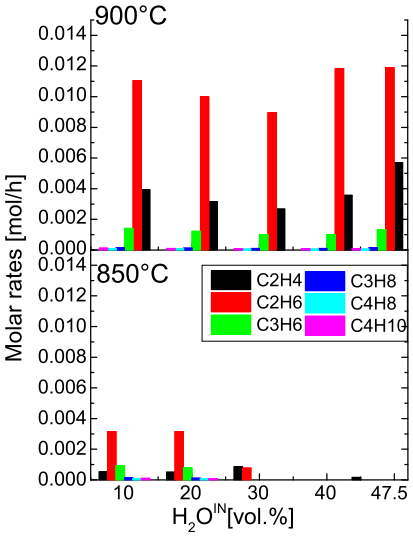

(d) Reactor concept fully loaded with corundum

Figure 3.7: Details of molar coke-precursor formation rates observed using the different reactor configurations and the H_2O test protocol at 1123 K and 1173 K (850 and 900°C, respectively)

3.3 Conclusions from the study on the H_2 and H_2O test protocols

The results of this study were simulated by Deutschmann's group at Karlsruhe Institute of Technology to compare the experimental results and the numerical model developed on the basis of experimental results. The mechanism of coke-precursor formation is explained by methane pyrolysis and further coupling of radicals to larger hydrocarbons[22].

The addition of H_2 to the feed stream limits methane pyrolysis and, therefore, facilitates coke-free oper-

ations. Furthermore, the higher the concentration of H_2 in the feed stream, the lower are the formation rates of the coke precursors. These simulated results fit well with the experimental observations[22].

The addition of H_2O to the feed stream shows no particular effect and, therefore, a strong coking trend is already observed experimentally at 1223 K (950°C). Various coke precursors are identified experimentally, from ethane/ethylene up to butane/butene when using the H_2O test protocol. This trend could be confirmed by the simulations. Moreover, the simulations show that higher hydrocarbons like benzene are also present[22], but could not be detected with GC; probably the benzene adsorbed on the corundum surface because the benzene concentration in the outlet stream should increase to 1500 ppm as the H_2O concentration decreases to 10 vol.% H_2O for CO_2 reforming[22].

The long residence time in the hot zone without the use of H_2 addition leads to enhanced formation rates of coke precursors[22].

Addition of H_2 and H_2O to the feed stream results in different coke-precursor formation rates; this is explained by the fact that H_2O acts as an oxidant in methane reforming and also confirms that methane cracking is the most important route towards coke deposition[22].

Finally, the impact of the gas-phase reactions on the catalytic performance in methane reforming in the presence of CO_2 as well as H_2 and/or H_2O can support the design of the technical reactors.

Part V

Pt-based catalysts for CH_4 reforming in the presence of H_2O and CO_2 - A kinetic study

1 Pt-based catalysts in CH_4 reforming in presence of H_2O and CO_2: State of the art

The activity and stability of noble metals in the reforming of hydrocarbons is well known[10;34;61;276]. Among Ir, Rh, Ru, Pd, and Pt, Pt-based catalysts have been the most extensively studied, starting from steam reforming in the 50's[277–281] to partial oxidation[280;282] but also specifically for CO_2 reforming of methane[33;283–293].

In addition to the type of active metal selected for the reforming reaction, the choice of the support is of major importance since it strongly influences the reforming mechanism[287] and, therefore, catalyst performance. γ-alumina[33;287;288;290;291;294], zirconia[33;284;287;288;290;291;294], and titania[284;290;291] have been widely studied, and especially ZrO_2 has been found to show higher resistivity against coking[290] because of a higher coke gasification rate over ZrO_2 than over Al_2O_3. Nevertheless, decomposition of methane has been found to proceed slower over Pt/ZrO_2 than over Pt/Al_2O_3[33].

Three different phases of pure zirconia exist, as can be seen in Fig. 1.1.

(a) The monoclinic structure (space group number 14: $P12_1/c1$, fluorite-type[295]) is stable from room temperature up to about 1373 K (1100°C)[296;297]. This defect phase is built with one Zr atom surrounded by seven O atoms[296].

(b) The tetragonal structure (space group number 137: $P4_2/nmc$[295]) remains stable above 1373 K (1100°C) up to around 2573 K (2300°C)[297].

(c) The cubic structure (space group number 225: $Fm\bar{3}m$[295]) is stable above circa 2573 K (2300°C)[297].

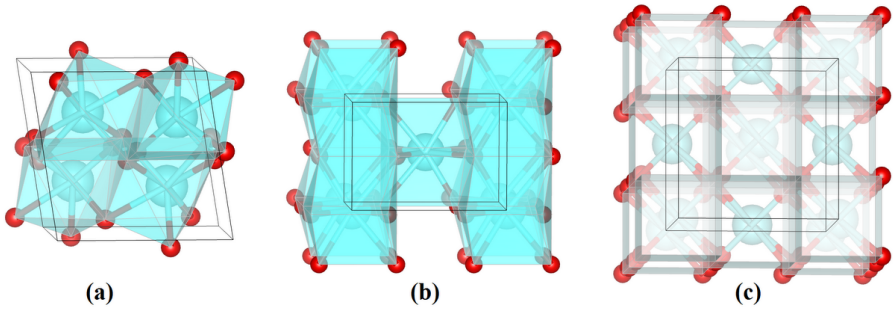

Figure 1.1: Zirconia unit cells (simulated with the Vesta software[298]); Zr (blue large atom) and O (red small atom), (a) monoclinic[299], (b) tetragonal[300], (c) cubic[301]

In the usual temperature range of steam- and CO_2- reforming applications, pure undoped ZrO_2 is found in the monoclinic structure with a low specific surface area. Therefore, the use of doped zirconia modifications is required in order to obtain a higher and more stable specific surface area of the zirconia support for catalytic applications.

Zirconia modifications with ceria[286;288;302], lanthanum oxide[286], and/or silica[285;292;293] are reported to improve catalyst stability and activity in reforming with CO_2. Ceria is known to form a large variety of mixed oxides with zirconia[303]; ceria addition generally improves the oxygen storage capacity as well as redox properties and, therefore, enhances the rate of coke gasification over zirconia[286;302]. Due to close contact between Pt and CeO_2[302] it may also inhibit Pt-metal particle growth[286]. Zirconia modified with lanthanum oxide has a significantly improved thermal stability, up to 1173 K (900°C)[304;305], and resistance against Pt-metal particle growth[286]. Finally, silica-modified zirconia improves the thermal stability of zirconia[292], but also promotes the formation of a bimodal pore support that significantly increases the specific surface area[285].

The mechanism of reforming with steam and/or CO_2 on Pt consists of methane decomposition through

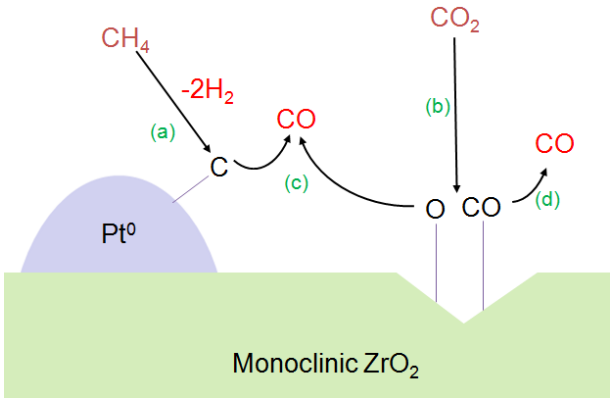

Figure 1.2: Mechanism proposed for reforming of methane with carbon dioxide (taken from[33]), a) methane decomposes over Pt particle, b) CO_2 adsorbed dissiociatively on monoclinic zironia defect, c) the resulting adsorbed carbon reacts with adsorbed oxygen to generate CO, d) adsorbed CO desorbs.

a stepped and sequential elementary abstraction (C-H) of CH_4 over Pt[306] by first forming CH_x* and then C* (Eqs. 1.19 to 1.22 in part II). The adsorbed carbon C* can react further with O* stemming from CO_2 or/and H_2O dissociation on the catalyst surface[10]. This explains how CO is produced from C* and with H_2 as "by-product". Souza et al.[294] proposed a mechanism for CO_2 reforming over Pt supported on ZrO_2: methane decomposition over Pt particles and CO_2 activation over zirconia (Fig. 1.2). A similar mechanism with steam reforming of ethanol is proposed by Takanabe et al.[307], where ethanol decomposes on Pt, whereas H_2O adsorbs dissociatively on the zirconia defects, and the reaction occurs at the interface of Pt and ZrO_2. The rate-determining step in steam and CO_2 reforming is assumed to be the activation of methane by the first C-H bond breaking[105;107].

Bitter et al.[276;289;290] extensively studied the dispersion of Pt particles over undoped zirconia. They reported that an increase of the Pt loading over ZrO_2 after calcination at 923 K (650°C) for 15 h in air leads

to a significant decrease of Pt-particle dispersion above a Pt loading of 0.7 wt.%[289]. In their study[289], the Pt-particle dispersion decreased from 100% down to 58% as the Pt loading is increased from 0.5 to 2 wt.%. Bitter et al.[290] have also reported the influence of a 15 h-calcination in air of 1 wt. % Pt/ZrO_2 at 923, 1023, 1123 K (650, 750, and 850°C, respectively) on the Pt-particle dispersion, which decreased from 82 to 47 to 34% after calcination at 923, 1023, 1123 K, respectively (650, 750 and 850°C, respectively)[290].

2 Experimental part

This section is divided into two parts: first an optimization study of the support of Pt-based catalysts for reforming with steam, and second, a kinetic study of reforming in presence of H_2O, as well as H_2O and CO_2 over the optimized Pt-based catalyst supported on modified zirconia.

2.1 Design of experiments for the study of Pt-based catalysts over zirconia supports

The design of experiments is based on Pt/ZrO_2 as an initial benchmark, and further modifications of the zirconia are performed to identify the support that delivers the highest stability and activity in steam reforming of methane with a steam-to-carbon ratio of one. In this study, the modification of zirconia with SiO_2, La_2O_3, and CeO_2 are studied in steam reforming of methane.

2.1.1 Catalyst preparation

The various Pt-based catalysts prepared by the wet impregnation technique are presented in Tab. 2.1. The selected support is crushed until the desired split of 500-1000 μm is reached. About 60 ml of support split is then impregnated with an excess of water that contains the chosen platinum precursor and cerium nitrate hexahydrate. The catalyst is impregnated in a rotary evaporator for 4 h at 353 K (80°C) and a

Short Name	Support	Support content [wt.%]	Impregnation with	Final composition after impregnation
PtZ	XZO 880* - ZrO_2 MEL Chemicals	ZrO_2	Pt-nit.	1 wt.% Pt
PtSZ	Saint Gobain NorPro SZ 31107	ZrO_2/SiO_2=95/5	EA-Pt	1 wt.% Pt
PtCSZ	Saint Gobain NorPro SZ 31107	ZrO_2/SiO_2=95/5	EA-Pt + Ce-nit.	1 wt.% Pt+5.8 wt.% Ce
PtCLZ	Saint Gobain NorPro SZ 61156	ZrO_2/La_2O_3=90/10	EA-Pt + Ce-nit.	1 wt.% Pt+5.8 wt.% Ce

Table 2.1: Overview of Pt-based catalysts; * $Zr(OH)_4$ precursor shaped and calcined to obtain zirconia split; nit., nitrates; EA, bis(ethanolammonium)-hexahydroxyplatinate

pressure of 200 mbar. After impregnation, the catalyst split is aged for 1 h. Finally, the dried split is calcined in a rotary flask with a ramp of 5 $K.min^{-1}$ to 1123 K (850°C) and calcined for 2 h in air.

Commercially available supports are used in the form of pellets, except for pure ZrO_2, which is prepared from zirconium hydroxide (XZO 880/01 from MEL Chemicals). For this, the powder is calcined in a rotating flask at 723 K (450°C) for 2 h in air and compacted three times between corrugated cylinders at 240 bar. The resulting shaped material is then crushed to a fraction of 500-1000 μm.

2.1.2 Catalyst characterization

All samples are analyzed by X-Ray Diffraction (XRD), N_2 physisorption, scanning transmission electron microscopy (STEM), and temperature-programmed desorption (TPD) of preadsorbed CO.
The powder X-ray diffraction is performed using Cu $K_{\alpha 1}$ (λ=1.5405980 Å) at 40 mA and 40 kV with a diffractometer D8-Discover (Bruker AXS). The patterns are obtained for angular positions from 16.3° up to 53.5° and a precision of 0.02°. The Match! software (Crystal Impact) is used for phase identification and quantification based on the International Center for Diffraction Data and the RIR method. Missing entries are simulated on the basis of single crystals coupled with the existing database.
Samples for N_2 physisorption are first preconditioned at 573 K (300°C) for 1 h in N_2 flow prior to analysis. Specific surface areas are determined on the basis of a five-point adsorption isotherm.
Images from scanning transmission electron microscopy (STEM) are recorded at low energies up to 30 keV at the Laboratory of Electron Microscopy (STEM) in Karlsruhe Institute of Technology with a High-Angle Annular Dark-Field (HAADF), and energy-dispersive X-ray spectroscopy is used to obtain the local elementary composition.
Dispersion measurements are performed with temperature-programmed desorption of CO in collaboration with the Deutschmann's group. The measurements are performed as reported by Karakaya and Deutschmann[200].

2.1.3 Catalyst screening

The different catalysts prepared are tested in a single reactor (prototype unit) at 1123 K (850°C), 21 bar, and with a GHSV of 3800 h^{-1} under steam-reforming conditions ($CH_4/H_2O/Ar$ = 47.5/47.5/5 (vol.%)). The pressure is increased by slightly closing the downstream valve under a constant N_2 flow. When the pressure stabilizes at 21 bar, the reactor is heated up to 1123 K (850°C) under N_2. When temperatures and pressure are stabilized, CH_4 and H_2O contents are increased simultaneously and stepwise while the N_2 content is decreased.

2.2 Study of kinetics on Pt-based catalysts

For the kinetic study, the catalyst exhibiting the highest activity and stability under steam-reforming conditions is synthesized again by starting with a carrier split of 315-500 μm and is tested in the 16-fold unit at atmospheric pressure in a temperature range of 1023-1173 K (750-900°C) and a GHSV range of 3600-41225 h^{-1}. The different operating conditions for reforming used are detailed in Tab. 2.2.

Phase	Short Name	CH_4 [vol.%]	CO_2 [vol.%]	H_2O [vol.%]	Ar in feed [vol.%]
1	SteamRef	47.5	-	47.5	10
2	SteamRef with CO_2 addition	36	18	36	10
3	CO_2 ref. with 36 vol.%H_2O	28	28	36	10
4	CO_2 ref. with 30 vol.%H_2O	30	30	30	10

Table 2.2: Feed compositions used for the kinetic study

The kinetic study is performed in the 16 reactors as described in the Fig 2.1 with the four different reforming conditions. The design of experiments used allows to study the influence of the temperature, the GHSV, and the influence of corundum for each four reforming operating conditions. A blank reactor filled with corundum split is used to quantify the impact of possible gas-phase reactions and evaluate the "inert" character of corundum: in each reactor a ceramic tube is present and may influence the catalytic performance.

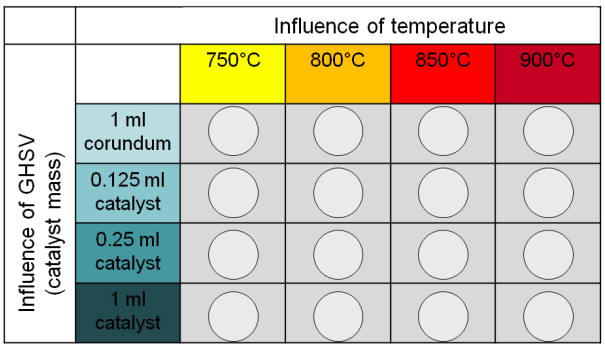

Figure 2.1: Overview of the catalyst test design tested with the four different feeds used for the kinetic study

The catalysts are studied under steam reforming, and after 40 h the next phase is tested. The plant is started the same way as previously performed for the steam-reforming conditions in the prototype unit.

3 Results of the Pt-based catalyst design and kinetic study for the optimized catalyst

3.1 Influence of various supports on steam reforming at high pressure

The study on the support of Pt-based catalysts focuses on improving the stability and the activity of the catalyst in steam reforming of methane. The fresh catalysts are characterized by XRD, N_2 physisorption, STEM images, and the TPD of CO; after testing, the spent catalyst is also analyzed by using the same methods.

3.1.1 Pt/ZrO_2 (PtZ) in steam reforming at high pressure

The catalyst synthesized by wet impregnation has Pt nanoparticles of about 37 nm diameter dispersed over monoclinic zirconia nanocrystallites of 28 nm in diameter exhibiting a specific surface area of 2 $m^2.g^{-1}$ (Tab. 3.1). The specific surface area of the catalyst is relatively low; however, the Pt dispersion of 12.1% is satisfactory in comparison with the Pt/ZrO_2 catalytic powder of Bitter et al.[290] (specific surface area of 18 $m^2.g^{-1}$ and 34% Pt-particle dispersion).

Pt/ZrO_2	Phases from XRD analysis	$\varnothing_{Pt}/\varnothing_{Support}$ [nm]	Dispersion of Pt^0 [%]	Specific surface area [$m^2.g^{-1}$]
fresh	Pt/m-ZrO_2	37/28	12.1	2

Table 3.1: Results of analysis (XRD, N_2 physisoprtion, TPD) of the fresh catalyst Pt/ZrO_2 (PtZ); m-ZrO_2, monoclinic zirconia. The particle size is obtained from XRD patterns and calculated with the Scherrer formula.

The PtZ catalyst is thus tested in steam reforming of methane under 21 bar (Fig. 3.1). The catalyst shows a stable performance at the thermodynamic reforming equilibrium for 10 h; then a strong deactivation is observed. For this reason, the catalyst is unmounted and analyzed. The results are presented in Tab. 3.2. The XRD analysis shows that the phase composition of the samples remains identical. The spent catalyst exhibits a slightly larger crystallite size due to sintering enhanced by the long thermal treatment at 1123 K (850°C) under high partial pressure of steam. A specific surface area loss of one order of magnitude is observed, but the Pt dispersion stays relatively constant.

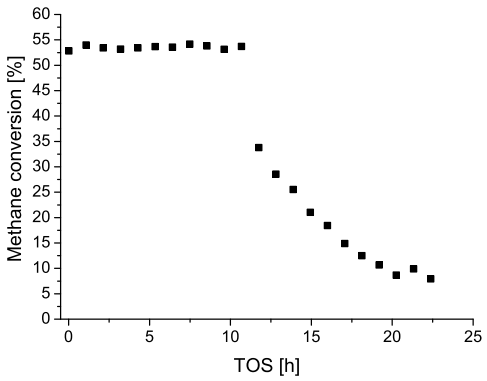

Figure 3.1: Performance in steam reforming of Pt/ZrO_2 (PtZ) with a steam/carbon ratio of unity, at 1123 K (850°C), 21 bar, and 3800 h^{-1}

Pt/ZrO_2	Phases from XRD analysis	$\varnothing_{Pt}/\varnothing_{Support}$ [nm]	Dispersion of Pt^0 [%]	Specific surface area [$m^2.g^{-1}$]
fresh	Pt/m-ZrO_2	37/28	12.1	2
spent	Pt/m-ZrO_2	43/42	11.0	0.2

Table 3.2: Comparison of fresh and spent catalyst Pt/ZrO_2 (PtZ); m-ZrO_2, monoclinic zirconia. The particle size is obtained from the XRD patterns and the Scherrer formula.

Because the catalyst reaches the thermodynamic-equilibrium conversion from the beginning, a possible decrease of the activity due to loss of specific surface area cannot be observed in the initial period but only after a threshold is reached after 10 h of steam reforming. The loss of specific surface area is likely to result from the effect of steam at high temperature, which is known to favor sintering[36;132] especially in the case of monoclinic zirconia[293].

The specific surface area of the support is believed to act as the active surface for steam adsorption[307] while methane decomposes on Pt, the resulting reaction occurring at the interface of the metallic Pt particles and zirconia. Therefore, a lower specific surface area results in a lower interfacial area and thus deactivation.

The thermal stability of the catalyst can be improved by addition of a small amount of silica. Therefore, materials that maintain a high specific surface area even under high temperature for a relatively long period of time[292;293] can be synthesized.

3.1.2 Pt/SiO_2-ZrO_2 (PtSZ) in steam reforming at high pressure

The impregnation with Pt salt is performed on a zirconia split modified with 5 wt.% SiO_2.

The analytic data are displayed in Tab. 3.3 and show, compared to PtZ, that the specific surface area is significantly increased, as expected, but the Pt dispersion is lower. Images from STEM analysis show small Pt nanoparticles of 10-60 nm in diameter (e.g. Fig. 3.2). XRD analysis shows that the support consists mainly of monoclinic zirconia with traces of tetragonal zirconia and free SiO_2.

Pt/SiO_2-ZrO_2	Phases from XRD analysis	$\varnothing_{Pt}$ [nm]	Dispersion of Pt^0 [%]	Specific surface area [$m^2.g^{-1}$]
fresh	Pt/m-ZrO_2 +SiO_2+ ε t-ZrO_2	10-60	4.2	76

Table 3.3: Results of analysis (XRD, N_2 physisoprtion, STEM, TPD) of the fresh catalyst Pt/SiO_2-ZrO_2 (PtSZ); m-ZrO_2: monoclinic zirconia; t-ZrO_2: tetragonal zirconia; ε, side phase or traces. The particle size is obtained from the STEM study.

Only a very low activity is observed, with 8% of methane conversion (Fig. 3.3). Therefore, the catalytic test is interrupted after 5 h of runtime, and the spent catalyst is used for further characterizations.

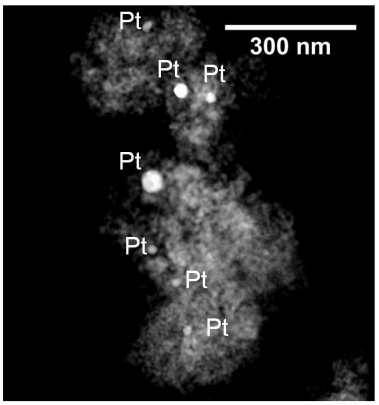

Figure 3.2: STEM of fresh Pt/SiO_2-ZrO_2 (PtSZ)

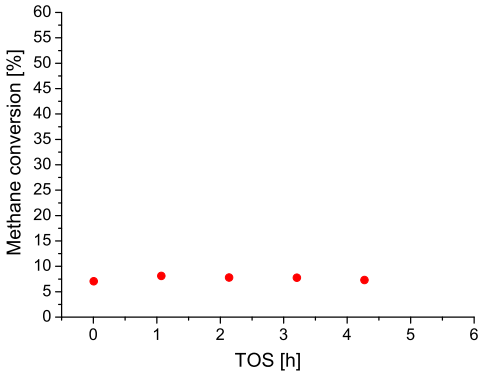

Figure 3.3: Performance in steam reforming of Pt/SiO_2-ZrO_2 (PtSZ) with a steam-to-carbon ratio of unity, at 1123 K (850°C), 21 bar, and 3800 h^{-1}

The characterization results of the spent catalyst are compared with the characterization results of the fresh catalyst and are shown in Tab. 3.4. Comparison of XRD analyses shows no change in the phase composition and only a moderate sintering effect on Pt particles. The specific surface area exhibits a loss of about 50% while the Pt dispersion is about three times lower. In addition to detrimental effects on the catalytic properties, the catalyst does not show any change in activity during the runtime. The low activ-

ity could result from the presence of free SiO_2 [292]. Indeed, Reddy et al. [292] observed a low performance of Pt/SiO_2-ZrO_2 under CO_2 reforming when free silica can be identified in the catalyst. Moreover, Bitter et al. [289] also reported a low activity of Pt/SiO_2 in CO_2 reforming of methane at atmospheric pressure and 923 K (650°C).

Pt/SiO_2-ZrO_2	Phases from XRD analysis	$\varnothing_{Pt}/\varnothing_{Support}$ [nm]	Dispersion of Pt^0 [%]	Specific surface area [$m^2.g^{-1}$]
fresh	Pt/m-ZrO_2 +SiO_2+ ε t-ZrO_2	10-60	4.2	76
spent	Pt/m-ZrO_2 +SiO_2+ε t-ZrO_2	10-80	1.1	51

Table 3.4: Comparison of fresh and spent catalyst Pt/SiO_2-ZrO_2 (PtSZ); m-ZrO_2: monoclinic zirconia; t-ZrO_2: tetragonal zirconia. The particle size is obtained from the STEM study.

The presence of free SiO_2 on the catalyst surface could also have a tendency to embed Pt particles as reported for Pd particles [308]. Kim et al. [309] have also reported that Pt particles have a low interaction with SiO_2, leading to sintering of Pt particles at low temperatures. Sintering of the Pt particles is not observed here, maybe because the Pt particles are already partially embedded from the beginning.

3.1.3 Pt-CeO_2/SiO_2-ZrO_2 (PtCSZ) in steam reforming at high pressure

The same SiO_2-ZrO_2 support as for PtSZ is used and impregnated with Pt and Ce salts. The resulting catalyst is characterized, and results are displayed in Tab. 3.5.
The XRD analysis shows that the catalyst contains the same phase composition as PtSZ but with a ceria-rich mixed oxide of ceria-zirconia. The dispersion of Pt particles is greatly enhanced on addition of ceria while the specific surface area is similar to the catalyst without ceria. The Pt-particle size observed in electron microscopy images of this study reveals a wider distribution of the Pt-particle size than without addition of ceria.

Pt-CeO_2 /SiO_2-ZrO_2	Phases from XRD analysis	$\varnothing_{Pt}$ [nm]	Dispersion of Pt^0 [%]	Specific surface area [$m^2.g^{-1}$]
fresh	Pt/m-ZrO_2+$(Ce/Zr)O_2$ +SiO_2+ε t-ZrO_2	5-120	22.3	71

Table 3.5: Results of analysis (XRD, N_2 physisoprtion, STEM, TPD) of the fresh catalyst Pt-CeO_2/SiO_2-ZrO_2 (PtCSZ); m-ZrO_2: monoclinic zirconia; t-ZrO_2: tetragonal zirconia; $(Ce/Zr)O_2$, mixed oxide of ceria and zirconia. The particle size is obtained from the STEM study.

The stability of catalytic performances as well as the activity are significantly improved, as can be seen in Fig. 3.4. The addition of ceria enhances the methane conversion in steam reforming. In addition to a high initial activity, the catalyst deactivates slowly. The test is interrupted to perform further characterizations.

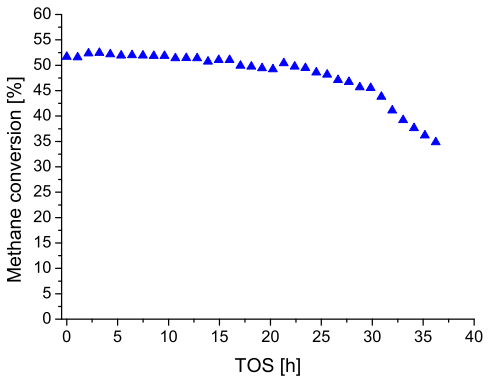

Figure 3.4: Performance in steam reforming of Pt-CeO_2/SiO_2-ZrO_2 (PtCSZ) with a steam-to-carbon ratio of unity, at 1123 K (850°C), 21 bar, and 3800 h^{-1}. The particle size is obtained from the STEM study.

The results of the spent-catalyst analysis are shown in Tab. 3.6. The same phase composition is identified; however, the mixed oxide of ceria and zirconia is not ceria rich anymore. Because ceria is located on the surface of the catalyst, a long thermal treatment in the presence of steam is likely to favor the diffusion of ceria into the bulk as the support sinters. In addition, the size of the Pt nanoparticles is relatively similar. The TPD measurements display a significant decrease in Pt dispersion that may be due to partially embedded Pt particles after the ceria layer diffused into the bulk.

Pt-CeO_2 /SiO_2-ZrO_2	Phases from XRD analysis	$\varnothing_{Pt}$ [nm]	Dispersion of Pt^0 [%]	Specific surface area [$m^2.g^{-1}$]
fresh	Pt/m-ZrO_2+(Ce/Zr)O_2 +SiO_2+ε t-ZrO_2	5-120	22.3	71
spent	Pt/m-ZrO_2+(Ce/Zr)O_2 +SiO_2+ε t-ZrO_2	10-120	3.7	45

Table 3.6: Results of analysis (XRD, N_2 physisoprtion, STEM, TPD) of the fresh catalyst Pt-CeO_2/SiO_2-ZrO_2 (PtCSZ); m-ZrO_2: monoclinic zirconia; t-ZrO_2: tetragonal zirconia; (Ce/Zr)O_2, mixed oxide of ceria and zirconia. The particle size is obtained from the STEM study.

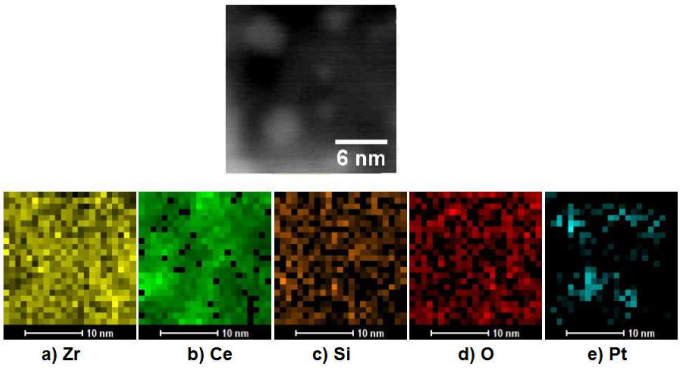

Figure 3.5: Element mapping in STEM of spent Pt-CeO_2/SiO_2-ZrO_2 (PtCSZ)

In addition, element mapping is performed on a sample containing small Pt nanoparticles (Fig. 3.5). The different elements of the support are well distributed. This shows that the impregnation with Ce salt is efficient because the metal is highly dispersed over the surface even after the reaction. Pt is relatively well distributed on the analyzed surface, and no particular variation of the support composition is found in the Pt-rich regions.

3.1.4 Pt-CeO_2/La_2O_3-ZrO_2 (PtCLZ) in steam reforming at high pressure

The catalyst is prepared like PtCSZ, but now the La_2O_3-ZrO_2 support is used. The characterization results are given in Tab. 3.7. The catalyst is mainly made of lanthanum oxide-zirconia mixed oxide with the side phase of the ceria-rich ceria-zirconia mixed oxide. The Pt-particle size distribution is relatively broad, ranging from 50 up to 1000 nm, while the specific surface area is comparable to PtCSZ and the dispersion is even higher than for PtCSZ.

PtCLZ has a stable activity for 20 h and deactivates very slightly to reach about 45% of methane conversion after 65 h of runtime (Fig. 3.6). This catalyst is the most stable studied so far. After 65 h of runtime, the test is stopped and the spent catalyst analyzed.

Pt-CeO_2 /La_2O_3-ZrO_2	Phases from XRD analysis	$\varnothing_{Pt}$ [nm]	Dispersion of Pt^0 [%]	Specific surface area [$m^2.g^{-1}$]
fresh	Pt/$La_{0.1}Zr_{0.9}O_{1.95}$ +$(Ce/Zr)O_2$	50-1000	33.9	69

Table 3.7: Results of analysis (XRD, N_2 physisoprtion, STEM, TPD) of the fresh catalyst Pt-CeO_2/La_2O_3-ZrO_2 (PtCLZ); m-ZrO_2: monoclinic zirconia; $(Ce/Zr)O_2$, mixed oxide of ceria and zirconia. The particle size is obtained from the STEM study.

The characterization results are shown in Tab. 3.8. The XRD analysis shows that the phase distribution is different after reaction, with appearance of monoclinic zirconia. The side phase of the ceria-zirconia mixed oxide changes also from Ce-rich to Ce-poor.

Indeed, $La_{0.1}Zr_{0.9}O_{1.95}$ decomposes mostly in monoclinic zirconia and a La_2O_3-rich mixed oxide of lanthanum oxide and monoclinic zirconia. A part of the free monoclinic zirconia can form a mixed oxide with the initial ceria-zirconia mixed oxide, changing its composition from ceria-rich to a poorer ceria content due to the inclusion of zirconia within this mixed oxide. This phase segregation is promoted by high temperature and a high partial pressure of the steam. As a result, the specific surface area is about two orders of magnitude lower and the dispersion of Pt decreased by one order of magnitude.

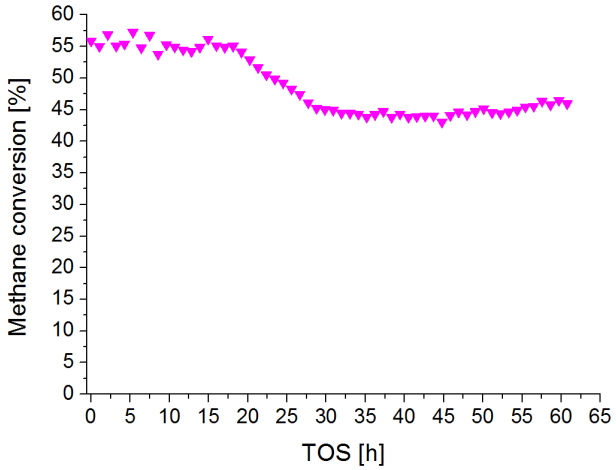

Figure 3.6: Performance in steam reforming of Pt-CeO_2/La_2O_3-ZrO_2 (PtCLZ) with a steam/carbon ratio of unity, at 1123 K (850°C), 21 bar and 3800 h^{-1}.

Pt-CeO_2 /La_2O_3-ZrO_2	Phases from XRD analysis	$\varnothing_{Pt}$ [nm]	Dispersion of Pt^0 [%]	Specific surface area [$m^2.g^{-1}$]
fresh	Pt/$La_{0.1}Zr_{0.9}O_{1.95}$ +(Ce/Zr)O_2	50-1000	33.9	69
spent	Pt/m-ZrO_2 +(La/Zr)O_x+(Ce/Zr)O_2	50-1000	2.9	0.7

Table 3.8: Comparison of fresh and spent catalyst Pt-CeO_2/La_2O_3-ZrO_2 (PtCLZ); m-ZrO_2: monoclinic zirconia; (Ce/Zr)O_2, mixed oxide of ceria and zirconia; (La/Zr)O_x mixed oxide of lanthanum oxide and zirconia. The particle size is obtained from the STEM study.

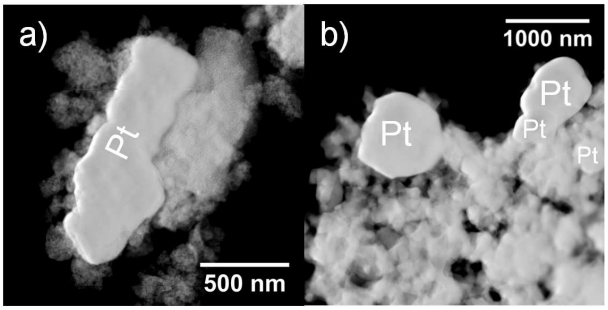

Figure 3.7: STEM of a) fresh and b) spent Pt-CeO_2/La_2O_3-ZrO_2 (PtCSZ)

The Pt particle-size distribution evaluated by using STEM images remains quite large and about 50-1000 nm at the beginning and after reforming. The STEM images obtained on fresh and spent catalyst show the presence of large Pt particles (Fig. 3.7). These large particles are still found on the support in comparison with PtCSZ. Apparently, even with a lower dispersion, the catalyst retains a sufficient

activity in steam reforming despite the very high loss of specific surface area.

3.1.5 Comparison of performance for the various Pt-based catalysts

The optimization of the Pt-based catalysts with various zirconia supports is successful and their performances are compared in Fig. 3.8. Pt/ZrO_2 exhibits a high activity but only a low stability due to a loss of specific surface area caused by recrystallization. A relatively high specific surface area is necessary to maintain a sufficient interfacial area between the Pt nanopraticles and the defect-rich monoclinic zirconia where methane decomposes and H_2O can adsorb dissociatively[307], respectively. If the specific surface area is lowered, this interfacial area decreases also and deactivation is observed. The addition of SiO_2 is successful to obtain a higher thermal stability as well as a high specific surface area; however, the presence of free silica lowers the activity[292], probably because the Pt particles are at least partially embedded in SiO_2, like Pd in SiO_2[308].

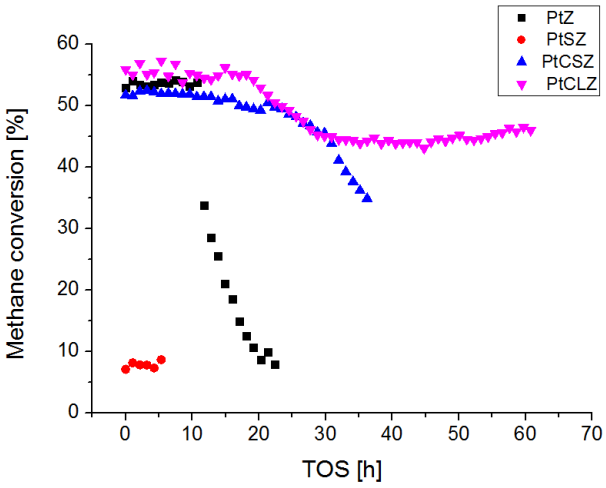

Figure 3.8: Comparison of performance under steam reforming of all zirconia-based supports

The addition of CeO_2 to PtSZ can consequently increase the activity and the dispersion of Pt nanoparticles without lowering the specific surface area significantly; however, the Pt nanoparticles are likely to be embedded after the Ce atoms migrate into the catalyst bulk. Finally, the use of La_2O_3 instead of SiO_2 allows for the activity for steam reforming to be stabilized close to the thermodynamic equilibrium thanks to the mixed oxide of lanthanum oxide and zirconia in the bulk, with ceria-zirconia mixed oxide on the catalyst surface where the Pt nanoparticles are deposited. The PtCLZ catalyst shows high activity and high stability over a period of 65 h under steam reforming with a steam-to-carbon ratio of one at 21 bar, 1123 K (850°C), and a GHSV of 3800 h^{-1}.

An overview of the different zirconia modifications is suggested in Fig. 3.9. The monoclinic zirconia needs to be stabilized to maintain a sufficient specific surface area. The modification of zirconia with SiO_2 improves the thermal stability of the doped zirconia support; however, the Pt particles probably tend

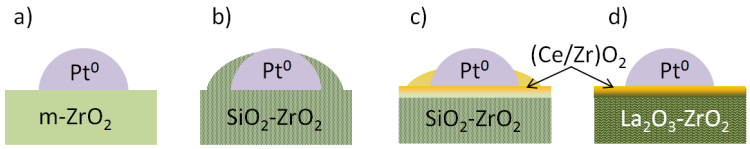

Figure 3.9: Schematic drawing of the Pt-based catalysts with various supports; a) Pt/ZrO_2; b) Pt/SiO_2-ZrO_2; c) Pt-$CeO_2/SiO_2/ZrO_2$, d) Pt/La_2O_3-ZrO_2; m-ZrO_2, monoclinic zirconia

to be embedded in the support. The use of a ceria layer results in non-embedded Pt-particles; however, with the diffusion of ceria into the bulk the Pt particles can be also slowly embedded after a long period of time. The use of La_2O_3-ZrO_2 instead of SiO_2-ZrO_2 improves the stability of the catalyst because the support does not have the tendency to embed the Pt particles after diffusion of the ceria layer through the bulk.

3.2 Results of the kinetic study on Pt-based catalyst

A kinetic approach to reforming in the presence of H_2O and CO_2 is performed with PtCLZ in order to improve the kinetic model over Pt-based catalyst proposed by the DETCHEM platform developed by Deutschmann's group. The use of La_2O_3 and CeO_2 promoters does not change the mechanism for ZrO_2 [286] and, therefore, PtCLZ is preferred over PtZ, PtSZ, and, PtCSZ for the kinetic study.
This study is based on temperature and GHSV variation at atmospheric pressure. The GHSV variation is achieved by varying the catalyst mass in the reactor at a constant absolute flow. For this reason, each catalytic bed exhibits a particular pressure drop that is significant compared to atmospheric pressure. As a result, the distribution of the feed rate may vary from reactor to reactor and the GHSVs measured are slightly different. Therefore, a GHSV range is given instead of a single theoretical value for this study. The pressures also vary from reactor to reactor between 1.09-1.34 bar.
For each reforming condition, the catalytic performances are compared to the thermodynamic equilibrium. The experiments reaching the thermodynamic equilibrium are labeled with a star (*) in the graphics presenting the TOFs of methane and CO_2 conversions depending on operating temperature and GHSV range. For each reforming conditions, the TOFs of methane and CO_2 conversions are first presented at a "constant" GHSV to observe the effect of the operating temperature and, second, the effect of the GHSV is presented at constant temperature.

3.2.1 Kinetic study under steam reforming

The kinetic study is first performed under steam reforming conditions with steam-to-carbon ratio of one. The conversions of methane and CO_2 as well as the H_2/CO ratios obtained are plotted in Fig. 3.10 for the different GHSVs within a temperature range of 1023-1173 K (750-900°C). The catalytic performances are compared to those at the thermodynamic equilibrium.

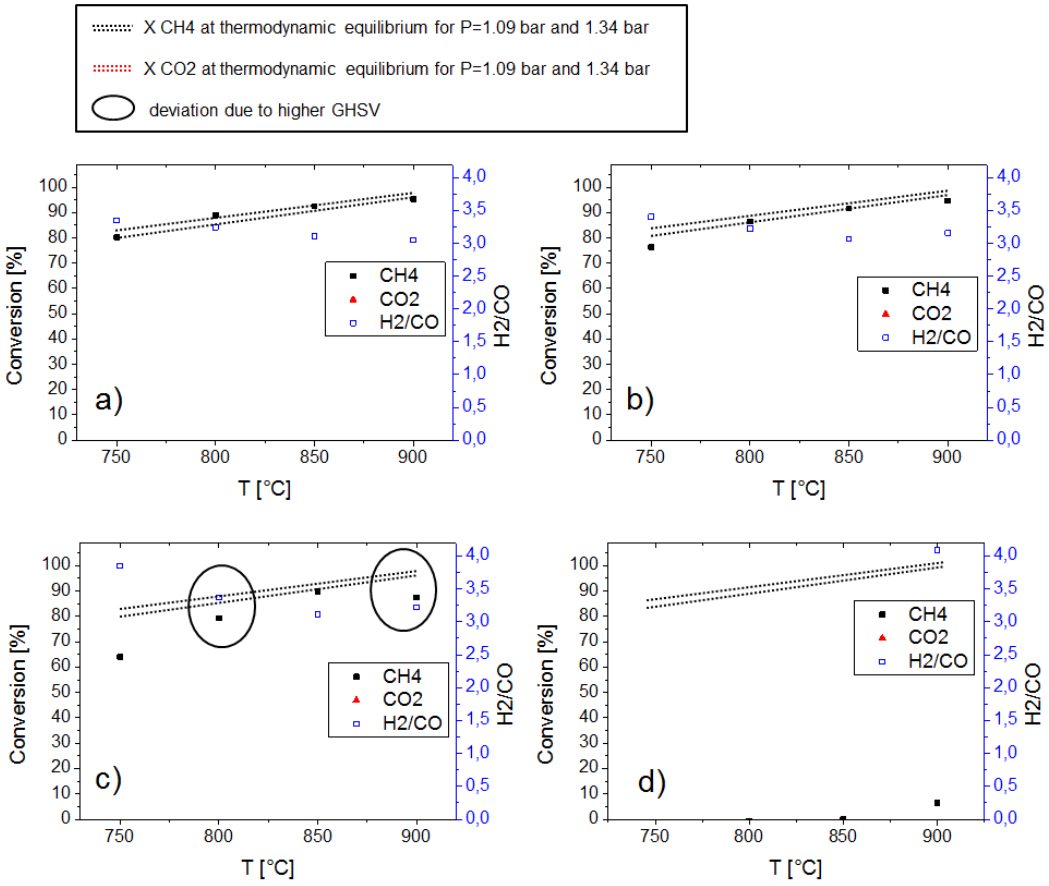

Figure 3.10: Performance of PtCLZ under steam reforming at different GHSVs, a) low (3604-4073 h^{-1}), b) medium (15593-17288 h^{-1}), c) high (33559-41225 h^{-1}), whereas d) corresponds to the blank reactor filled with corundum in a temperature range of 1023-1173 K (750-900°C) compared to the thermodynamic equilibrium.

In Figs. 3.10-a), 3.10-b), and 3.10-c), the thermodynamic equilibrium of steam reforming is reached in most cases. At low GHSVs, the thermodynamic equilibrium of steam reforming is reached already at 1023 K (750°C), at medium GHSVs the thermodynamic equilibrium of steam reforming is reached above 1073 K (800°C), and for high GHSVs above 1123 K (850°C). At a high GHSV range (33559-41225 h^{-1}), a significant deviation from the thermodynamic equilibrium of reforming is observed at 1073 and 1173 K (800 and 900°C respectively) due to GHSV deviations. Indeed, at these temperatures, the GHSV is about 30% higher. This explains why at 1173 K (900°C) and high GHSV the equilibrium is not reached whereas the equilibrium is reached at 1123 K (850°C) and high GHSV.

Corundum shows only a minor activity under steam reforming conditions with a maximum in methane conversion at 1173 K (900°C) of less than 7%. This confirms that corundum can be used as an "inert" material under these reaction conditions.

In order to compare the catalyst activity despite the variation of the catalyst mass, the TOFs of methane and CO_2 conversions are used. The results for the different GHSVs are presented in Fig 3.11 to demonstrate the influence of temperature on the TOFs of methane conversion.

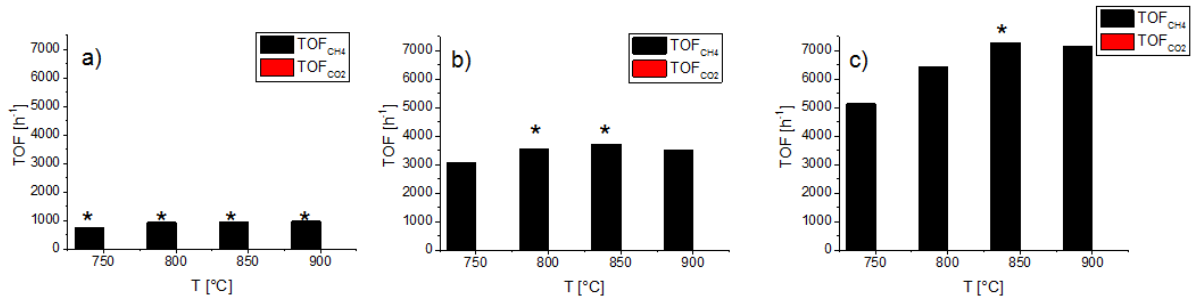

Figure 3.11: TOF of CH_4 conversions over PtCLZ under steam reforming at different GHSVs, a) low (3604-4073 h^{-1}), b) medium (15593-17288 h^{-1}), c) high (33559-41225 h^{-1}) in a temperature range of 1023-1173 K (750-900°C), * catalyst working at thermodynamic equilibrium

The TOFs of methane conversion are almost constant as long as thermodynamic equilibrium is reached. When the catalyst achieves thermodynamic equilibrium of steam reforming for a given mass of catalyst, the TOFs calculated are identical because the same amount of methane is converted by the same amount of Pt. As soon as the catalyst performances are below the thermodynamic equilibrium of steam reforming, the TOF of methane conversion increases with operating temperature.

The TOFs could be also plotted for a given temperature to demonstrate the effect of GHSVs as shown in Fig. 3.12. In addition to the fact that the catalyst reaches thermodynamic equilibrium of steam reforming in most cases, the overall trend shows a TOF increase as the GHSV is increased.

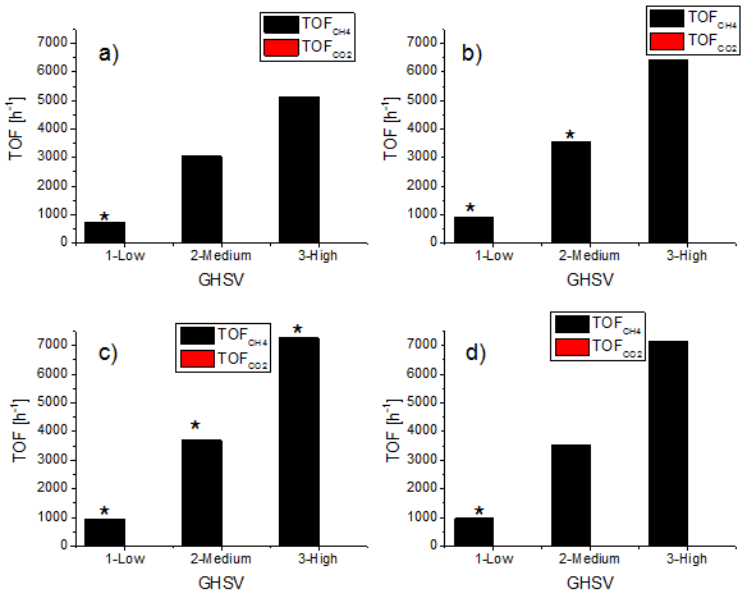

Figure 3.12: TOFs of CH_4 conversions over PtCLZ under steam reforming at different GHSVs, a) 1023 K (750°C), b) 1073 K (800°C), c) 1123 K (850°C), and d) 1173 K (900°C), in a GHSV range: low GHSV (3604-4073 h^{-1}); medium GHSV, (15593-17288 h^{-1}); high GHSV, (33559-41225 h^{-1}); * catalyst working at thermodynamic equilibrium

3.2.2 Kinetic study under steam reforming with CO_2 addition

The study made for steam reforming is repeated for steam reforming with CO_2 addition.
An overview of the performance achieved by each of the 16 reactors is displayed in Fig. 3.13.
At low GHSVs, once again the thermodynamic equilibrium is reached at all temperatures: at medium GHSVs only the catalyst at 1023 K (750°C) does not reach the thermodynamic equilibrium, and at high GHSVs only the catalyst at 1123 K (850°C) achieved thermodynamic equilibrium. The blank reactor shows a low activity comparable with steam reforming, that is, about 7% methane conversion. This confirms that the corundum is "inert".

The comparison between performances is then achieved on the basis of the TOFs of methane or CO_2 conversions. Both TOFs can be plotted at "constant" GHSV to demonstrate the effect of the temperature (Fig. 3.14). As reported for steam reforming, only a general trend is observed, showing that an increase of TOFs of methane and CO_2 conversions is observed as the temperature increases if the thermodynamic equilibrium of reforming is not reached. At thermodynamic equilibrium of reforming the TOFs are equal for a given GHSV.

The TOFs of methane or CO_2 conversions can be also plotted at constant temperature to demonstrate the effect of different GHSVs (Fig. 3.15). Increasing the GHSV leads to an increase of both of these TOFs if the thermodynamic equilibrium of reforming is reached or not.

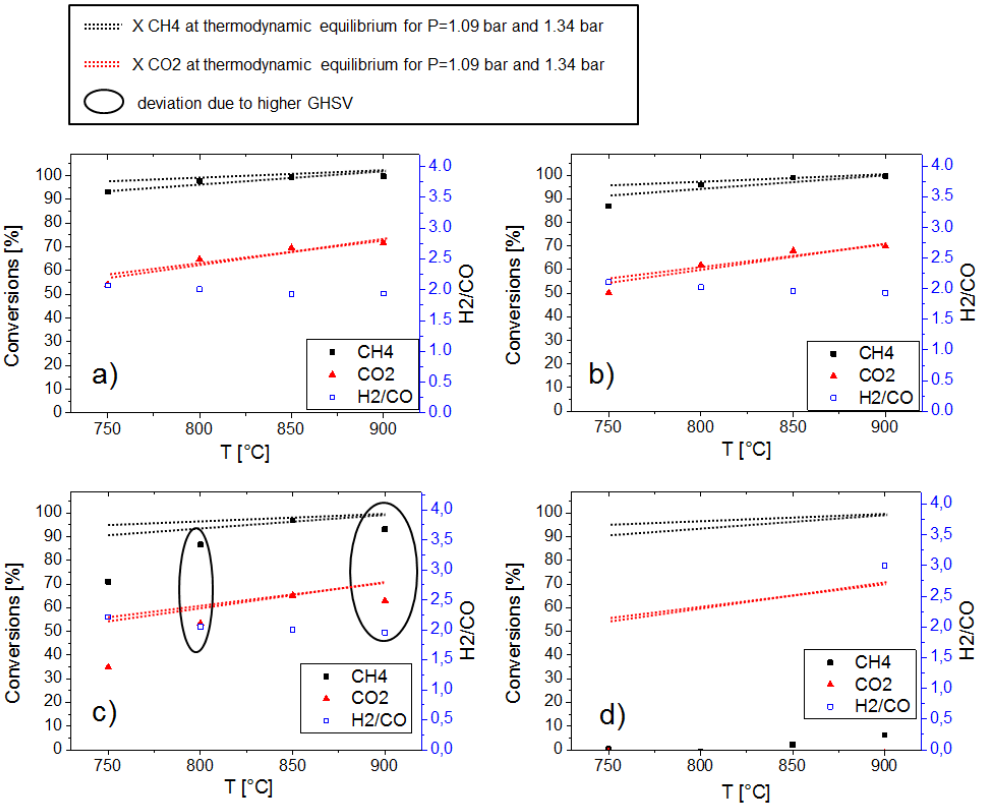

Figure 3.13: Performance of PtCLZ under steam reforming with CO_2 addition at different GHSVs, a) low (3604-4073 h^{-1}), b) medium (15593-17288 h^{-1}), and c) high (33559-41225 h^{-1}), while d) is the blank reactor filled with corundum in a temperature range of 1023-1173 K (750-900°C) compared to the thermodynamic equilibrium.

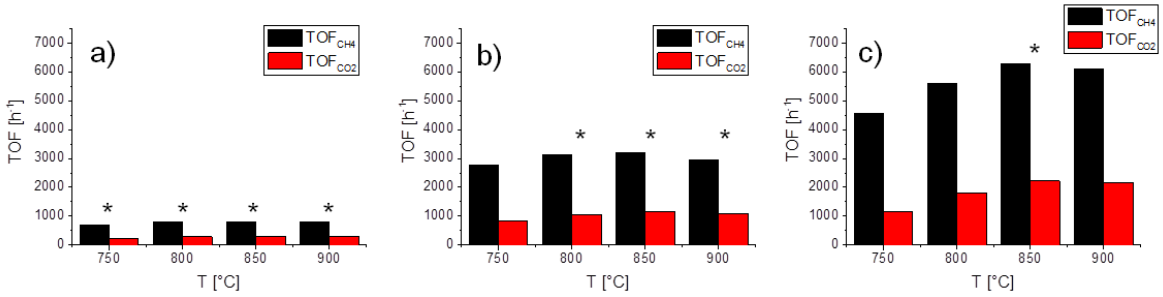

Figure 3.14: TOFs of CH_4 and CO_2 conversions over PtCLZ under steam reforming with CO_2 addition at the different GHSV, a) low (3604-4073 h^{-1}), b) medium (15593-17288 h^{-1}), c) high (33559-41225 h^{-1}) , in a temperature range of 1023-1173 K (750-900°C), * catalyst working at thermodynamic equilibrium

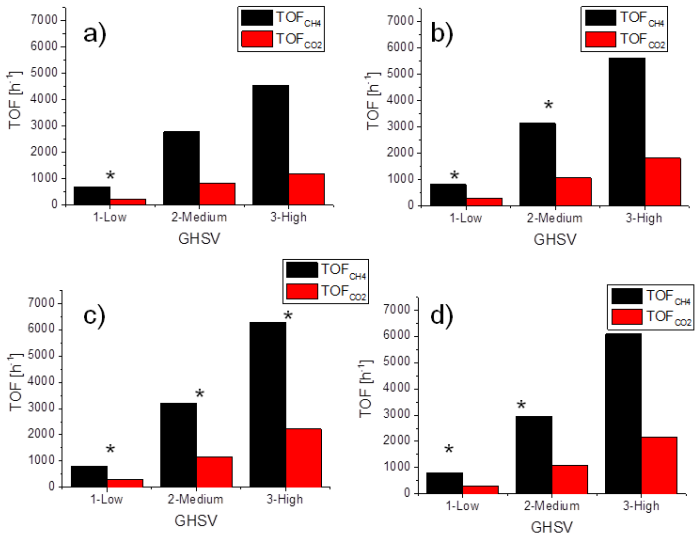

Figure 3.15: TOFs of CH_4 and CO_2 conversions over PtCLZ under steam reforming with CO_2 addition at the different GHSV, a) 1023 K (750°C), b) 1073 K (800°C), c) 1123 K (850°C), and d) 1173 K (900°C), in a GHSV range: low GHSV (3604-4073 h^{-1}); medium GHSV, (15593-17288 h^{-1}); high GHSV, (33559-41225 h^{-1}); * catalyst working at thermodynamic equilibrium.

The increase of GHSV at 1023 K (750°C) is particularly interesting because the experiments at 1023 K (750°C) are the only ones at which the thermodynamic equilibrium is hardly achieved. The increase of the GHSV promotes principally the TOFs of methane conversion, showing that methane conversions occur faster than CO_2 conversions at 1023 K (750°C). CO_2 can then react with H_2 by RWGS or CH_4 in CO_2 reforming.

3.2.3 Kinetic study under CO_2 reforming with 36 vol.% H_2O

The conversions and the resulting H_2/CO ratios obtained are plotted in Fig. 3.16 for the different GHSV ranges and a temperature range of 1023-1173 K (750-900°C). The performances are compared with the thermodynamic equilibrium.

The experiments that reach the thermodynamic equilibrium of reforming do not change (low GHSV, medium GHSV above 1073 K (800°C), high GHSV at 1123 K (850°C). The activity of corundum remains low over the temperature range of 1023-1173 K (750-900°C) in steam reforming when adding CO_2.

The TOFs of methane and CO_2 conversions are plotted at "constant" GHSV to demonstrate the effect of temperature (Fig. 3.17). In addition to the general trend observed in all cases up to now, the TOFs of methane conversion decrease with lower partial pressure of steam, that is to say TOFs of methane conversion are higher under steam reforming than under steam reforming with CO_2, which are also higher than under CO_2 reforming with 36 vol.% H_2O. In the same way, the increase of CO_2 partial pressure leads also to an increase of the TOFs of CO_2 conversions.

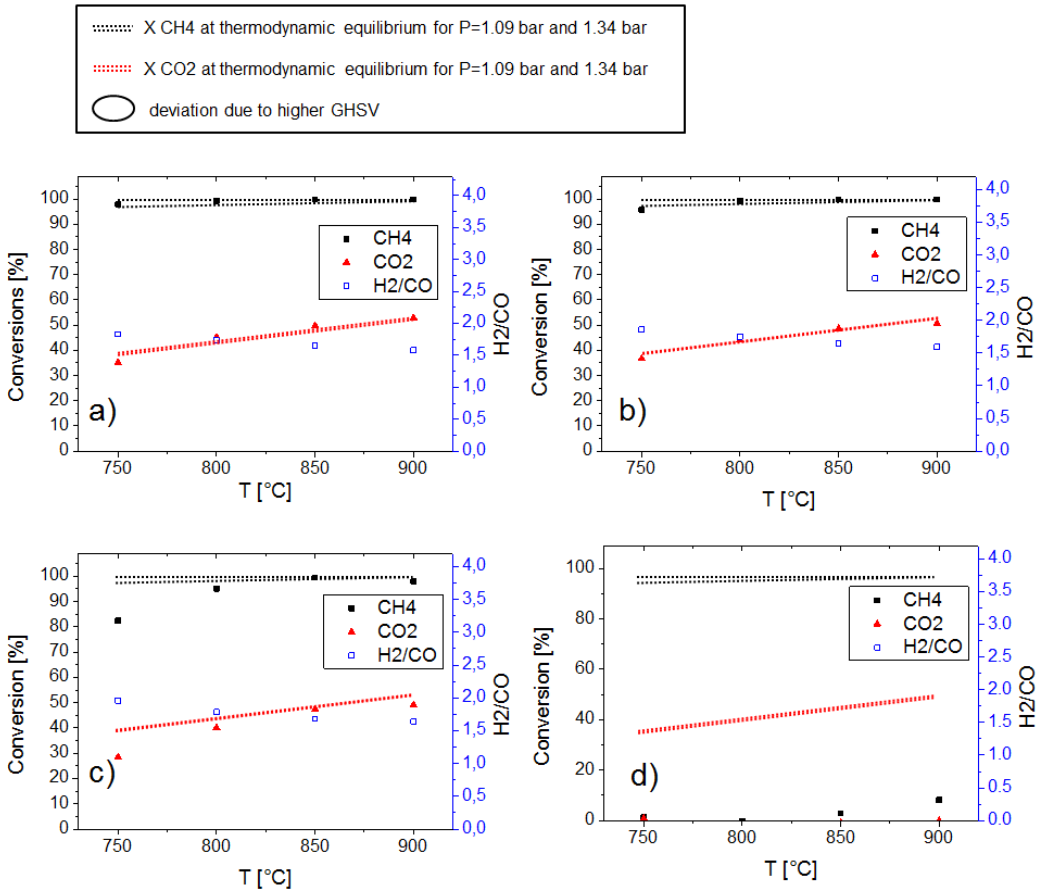

Figure 3.16: Performance of PtCLZ under CO_2 reforming with 36 vol.% H_2O at different GHSVs, a) low (3604-4073 h^{-1}), b) medium (15593-17288 h^{-1}), and c) high (33559-41225 h^{-1}), whereas d) corresponds to the blank reactor filled with corundum in a temperature range of 1023-1173 K (750-900°C) compared to the thermodynamic equilibrium

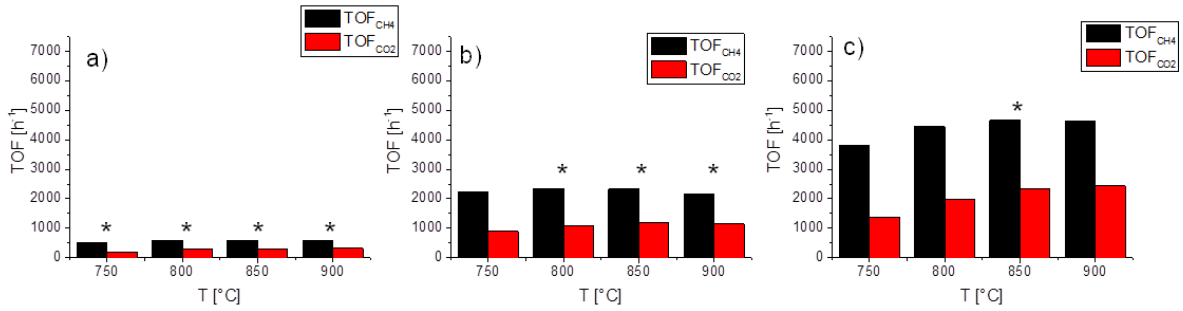

Figure 3.17: TOFs of CH_4 and CO_2 conversions over PtCLZ under CO_2 reforming with 36 vol.% H_2O at different GHSVs, a) low (3604-4073 h^{-1}), b) medium (15593-17288 h^{-1}), and c) high (33559-41225 h^{-1}), in a temperature range of 1023-1173 K (750-900°C), * catalyst working at thermodynamic equilibrium

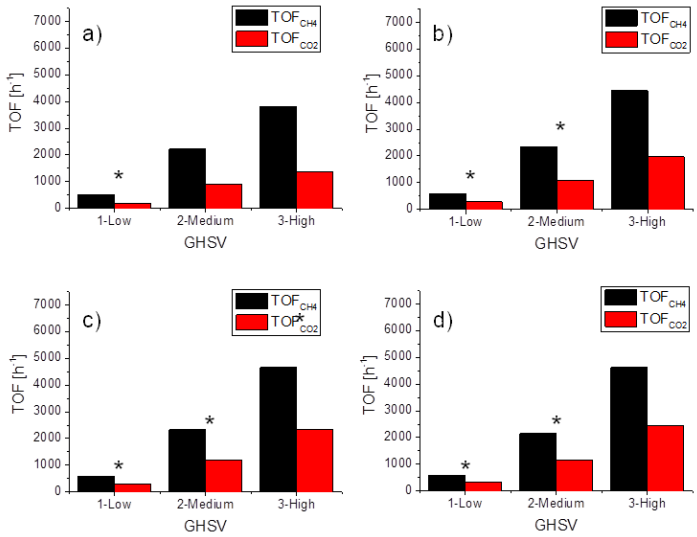

Figure 3.18: TOFs of CH_4 and CO_2 conversions over PtCLZ under CO_2 reforming with 36 vol.% H_2O at different GHSVs, a) 1023 K (750°C), b) 1073 K (800°C), c) 1123 K (850°C), and d) 1173 K (900°C), in a GHSV range: low GHSV (3604-4073 h^{-1}); medium GHSV, (15593-17288 h^{-1}); high GHSV, (33559-41225 h^{-1}); * catalyst working at thermodynamic equilibrium

The plots can also be presented at constant temperature to demonstrate the effect of the various GHSVs (Fig. 3.18). At 1023 K (750°C), the GHSV increase also results in TOFs of methane conversion that are higher than TOFs of CO_2 conversion. The effect is, however, less significant than those observed in the last section for steam reforming with CO_2 addition: less H_2O is available to increase the rate of steam reforming and the methane partial pressure is lower.

A higher steam-to-methane ratio (H_2O/CH_4 higher than one) preferentially increases the methane conversions as the GHSV is increased. This confirms that methane reacts preferentially with steam whereas CO_2 reacts in a second step with either the produced H_2 by RWGS or/and with methane by CO_2 reforming.

3.2.4 Kinetic study under CO_2 reforming with 30 vol.% H_2O

The performance overview is displayed in Fig. 3.19. The experiments showed that the thermodynamic equilibrium is reached at low GHSVs, at medium GHSVs above 1023 K (750°C), and at high GHSVs at 1123 K (850°C). The differences to the previous operating conditions (CO_2 reforming with 36 vol.% H_2O) are only minimal; therefore, only little differences with the previous observations are achieved.

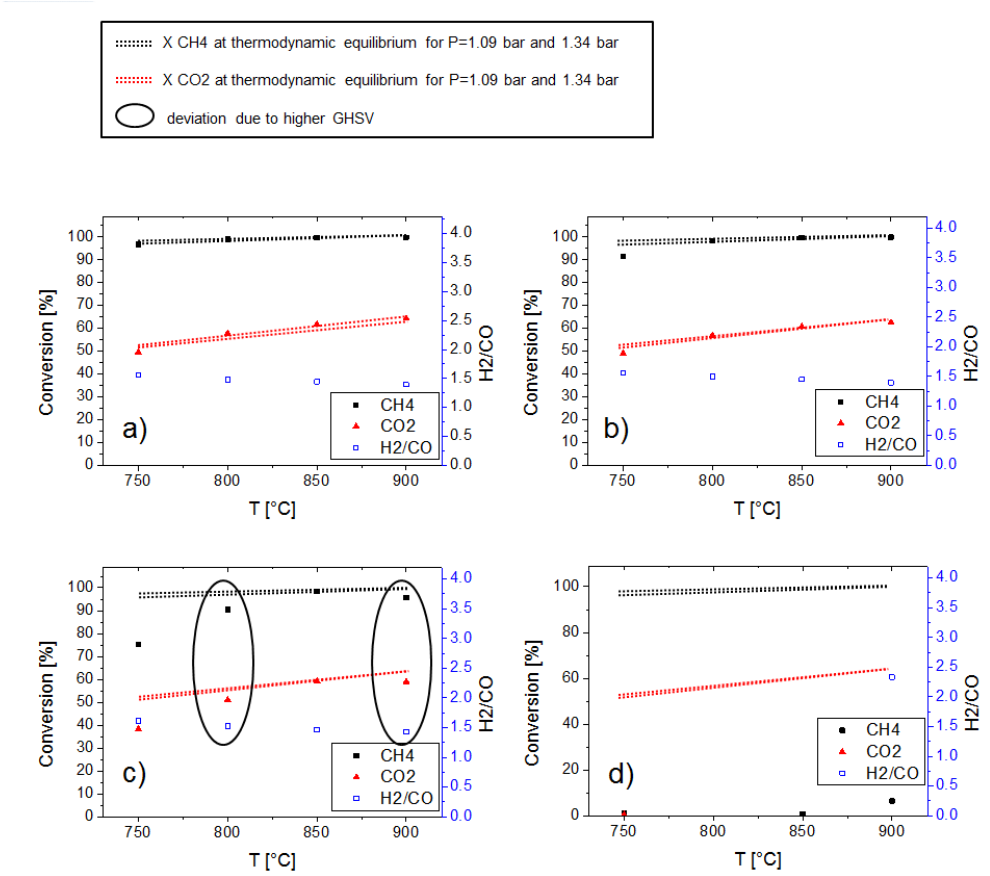

Figure 3.19: Performance of PtCLZ under CO_2 reforming with 30 vol.% H_2O at different GHSVs, a) low (3604-4073 h^{-1}), b) medium (15593-17288 h^{-1}), c) high (33559-41225 h^{-1}), whereas d) corresponds to the blank reactor filled with corundum in a temperature range of 1023-1173 K (750-900°C) compared to the thermodynamic equilibrium.

The plots at "constant" GHSV show the influence of temperature in Fig. 3.20. Only the graphic of the high GHSV ranges shows a slight increase in GHSV as the temperature increases, as it is expected. For $CH_4/CO_2/H_2O$=1/1/1, TOFs of methane conversion are still higher than TOFs of CO_2 conversions, confirming that steam reforming takes place first before CO_2 can react. Moreover, it is still unclear how CO_2 reacts in mixed-steam CO_2 reforming. Indeed, CO_2 can react with CH_4 or with H_2 from steam reforming. Due to the TOFs of methane conversion being higher than the TOFs of CO_2 conversion, if CO_2 reacts with CH_4 it would be at a lower reaction rate than for steam reforming.

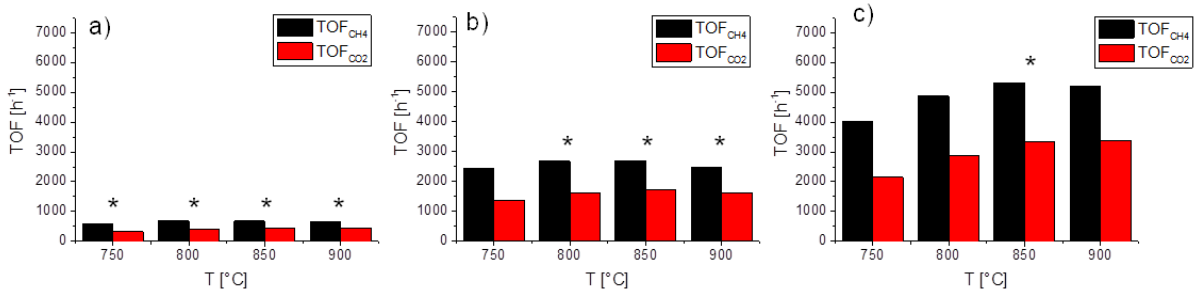

Figure 3.20: TOFs of CH_4 and CO_2 conversions over PtCLZ under CO_2 reforming with 30 vol.% H_2O at different GHSVs, a) low (3604-4073 h^{-1}), b) medium (15593-17288 h^{-1}), c) high (33559-41225 h^{-1}), in a temperature range of 1023-1173 K (750-900°C), * catalyst working at thermodynamic equilibrium

The plots can also be presented at constant temperature to demonstrate the effect of GHSV (Fig. 3.21). For these operating conditions, the increase of the GHSV range at 1023 K (750°C) does not show clearly if TOFs of methane conversion increase faster than TOFs of CO_2 conversion.

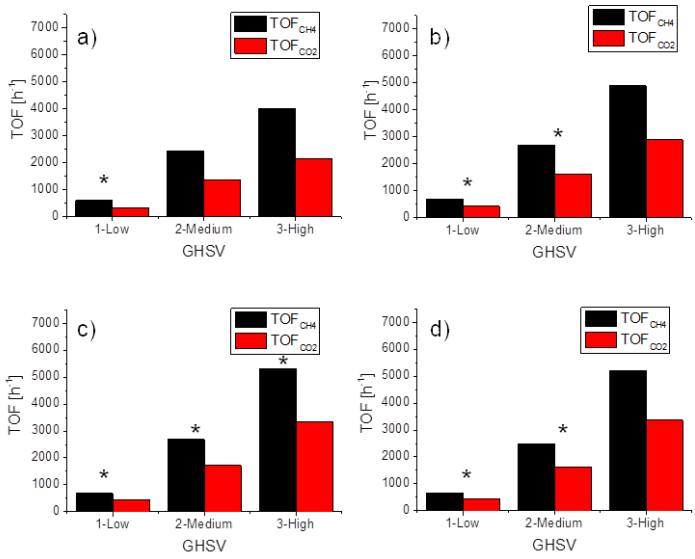

Figure 3.21: TOFs of CH_4 and CO_2 conversions over PtCLZ under CO_2 reforming with 30 vol.% H_2O at different GHSVs, a) 1023 K (750°C), b) 1073 K (800°C), c) 1123 K (850°C), and d) 1173 K (900°C), in a GHSV range: low GHSV (3604-4073 h^{-1}); medium GHSV, (15593-17288 h^{-1}); high GHSV, (33559-41225 h^{-1}); * catalyst working at thermodynamic equilibrium

The trend observed on TOFs of methane and CO_2 conversion is confirmed, higher partial pressures of H_2O or CO_2 lead to higher TOFs of methane or CO_2 conversion, respectively.

3.3 Conclusions

The zirconia support of the Pt-based catalysts has been optimized to enhance activity as well as stability of the catalyst. The following scheme has been proposed to interpret the performance of the various supports of the Pt-based catalysts (Fig. 3.22).

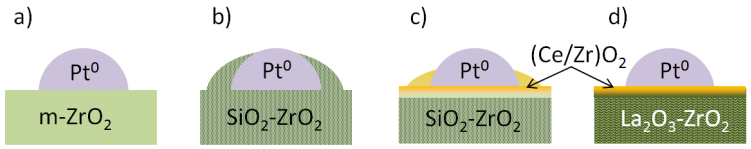

Figure 3.22: Schematic drawing of the Pt-based catalysts with various supports; a) Pt/ZrO_2; b) Pt/SiO_2-ZrO_2; c) Pt-$CeO_2/SiO_2/ZrO_2$, d) Pt/La_2O_3-ZrO_2; m-ZrO_2, monoclinic zirconia

Pt/ZrO_2 catalyst (a) is not stable enough to perform in the high-temperature steam reforming of methane because the monoclinic zirconia is not thermally stable. Therefore, the use of SiO_2 to modify zirconia (b) can improve the thermal stability of the catalyst; however, the Pt particles are not "active" probably due to the formation of embedded Pt particles. The use of a ceria layer (c) on such a catalyst can delay the embedding process; however, after a long period of time the ceria layer diffuses into the bulk. As a result, the support now only very lightly doped with ceria could still embed the Pt particles. The use of the La_2O_3-ZrO_2 with a ceria layer as a support for the Pt particles (d) results in a thermally stable support with relatively high stability and high activity. The ceria layer can still diffuse through the bulk; however, the bulk does not embed the Pt particles.

The performance of Pt-CeO_2/La_2O_3-ZrO_2 under steam reforming of methane with a steam-to-carbon ratio of one at 21 bar and 1123 K (850°C) with a GHSV of 3800 h^{-1} shows high stability and activity (5% absolute below the expected thermodynamic equilibrium) for more than 60 h. This catalyst is, therefore, chosen for the kinetic study.

The kinetic study over Pt-CeO_2/La_2O_3-ZrO_2 (d) shows that the influence of the temperature as well as the influence of the GHSV for these operating conditions are not optimal for a kinetic study since most of the experiments achieve thermodynamic equilibrium.
The study with corundum shows that only at 1173 K (900°C) and the four different reforming operating conditions (steam reforming, steam reforming in the presence of H_2O, and CO_2 reforming in the presence of 36 vol.% and 30 vol.% water, respectively), the impact of the gas-phase reactions is rather low, while corundum is observed to be inert.
The influence of kinetics is mainly observed at 1023 K (750°C), as the thermodynamic equilibrium is not reached. Under these operating conditions it can be observed that TOFs of methane and CO_2 conversion increase as the partial pressure of steam and CO_2 increases, respectively. The TOFs of methane conversions are always higher than the TOFs of CO_2 conversions because steam reforming proceeds

faster. Indeed, TOFs of methane conversion increase faster than TOFs of CO_2 conversion as the GHSV is increased.

Part VI

Ni-based spinels for steam reforming in the presence of CO_2

1 Ni/MgO-Al_2O_3 as catalyst for steam reforming in the presence of CO_2: State of the art

Ni/MgO-Al_2O_3 catalysts have a high potential for reforming applications and have already been highlighted by Haldor Tops∅e, who dispersed Ni on $MgAl_2O_4$ [310–312]. This readily available and robust catalytic system has been developed since the 70's.

An advantage of the carrier system is the high thermal stability of $MgAl_2O_4$, the Mg-spinel, which has given its name to the spinel group and exhibits a cubic structure of the space group number 227: $Fd\bar{3}m$ [295]. The unit cell of $MgAl_2O_4$, shown in Fig. 1.1, is made of 32 face-centered cubic cells of O^{2-} anions, in which one eighth of the defect tetrahedrons are occupied by Mg^{2+} cations and half of the defect octahedra are occupied by Al^{3+} cations.

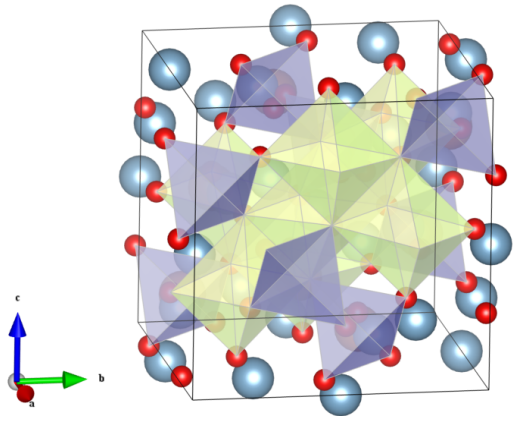

Figure 1.1: Lattice structure of spinel: O, red atoms; Al, blue atoms in purple octahedra; Mg, yellow atoms in yellow tetrahedra (drawn with the Vesta software [298])

The spinel formula for a unit cell is $A_8B_{16}O_{32}$, usually written AB_2O_4, where A and B are divalent and trivalent cations, respectively, for a so-called normal spinel. Inverse spinels have also been identified, like $CoFe_2O_4$ or Fe_3O_4, with formula $B(AB)O_4$, where A occupies the octahedron defect sites and B the half of the tetrahedron defect sites. Real spinels are better represented with the formula $(A_{1-x}B_x)[A_{x/2}B_{1-x/2}]_2O_4$, where parentheses () and brackets [] describe the tetrahedral and octahedral defect sites, respectively. x represents the inversion degree and is equal to 2/3 in case of a fully random cation distribution. Ni aluminium spinel, for instance, is described typically with x=0.75 [313].

A large variety of spinels exists. For instance, A can be Mg, Cr, Mn, Fe Co, Ni, Cu, Zn, Cd, Sn and B can be Al, Ga, In, Ti, V, Cr, Mn, Fe, Co, Rh, and Ni[313].
γ-Alumina is ordered as a so-called defect spinel because Al^{3+} is not only located in the octahedral but also in the tetrahedral defect sites, leaving free octahedral defect sites in its structure[313].

The use of hydrotalcite clay-derived materials as precursor for reforming catalysts has been reported by Bhattacharyya et al.[314–318], who found that the use of such catalyst precursors improves considerably the reforming operations under more severe operating conditions[314]. This breakthrough in catalysis research for reforming applications has led to extensive investigations of Ni-Mg-Al oxidic systems based on hydrotalcite-like precursors[319–332]. The reasons for this surge of interest in hydrotalcite-like materials are due to its interesting properties[333]:

- achievable high surface area,
- basic properties of the carrier system,
- formation of mixed oxides thermally stable with very small crystallite size; reduction of such oxides leads to thermally stable small metal crystallites,
- possible reconstruction of the hydrotalcite structure at mild conditions thanks to contact of aqueous solutions containing various anions.

The layered structure of the hydrotalcite ($Mg_6Al_2(OH)_{16}CO_3.4H_2O$) is presented in Fig. 1.2. The structure presents a brucite layer with an interlayer containing water and carbonate anions.
Hydrotalcite-like compounds belong to the family of layered double hydroxides and have the general chemical formula $[M^{II}_{1-x}M^{III}_x(OH)_2][A^{n-}_{n/x}.zH_2O]$[335], where M^{II} and M^{III} are di- and trivalent cations, respectively, that are located in the octahedral position of the hydroxide layers. The atomic ratio of $M^{III}/(M^{II}+M^{III})$ is represented by x. A^{n-} is an interlayer anion and z is the number of interlayer water molecules[336;337]. In case of Mg^{2+} and Al^{3+} cations, Miyata[338] reported the variation of M^{II}/M^{III} from 4/1 to 2/1 ($0.20 \leq x \leq 0.33$). Typically, a coprecipitation method is used to synthesize such hydrotalcite-like precursors[329–331]. Synthesis with various anions A^{n-} such as nitrate salt of Ni in the presence of water can be used for reconstruction of the double layer hydroxides, as reported by Takehira et al.[319–322]. Indeed, Ni^{2+} can be partially exchanged with Mg^{2+} in such cases.
The common point of the hydrotalcite-like materials is the high specific surface area of mixed oxides obtained after precursor calcination at temperatures up to 1123 K (850°C)[339]. Higher calcination temperatures give rise to segregation into stoichiometric spinel and oxide phases or solid solutions, depending on composition, and a significant decrease in specific surface area[339]. Furthermore, above 1123 K (850°C), the formation of $NiAl_2O_4$ is also reported for Ni-rich samples due to the appearance of a reduction peak at higher temperatures in TPR analysis[339].

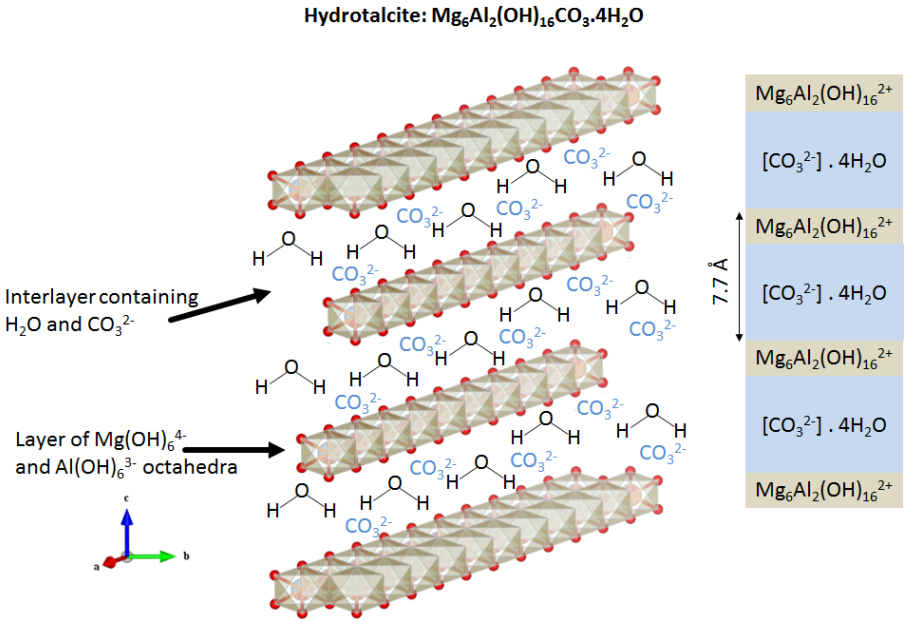

Figure 1.2: Layered structure of hydrotalcite ($Mg_6Al_2(OH)_{16}CO_3.4H_2O$)-forming layers of brucite ($Mg_6Al_2(OH)_{16}^{2+}$) containing octahedra of $Mg(OH)_6^{4-}$ and $Al(OH)_6^{4-}$ with an interlayer containing water and anion(s) ($CO_3^{2-}.4H_2O$) (drawn with the Vesta software[298] and adapted from[314;334])

Regarding catalyst performance in mixed-steam CO_2 reforming ($CH_4/CO_2/H_2O$=31/38/31 and 36/45/18), Bhattacharyya et al. demonstrated the superior activity and stability of hydrotalcite-like Ni-based catalysts[314] compared with a commercial catalyst made of about 10 wt.% Ni on $MgAl_2O_4$ at 1089-1143 K (816-870°C), at 20 bar, and GHSV range of 7200-100000 h^{-1}. $NiMg_5Al_2O_9$ has been reported to perform, after an induction time, at thermodynamical equilibrium for 10 days without any indication of coke formation[314]. Recently, Yoon et al. have reported a high performance in mixed-steam CO_2 reforming of Ni over $MgAl_2O_4$ based on hydrotalcite-like precursors[215;222;223], and promotion through CeO_2-ZrO_2 has been further investigated by Jun et al.[224;225]. They patented this catalytic system[226] for reaction temperatures between 1073-1273 K (800-1000°C), at 0.5 and up to 20 bar, with a $CH_4/H_2O/CO_2$ ratio in the range of 1/1-2/0.3-0.6 and a space velocity from 1000 up to 500000 h^{-1}.

The final catalysts obtained are generally Ni supported on $MgAl_2O_4$ with a possible side phase of Al_2O_3 or MgO. Wei and Iglesia[107] have studied the mechanism of methane reforming in the presence of H_2O and CO_2 on Ni/MgO. It is reported that the C-H bond breaking of methane is the rate-determining step[10]. The general mechanism of reforming over such Ni-based catalyst is identical as the mechanism described in section 1.4 in part II.

2 Design of procedures for the synthesis of Ni-based spinel catalysts

In this chapter, the synthesis of the Ni-based spinel $Ni_{14}Mg_{29}Al_{57}O_x$ is performed with different methods. A new unconventional route, molten-salt impregnation, is tested and compared with other classical preparation routes such as precipitation and spray drying. The stoichiometry is chosen in such a way that a final catalyst made of $Ni/MgAl_2O_4$ is obtained.

2.1 New unconventional catalyst preparation (benchmark catalyst)

A synthesis based on the impregnation of an hydrotalcite-like carrier material in a molten nitrate salt is tested for the preparation of $Ni_{14}Mg_{29}Al_{57}O_x$. In order to achieve the Mg/Al ratio of 1/2, the hydrotalcite-like carrier PURAL® MG30 from Sasol is selected. PURAL® MG30 contains the hydrotalcite material but also a significant amount of pseudoboehmite due to the high aluminum content[340] of PURAL® MG30. The pseudoboehmite has also a layered structure, as can be seen in Fig. 2.1, with an interlayer containing hydroxide groups.

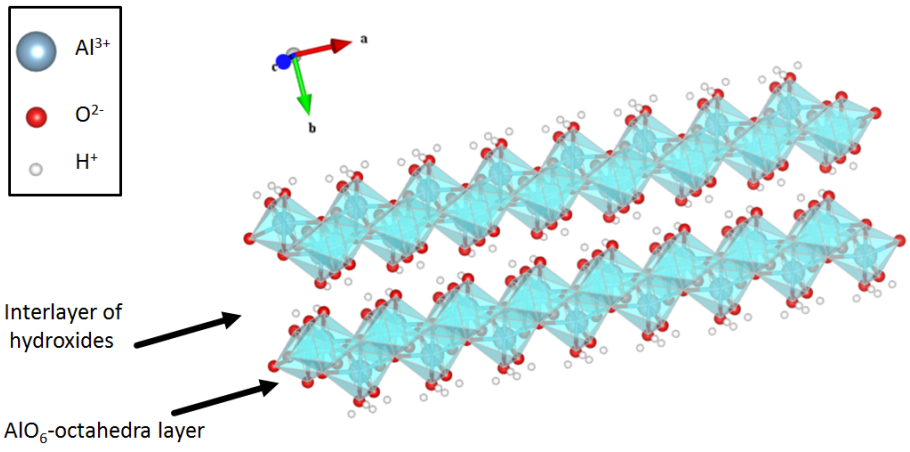

Figure 2.1: Layered structure of pseudoboehmite γ-AlO(OH), drawn with the Vesta software[298]

The synthesis through the molten-salt impregnation consists of spreading molten Ni nitrate hexahydrate over the PURAL® MG30 carrier. For this, the desired amount of Ni nitrate hexahydrate is stirred manually at room temperature in a beaker containing the PURAL® MG30 carrier and left in a drying oven at 393 K (120°C) covered with a watch glass to avoid water evaporation and recrystallization of the sample

at room temperature. The beaker content is homogenized at 393 K (120°C). Both of these operations are repeated until a high dispersion is reached. The precursor is then carefully precalcined in a rotary flask up to 698 K (425°C) for 4 h to slowly eliminate water, nitrates, and carbonates. An amount of 5 wt.% of graphite is added as lubricant to the precalcined precursor, which is then shaped into tablets of 13 mm diameter and a height of 5 mm by applying an axial force of 30 kN. The resulting tablets are then crushed to obtain the desired split of 500-1000 µm, which is then calcined by heating at a ramp of 5 K.min^{-1} up to 1223 K (950°C) for 4 h in synthetic air.

2.2 Other preparation methods used for Ni-based spinels ($Ni_{14}Mg_{29}Al_{57}O_x$)

In order to benchmark the preparation of the catalyst prepared by molten-salt impregnation, other synthesis methods are used to prepare catalysts with the same stoichiometry ($Ni_{14}Mg_{29}Al_{57}O_x$), but the precalcination, shaping, crushing, and final calcination are kept identical, if possible, as it can be seen in Tab. 2.1.

Short name	Carrier precursor	Addition of nit. hex.	Preparation method	Shaping
MSI	Pural MG30	Ni	Molten-salt impregnation	13 x 5mm tablets
PRC	Al nit. hex.	Ni+Mg	Precipitation	Compactor
SD	Pural MG30	Ni	Spray drying	13 x 5mm tablets

Table 2.1: Overview of the all prepared Ni-based spinels with $Ni_{14}Mg_{29}Al_{57}O_x$ stoichiometry calcined at 1223 K (950°C); nit. hex., nitrate hexahydrate

The synthesis method used for precipitation and spray drying is detailed below:

- The sample "PRC" is synthesized by coprecipitation. The desired amount of nitrate salts is dissolved in deionized water to obtain an ionic solution containing 1 mol.l^{-1} of Mg^{2+}, Al^{3+}, or Ni^{2+}; a sodium carbonate solution of 1 mol.l^{-1} is also prepared, which serves as the precipitating agent. Both vessels are heated at 343 K (70°C) under vigorous stirring. When the temperature is reached in both vessels, 840 ml of nitrate solution is added dropwise to the carbonate solution over the course of 30 min at 343 K (70°C) under vigorous stirring until the pH value reaches 8.5. After 1 h of passing an air stream through the suspension, the precipitate is filtered and washed with deionized water to eliminate the excess of nitrate.

  The solid is harvested and redispersed in water to reach a solid content of 5 wt.%. This solution is sprayed with a flow of 18 ml.min^{-1} at 623 K (350°C) using a nozzle of 1 mm diameter with an air scale division of 40% from the top to the lower part of the spray tower. The primary pressure of air to spray the slurry is about 2 bar. The catalyst powder is obtained at the bottom of the tower before the exhaust.

  After precalcination, the catalyst precursor undergoes shaping between corrugated cylinders pressed

at 200 bar (compactor) four times before sieving and final calcination as described for the molten-salt impregnation.

- The sample "SD" is prepared by spray drying. For this, a slurry made of the hydrotalcite-like carrier PURAL® MG30 from Sasol with Ni nitrate hexahydrate is prepared. Ni nitrate hexahydrate is dissolved in water, and the carrier powder is added under vigorous stirring to reach a solid content of about 20 wt.%. Spray drying is then performed with a flow rate of 22 ml.min^{-1} at 623 K (350°C); two samples harvested at the bottom of the tower before the exhaust are analyzed by XRF before mixing. The dried precursor is precalcined, shaped, crushed, and calcined in synthetic air with a ramp of 5 K.min^{-1} at 1223 K (950°C) for 4 h.

2.3 Characterization of the Ni-based spinels

As standard measurements, all catalysts are analyzed with XRD and N_2 physisorption. Furthermore, the spent catalysts are further characterized after testing with XRD.

All catalysts are characterized by XRD using Cu $K_{\alpha 1}$ (λ=1.5405980 Å) at 40 mA and 40 kV with a diffractometer D8-Discover (Bruker AXS). The patterns are obtained with an angular position from 16.3 up to 53.5° and a precision of 0.02°. The Match! software (Crystal Impact) is used for phase identification based on the International Center for Diffraction Data and the RIR method.
Furthermore, elemental-composition determination is achieved by performing XRF on dried samples obtained from spray drying with an Eagle III spectrometer (Röntgenanalytik Messtechnik GmbH) equipped with a Rh anode. The spectrometer operates under vacuum at 25 kV and 500 µA.

Determination of the specific surface area of catalyst samples is achieved with N_2 physisorption and the BET method. First, samples are preconditioned at 573 K (300°C) for 1 h in nitrogen flow prior to analysis. Sample-specific surface areas are then determined on the basis of a five-point adsorption isotherm by the BET-method using a TriStar II (Micromeritics).

The benchmark catalyst prepared by molten-salt impregnation is selected for further investigations with TPR, mercury porosimetry, and electron microscopy.

The mercury-porosimetry measurements are executed in collaboration with BASF SE in Ludwigshafen. A sample of about 0.5 g is analyzed by AutoPore IV 9500 (Micromeritics) that is able to characterize pores from 0.0030 up to 300 µm. To remove potentially physisorbed gases, the sample is set under vacuum (70 mm Hg) for 20 min. Thanks to the Washburn equation, the pore-size distribution is then evaluated based on the measurement of the mercury uptake as a function of the pressure.

TPR is performed at BASF with AutoChem II 2920 (Micromeritics) equipped with a Thermal Conductivity Detector (TCD). A flow of 50 sccm (under standard temperature and pressure) of forming gas (5 vol.% H_2 in N_2) is used on about 200 mg of catalyst sample, which is heated to 1173 K (900°C) at a ramp of 5 K.min^{-1}. The results are plotted as response of TCD signal against temperature; peaks are observed at the characteristic reduction temperatures.

SEM measurements are performed in collaboration with BASF. SEM images are recorded at 20 kV from back scattered electrons. In addition, energy-dispersive X-ray spectroscopy at 20 kV is used for element mapping.

2.4 Preformation study of the Ni-based spinel catalyst prepared by molten-salt impregnation

In order to understand the reduction mechanism of the material under investigation, the benchmark catalyst sample is further investigated in a preformation study. The samples are reduced separately in a special unit (Fig. 2.2). This unit features 4-fold reactors made of quartz glass that are fed with a feed of the same composition, but since every reactor is heated by a separate furnace, the temperature can be varied from sample to sample.

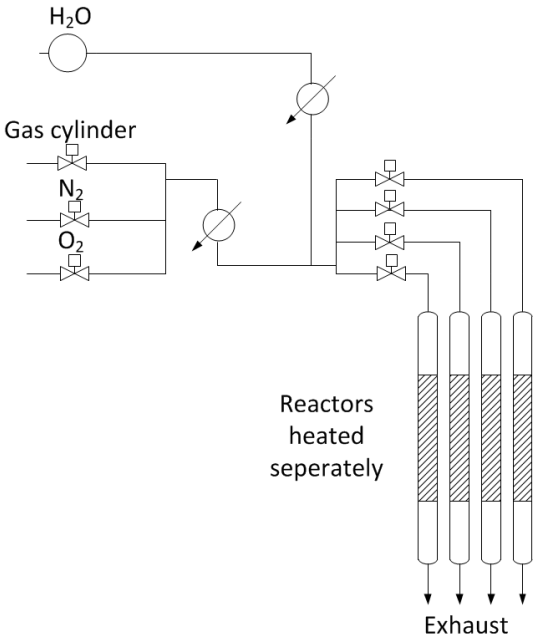

Figure 2.2: Four-fold unit used for the preformation study

Various parameter influences have been studied, such as preformation temperature, hold time, and gas atmosphere, that include the addition of steam and CO_2 to the initial forming gas. The overview of the

34 preformed samples is presented in Tab. 2.2. The heating ramp for this experiment design is fixed at 5 K.min^{-1}.

Set temperatures [K] ([°C])	Hold time [h]	Catalyst volume [ml]	Gas atmosphere [vol.%]
673, 873, 903, 943, 973, 1023, 1073, 1173 (400, 600, 630, 670, 700, 750, 800, 900)	4	6.5	F.G.5
1173 (900)	165	6.5	F.G.5
673, 873, 903, 943, 973, 1023, 1073, 1173 (400, 600, 630, 670, 700, 750, 800, 900)	4	6.5	F.G.5+10% H_2O
1173 (900)	165	6.5	F.G.5+10% H_2O
673, 873, 903, 943, 973, 1023, 1073, 1173 (400, 600, 630, 670, 700, 750, 800, 900)	4	6.5	F.G.5+10% CO_2
673, 873, 903, 943, 973, 1023, 1073, 1173 (400, 600, 630, 670, 700, 750, 800, 900)	4	6.5	F.G.5+10% H_2O+5% CO_2

Table 2.2: Design of experiments of preformation conditions used on the benchmark Ni-based spinel catalyst. F.G.5; forming gas with 5 vol.% H_2 in 95 vol.% N_2

About 5 g (6.5 ml) of calcined sample is loaded in each reactor. The reactors are set under the desired gas atmosphere with a flow of 150 sccm per reactor. The reactors are then heated up to the set temperature at 5 K.min^{-1}. At the end of the reduction, the reactor is cooled down under N_2 and the samples are passivated by stepwise substitution of N_2 with synthetic air.
The samples are then analyzed by means of X-ray diffraction and N_2 physisorption; in addition, their loose bulk density is measured with the aid of a scales and a measuring cylinder.

2.5 Test protocol for the catalyst screening

The reactor configuration used for the molten-salt impregnation (MSI) benchmark catalyst test corresponds to the configuration (d) of section 2.1 in part IV, in which 20 ml of 500-1000 µm split catalyst is tested in the isothermal zone with a prebed of corundum. The benchmark catalyst is tested in the screening unit.

Following the investigation of the gas-phase reactions, the H_2 test protocol has been chosen because of its stability. The test protocol is slightly adapted from the H_2 test protocol of the gas-phase reaction investigations and described in Tab. 2.3.

The test is repeated in the screening unit with the precipitated catalyst; however, the corundum prebed is

omitted and only 20 ml of catalyst is tested with an empty prebed. Unfortunately, the catalyst prepared by spray drying has not been tested yet.

Phase	Temperature [K] ([°C])	CH_4 [vol.%]	CO_2 [vol.%]	H_2O [vol.%]	H_2 [vol.%]	Ar [vol.%]
1	1123 (850)	47.5	-	47.5	-	5
2	1123 (850)	26.0	29.0	40	-	5
3	1123 (850)	26.0	29.0	-	40	5
4	1123 (850)	30.8	34.2	-	30	5
5	1223 (950)	30.8	34.2	-	30	5
6	1223 (950)	35.5	39.5	-	20	5
7	1223 (950)	40.3	44.7	-	10	5
8	1223 (950)	40.3	44.7	5	5	5
9	1223 (950)	40.3	44.7	10	-	5

Table 2.3: Feed composition and reactor temperature for the H_2 test protocol performed at 21 bar with a CH_4/CO_2 ratio of 0.9

The catalysts are "preformed" at 723 K (450°C) for 10 h before the unit is started as in the Pt-based catalyst section 2.1.3 in part V under steam reforming. After stabilization of the catalytic activity, CO_2 is then used in the feed stream with a CH_4/CO_2 ratio of 0.9 and 40 vol.% H_2O (phase 2) before substitution of H_2O with H_2 (phase 3). H_2 is then substituted with CO_2 and CH_4 simultaneously while keeping the CH_4/CO_2 ratio of 0.9. At phase 5, the temperature is increased to the limit of coke deposition and at phase 8 and 9 H_2 is replaced with H_2O stepwise. However, "pure" CO_2 reforming with even severer operating conditions than phase 9 is not especially attractive since about 10 vol.% H_2O are expected at thermodynamic equilibrium in CO_2 reforming anyway. Therefore, addition of 10 vol.% H_2O directly to the feed stream is used to make the operating conditions slightly milder for the desired target reaction.
Each phase is tested at least 30 h until the catalytic activity is stable.
The comparison of H_2 and H_2O test protocols is performed on the benchmark catalyst at 1123 K (850°C) with the same GHSV and pressure. The adapted H_2O test protocol used is given in Tab. 2.4. In this protocol, the temperature is maintained at 1123 K (850°C) to minimize the effect of gas-phase reactions.

Phase	Temperature [K] ([°C])	CH_4 [vol.%]	CO_2 [vol.%]	H_2O [vol.%]	H_2 [vol.%]	Ar [vol.%]
1	1123 (850)	47.5	-	47.5	-	5
2	1123 (850)	26.0	29.0	40	-	5
3	1123 (850)	26.0	29.0	-	40	5
4	1123 (850)	30.8	34.2	-	30	5
5	1123 (850)	35.5	39.5	-	20	5

Table 2.4: Feed composition and reactor temperature for the adapted H_2O test protocol at 1123 K (850°C) and 21 bar with a CH_4/CO_2 ratio of 0.9

Finally, 78 ml of the MSI benchmark catalyst are tested in the reactor with the same usual conditions (no GHSV adaption, same molar flow rate); the H_2O test protocol given in Tab. 2.4 performed at 1173 K

(900°C) to maximize activity.

3 Results of Ni-based spinel catalysts

The catalysts are synthesized and systematically analyzed by means of XRD and N_2 physisorption prior to testing. The benchmark MSI catalyst is chosen for further analysis like SEM, mercury porosimetry, and TPR. The preformation study is conducted on the MSI catalyst and interpreted by using XRD, specific surface area, and LBD. The catalytic tests are conducted with the H_2 test protocol on the MSI and PRC Ni-based spinels synthesized, whereas the SD catalysts synthesized by new routes has not been tested yet. Finally, the H_2O test protocol is used to test the MSI catalyst in two different configurations to fulfill industrially relevant conditions, with 20 ml of catalyst without prebed and 78 ml of catalyst including a catalyst prebed. The traces of product from methane pyrolysis and coupling are also analyzed to interpret the impact of the gas-phase reactions.

3.1 Characterization results of the freshly prepared Ni-based spinels

3.1.1 Ni-based spinel prepared by MSI

After synthesis, the benchmark catalyst is characterized by XRD and N_2 physisorption; in addition, the loose bulk density (LBD) is calculated prior to reactor filling. These results are presented in Tab. 3.1.

Short name	Ni [mol.%]	Mg [mol.%]	Al [mol.%]	Crystallographic phases	Specific surface area [$m^2.g^{-1}$]	LBD [$g.ml^{-1}$]
MSI	14	29	57	$Ni_{0.5}Mg_{0.5}O$+$(Ni/Mg)Al_2O_4$	42.4	0.771

Table 3.1: X-ray diffraction and N_2-physisorption results as well as LBD for the benchmark Ni-based spinel (MSI) as 500-1000 µm split after calcination in air at 1223 K (950°C)

The mixed oxides of $Ni_{0.5}Mg_{0.5}O$ and $(Ni/Mg)Al_2O_4$ are identified as the main phases of the benchmark catalyst (Fig. 3.1). A specific surface area of 42.4 $m^2.g^{-1}$ as well as a light LBD are obtained after calcination at 1223 K (950°C).

Ni^{2+} and Mg^{2+}, with a similar ionic radius and the same crystal structure of spinel ($Fd\bar{3}m$) and of MgO/NiO ($Fm\bar{3}m$), can form mixed oxides, as it has already been observed with $(Mg/Ni)O$[341] and $(Ni/Mg)Al_2O_4$[339;342].

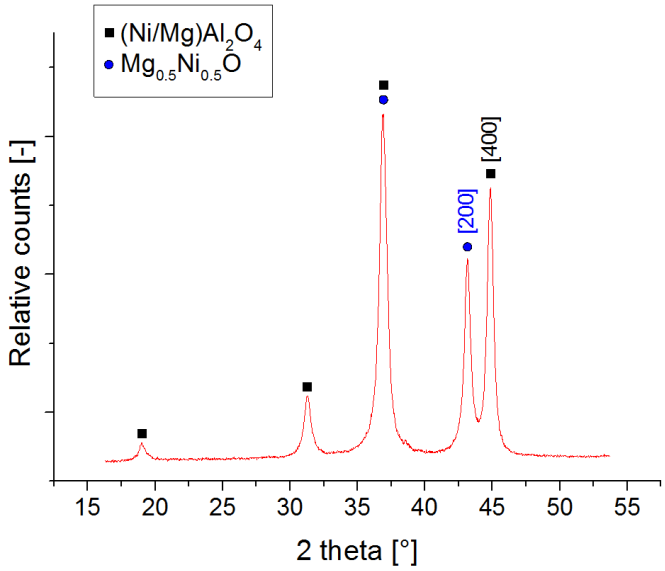

Figure 3.1: Diffractogram of MSI benchmark Ni-based spinel catalyst ($Ni_{14}Mg_{29}Al_{57}O_x$) after calcination at 1223 K (950°C) in air

The mixed oxides observed in the Fig. 3.2 are highlighted by the 2θ values, which are located between the reflexes of the pure NiO and MgO or $NiAl_2O_4$ and $MgAl_2O_4$. Indeed, as the Ni content increases with respect to Mg content in the mixed oxide, the (200) reflex of (Mg/Ni)O and the (400) reflex of spinel shift to larger 2θ angles. This is due to the substitution of Mg^{2+} with Ni^{2+} within the MgO lattice. Because Ni^{2+} is smaller than Mg^{2+}, the cubic lattice shrinks and the reflexes shift to larger 2θ angles. The same effect can be observed with substitution of Mg^{2+} with Ni^{2+} in the $MgAl_2O_4$ lattice.

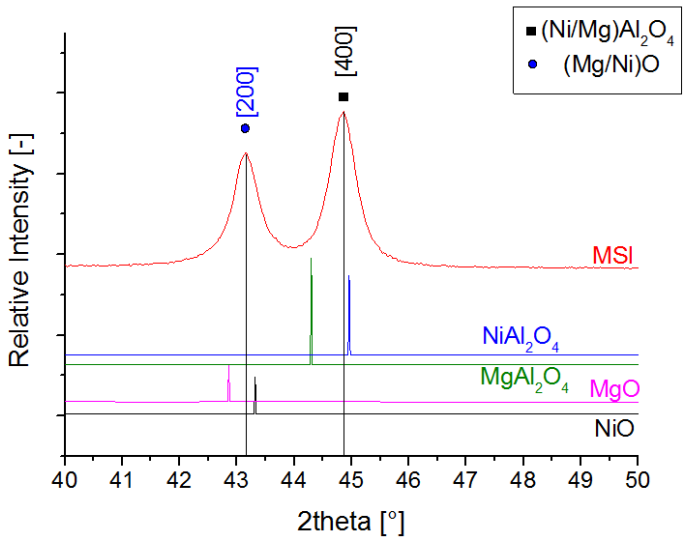

Figure 3.2: Highlight of reflex shifts in XRD pattern from MSI due to the formation of mixed oxides with a zoom on the reflexes (200) of (Mg/Ni)O mixed oxide and (400) of $(Mg/Ni)Al_2O_4$ mixed oxide and comparison with simulated XRD patterns of $NiAl_2O_4$, $MgAl_2O_4$, NiO, and MgO

Because metallic Ni is the active metal in reforming, TPR analysis shows, which temperature is required

to obtain Ni^0 from Ni^{2+}. Fig. 3.3 shows a single large peak at 1026 K (753°C) characteristic of Ni^{2+} reduction in (Ni/Mg)O [341] but possibly also of (Ni/Mg)Al_2O_4 [330]. Coleman et al. [330] reduced a (Mg/Ni)O mixed oxide at 1063 K (790°C) and $NiAl_2O_4$ at 1123 K (850°C). These samples have been prepared in two steps: first the coprecipitation of Mg and Al nitrate salts with sodium carbonate; after calcination at 1123 K (850°C), these supports are impregnated with Ni nitrates in deionized water with subsequent calcination at 1123 K (850°C) in air for 5 h [330]. The higher temperature observed by Coleman et al. [330] may result from a higher heating rate (10 K.min^{-1} instead of 5 K.min^{-1}).

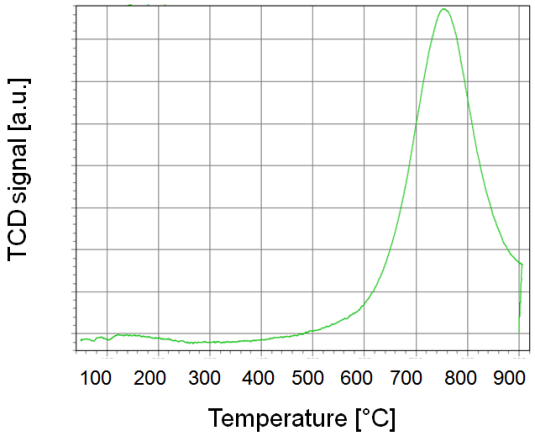

Figure 3.3: Curve representing the consumption of H_2 in temperature-programmed reduction of benchmark catalyst (MSI)

Of major interest for the improvement of mass transfer is the size of macro- and mesopores. These are characterized by mercury porosimetry, and the results are shown in Fig. 3.4. A bimodal pore distribution with large (>100 µm) and small pores (1-0.01 µm) is identified, yielding a pore volume of 0.8 ml.g^{-1}.

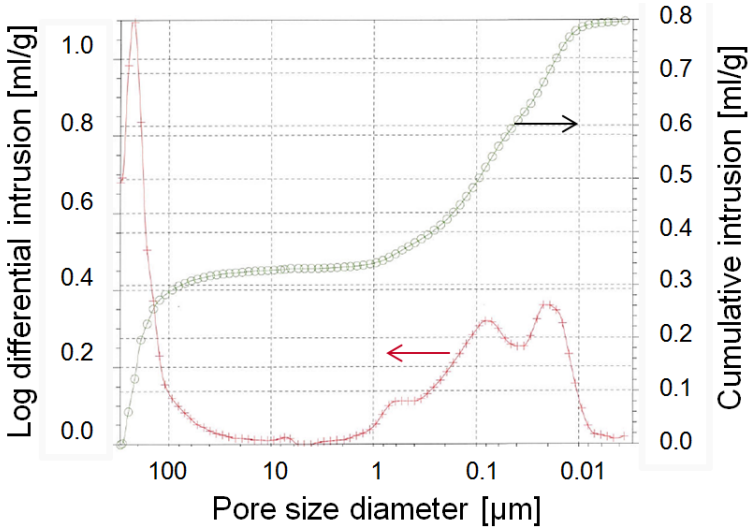

Figure 3.4: Pore distribution of benchmark catalyst (MSI) after calcination at 1223 K (950°C) obtained by mercury porosimetry

The SEM investigation on the final catalyst (Fig. 3.5) shows a variation of composition within the catalyst grains (dark/bright spots).

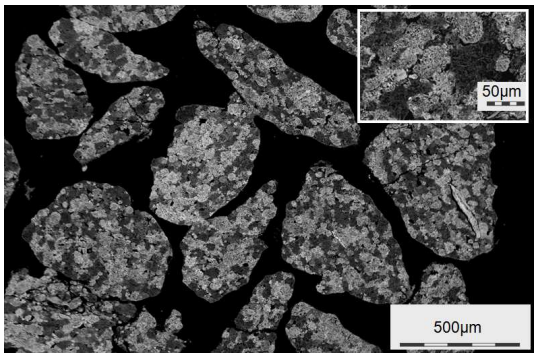

Figure 3.5: SEM imaging of benchmark catalyst (MSI) showing the relative inhomogeneity

Analysis of the composition of one region is conducted on one grain (Fig. 3.6). Element mapping allows to identify bright spots as Ni-rich as well as Mg- and Al-poor spots and the other way around for dark spots in the SEM images. The molten-salt impregnation does not achieve a very high Ni dispersion compared to Al or Mg distribution over the catalyst grain.

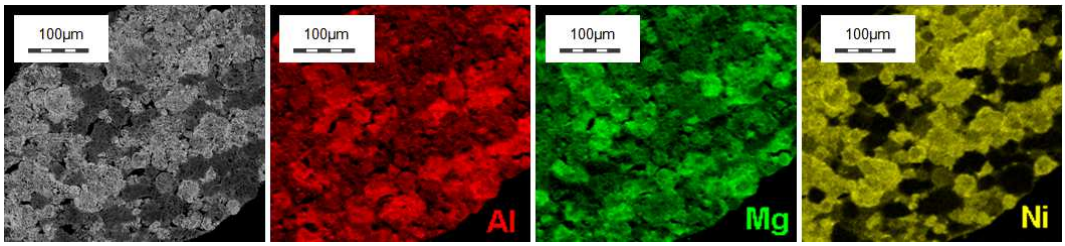

Figure 3.6: SEM imaging of benchmark catalyst (MSI) showing elemental mapping of Mg, Ni, and Al on the original image (left side)

3.1.2 Other preparation routes for the Ni-based spinel catalysts

In order to benchmark the catalyst prepared by molten-salt impregnation, other classical synthesis routes are investigated, such as precipitation and spray drying.

The results of analysis after calcination at 1223 K (950°C) are given in Tab. 3.2. The phases observed in the XRD patterns are comparable to the mixed oxides obtained for the MSI catalyst, except for the sample prepared by precipitation that shows traces of precipitating agent (sodium), while the presence of Si could be a result of the high basicity of the Na_2CO_3 solution that dissolved Si from the beaker glass. The alternative preparation routes chosen to benchmark our previous catalyst results in lower specific surface areas especially when the hydrotalcite-like carrier is not used like in precipitation. The specific surface area of the benchmark catalyst is four times larger than after precipitation and 50% larger than for the sample prepared by spray drying.

The lower specific surface area and higher LBD of PRC compared with MSI catalyst are probably due to the difference in shaping: the compactor uses higher pressures than the tablet machine; therefore, the specific surface area and the LBD are likely to be lower in the PRC case. The SD catalyst has probably a specific surface area lower than that of the MSI catalyst because of the long thermal treatment in the spray tower.

Short name	Ni [mol.%]	Mg [mol.%]	Al [mol.%]	Crystallographic phases	Specific surface area [$m^2.g^{-1}$]	LBD [$g.ml^{-1}$]
MSI	14	29	57	(Ni/Mg)O+(Ni/Mg)Al_2O_4	44.4	0.771
PRC	14	29	57	Ni/Mg)O+(Ni/Mg)Al_2O_4 +$Mg_{0.9}Si_{1.1}Na_{1.8}O_4$	11.4	1.060
SD	14	29	57	(Ni/Mg)O+(Ni/Mg)Al_2O_4	30.3	-

Table 3.2: Comparison of X-ray diffraction and N_2-physisorption results as well as loose bulk density (LBD) of newly synthesized Ni-based spinel catalyst as 500-1000 µm split

Details of the XRD patterns are presented in Fig. 3.7. Apart from the presence of impurities in PRC, the phase composition of PRC and SD appears to be close to the MSI-catalyst phase composition.

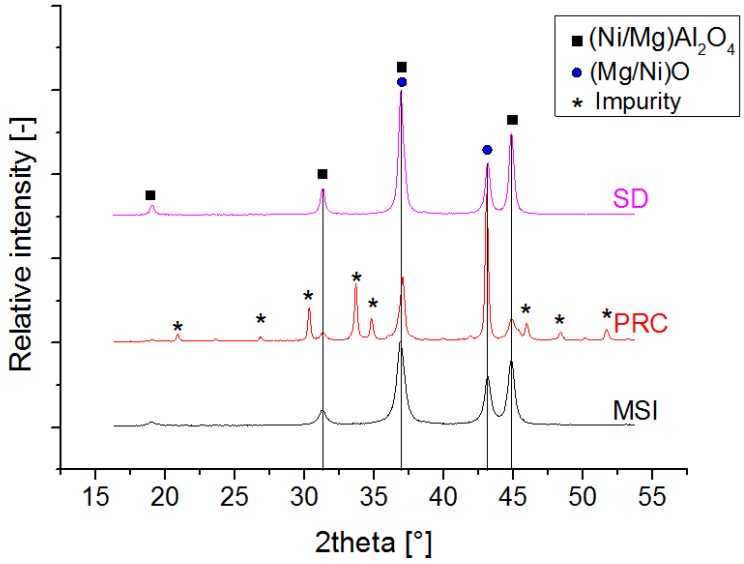

Figure 3.7: Comparison of XRD patterns of the three Ni-based spinel catalysts with the various synthesis routes (MSI, PRC, SD)

The particle size resulting from these new preparation routes is displayed in Tab. 3.3. The precipitation route as well as the spray drying route with PURAL® MG30 lead to a 50% larger particle size than observed for the benchmark catalyst. It can be concluded that the homogeneity of the benchmark catalyst is probably higher.

In order to obtain a highly homogeneous catalyst precursor, the spray-dried samples obtained in the

Short name	Ni [mol.%]	Mg [mol.%]	Al [mol.%]	Particle size (Ni/Mg)O [nm]	Particle size (Ni/Mg)Al_2O_4 [nm]
MSI	14	29	57	20	18
PRC	14	29	57	40	24
SD	14	29	57	30	30

Table 3.3: Comparison of crystallite size of (Ni/Mg)O and (Ni/Mg)Al_2O_4 calculated with the Scherrer equation for all preparation routes

tower and before exhaust should have a similar composition. For this reason, XRF-analysis is performed on these both samples. The XRF-device delivers "uncalibrated" values for Ni, Mg, and Al and can be compared with the values of the benchmark catalyst after calcination at 1223 K (950°C), see Tab. 3.4 as reference.

Short name	Position	Ni [wt.%]	Mg [wt.%]	Al [wt.%]
MSI	Reference	28	39	33
SD	Tower	31	50	18
	Exhaust	23	26	51

Table 3.4: Comparison of XRF analysis on both samples obtained after spray drying with the various carriers. Molten-salt-impregnation Ni-based spinel catalyst after calcination at 1223 K (950°C) is used as reference.

Both samples are clearly different, one Al-rich, the other Mg-rich.
Using PURAL® MG30 with the spray drying preparation route appears to result in the segregation of hydrotalcite (Mg/Al=3/1) and boehmite. Both of these samples can be mixed to synthesize the SD catalyst; however, the XRD pattern of the final catalyst shows that the resulting crystallites of (Ni/Mg)O and (Ni/Mg)Al_2O_4 are about 50% larger than for the MSI catalyst (Tab. 3.3).

3.2 Preformation study of MSI catalyst

The preformation of the MSI catalyst studied with various gas atmospheres are found to be relatively similar to the preformation with forming gas 5 (5 vol.% H_2 in N_2) (Fig 3.8). Metallic Ni is identified at about 943 K (670°C) in the XRD patterns. During preformation, the (Ni/Mg)O and (Ni/Mg)Al_2O_4 reflexes are shifted because Ni^{2+} leaves the (Ni/Mg)O and (Mg/Ni)Al_2O_4 lattices. TPR (Fig. 3.3) has shown that the reduction starts already at 873 K (600°C); however, Ni^0 is detected at higher temperatures by XRD because very thin particles of Ni^0 are not identifiable. As the temperature of preformation increases MgO phase content decreases. Indeed, the reduced Ni located in $NiAl_2O_4$ leaves free γ-alumina, but this phase cannot be identified because MgO and γ-alumina react together to form further $MgAl_2O_4$. The PURAL MG30 carrier contains a Mg/Al ratio of 1/2, which corresponds to the $MgAl_2O_4$ stoichiometry. A light excess of Mg is found in the initial stoichiometry of the carrier explaining why MgO traces remain after preformation. Above 1073 K (800°C), no further change in phase content is observed on the preformed catalyst, which contains Ni over $MgAl_2O_4$ with traces of MgO.

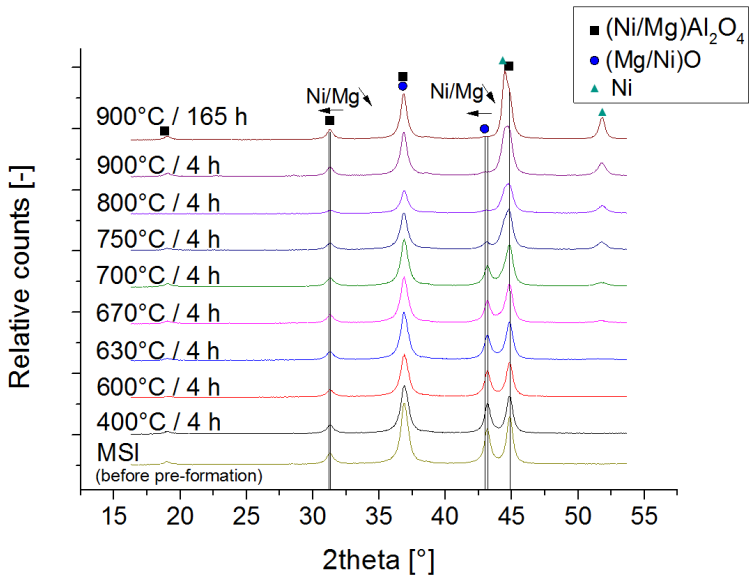

Figure 3.8: XRD patterns of preformed samples under forming gas 5 (5 vol.% H_2 and 95 vol.%N_2) from 673 up to 1173 K (400 up to 900°C) are compared to the benchmark catalyst (MSI) before preformation.

A change in color is observed as the samples are reduced. Indeed, the samples are green prior to testing due to the presence of NiO and $NiAl_2O_4$. As Ni^{2+} is reduced to metallic Ni^0, the color turns first grey and then black, the color of Ni^0. $MgAl_2O_4$ is white and, therefore, does not interfere with the color change.

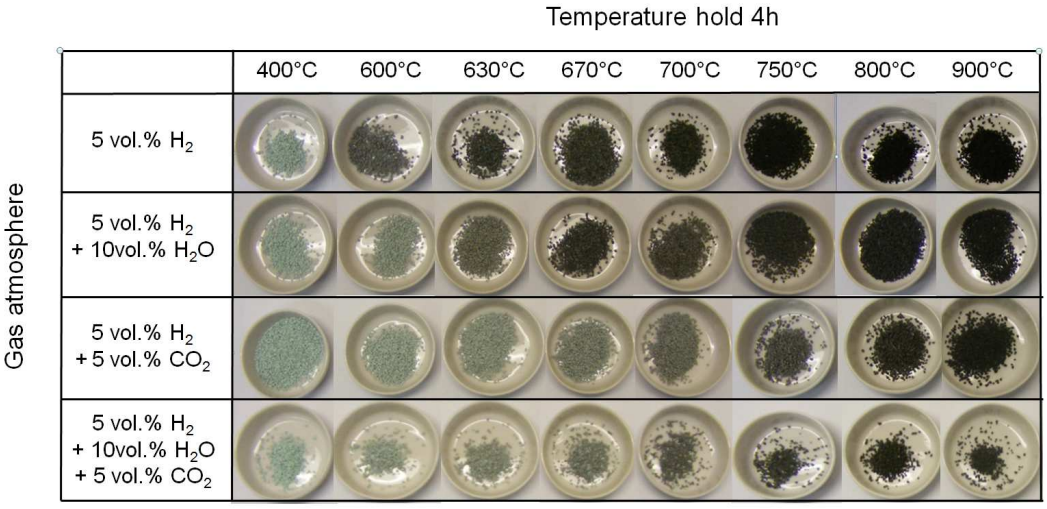

Figure 3.9: Pictures showing the color change of the preformed samples for the four different preformation programs from 673 up to 1173 K (400 up to 900°C)

The pictures of the 32 samples preformed for 4 h are shown in Fig. 3.9. The initial color of preformed catalyst is present up to 673 K (400°C). Differences appear at 873 K (600°C) with changes in sample color even if XRD patterns cannot confirm the presence of metallic Ni. Ni^{2+} reduction starts at around

this temperature according to TPR analysis (Fig. 3.3). Further changes in color are not observed above 1023 K (750°C); however, traces of MgO still react with Al_2O_3 to $MgAl_2O_4$. The color change can be used as a characteristic for the identification of metallic Ni, proving that reduction occurs.

The addition of steam at the preformation step leads to an increase in the induction time of Ni^{2+} reduction; CO_2 addition also increases the induction time but to a larger extent.

The XRD patterns of all samples are used for the calculation of particle size by the Scherrer formula. The results are shown in Fig. 3.10. The particle size of $(Mg/Ni)Al_2O_4$ and (Mg/Ni)O is relatively constant; only at 1173 K (900°C) a discernible increase in particle size of spinel is seen. Regarding the particle size of metallic Ni, a higher preformation temperature leads to a significant increase of particle size especially if steam is used. The preformation only with H_2 is optimal to avoid sintering of Ni nanoparticles.

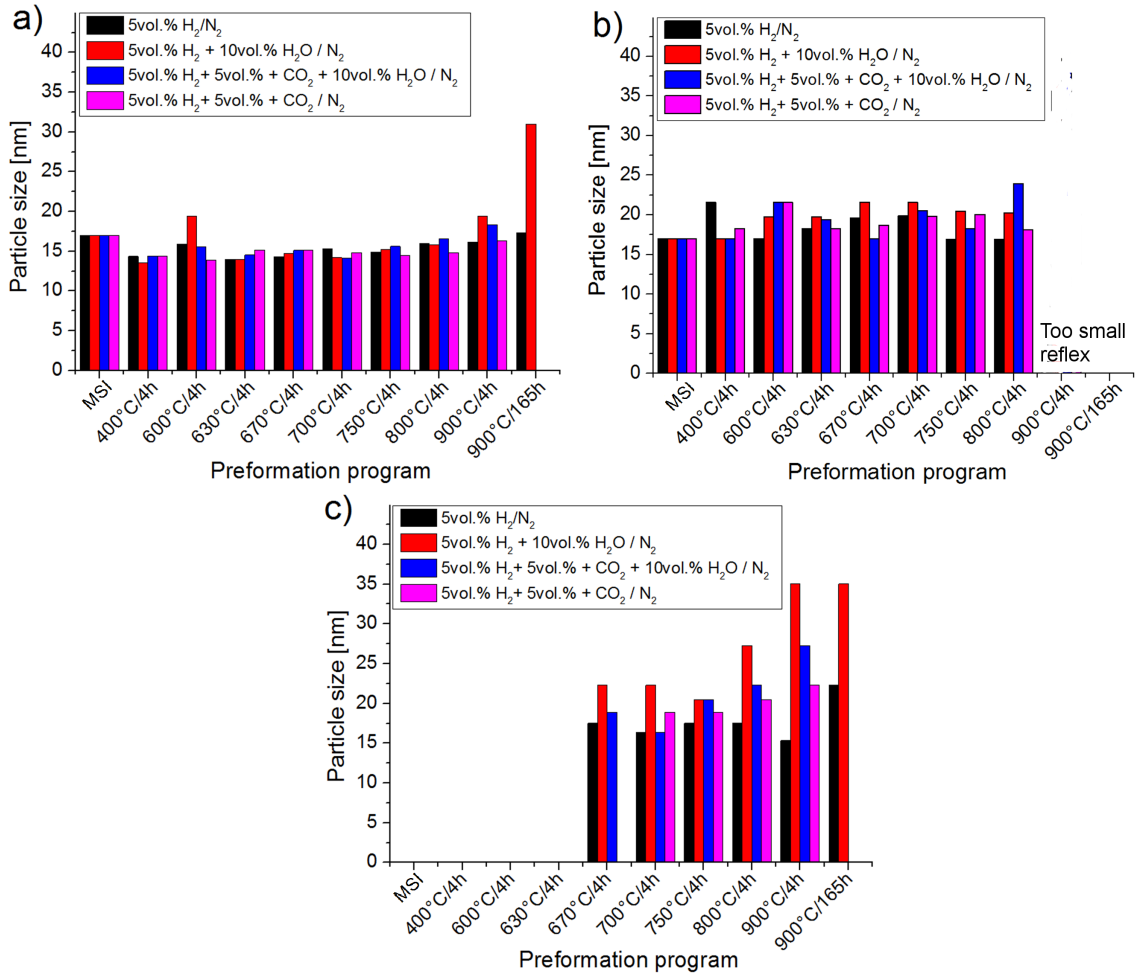

Figure 3.10: Comparison of particle size of a) $(Ni/Mg)Al_2O_4$, b) (Ni/Mg)O, and c) Ni^0 calculated with Scherrer formula for the MSI catalyst preformed at temperatures up to 1173 K (900°C) compared with the MSI catalyst after calcination

The specific surface areas and LBD are measured and plotted in Fig. 3.11. The specific surface areas

decrease with higher temperature of about 10% while longer preformation in the presence of steam promotes sintering and loss of specific surface area[36;132]. The loss of specific surface area starts at 1023 K (750°C) and could be limited by the use of H_2 only.
A change in LBD is not observed because the "signal-to-noise" ratio is too high to perceive a trend.

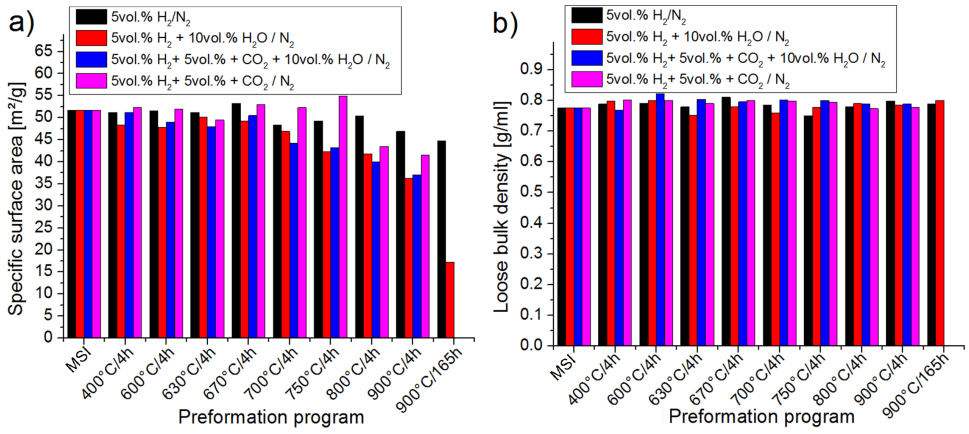

Figure 3.11: Comparison of a) specific surface areas and b) loose bulk densities (LBD) for the MSI catalyst preformed up to 1173 K (900°C) compared with the MSI catalyst after calcination

The preformation of the benchmark catalyst is well understood. Using a high preformation temperature leads to a faster reduction of Ni^{2+} and formation of more spinel-phase content. The preformation step should ideally be achieved only under H_2 in N_2. Nevertheless, the catalyst has to resist to steam and CO_2 partial pressure present in the catalytic bed during reforming operations. In this case, sintering of Ni^0 nanoparticles and a much slower preformation process can be expected. From this point of view, only catalytic tests can reveal, if the Ni nanoparticle generation and their stabilization is sufficient to achieve high activity and stability over a long period of time.

3.3 Performance overview of Ni-based spinel catalysts

The catalysts prepared by molten-salt impregnation (MSI) and precipitation (PRC) are tested with the H_2 test protocol and their test performances are compared (Tab. 3.5). The 20 ml of MSI catalyst is tested with a corundum prebed while the 20 ml of PRC catalyst is tested without the corundum prebed.

The two catalysts showed similar performance during the two first phases of the test protocol in the presence of water. Both catalysts show that they can almost achieve thermodynamic equilibrium for the first two phases. However, after switching from H_2O to H_2 the catalytic activity and the catalyst performances are different. The MSI catalyst shows high methane activity whereas the PRC catalyst shows only poor methane activation before the reactor was plugged probably due to the syngas being very CO rich (H_2/CO ratio of 0.6) and the high pressure. Finally, after substitution of H_2 by H_2O, the MSI catalyst achieves almost the thermodynamic reforming equilibrium under CO_2 reforming with CH_4/CO_2=0.9 and

#	Catalyst			Steam Ref.	Ref. with 40vol. % H_2O	Ref. with 40vol.% H_2	Ref. with 30vol.% H_2	Ref. with 30vol. % H_2	Ref. with 20vol.% H_2	Ref. with 10vol.% H_2	Ref. with 5vol.% H_2O + 5vol.% H_2O	Ref. with 10vol. % H_2O
				850°C				950°C				
		CH_4/CO_2	**Phase**	**1**	**2**	**3**	**4**	**5**	**6**	**7**	**8**	**9 (100h)**
1	MSI with corundum prebed	0.9	X CH_4 X CO_2 H_2/CO	46 - 3.9	66 33 1.6	38.4 73.8 1.47	45.6 73 1.2	67 73 1.0	63 72 1.0	57 67 0.8	67 67 0.8	82 74 0.9
2	PRC without corundum prebed	0.9	X CH_4 X CO_2 H_2/CO	41 - 4.2	70 31 1.6	4 43 1.6	4 22 2.5	29 65 1.2	31 60 0.9	33 52 0.6		
-	Thermodynamic Equilibrium	0.9	X CH_4 X CO_2 H_2/CO	53.0 - 3,83	80 37.9 1.55	38.4 73.8 1.47	45.6 73.0 1.16	71 86 1.24	74.9 85.6 1.04	78.0 85.2 0.89	81.9 82.1 0.91	85.2 78.7 0.91

Table 3.5: Test performances of the Ni-based spinels prepared by MSI and precipitation during the H_2 test protocol at temperatures ranging from 1123 up to 1223 K (850 up to 950°C) compared with the thermodynamic reforming equilibrium. Phases are detailed in section 2.3; Ref., reforming with a CH_4/CO_2 ratio of 0.9. The target reaction is achieved at phase 9 and is tested for 100 h. Green color states that the catalyst exhibits full carbon recovery, orange that the carbon recovery decreases due to coking, and grey that the performances are not tested under the given conditions.

additional 10 vol.% H_2O at 1223 K (950°C), 21 bar, and with a GHSV of 3800 h^{-1}.

The difference observed in performance is probably due to the impact of the gas-phase reactions and particularly the presence of the prebed. Indeed, the presence of the corundum prebed allows to start the CO_2 activation by RWGS with formation of steam that can react directly with methane and, therefore, improves methane activation. The absence of prebed enhances the formation of coke precursors in the gas phase, particularly at 1223 K (950°C). These coke precursors can deposit on the catalyst surface and provoke reactor plugging. Moreover, the absence of a prebed reduces the H_2O formation rate and, therefore, methane is hardly activated in the short catalytic bed due to a short residence time in the catalytic bed.

In addition to the presence of the corundum prebed, the unexpected high stability and activity of the MSI catalyst could be due to the moderate acid-base character of the $MgAl_2O_4$ main phase content in the catalyst[330]. In addition, the large mesopores/macropores observed in Fig. 3.4, but also the low LBD, for the MSI catalyst should also improve mass transfer and, therefore, limit amorphous coke formation and stabilize the Ni nanoparticles[343].

Of particular interest is that the expected H_2/CO ratio of one can be achieved with about 10 vol.% H_2O in CO_2 reforming (phase 9 in Tab. 2.3) but also with 20-30 vol.% H_2 (phases 6 and 7 in Tab. 2.3); however, the operating conditions of phase 6 and 7 are not industrially attractive because pure H_2 is relatively expensive and not always readily available. Moreover, phase 9 offers higher conversions of methane and CO_2. The PRC catalyst achieves also a H_2/CO ratio of one at phase 6, but further testing with higher

severity shows that high activity of RWGS and poor methane activation gives high CO concentrations and thus a very low H_2/CO ratio, synonymous of a higher coking risk by CO disproportionation. Furthermore, coke-precursor analysis, displayed in Tab. 3.6, shows that only ethane and ethylene are identified. During the first two phases with a high steam concentration in the feed stream no coke precursors are observed. Later in the test phases, decreasing the amount of H_2 in the feed stream results in an increase of coke-precursor concentrations. When H_2 is replaced by steam the coke-precursor concentration appears to decrease in the last three phases (7, 8, and 9). In the case of the PRC catalyst, higher coke-precursor concentrations are identified especially prior to and during reactor plugging. Furthermore, after increasing the temperature from 1123 to 1223 K (850 to 950°C), the formation of coke precursors is "eliminated" (phases 4 and 5).

#	Catalyst			Steam Ref.	Ref. with 40vol. % H_2O	Ref. with 40vol.% H_2	Ref. with 30vol.% H_2	Ref. with 30vol. % H_2	Ref. with 20vol.% H_2	Ref. with 10vol.% H_2	Ref. with 5vol.% H_2O + 5vol.% H_2O	Ref. with 10vol. % H_2O
				850°C				950°C				
		CH_4/CO_2	**Phase**	**1**	**2**	**3**	**4**	**5**	**6**	**7**	**8**	**9 (100h)**
			Conc. [ppm]									
1	MSI with corundum prebed	0.9	C_2H_6 C_2H_4 C_2^+	- - -	- - -	- - -	- - -	- - -	- - -	30-100 0-40 -	30-50 - -	- - -
2	PRC without corundum prebed	0.9	C_2H_6 C_2H_4 C_2^+	- - -	- - -	- - -	50-75 - -	- - -	50-100 - -	125-500 0-200 -		

Table 3.6: Comparison of coke precursor concentration measured in product stream for the MSI and PRC catalytic test during the H_2 test protocol for temperatures ranging from 1123 up to 1223 K (850 up to 950°C). Green color states that the catalyst exhibits full carbon recovery, orange that the carbon recovery decreases due to coking, and grey that the performance are not tested under the given conditions.

First, the MSI catalyst shows a very low formation of coke precursors at low concentrations of H_2 that disappear as H_2 is replaced by H_2O because the catalyst is able to convert these coke precursors probably by a faster activation of hydrocarbons by steam, which is already present at the upper end of the reactor. The PRC catalyst and its reactor configuration show higher coke-precursor formation up to reactor plugging, probably because the high concentrations of coke precursors at low H_2 content could not be "handled" by the catalyst on which coke remained. Moreover, the temperature increase from 1123 to 1223 K (850 to 950°C) can suppress the formation of ethane (phases 4 and 5) because it is probably easier to reform than at 1123 K (850°C).

3.3.1 Influence of test protocol on performance of Ni-based spinel catalyst prepared by MSI

The benchmark catalyst is now used for further investigation with the H_2O test protocol. Indeed, reforming with H_2O instead of H_2 is economically more attractive for industrial purposes. The performance

comparison is presented in Tab. 3.7.

#	Catalyst				Steam Ref.	Ref. with 40vol. % H_2O	Ref. with 30vol.% H_2 (1) or H_2O (2)	Ref. with 20vol.% H_2O
					850°C			
		Test protocol	**CH_4/CO_2**	**Phase**	**1**	**2**	**3**	**4 (150h)**
1	MSI with corundum prebed	With H_2	0.9	X CH_4 X CO_2 H_2/CO	46 - 3.9	66 33 1.6	45.6 73 1.2	
2	MSI without corundum prebed	With H_2O	0.9	X CH_4 X CO_2 H_2/CO	52-32 - 3.5-4.4	17-47 38-32 1.1	50-45 38-32 1-1.1	38 35 0.9
-	Thermodynamic Equilibrium	With H_2O	0.9	X CH_4 X CO_2 H_2/CO	53.0 - 3.83	80.0 37.9 1.55	72.8 49.0 1.3	67.6 58.0 1.05

Table 3.7: Comparison of MSI catalyst performance (20ml catalyst) with (1) H_2 test protocol and (2) H_2O test protocol at 1123 K (850°C) with and without prebed. Green color states that the catalyst exhibits full carbon recovery and grey that the performances are not tested under the given conditions.

At the beginning of the H_2O test protocol, conversions evolve with time on stream. For this reason, the starting and final values of conversions as well as H_2/CO ratios are given. The methane conversions are far from thermodynamic equilibrium of reforming with the H_2O test protocol; however, similar performances are achieved at the end of phase 3, with methane conversions equal to 45% for both protocols. The same methane conversions would be expected in phase 2; however, the next phase is tested instead of waiting for catalyst performance activation under the H_2O test protocol.

The use of the H_2 test protocol causes first a faster preformation of the catalyst. Second, the H_2 test protocol increases only the CO_2 conversions and H_2/CO ratio because H_2 from the H_2 test protocol, initially present in the feed stream, can preform the catalyst unlike the H_2O test protocol.
The H_2O test protocol on the MSI catalyst delivers also a H_2/CO close to unity for more than 150 h in the presence of 20 vol.% H_2O and CH_4/CO_2=0.9/1; however, a long induction time is required for preformation in phases 1, 2, and 3. Indeed, the impact of the gas-phase reactions is significant in the absence of the corundum prebed and could explain the long preformation time necessary to preform the MSI catalyst.

Bhattacharyya et al.[314] have studied the influence of Mg^{2+} substitution with Ni^{2+} in hydrotalcite. The top-performer $Mg_5Ni_1Al_2O_4$ exhibits also under extremely high GHSV (14400 h^{-1}) an induction time of 24 h with a low steam content. After preformation, the catalyst studied by Bhattacharyya et al.[314] achieved thermodynamic equilibrium without coke formation. Even if the catalyst composition is relatively different to the MSI-catalyst stoichiometry ($Ni_{14}Mg_{29}Al_{57}O_x$) and appears to show similar prefor-

mation behavior. The performance observed with the MSI catalyst is significantly lower with steam, but thermodynamic reforming equilibrium of phase 3 and 4 with the H_2 test protocol is still achieved. The reason for this difference in performance is very likely to be due to the preformation of the MSI catalyst, which is incomplete at the beginning of the H_2O test protocol.

Finally, the measurement of coke precursors is achieved; however, none of the typical coke precursors have been identified in the different phases of the MSI catalyst tested without prebed and with the H_2O test protocol presented in the Tab. 3.7.
This observation could be the result of the moderate temperature 1123 K (850°C). As a result, only low concentrations of coke precursors are achieved. Due to these low concentrations, the catalyst can probably convert them easily to H_2, methane, and CO and limit their impact.

3.3.2 Influence of reactor configuration with H_2O test protocol on performance of Ni-based spinel catalyst prepared by MSI

As it has been already pointed out in the gas-phase reaction study (part IV), the use of a "full" bed like the configuration (d) (78 ml of catalyst with corundum in the cold zone) could limit the influence of the gas-phase reactions in comparison with configuration (c) (20 ml of catalyst without prebed). In addition, the H_2O test protocol is conducted at 1173 K (900°C) instead of 1123 K (850°C) to improve the activity of the catalyst. The results are presented in Tab. 3.8.

#	Catalyst				Steam Ref.	Ref. with 40vol.% H_2O	Ref. with 30vol.% H_2O
					850°C		
		Temper.	**CH_4/CO_2**	**Phase**	**1**	**2**	**3**
1	MSI (20ml) without corundum prebed	850°C	0.9	X CH_4 X CO_2 H_2/CO	52-32 - 3.5-4.4	17-47 38-32 1.1	50-45 38-32 1-1.1
2	MSI (78ml) with 10ml corundum prebed	900°C	0.9	X CH_4 X CO_2 H_2/CO	6-21 - 6.5-5.3	26-37 15-17 1.5	34 25 1.1
-	Thermodynamic Equilibrium	850°C	0.9	X CH_4 X CO_2 H_2/CO	53.0 - 3.83	80.0 37.9 1.55	72.8 49.0 1.3

Table 3.8: Comparison of the influence of reactor configuration (20 ml catalyst without corundum prebed and 78 ml catalyst) on performance of the MSI catalyst.

The stability of the performance is improved by increasing the catalyst volume; however, the performances are still lower than with 20 ml of catalyst. This is contrary to the expectation that higher conversions should result when using a larger quantity of catalyst. A possible explanation is that the catalyst is not fully preformed and, therefore, exhibits lower performances. Phases 1, 2, and 3, as discussed in the previous section, require long periods of preformation time.
The analysis of coke-precursor formation is shown in Tab. 3.9. The use of 20 ml of catalyst without

prebed at 1123 K (850°C) shows that the formation of coke precursors cannot be detected whereas the use of a full catalyst bed at 1173 K (900°C) results in the formation of ethylene. The coke-precursor concentration increases from steam reforming up to phase 3.

#	Catalyst	Test protocol	CH_4/CO_2	Phase / Conc. [ppm]	Steam Ref. (1)	Ref. with 40vol.% H_2O (2)	Ref. with 30vol.% H_2 (1) or H_2O (2) (3)
1	20ml MSI without corundum prebed	With H_2O @850°C	0.9	C_2H_6 C_2H_4 C_2^+	- - -	- - -	- - -
2	78 ml MSI including "catalyst prebed"	With H_2O **@900°C**	0.9	C_2H_6 C_2H_4 C_2^+	- 210 -	- 50-80 -	- 80-100 -

Table 3.9: Comparison of coke-precursor concentrations measured in product stream for the MSI catalytic test at 1123 K (850°C) for different reactor configurations

The use of a higher temperature, 1173 K (900 °C) instead of 1123 K (850°C), could explain the increase of ethylene concentration. Moreover, because the catalyst is probably not fully preformed as suggested, this could result in a lower conversion of ethylene on metallic Ni and, therefore, in a higher concentration of ethylene in the product stream.

3.4 Characterization of the spent Ni-based spinels

The spent MSI and PRC catalysts are collected for XRD characterization and compared to the XRD patterns of the fresh catalysts.

The PRC catalyst prepared by precipitation is analyzed before and after the H_2 test protocol by means of XRD. The XRD patterns of the fresh catalyst and the spent catalyst harvested at the very top and at the bottom of the catalytic bed are displayed in Fig. 3.12.

The spent catalyst samples consist of $MgAl_2O_4$, Ni^0 and traces of MgO; in addition, traces of the impurity are still identifiable. Moreover, the presence of graphite is detected, particularly at the top of the catalytic bed.

The impurities are mostly eliminated after performing the H_2 test protocol, and the phases expected after preformation of the MSI catalyst are identified. It is worth noticing that the top of the catalytic bed undergoes strong deactivation by coking as the feed enters the top of the catalytic bed. Indeed, the feed contains at this point beside CH_4, CO_2, H_2, H_2O, and CO the product of the gas-phase reactions. Furthermore, the top of the catalytic bed is expected to be cooled down by highly endothermic steam reforming

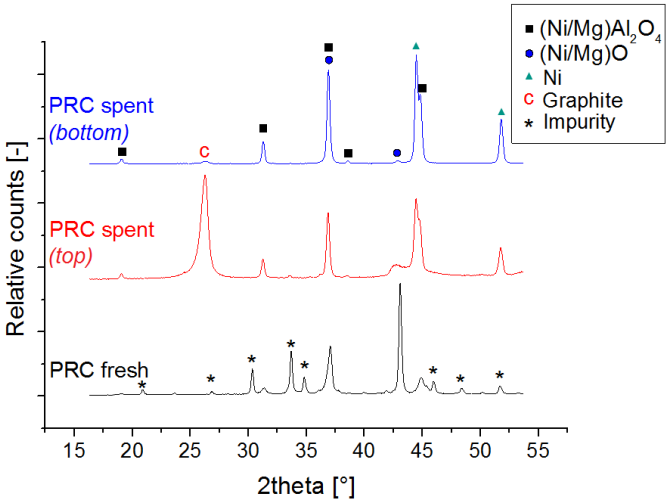

Figure 3.12: Comparison of the Ni-based spinel catalyst prepared by precipitation (PRC), fresh and spent after H_2 test protocol. The spent catalyst is harvested at the top and the bottom of the catalytic bed.

at the top of the catalytic; as a result, the coke precursors originating from the gas-phase reactions are likely to deposit and start coking on the top of the catalytic bed, as it is often observed in the practice.

The XRD patterns of the MSI catalyst, fresh, after preformation at 1223 K (950°C) for 165 h in presence of H_2 and H_2O, as well as spent after the H_2 test protocol, are shown in Fig. 3.13 and summarized in Tab. 3.10. Unmounting the reactor, in which the MSI catalyst has been tested, is challenging due to formation of coke between the primary ceramic tube and metal tube that blocked both tubes because of the breakdown of N_2 flushing during this catalytic test. The reactor is sawn open to harvest the spent catalyst; however, corundum fines from the ceramic tube contaminates the spent catalyst samples as seen in the spent MSI-catalyst XRD patterns. The spent sample exhibits the same phases as the preformed: metallic Ni and $MgAl_2O_4$ with traces of MgO. In addition, traces of graphite are found in the spent catalyst due to coking as well as corundum impurities stemming from the sawn ceramic tube.

The specific surface area is found to be ten times lower than after catalyst preparation. The specific surface area of the spent catalyst could be falsified due to the presence of graphite/coke, which exhibits a very high specific surface area.

Short name	Ni [mol.%]	Mg [mol.%]	Al [mol.%]	Crystallographic phases	Specific surface area [$m^2.g^{-1}$]
Fresh MSI	14	29	57	$Ni_{0.5}Mg_{0.5}O$+$(Ni/Mg)Al_2O_4$	42.4
Spent MSI	14	29	57	Ni+$MgAl_2O_4$+MgO *	4.6

Table 3.10: Comparison of X-ray diffraction and N_2-physisorption results of MSI fresh and spent.* Impurities from the ceramic tubes inserted in the reactor are also identified.

The different crystallites of the catalyst undergo sintering during the H_2 test protocol (Tab. 3.11), which is

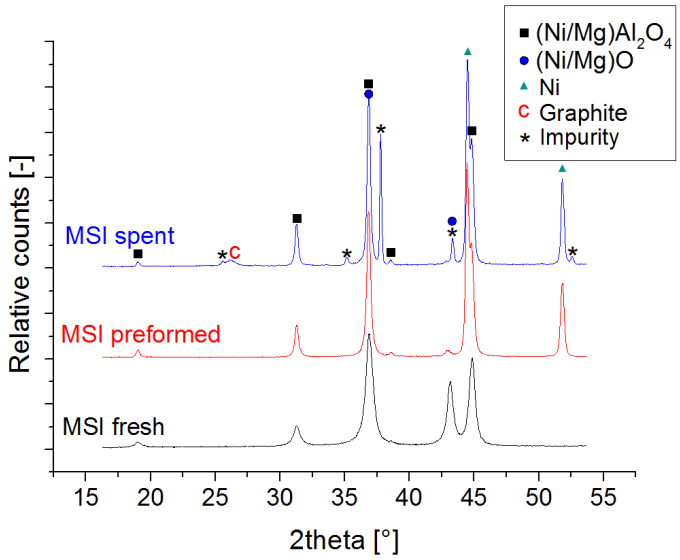

Figure 3.13: Comparison of the benchmark Ni-based spinel catalyst, fresh, reduced 165 h under 5vol.% H_2 + 5vol.% H_2O in N_2, and spent after the H_2 test protocol

Short name	Ni [mol.%]	Mg [mol.%]	Al [mol.%]	Particle size Ni^0 [nm]	Particle size (Ni/Mg)O [nm]	Particle size (Ni/Mg)Al_2O_4 [nm]
Fresh MSI	14	29	57	-	20	18
Spent MSI	14	29	57	49	-	36

Table 3.11: Comparison of crystallite sizes of Ni^0, (Ni/Mg)O, and (Ni/Mg)Al_2O_4 calculated with the Scherrer equation for the benchemark Ni-nased catalyst prepared by MSI

enhanced by high temperatures and the presence of steam. The particle size of (Mg/Ni)O and (Mg/Ni)Al_2O_4 is roughly about 20 nm for the fresh catalysts while the particle size of $MgAl_2O_4$ and MgO (if measurable) on the spent catalyst is about 2 times larger. The spinel particle size is particularly resistant to sintering while Ni is more sensitive.

3.5 Conclusions

New preparation methods of Ni-based spinel catalysts with the selected stoichiometry $Ni_{14}Mg_{29}Al_{57}O_x$ are investigated. Classical preparation routes are used to benchmark the catalyst prepared by MSI on a hydrotalcite-like carrier (PURAL® MG30). The spray-drying route based on PURAL® MG30 is found to be unattractive because of segregation of the hydrotalcite-like compound and boehmite during the spray-drying operation, which results in the formation of larger crystallites after final calcination. The PRC catalyst prepared by coprecipitation suffers from the presence of impurities and relatively low specific surface area.

The preformation mechanism of the MSI catalyst is well understood. The mixed oxides obtained after calcination at 1223 K (950°C) are $Ni_{0.5}Mg_{0.5}O$ and $(Ni/Mg)Al_2O_4$. During preformation in the presence of H_2, Ni^{2+} is reduced above 973 K (700°C), which leaves free MgO and γ-alumina that react further to form $MgAl_2O_4$. If the preformation is conducted in the presence of H_2O and/or CO_2 a significant induction period of time is observed before the catalyst is completely preformed.

The Ni-based spinel catalyst prepared by MSI is a new candidate for the industrial CO_2 reforming at high pressure with addition of 10 vol.% H_2O. After almost 600 h of runtime, the MSI catalyst exhibits a high stability with a spinel-particle size of 35 nm and metallic Ni nanoparticles of about 50 nm, which corresponds to a size increase of about 50%, while the specific surface area is decreased by one order of magnitude after the long thermal treatment. This could be limited by using lower operating temperatures and low partial pressure of steam as emphasized in the preformation study.

The precipitated catalyst (PRC) is able to deliver the desired H_2/CO ratio of one; however, it has not been proven to activate methane. In addition, due to the relatively low specific surface area and the presence of impurities in the fresh catalyst, further tests are not conducted.

The use of H_2 is suitable to achieve high performances of CO_2 reforming with 10 vol.% H_2O; however, the H_2O test protocol should be preferred for industrial purposes. The use of the reactor configuration with 20 ml catalyst without prebed and H_2O test protocol leads to an instability of the catalyst performance probably due to a significant impact of gas-phase reactions. As stabilization of performances is observed during the H_2O test protocol, similar conversions of methane are achieved with H_2O and H_2 test protocol. CO_2 conversions are higher with the H_2 test protocol due to enhanced RWGS. The use of a full-bed catalyst can help to minimize the influence of gas-phase reactions; however, full catalyst preformation takes relatively long to achieve optimized performances.

The analysis of coke-precursor concentration in the outlet stream shows that the MSI catalyst can convert the coke precursors in most cases especially at low-severity operating conditions because they are not

detected in the product stream. As the concentration of the coke precursors increases the coking risk is also increased. Using high temperatures may be helpful to minimize the impact of coke precursors and gas-phase reactions on the catalyst; however, the catalyst must exhibit high activity and be fully formed in case of MSI catalyst, otherwise coking is expected to occur.

The performances achieved with the catalysts prepared by MSI in case of the H_2 test protocol and H_2O test protocol with 20 ml and 78 ml of catalyst have been extrapolated to improve the reforming mechanism in the presence of steam and/or CO_2 on Ni-based catalysts developed with the DETCHEM platform by K. Herrera Delgado in the Deutschmann's group at Karlsruhe Institute of Technology (KIT)[214;344].

Part VII

Ni-based hexaaluminates as catalysts in reforming reactions in the presence of CO_2

The content of this part consists of the reuse of the two articles published about Ni hexaaluminates[240;241] during this PhD thesis .

1 Ni hexaaluminates in reforming reactions: State of the art

Hexaaluminates are regarded as promising candidates for catalytic reactions conducted at high temperatures due to their high thermal stability, retention of high specific surface area, and strong inhibition of crystal growth in the normal direction of the planar structure[345–347] (space group number 194: $P6_3/mmc$[295]). Transition metal-substituted hexaaluminates have the general formula $AB_yAl_{12-y}O_{19-\delta}$, where A is a mono-, di-, or trivalent cation, for instance Na, Ba, Sr, or La, which resides in the mirror plane between spinel blocks of close-packed oxide ions made of 4 layers, and B is a dopant cation, in our case B=Ni, but it could also be Fe or Co[46;47], that are tetrahedrally coordinated, which is typical for Al^{3+} in spinel blocks near the mirror plane[47]. As a result, for Ni hexaaluminates only little changes in thermal stability are observed compared to the unsubstituted materials[348–350]. The charge neutrality of the framework is achieved because of cation vacancies in the mirror planes of the hexaaluminate lattice[351;352]. The high dispersion of Ni^{2+} within the hexaaluminate structure is said to be beneficial for a high dispersion of the active center after reduction[47;240;241]. The stability of the high dispersion of Ni^0 nanoparticles is fundamental to maintain a high and stable activity in reforming reactions and to minimize the carbon deposition, since common understanding is that larger Ni^0 nanoparticles lead to enhanced carbon deposition[38–41;242].

Only few hexaaluminate materials have the ideal stoichiometry $AAl_{12}O_{19}$, for example, magnetoplumbites[221] $CaAl_{12}O_{19}$[353;354], or $SrAl_{12}O_{19}$[355]. Non-stoichiometric compositions are observed for almost all β-alumina materials and for materials incorporating trivalent lanthanide ions in magnetoplumbite structures[356;357]. Such non-stoichiometric compositions are due to defect formation in the hexaaluminate framework, which plays a major role in the charge compensation in hexaaluminate materials[221].

The ionic radius and the valence of the mirror-plane cation A influence the type of the structure[221], which can be classified into magnetoplumbite types (e.g. A = La or Sr) or β-alumina types (e.g. Ba), as displayed in Fig. 1.1. The difference between both lattices can be observed in the mirror plane of the unit cell. For magnetoplumbites, four Al^{3+} cations, three O^{2-} anions, and the A cation are located in the mirror plane of the unit cell, while for β-aluminas only the A cation and one O^{2-} anion are located in this plane. The β-aluminas are divided into two subcategories: the β'-alumina and β"-alumina, which

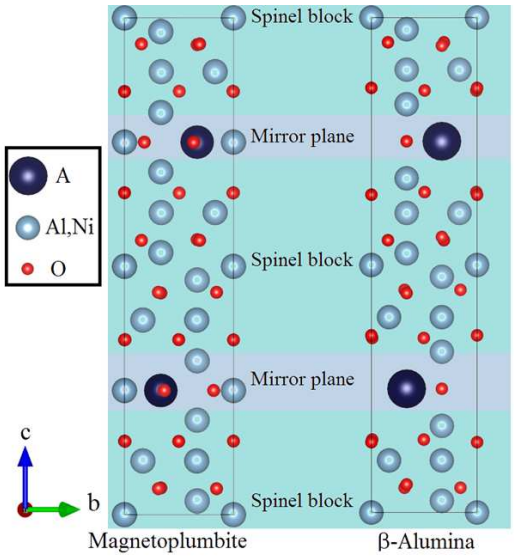

Figure 1.1: Structural representation of the hexaaluminate structures: magnetoplumbite and β-alumina (simulated with the Vesta software[298] and taken from[240])

have a Ba-poor or Ba-rich lattice, respectively[358]. These different classes are summarized in Fig. 1.2.

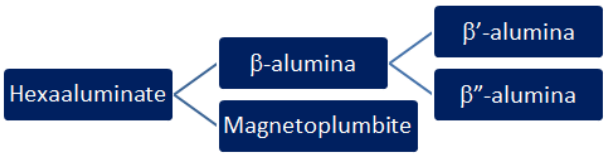

Figure 1.2: The different types of hexaaluminates

In reforming processes, Ni-based catalysts have to typically undergo a reduction step prior or during reforming operations. Ni hexaaluminates are typically fully reduced at temperatures above 1073 K (800°C)[359]. Machida et al.[345;346] demonstrated that the oxygen monolayer located in the mirror plane is less tightly bound in the lattice than the oxygen in the spinel blocks and provides, therefore, a preferential path for oxide ion diffusion.

For CO_2 reforming of methane over Ni hexaaluminates, it is important to understand the formation and nature of catalytically active sites. Methane chemisorbs preferentially on metallic Ni whereas CO_2 is chemisorbed probably preferentially on the large mirror-plane cations, as demonstrated by Gardner et al. with Ba-hexaaluminates[360]. They have quantified the basic site density over the catalyst surface depending on the segregation of Ba on the surface. Based on CO_2 adsorption measurements, it has been suggested that the adsorption sites for CO_2 physisorption are sites containing exposed BaO that has segregated from the bulk phase[360]. It could be demonstrated that the amount of adsorbed CO_2 decreased as the degree of Ni^{2+} substitution increased in materials with the stochiometry range $Ba_{0.75}Ni_yAl_{12-y}O_{19-\delta}$ with y=0.4, 0.6 ,1.

Several routes are reported for the synthesis of hexaaluminates: coprecipitation of nitrate precursors[46;47;351;361], solid-state routes[361], alkoxide methods[228;362], or polyol routes[169;245;363;364]. A new synthesis method[365] is used to obtain samples with a high hexaaluminate content as well as high specific surface areas. It has been found that this new preparation route is giving optimal catalyst precursors, among other synthesis routes (combustion synthesis, precipitation, colloidal synthesis, polyol-route), leading to direct formation of hexaaluminate at relatively low temperature with high specific surface area. Indeed, the formation of a highly homogeneous nanopowder allows to directly synthesize hexaaluminate without the formation of intermediate crystalline phases such as $BaAl_2O_4$, $LaAlO_3$, $SrAl_2O_4$, BaO, La_2O_3, SrO, and alumina phases to maximize the hexaaluminate content. As a result, the high homogeneity of the nanomaterial lowers the temperature of hexaaluminate formation.

Beside the partial oxidation of hydrocarbons[40;46;228;359] and catalytic combustion[351;352], Ni hexaaluminate materials are used in CO_2 reforming[169;243;245;246;360;361;363;364] or in mixed-steam CO_2 reforming[361] (MSCR). The most studied hexaaluminate materials in reforming and partial oxidation of hydrocarbons are based on Ba,Ni[360;361] and La,Ni hexaaluminates[169;245;364].
Gardner et al. have studied the influence of the mirror-plane cation[242] as well as the degree of Ni^{2+} substitution[47] in the hexaaluminate materials for partial oxidation of middle distillates[46]. $BaNi_{0.4}Al_{11.6}O_{19-\delta}$ and $SrNi_{0.4}Al_{11.6}O_{19-\delta}$ have been identified as superior performers in the reaction[242]. The reasoning why these materials display superior behavior in the partial oxidation of *n*-tetradecane is that adsorbed hydrocarbons are less strongly adsorbed onto catalyst surfaces and are, therefore, less prone to undergo coking, compared with $LaNi_{0.4}Al_{11.6}O_{19-\delta}$, in the partial oxidation of *n*-tetradecane. Recently, Gardner et al.[360] have reported the influence of Ni^{2+} substitution in $Ba_{0.75}Ni_yAl_{12-y}O_{19-\delta}$ with y=0.4, 0.6, and 1 in the CO_2 reforming of methane at pressures of 2 bar and temperatures of 1173 K (900°C). It has been found that lower degrees of Ni^{2+} substitution improve the resistance against coking while the activity decreases slightly with a lower substitution degree[360]. On the other hand, Xu et al.[246] have studied first the influence of the mirror-plane cation in reforming and found that $LaNiAl_{11}O_{19-\delta}$ exhibits the highest activity and resistance against coke formation compared with $BaNiAl_{11}O_{19-\delta}$, $CaNiAl_{11}O_{19-\delta}$, and $SrNiAl_{11}O_{19-\delta}$.

The effect of the doping cation B has been further investigated by Wang et al.[169;364]. Different series of $LaNi_xMg_{1-x}Al_{11}O_{19-\delta}$ and $LaNi_xCo_{1-x}Al_{11}O_{19-\delta}$ have shown that Co and Mg can enhance activity and stability of La,Ni hexaaluminates against sintering and coking[169;364]. Finally, Liu et al.[247;366] reported improved performance of La,Ni hexaaluminates by partial substitution of La^{3+} with Pr^{3+}. $La_{0.8}Pr_{0.2}NiAl_{11}O_{19}$ has been reported to be a superior performer in CO_2 reforming of methane at atmospheric pressure and 1023 K (750°C); with an input flow rate of 30 ml.min^{-1} for 0.2 g catalyst exhibited high and stable CH_4 and CO_2 conversions of 89% and 95%, respectively, and after 300 h only 0.75 g of coke per gram of catalyst was detected[247].

2 Design of experiments of the Ni hexaaluminate library

In order to assess the performance of Ni hexaaluminates ($ANi_yAl_{12-y}O_{19-\delta}$) in CO_2 reforming of methane under pressure, the catalysts are characterized before as well as after the reduction step and finally by a catalytic test. The parameters used for the study are the degree of Ni^{2+} substitution, the mirror-plane cation (La, Sr, and Ba) and the calcination temperature (Fig. 2.1). A total of 16 Ni hexaaluminates are synthesized.

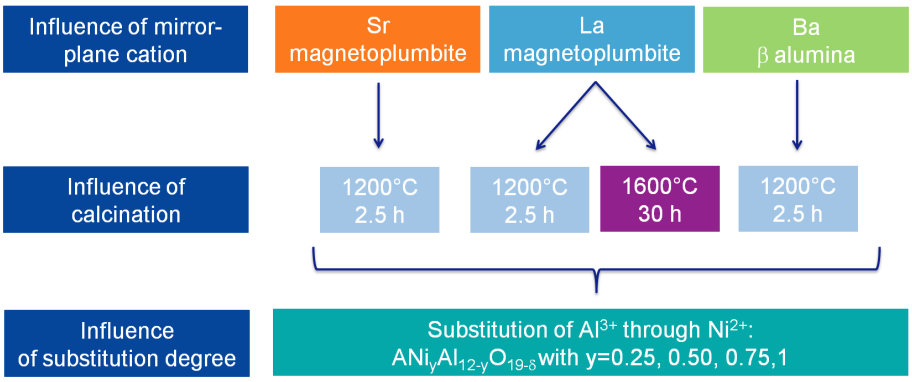

Figure 2.1: Design of experiment to assess the catalytic properties of $ANi_yAl_{12-y}O_{19-\delta}$ of magnetoplumbite and β-alumina type (taken from [240;367])

2.1 Ni hexaaluminate synthesis

Ni hexaaluminates are prepared based on the best synthetic methods[368] to obtain hexaaluminate with high specific surface area at low temperature. This is achieved by the freeze-drying route.

The nitrate salts of Ni and Ba, La, or Sr are dissolved in as few as possible deionized water in a beaker. The solution is stirred as strong as possible to obtain a "homogeneous" slurry after the addition of pseudoboehmite in powder form (Disperal® from Sasol). After 15 min ageing, the slurry is added dropwise into liquid N_2 in a dish-shaped Dewar flask under stirring. The frozen solid is then freeze dried for 96 h at 243 K (-30°C) under a pressure of 2 mbar in a stainless steel dish. The resulting precursor is then calcined at respective temperatures of 1473 K (1200°C) for 2.5 h or 1873 K (1600°C) for 30 h in a muffle furnace under air.

The samples are characterized by the means of XRD and N_2-physisorption analysis. Additional measurements are conducted by electron microscopy.

2.2 Reducing treatment of the Ni-hexaaluminate samples

Understanding the reduction mechanism is vital in order to improve the dispersion of the metallic Ni nanoparticles on the hexaaluminate surface. For this reason, all samples have been investigated after calcination and reduction by further analysis (XRD and STEM).

The reduction procedure is conducted with 2 ml of Ni hexaaluminate in fixed-bed configuration in a 4-fold reduction unit (Fig. 2.2 in part VI) by heating the samples at a ramp of 5 K.min^{-1} to 1173 K (900°C) with a dwell time of 3 h and a flow rate of 150 sccm of 5 vol.% H_2 in N_2. The reduced samples are then cooled down under N_2 atmosphere, and finally the reduced samples undergo passivation at room temperature with air.

A summary of samples is given in Tab. 2.1.

Short name	Calcination	Stoichiometry aimed	Name after reduction at 1173 K (900°C)
LaNi1-1600	1873 K (1600°C) / 30 h	$LaNi_1Al_{11}O_{19-\delta}$	LaNi1-1600-red
LaNi0.75-1600	"	$LaNi_{0.75}Al_{11.25}O_{19-\delta}$	LaNi0.75-1600-red
LaNi0.5-1600	"	$LaNi_{0.5}Al_{11.5}O_{19-\delta}$	LaNi0.5-1600-red
LaNi0.25-1600	"	$LaNi_{0.25}Al_{11.75}O_{19-\delta}$	LaNi0.25-1600-red
LaNi1-1200	1473 K (1200°C) / 2.5 h	$LaNi_1Al_{11}O_{19-\delta}$	LaNi1-1200-red
LaNi0.75-1200	"	$LaNi_{0.75}Al_{11.25}O_{19-\delta}$	LaNi0.75-1200-red
LaNi0.5-1200	"	$LaNi_{0.5}Al_{11.5}O_{19-\delta}$	LaNi0.5-1200-red
LaNi0.25-1200	"	$LaNi_{0.25}Al_{11.75}O_{19-\delta}$	LaNi0.25-1200-red
BaNi1	1473 K (1200°C) / 2.5 h	$BaNi_1Al_{11}O_{19-\delta}$	BaNi1-red
BaNi0.75	"	$BaNi_{0.75}Al_{11.25}O_{19-\delta}$	BaNi0.75-red
BaNi0.5	"	$BaNi_{0.5}Al_{11.5}O_{19-\delta}$	BaNi0.5-red
BaNi0.25	"	$BaNi_{0.25}Al_{11.75}O_{19-\delta}$	BaNi0.25-red
SrNi1	1473 K (1200°C) / 2.5 h	$SrNi_1Al_{11}O_{19-\delta}$	SrNi1-red
SrNi0.75	"	$SrNi_{0.75}Al_{11.25}O_{19-\delta}$	SrNi0.75-red
SrNi0.5	"	$SrNi_{0.5}Al_{11.5}O_{19-\delta}$	SrNi0.5-red
SrNi0.25	"	$SrNi_{0.25}Al_{11.75}O_{19-\delta}$	SrNi0.25-red

Table 2.1: Overview of all hexaaluminate samples prepared by the freeze-drying route

After reduction, the 16 samples are analyzed by XRD and STEM (or SEM for the sample at 1873 K (1600°C)).

The reduced samples are not used for the catalytic test. An in-situ reduction is preferred here.

2.3 Characterization of Ni hexaaluminates

XRD is performed on the 32 samples at the TU München using Cu $K_{\alpha 1}$ (λ=1.541874 Å) at 40 mA and 40 kV by means of an X"Pert Pro device (Philips). The patterns are obtained with angular positions rang-

ing from 4.990° up to 69.976°. Match![369] software (Crystal Impact) is used for phase identification and quantification thanks to the International Center for Diffraction Data and the RIR method. Determination of lattice parameters is performed with the UnitCell software[370], which uses a least-squares refinement program to retrieve unit cell constants from diffraction data.
Samples for N_2-physisorption measurements are first preconditioned at 573 K (300°C) for 1 h in N_2 flow prior to analysis. Sample-specific surface areas are determined by the BET-method using a TriStar II (Micromeritics). Specific surface areas are determined on the basis of a five-point adsorption isotherm.
Electron microscopic techniques are used for the analysis of reduced samples. These measurements are executed at TU München (SEM) and at BASF (STEM). At the TU München, the particle morphologies of the samples calcined at 1873 K (1600°C) before and after reduction are obtained on a JOEL JSM-7500F scanning electron microscope operated at 1.0 kV. For imaging, samples are placed on carbon spots. At BASF, STEM measurements are performed by a FEI Tecnai G20 for the samples calcined at 1473 K (1200°C) after reduction at 20 kV with energy-dispersive X-ray spectroscopy and high-angle annular dark field.

2.4 Ni hexaaluminate catalytic test

Each sample in Tab. 2.1 has been tested in collaboration with the Technische Universität München in a differential recycling reactor. The samples are reduced in 20 vol.% H_2 in N_2 at 1073 K (800°C) for 2 h and are tested under 10 bar at 1123 K (850°C) with a recycling flow rate of 100 sccm for 10 h.

The catalytic-performance evaluation is achieved in two steps: first, the influence of the degree of Ni^{2+} substitution is achieved by comparing the selectivity to methane conversion and the selectivity to coke (deactivation rate) within all 4 material series ($LaNi_y$-1600, $LaNi_y$-1200, $SrNi_y$, $BaNi_y$, y being the substitution degree); second, the performances of all the catalysts are ranked by comparing conversion degrees and deactivation rates.

The calculation of the TOF for methane consumption is based on data obtained in the first 30 min and represented as the methane-consumption-rate coefficient divided by the mass of metallic Ni found in the sample after reduction. It is evident that these data, especially with regard to the "TOF", are not based on Ni dispersion measurements, but allow appropriate comparison of the material libraries in this study. Finally, for the final catalyst ranking, the conversions achieved after 10 h of runtime are selected.

Because most catalysts yield a product gas very close to the thermodynamic equilibrium after 10 h of runtime, as illustrated in Fig. 2.2-a, a second parameter is used to characterize the coke selectivity and the deactivation rate, respectively, of each material so that activity and stability can be optimally compared. The estimation of the deactivation rate is illustrated in Fig. 2.2-b, where the CO concentration appears to

decrease after reaching a maximum. The deactivation rate observed is assumed to be mostly due to CO disproportionation and is defined as the ratio of $\Delta C_{CO}/\Delta$ t, which is drawn in Fig. 2.2-b.

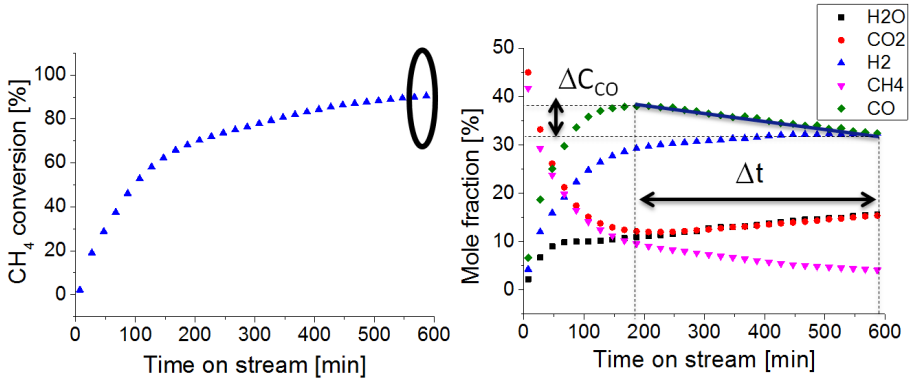

Figure 2.2: Description of the parameters used for the performance evaluation of Ni hexaaluminates (adapted from[241])

3 Results of Ni hexaaluminate study

3.1 La,Ni hexaaluminates calcined at 1873 K (1600°C)

After calcination at 1873 K (1600°C) for 30 h, the materials sintered at high temperature have a very low specific surface area (<0.1 $m^2.g^{-1}$), but these materials exhibited a very high phase purity above 90 wt.% as shown in Tab. 3.1. For La,Ni hexaaluminates, magnetoplumbite-like structures are identified, with characteristic reflexes at 2θ=32.1°, 34.0°, and 36.1°, while only traces of $LaAlO_3$ perovskite are found. As the Ni content increases in the samples, hexaaluminate purity decreases. This shows that if the degree of Ni^{2+} substitution within the hexaaluminate lattice is kept rather low, full insertion of Ni inside the hexaaluminate lattice can be ensured. These samples are chosen as model catalyst for La,Ni hexaaluminates.

	Calcined samples		Reduced samples	
Stoichiometry	Hexaaluminate [wt.%]	Specific surface area [$m^2.g^{-1}$]	% Ni reduced [mol.%]	∅ Ni^0 (SEM) [nm]
y=0.25	98	<0.1	∼30	9-36
y=0.5	98	<0.1	∼20	8-28
y=0.75	96	<0.1	∼40	7-27
y=1	90	<0.1	∼40	7-19

Table 3.1: Semi-quantitative phase analysis as well as specific surface area before reduction, and quantification of amount of reduced Ni^{2+} as well as Ni^0 particle size from SEM imaging after reduction of La,Ni hexaaluminates ($LaNi_yAl_{12-y}O_{19-\delta}$) calcined at 1873 K (1600°C)

After reduction, a minimal change in the XRD patterns is observed due to the presence of traces of metallic Ni. Indeed, according to the XRD-pattern analysis from Match! with the RIR method, about 30 wt.% of Ni^{2+} in the hexaaluminate framework is reduced in the samples, while the hexaaluminate-phase content remains unaffected, as already reported by Xu et al.[246]. Metallic Ni crystallizes with a face-centered-cubic (fcc) lattice structure, and the characteristic reflexes at 2θ=44.4° and 51.7° are observed. The fact that Ni is only partially reduced may result from two factors. The small specific surface area of the materials may be the first reason because the reduction rate is assumed to be proportional to the gas/bulk interfacial area[183]. Secondly, Ni^{2+} is strongly stabilized within the hexaaluminate lattices[246] especially if the hexaaluminate materials are calcined at high temperature, like the Ba,Ni hexaaluminates studied by Gardner et al.[47] at calcination temperatures up to 1673 K (1400°C). The Ni^0 nanoparticle size remains almost constant in a broad range of 5-40 nm within this La,Ni hexaaluminate series.

The small size of the Ni^0 nanoparticles does not allow the use of the Scherrer equation to interpret the data from the XRD patterns of La,Ni hexaaluminates to support the observation of Ni^0 nanoparticle size analysis made by SEM. Indeed, small nanocrystalline Ni^0 particles display an extremely broad reflex with a very low intensity in the XRD patterns.

The determination of lattice parameters with regard to the hexaaluminate structure can be performed easily due to the well-crystallized material. The results are presented in Fig. 3.1. An increase in the crystallographic *a* axis (Fig. 3.1-a) and a decrease in the crystallographic *c* axis (Fig. 3.1-b) are observed with increasing Ni content in the calcined samples prior to reduction. This effect has already been reported in previous studies[47;352]. It has been suggested[350;371] that the substitution of a trivalent Al^{3+} cation with a larger divalent Ni^{2+} cation leads to the decrease of the *c* cell parameters, while the cell parameter *a* increases. Due to lattice neutrality, the lower amount of positive charges generated by this substitution is compensated by a local increase of mirror-plane-cation concentration, resulting in a stronger local bonding between the spinel blocks and the mirror plane[350;371]; however, after reduction of Ni^{2+} to Ni^0, a slight elongation of the crystallographic *c* axis is observed; the cell parameter *c* increases again (Fig. 3.1-b) probably due to loss of this local interaction. In addition, the lattice neutrality after substitution of Al^{3+} with Ni^{2+} may be also ensured by oxygen defect sites; however, it cannot be demonstrated here. Higher degrees of Ni^{2+} substitution increase the volume of the lattice (Fig. 3.1-c) because the Ni^{2+} ionic radius is larger than the Al^{3+} ionic radius. After expulsion of Ni^{2+} from the hexaaluminate framework during the reduction of Ni^{2+}, the cell parameters and the volume of hexaaluminates remain similar to the oxidic sample.

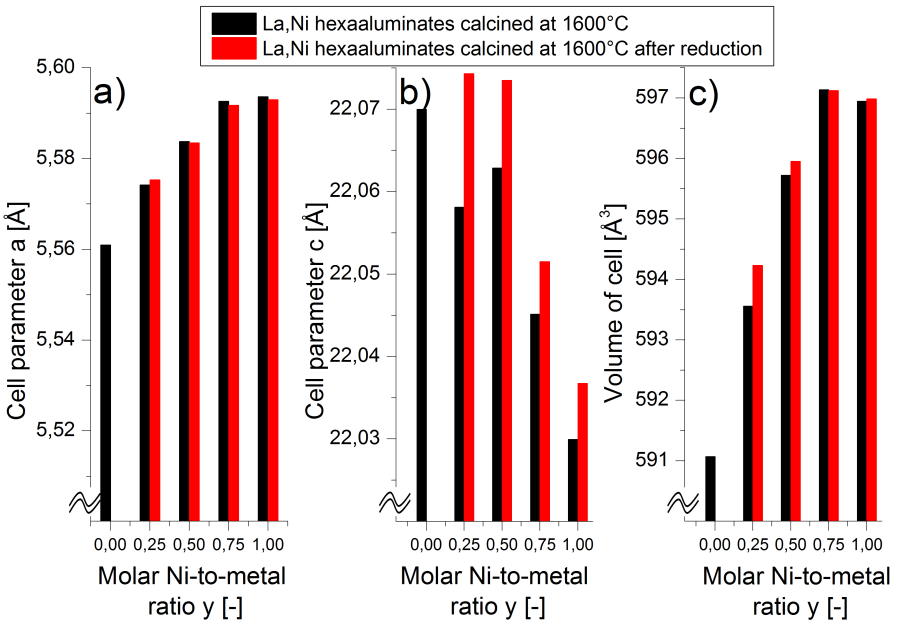

Figure 3.1: Determination of lattice parameters (*a*, *c*, unit cell volume) obtained from XRD patterns of La,Ni hexaaluminates ($LaNi_yAl_{12-y}O_{19-\delta}$) calcined at 1873 K (1600°C) before and after reduction: a) Cell parameter *a*, b) cell parameter *c*, c) volume of unit cell, reference for y=0 is taken from Crystallographic Database[372] (adapted from[240])

SEM images in Figs. 3.2-a and -c confirm that the hexaaluminate samples are well crystallized and show a morphology with hexagonal platelets. In Figs. 3.2-b and -d, which show samples after reduction, metallic Ni nanoparticles are found on the defect sites near the steps and edges[373–376]. Plain surfaces are seen as quite "Ni free". The localization of the Ni nanoparticles illustrates that their surface energy is minimized at edges and kinks, which improves the stability against sintering even under harsh thermal treatments.

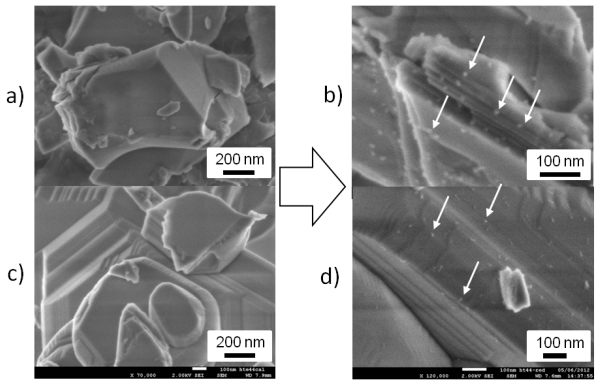

Figure 3.2: SEM images before and after reduction of $LaNi_yAl_{12-y}O_{19-\delta}$ calcined at 1873 K (1600°C). White arrows point out the Ni^0 nanoparticles (taken from[240]).

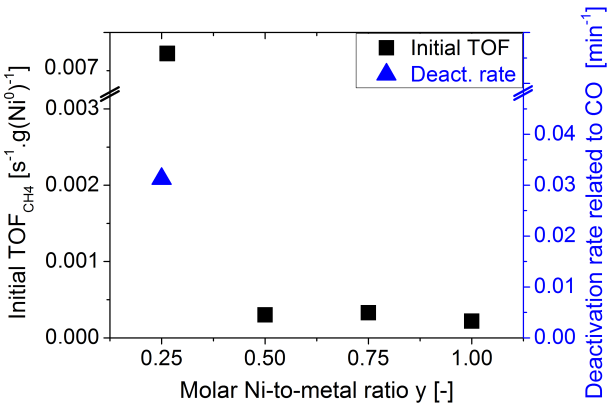

Figure 3.3: Initial TOFs of methane consumption and deactivation rate measured for the $LaNi_yAl_{12-y}O_{19-\delta}$ series after calcination at 1873 K (1600°C, adapted from[241])

The catalytic activity of these $LaNi_yAl_{12-y}O_{19-\delta}$ hexaaluminate materials in CO_2 reforming of methane as their deactivation rate are presented in Fig. 3.3. Only the La,Ni hexaaluminate sample with the lowest Ni content exhibits high activity, but strong deactivation is observed after high CO partial pressures are reached. Apparently at high CO partial pressures, CO decomposes into CO_2 and carbon via the Boudouard reaction[36], especially at high pressure[112], as illustrated in Fig. 2.2-b. WGS could also explain CO consumption but not with the excess of H_2 or lack of steam found in our case. The other La,Ni hexaaluminates ($y \geq 0.5$) display only poor activity.

3.2 La,Ni hexaaluminates calcined at 1473 K (1200°C)

The La,Ni hexaaluminates calcined at lower temperatures exhibit higher specific surface areas compared to the samples calcined at 1873 K (1600°C). In Tab. 3.2, it can be seen that the specific surface areas are found to decrease as the Ni content increases. In addition, the amount of hexaaluminate phase is somewhat lower than after calcination at 1873 K (1600°C) due to a higher defect concentration in the unsintered hexaaluminate framework; however, La,Ni hexaaluminates calcined at 1473 K (1200°C) remain relatively phase pure.

	Calcined samples		Reduced samples	
Stoichiometry	Hexaaluminate [wt.%]	Specific surface area [$m^2.g^{-1}$]	% Ni reduced [mol.%]	∅ Ni^0 (STEM/XRD) [nm]
y=0.25	89	14.6	100	10-100/19
y=0.5	88	10.8	100	10-105/24
y=0.75	90	7.3	∼70	15-140/32
y=1	84	8.5	100	15-100/32

Table 3.2: Semi-quantitative phase analysis as well as specific surface area before reduction, and quantification of amount of reduced Ni^{2+} as well as Ni^0 particle size from STEM imaging after reduction of La,Ni hexaaluminates ($LaNi_yAl_{12-y}O_{19-\delta}$) calcined at 1473 K (1200°C)

After reduction, Ni^{2+} is found to be fully - or almost fully - reduced to Ni^0 nanoparticles crystallizing in a fcc lattice, whereas the amount of hexaaluminate phase found in the diffractograms remains unchanged. After calcination at lower temperature and reduction, the size of the Ni^0 nanoparticles is considerably higher and tends to increase with a higher Ni content as confirmed by STEM and confirmed by analysis of diffractometric data by the Scherrer equation. This may be a result from sintering of Ni^0 nanoparticles with increasing Ni content and full reduction with expulsion of Ni^{2+} from the hexaaluminate lattice.

The results of lattice-parameter determination presented in Fig. 3.4 display a similar trend as observed for La,Ni hexaaluminates calcined at 1873 K (1600°C), showing larger lattice parameters *a* and *c* as the degree of Ni^{2+} substitution increases. However, after reduction, the hexaaluminate lattice parameters are found to be slightly smaller (Fig. 3.4-c). It can be speculated that this effect is due to the starting material being partially crystalline, exhibiting a significant defect density that is to a certain extent eliminated during reduction.

STEM investigations reveal a strong textural growth of Ni^0 nanoparticles on the surface of hexaaluminate platelets (Fig. 3.5). Indeed, a large number of characteristic tetrahedral Ni^0 nanoparticles (about 50 nm in size) can be seen on the hexaaluminate platelets, which are highlighted by white arrows in the Fig. 3.5.

The most appealing explanation for the appearance of the metallic Ni^0 tetrahedra on the (001) surface of the hexaaluminate platelets is obtained by visualizing the fcc structure of metallic Ni. Indeed, an octahe-

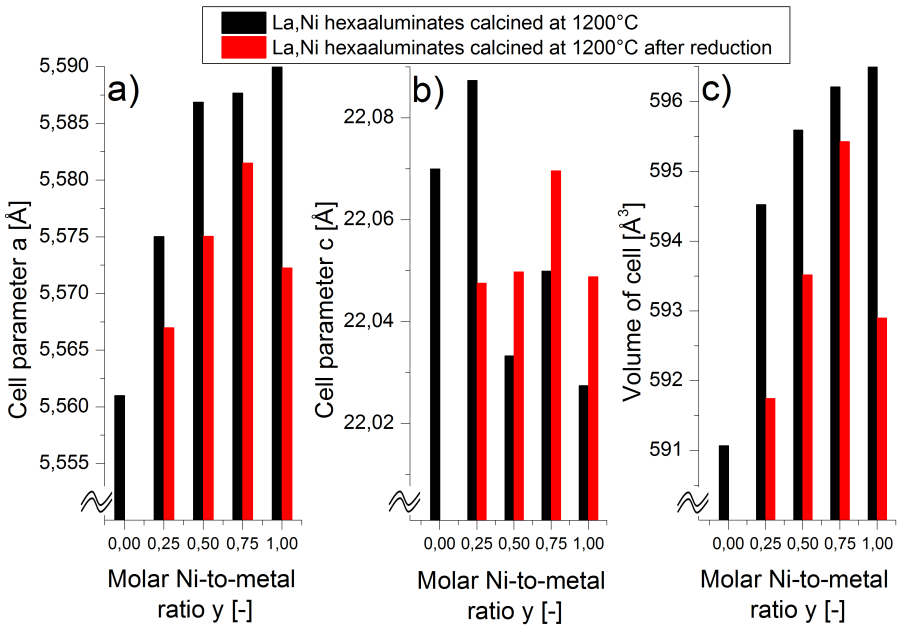

Figure 3.4: Determination of lattice parameters (a, c, unit cell volume) obtained from XRD patterns of La,Ni hexaaluminates ($LaNi_yAl_{12-y}O_{19-\delta}$) calcined at 1473 K (1200°C) before and after reduction: a) Cell parameter a, b) cell parameter c, c) volume of unit cell, reference for y=0 is taken from Crystallographic Database[372] (adapted from[240])

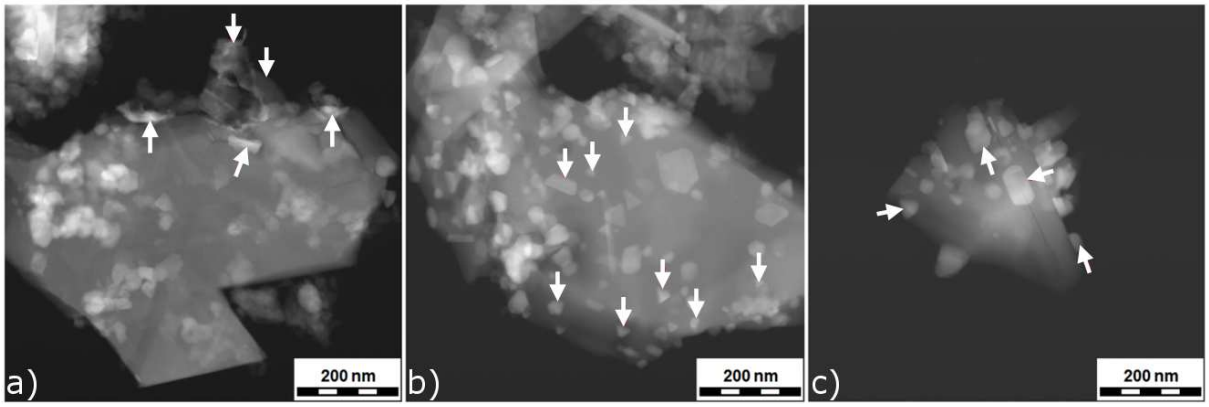

Figure 3.5: STEM images after reduction of $LaNi_yAl_{12-y}O_{19-\delta}$ calcined at 1473 K (1200°C): a) y=0.25, b) y=0.5, and c) y=0.75. White arrows point out the Ni^0 nanoparticles (adapted from[240])

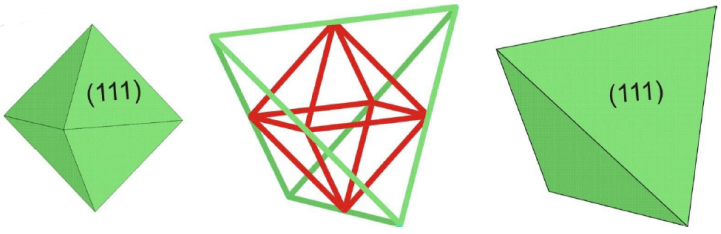

Figure 3.6: Drawing with simplified interactions between Ni^0 nanoparticles and hexaaluminate material showing the preferential growth direction of Ni^0 nanoparticles crystallized in a face-centered cubic structure (adapted from[240]). The Wulff construction should be used here for the determination of crystal forms[377]

dron of Ni^0 crystallizing in the fcc structure can easily be incorporated into an isostructural tetrahedron exposing the same index faces, as shown in the Fig. 3.6. This lattice configuration and crystal exposure of metallic Ni^0 atoms matches with the quasicubic close-packed lattice of the O^{2-} anions inside the spinel blocks, which are very likely to "terminate" the hexaaluminate lattice. The octahedron formed inside the fcc unit cell exhibits a faster growth of every of its second faces. Assuming that the centers of the faces grow faster than edges, the four centers of the fast-growing faces become the "vertices" of the observed tetrahedron. As the amount of reduced Ni increases, the average particle size of Ni^0 becomes larger, the textural growth appears to be less marked, and Ni^0 nanoparticles grow on hexaaluminate and then on the side phase due to excess of metallic Ni.

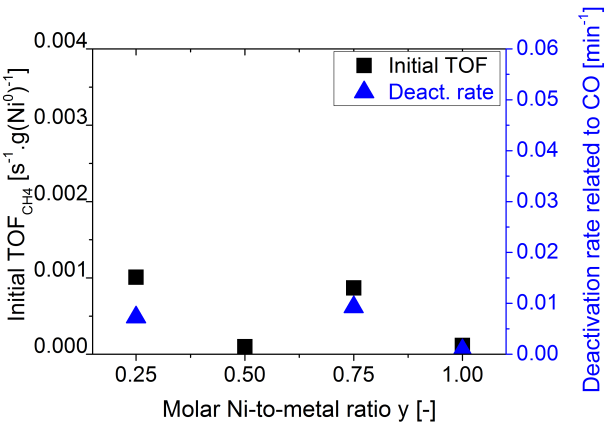

Figure 3.7: Initial TOF of methane consumption and deactivation rate measured for the $LaNi_yAl_{12-y}O_{19-\delta}$ series after calcination at 1473 K (1200°C, adapted from[241])

Compared to La,Ni hexaaluminates calcined at 1873 K (1600°C), the activity of La,Ni hexaaluminates calcined at 1473 K (1200°C) (Fig. 3.7) has only little influence on the initial TOF even at higher Ni contents. For $LaNi_{0.75}Al_{11.25}O_{19-\delta}$, the stability is improved but at the price of low initial TOF at moderate calcination temperatures. $LaNi_{0.75}Al_{11.25}O_{19-\delta}$ calcined at 1473 K (1200°C) is also found to be active, but it displays a significant deactivation rate through CO disproportionation, while $LaNi_{0.5}Al_{11.5}O_{19-\delta}$ and $LaNi_1Al_{11}O_{19-\delta}$ are only poorly active in the target reaction.

3.3 Sr,Ni hexaaluminates calcined at 1473 K (1200°C)

After calcination at 1473 K (1200°C), the Sr,Ni hexaaluminates exhibit a comparable hexaaluminate phase content than the La,Ni hexaaluminate samples, with characteristic reflexes of the magnetoplumbite structure at 2θ=34.3°, 36.4°, and 43.0°. $SrAl_2O_4$ is identified as side phase, and traces of γ-alumina are also detected. The specific surface areas are similar to the ones reported from other groups[378;379].

After reduction, Ni^{2+} is fully reduced - or almost fully reduced - to metallic Ni crystallizing in the fcc lattice. The amount of hexaaluminate phase remains constant, and the Ni^0-nanoparticle-size distribution is larger compared to La,Ni hexaaluminates. A slight increase in the Ni nanoparticle size is observed

Calcined samples			Reduced samples	
Stoichiometry	Hexaaluminate [wt.%]	Specific surface area [$m^2.g^{-1}$]	% Ni reduced [mol.%]	∅ Ni^0 (STEM) [nm]
y=0.25	80	26.0	100	20-150
y=0.5	81	22.3	∼90	25-170
y=0.75	83	29.3	100	50-210
y=1	83	24.6	100	20-150

Table 3.3: Semi-quantitative phase analysis as well as specific surface area before reduction, and quantification of amount of reduced Ni^{2+} as well as Ni^0 particle size from STEM imaging after reduction of Sr,Ni hexaaluminates ($SrNi_yAl_{12-y}O_{19-\delta}$) calcined at 1473 K (1200°C)

as the Ni content increases. This observation could not be supported by the Scherrer equation due to possible overlapping of Ni^0 reflexes.

The determination of lattice parameters from Sr,Ni hexaaluminate patterns is more difficult due to a lack of quality of the diffraction patterns. The interpretation of the results is, therefore, more complicated. After reduction, the unit cell volume shrinks probably due to a similar defect loss reported for La,Ni hexaaluminates calcined at 1473 K (1200°C) (Fig. 3.8-c). The sample $SrNi_{0.75}Al_{11.25}O_{19-\delta}$ exhibits no change in cell parameter after reduction; this might result from its higher crystallinity compared with other Sr,Ni hexaaluminate samples.

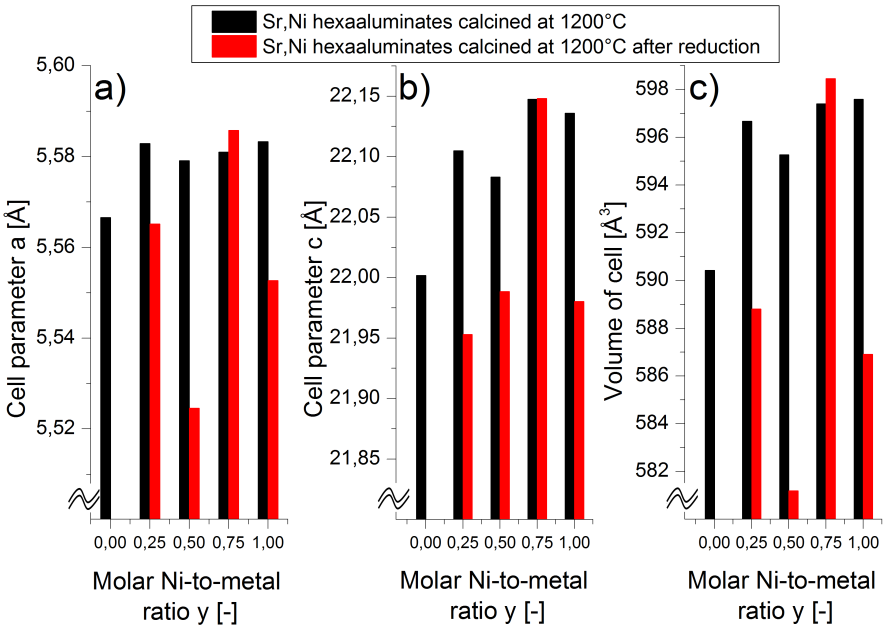

Figure 3.8: Determination of lattice parameters (*a*, *c*, unit cell volume) obtained from XRD patterns of Sr,Ni hexaaluminates ($SrNi_yAl_{12-y}O_{19-\delta}$) calcined at 1473 K (1200°C) before and after reduction: a) Cell parameter *a*, b) cell parameter *c*, c) volume of unit cell, reference for y=0 is taken from Crystallographic Database[372] (adapted from[240])

The STEM images (Fig. 3.9) also show a strong textural growth of Ni nanoparticles after reduction. The nanoparticles of metallic Ni crystallized in tetrahedral shape are also observed especially at low Ni loading (Fig. 3.9-a). As observed on La,Ni hexaaluminates calcined at 1473 K (1200°C), a higher Ni

content in the samples leads to a larger Ni nanoparticle size and a less marked textural growth (Fig. 3.9-b).

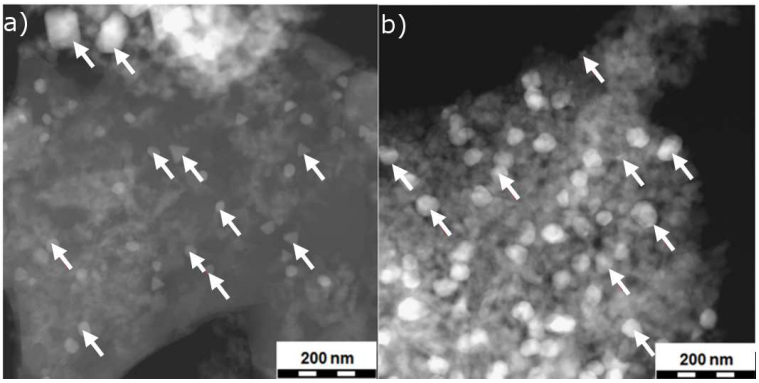

Figure 3.9: STEM images after reduction of $SrNi_yAl_{12-y}O_{19-\delta}$ calcined at 1473 K (1200°C, taken from[240]): a) y=0.25 and b) y=1 . White arrows indicate the Ni^0 nanoparticles.

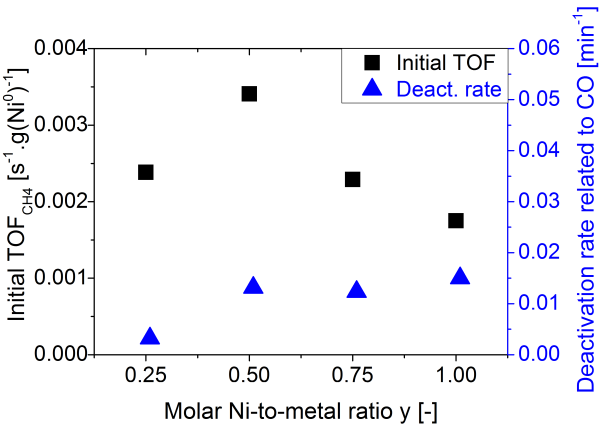

Figure 3.10: Initial TOFs of methane consumption and deactivation rates measured for the $SrNi_yAl_{12-y}O_{19-\delta}$ series after calcination at 1473 K (1200°C, adapted from[241])

In Fig. 3.10, it can be seen that the initial TOFs of methane consumption observed for Sr,Ni hexaaluminates are much higher compared to La,Ni hexaaluminates; however, detrimental effects on stability due to CO disproportionation is observed for most samples. High degrees of Ni^{2+} substitution ($y \geq 0.5$ in $SrNi_yAl_{12-y}O_{19-\delta}$) may enhance the initial TOF, but are certainly damaging to stability since higher Ni contents show stronger deactivation through the Boudouard reaction. $SrNi_{0.25}Al_{11.75}O_{19-\delta}$ displays optimal characteristics for the target reaction with a high TOF and very low deactivation rate.

$SrNi_{0.25}Al_{11.75}O_{19-\delta}$ is an interesting catalyst candidate due to the limited amount of reduced Ni^0 that can be stabilized over the surface defect sites on the Sr hexaaluminate platelets, which produces highly dispersed and stable Ni^0 nanoparticles. On the other hand, higher degrees of Ni^{2+} substitution ($y \geq 0.5$ in $SrNi_yAl_{12-y}O_{19-\delta}$) lead to the formation of larger Ni^0 nanoparticles not fixed on hexaaluminate platelets that increases deactivation through CO disproportionation.

3.4 Ba,Ni hexaaluminates calcined at 1473 K (1200°C)

The results from XRD-pattern analysis are presented in Tab. 3.4. The purity is as high as for La,Ni hexaaluminates, but the specific surface area of Ba,Ni hexaaluminates is increased and comparable to what has been reported previously[47;349;352].

Calcined samples			Reduced samples	
Stoichiometry	Hexaaluminate [wt.%]	Specific surface area [$m^2.g^{-1}$]	% Ni reduced [mol.%]	∅ Ni^0 (STEM) [nm]
y=0.25	87	13.8	100	50-150
y=0.5	93	20.9	100	60-130
y=0.75	88	29.0	100	40-260
y=1	73	24.5	100	40-220

Table 3.4: Semi-quantitative phase analysis as well as specific surface area before reduction, and quantification of amount of reduced Ni^{2+} as well as Ni^0 particle size from STEM imaging after reduction of Ba,Ni hexaaluminates ($BaNi_yAl_{12-y}O_{19-\delta}$) calcined at 1473 K (1200°C)

Ni^{2+} is fully reduced to metallic Ni, crystallizing in a fcc lattice, while the hexaaluminate phase remained after the reduction step; however, the further use of XRD patterns in the Scherrer equation to evaluate Ni^0 nanoparticle size is not possible due to overlapping reflexes of metallic Ni (fcc) and β"-alumina. The Ni^0 nanoparticle size observed by STEM is found to increase with higher Ni content as already noted for the magnetoplumbite samples calcined at 1473 K (1200°C). Ni^0 nanoparticle size is higher than that for La,Ni and Sr,Ni hexaaluminates.

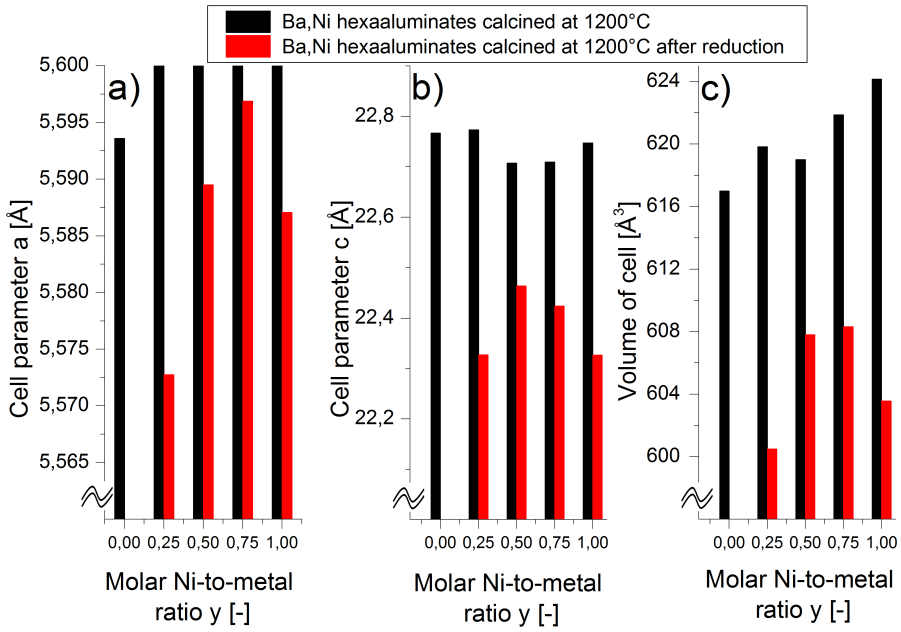

Figure 3.11: Determination of lattice parameters (*a*, *c*, unit cell volume) obtained from XRD patterns of Ba,Ni hexaaluminates ($BaNi_yAl_{12-y}O_{19-\delta}$) calcined at 1473 K (1200°C) before and after reduction: a) Cell parameter *a*, b) cell parameter *c*, c) volume of unit cell, reference for y=0 is taken from Crystallographic Database[372] (adapted from[240])

In Fig. 3.11, the results of the lattice-parameter determination are presented. The lack of reference XRD patterns leads to a complex evaluation; however, an increase in the cell parameter *a* and a decrease in the cell parameter *c* are observed with increasing Ni content in the samples as already explained above for La,Ni hexaaluminates. A smaller unit cell volume is observed after reduction probably due to loss of defects from the calcined material when Ni^{2+} leaves the β"-alumina lattice.

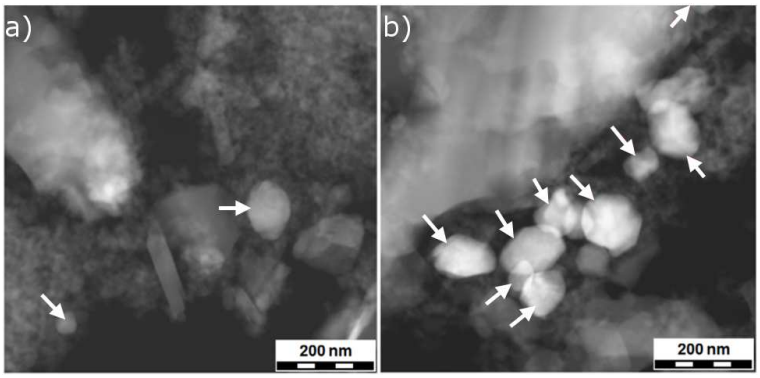

Figure 3.12: STEM images after reduction of $BaNi_yAl_{12-y}O_{19-\delta}$ calcined at 1473 K (1200°C): a) y=0.25 and b) y=0.5 (right). White arrows point out the Ni^0 nanoparticles (taken from[240])

STEM investigations on Ba,Ni hexaaluminates are performed and are presented in Fig. 3.12. Next to small Ni nanoparticles (Fig. 3.12-a), large Ni agglomerates are found as the Ni content is increased over $BaNi_{0.5}Al_{11.5}O_{19-\delta}$ (Fig. 3.12-b). The observations made on magnetoplumbite remain valid, the Ni content in the Ba,Ni hexaaluminate must be kept as low as y=0.25 in $BaNi_yAl_{12-y}O_{19-\delta}$ in order to yield materials with small metallic Ni nanoparticles where Ni^0 nanoparticles exhibit strong textural growth. If the Ni content is maladjusted in the synthesis of Ba,Ni hexaaluminates large Ni agglomerates are formed after reduction like in Fig. 3.12-b.

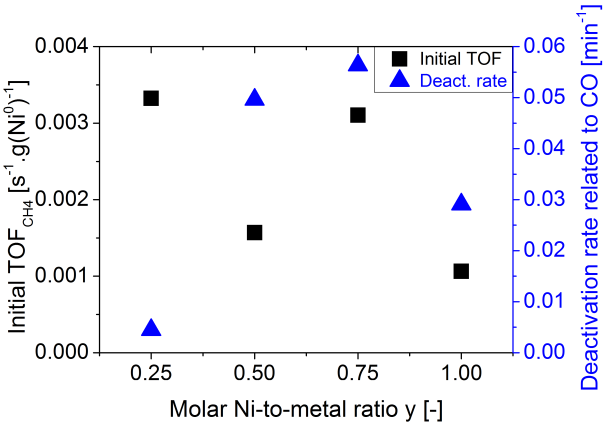

Figure 3.13: Initial TOF of methane consumption and deactivation rate measured for the $BaNi_yAl_{12-y}O_{19-\delta}$ series after calcination at 1473 K (1200°C, adapted from[241])

Finally, the performance evaluation shows similar results as for Sr,Ni hexaaluminates in Fig. 3.13. Only a very low degree of Ni^{2+} substitution (y=0.25 in $BaNi_yAl_{12-y}O_{19-\delta}$) shows high initial TOF and minor deactivation due to enhanced Ni^0 nanoparticle dispersion. The materials with higher Ni content (y≥0.5)

exhibit also high initial TOF; however, they do also show a strong deactivation by CO disproportionation that may be related to the larger Ni^0 nanoparticles formed by the higher content of reduced Ni^{2+} in the samples enhancing coke selectivity[37;38].

3.5 Postulated growth mechanism of Ni^0 nanoparticles on the hexaaluminate phase

Understanding the formation of the metallic Ni nanoparticles under reducing conditions is of major interest to control the textural growth of metallic Ni nanoparticles as well as their high dispersion in the form of very small Ni nanoparticles. Knowing the factors that control these two fundamental characteristics could lead to major breakthroughs in understanding the preparation and use of hexaaluminate catalysts for the reforming of methane under high-severity conditions. For this reason, a mechanistic proposal of the reduction of Ni hexaaluminate is introduced. The hopping mechanism for Ni reduction is postulated in Fig. 3.14 based on the STEM investigation performed. The proposed mechanism occurs stepwise[367]:

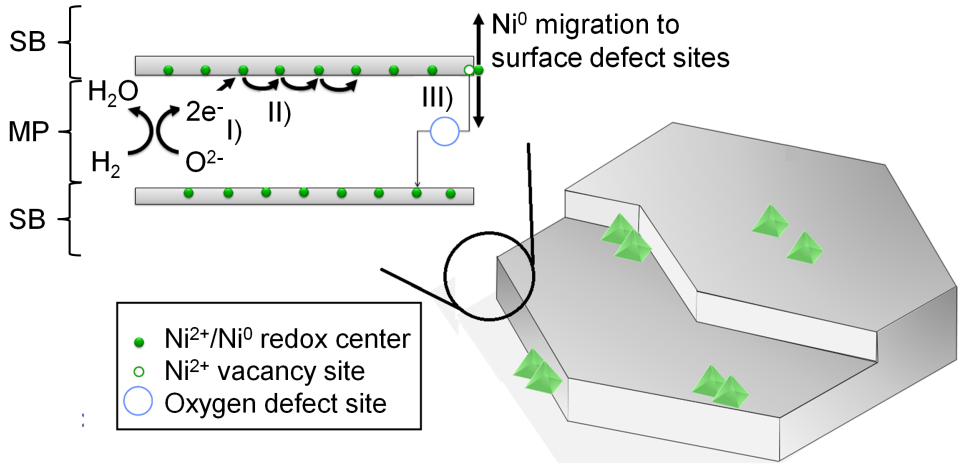

Figure 3.14: Simplified scheme, of the expected reduction mechanism (taken from[367]). (I) Following O^{2-} removal from the interlayer (MP) between the grey spinel blocks (SP), (II) the remaining electrons migrate to surface defect (III) where reduction of Ni^{2+} takes place (on the outer surface). The Ni^0 migrates to surface defect site to minimize its energy. The remaining defects migrate back to the bulk to decrease the spacial demand. As Ni^0 nanoparticles grow, they exhibit an ideal tetrahedral form originating from the Ni^0 fcc lattice (taken from[240]).

I) Oxygen is removed from the mirror plane between the spinel blocks, and an oxygen defect site as well as a negative potential of two electrons are generated. Indeed, it has been reported that O^{2-} is less tightly bound in the mirror plane than in the spinel blocks[47;345;346;380].

II) A Ni^{2+} cation, substituted in the hexaaluminate structure and prevailing near the mirror-plane region[47], migrates in the (001) plane up to the grain boundary[368].

III) At the grain boundary, Ni^{2+} is reduced over the outer surface of the hexaaluminate platelets. The

metallic Ni migrates to surface defect sites next to steps and edges[373–376], where Ni^0 can be regarded as a nucleation center. Ni^{2+} defect sites are thus created inside the mirror plane of the hexaaluminate lattice. This defect can migrate into the hexaaluminate bulk due to the decreased spacial demand caused by former oxygen defects[367].

As the reduction takes place, the proposed mechanism starts over and over again, while the growth of Ni^0 nanoparticles is observed on surface defects near the steps and edges (Fig. 3.2-b). High textural growth is confirmed by the formation of Ni^0 tetrahedra (Fig. 3.5-b and 3.9-a) with a face-centered cubic lattice. This lattice configuration of metallic Ni atoms matches with the quasicubic close-packed lattice of the O^{2-} anions inside the spinel blocks, which are very likely to "terminate" the hexaaluminate lattice. Indeed, the spinel layers are very likely to cover at least the basal plane of the hexaaluminate facets, as it has been demonstrated in the case of $Ba_{0.75}MnAl_{10}O_{17.25}$[362].

In Fig. 3.15, both cubic close-packed configurations of O^{2-} and Ni^0 are displayed showing how the Ni^0 lattice could grow on the basal planes (001) of hexaaluminate spinel blocks. As a result metallic Ni nanoparticles are expected to grow in the (001) direction of the hexaaluminate lattice corresponding to the (111) direction of the Ni^0 lattice. The tetrahedra obtained correspond only to the difference in kinetics of the crystal growth. Figs. 3.15-c and -c' shows how tetrahedra can result from a face-centered cubic lattice of Ni^0 as demonstrated in Fig. 3.6.

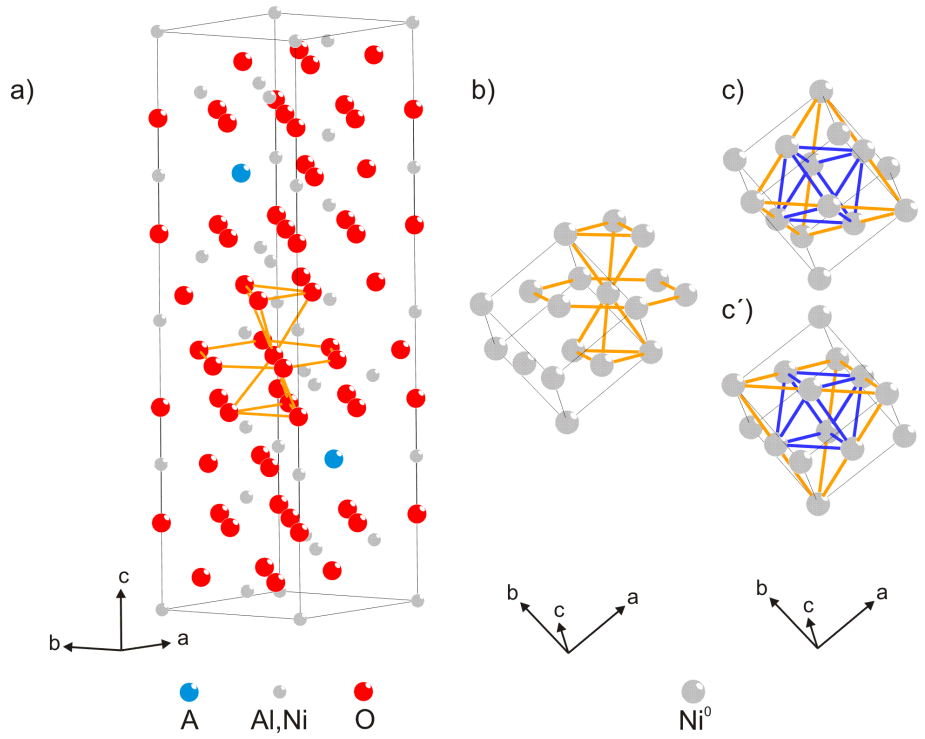

Figure 3.15: Interpretation of the Ni^0 crystal growth on hexaaluminate surface drawn with Diamond[381] (Crystal Impact); a) hexaaluminate with highlight of the quasicubic close-packed lattice of O^{2-} in (001) direction, b) face-centered cubic Ni^0 lattice; its cubic close packed lattice in the (111) direction highlighted, c) and c') resulting tetrahedral forms based on the growth of the Ni^0-lattice (taken from[240]).

As the metallic Ni nanoparticles grow, their textural growth effect is lost little by little and larger Ni^0 nanoparticles appear to be more spherical (Fig. 3.12-b). This is illustrated by Fig. 3.16. Furthermore, excess Ni^0 yields larger Ni^0 nanoparticles on particles of the side phases due to their insufficient stabilization on the hexaaluminate platelets[367] (Fig. 3.12-b). Excess Ni^0 in the form of larger particles may thus result in a higher coke selectivity[37;38] and is, therefore, undesired.

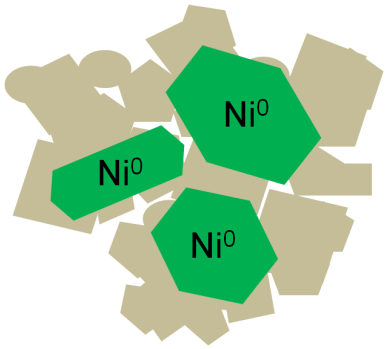

Figure 3.16: Sketch of large Ni^0 agglomerate growth in hexaaluminate and the side phase due to an excess of metallic Ni in the sample (adapted from[367])

Thanks to the suggested reduction mechanism, the identification of reasonable parameters required to achieve a controlled and enhanced dispersion of stabilized Ni^0 nanoparticles is possible:

- the amount of Ni used in the sample composition should be as low as y=0.25 with respect to the formula $ANi_yAl_{12-y}O_{19-\delta}$ and
- the calcination temperature should be kept adequate to maintain a sufficient concentration of surface defect sites over high specific surface area and small hexaaluminate crystallites.

Sticking to these two rules should ensure the formation of highly dispersed Ni^0 nanoparticles over high surface area to achieve a high activity and stability under CO_2 reforming of CH_4 at high pressure.

3.6 Structure-activity relationship of Ni hexaaluminates

Another possibility to illustrate the catalyst performance is to plot the CH_4 conversions after 10 h on stream against the deactivation rate as is shown in Fig.3.17. The hexaaluminate catalysts can be classified into three categories:

- highly stable but moderate activity
- highly active but poor stability
- highly active and stable

La,Ni hexaaluminates calcined at 1473 and 1873 K (1200°C and 1600°C, respectively) exhibit mostly moderate activity, while few exceptions are found to be highly active and deactivated rapidly. The Sr,Ni and Ba,Ni hexaaluminates are found to be very active, but tend to deactivate except if the Ni content in these hexaaluminate samples is lowered to a molar Ni-to-metal ratio of 0.25.

La,Ni hexaaluminates are not appropriate candidates for the CO_2 reforming reaction since they are either moderately active or deactivate significantly. The high calcination temperature of 1873 K (1600°C) leads to low specific surface areas as well as low degree of Ni^{2+} reduction and, therefore, exhibit low activity. $LaNi_{0.25}Al_{11.25}O_{19-\delta}$ calcined at 1873 K (1600°C) is an exception because this catalyst is highly active, but deactivates rapidly probably due to low density of surface defect sites necessary for Ni^0 nanoparticle stabilization. Indeed, the surface defects are very likely eliminated during the long calcination at very high temperature; consequently the Ni^0 nanoparticles sinter easily during CO_2 reforming at high temperature and form large Ni^0 agglomerates that enhance coke selectivity by CO disproportionation.
La,Ni hexaaluminates calcined at 1473 K (1200°C) display a higher activity probably due to higher specific surface area and reducibility of Ni^{2+}. The specificity of La,Ni hexaaluminates may be explained by the trivalent La cation, which may introduce a strong positive charge within the hexaaluminate lattice that is difficult to be compensated in comparison with divalent Sr and Ba cations that could have their positive charge balanced more easily.

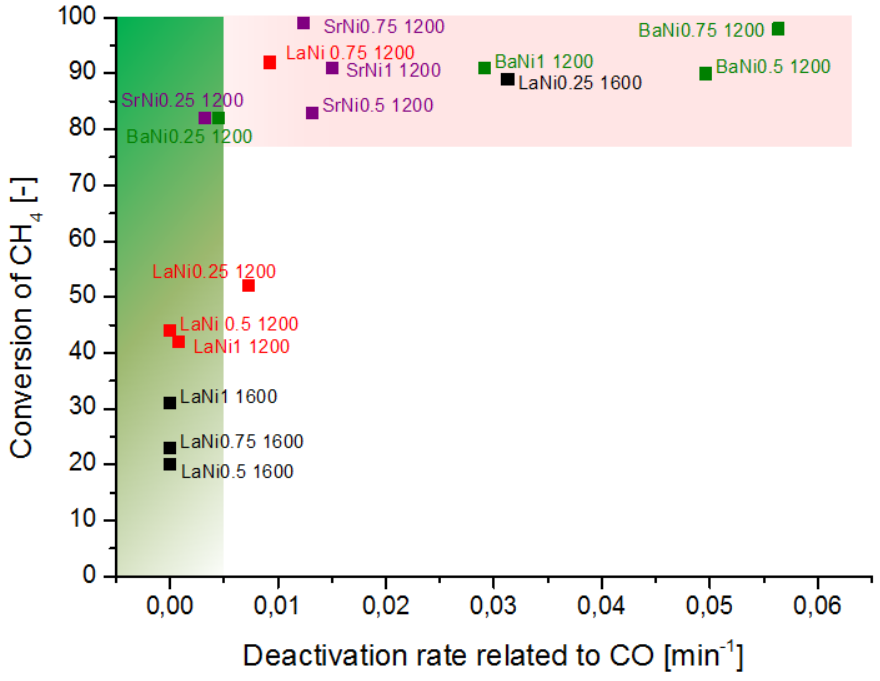

Figure 3.17: Performance overview of Ni hexaaluminates in CO_2 reforming of methane: final methane conversion after 10 h against deactivation rate by CO disproportionation (adapted from [241])

Ba,Ni and Sr,Ni hexaaluminates are found to deactivate easily unless the Ni content is kept at low levels. This clearly originates from the nature of metallic Ni nanoparticles that are larger according to the proposed reduction mechanism. Such behavior has been reported by Gardner et al.[360], who observed that a higher Ni content in $Ba_{0.75}Ni_yAl_{12-y}O_{19-\delta}$ hexaaluminates favored carbon deposition in CO_2 reforming of methane. In line with the experimental results of Chu et al.[40], the Ba,Ni hexaaluminates with the lowest amount of Ni exhibited the highest performance in partial oxidation of methane. In this case, the most stable and active catalyst among $BaNi_yAl_{12-y}O_{19-\delta}$ with y=0.3, 0.6, 0.9, and 1 is the one having the lowest degree of Ni^{2+} substitution (y=0.3). That can only support the Ni^0 growth mechanism proposed and even broaden the use of this mechanism to other applications, like partial oxidation of hydrocarbons, where highly dispersed Ni^0 nanoparticles could be used.
The magnetoplumbite structure seems to exhibit better stability than β-alumina-based materials. Furthermore, the increase of the ionic radius (La<Sr<Ba) seems to increase activity but also decrease stability against CO disproportionation. However, no correlation could be found between the hexaaluminate cell parameters and the performances (activity and stability).

3.7 Conclusions

The hexaaluminate synthesis by freeze drying is proven to be successful in the production of hexaaluminate materials with high purity at moderate calcination temperature with high specific surface area. The hexaaluminate stoichiometries used have a small excess of Ba, La, and Sr that leads to formation of a side phase with the presence of $BaAl_2O_4$, $LaAl_2O_4$, and $SrAl_2O_4$ respectively. These phases do not appear to be detrimental to the stability or activity in the CO_2 reforming of methane.

A reduction mechanism based on a "coupled electron-defect migration reduction" is postulated to describe the strong textural growth of Ni^0 nanoparticles and the performance of Ni hexaaluminates. This mechanism is essential to understand how the growth of Ni^0 nanoparticles can be controlled. To achieve the formation of highly dispersed Ni^0 nanoparticles on a high specific surface area, only the use of moderate calcination temperatures and a Ni content not higher than y=0.25 with respect to the formula $ANi_yAl_{12-y}O_{19-\delta}$ have been shown to be efficient. At different conditions larger and less stable Ni^0 nanoparticles are formed.

Sr,Ni and Ba,Ni hexaaluminates seem to guarantee high activity in the target reaction, while the Ni content should be kept below the sensible threshold of y=0.25 in $BaNi_{0.25}Al_{11.25}O_{19-\delta}$ and $SrNi_{0.25}Al_{11.25}O_{19-\delta}$. If this threshold is exceeded, Ni^0 nanoparticle stabilization is compromised.

La,Ni hexaaluminates appear to be either very active with high selectivity to coke or poorly active and highly stable.

Finally, calcination at moderate temperature yields an optimal amount of hexaaluminate with relative high number of specific surface area as well as high surface defect sites for stabilization of the Ni^0 nanoparticles.

The next step should consist of testing the samples with the highest activity and stability, $SrNi_{0.25}Al_{11.75}O_{19-\delta}$ and $BaNi_{0.25}Al_{11.75}O_{19-\delta}$, in our test unit at 21 bar and 1123 K (850°C) under different reforming conditions to establish the range of stability of such materials under industrially relevant conditions.

Part VIII

General conclusions and outlook

By minimizing the impact of the gas-phase reactions, catalytic systems developed in this thesis (Pt-based catalyst supported on modified zirconia, Ni-based spinels, and Ni-hexaaluminates) show that high activity and stability can be achieved in the mixed-steam CO_2 reforming of methane, and especially at high pressures with the production of syngas with a H_2/CO ratio of one.

- Impact of gas-phase reactions

  In order to achieve stable operations in the mixed-steam CO_2 reforming of methane, the impact of the gas-phase reactions should be minimized to avoid coking. Indeed, methane pyrolysis and further coupling result in the formation of coke precursors like ethylene that may cause reactor plugging by coke formation, typically in upstream from the catalytic bed. The effect of temperature is found to be determining in the formation of coke precursors, which are clearly identified above 1173 K (900°C). The use of higher temperatures increases exponentially the coke-precursor formation rates, which leads to reactor plugging with the H_2O test protocol at 1223 K (950°C).
  The addition of H_2 to the feed stream can efficiently limit the formation of coke precursors particularly above 30 vol.% in the feed stream. The addition of H_2O to the feed stream does not influence the formation rates of coke precursors, which are about two times higher at given operating conditions than with the addition of H_2. The differences observed after addition of H_2 and H_2O to the feed stream for the coke-precursor formation rates imply that H_2O acts as an oxidant in the methane reforming while it confirms that methane cracking is the most important route towards coke deposition.
  In the Deutschmann's group at KIT, the results of this study have been compared with existing mechanisms found in the literature and, as a result, a mechanism of homogeneous reactions has been implemented to the existing heterogeneous reaction mechanism using the DETCHEM platform in order to improve the simulations of technical reactors. In the next step, the simulations will be improved by computing the coke-deposition mechanism and quantifying the coke-deposition rate.

- Pt-based catalysts for CH_4 reforming in the presence of H_2O and CO_2

  The investigations performed on Pt-based catalysts show the important role that the modifications of the zirconia support play in steam reforming of methane when a steam-to-carbon ratio of one at 1123 K (850°C) and 21 bar is used. The use of undoped zirconia leads to a severe decrease of specific surface area down to 0.2 $m^2.g^{-1}$ after 24 h under steam reforming at 1123 K (850°C).
  Modifying zirconia with 5 wt.% of silica showed that silica can improve the thermal stability, giving a specific surface area of 50 $m^2.g^{-1}$ after performing steam reforming at 1123 K (850°C) for 5 h; however, such a support is not suitable for steam reforming due to poor catalytic activity (methane conversion of 8%) because the Pt particles are believed to be embedded in the silica. The use of a ceria surface layer on such silica-modified zirconia appears to achieve thermody-

namic equilibrium at the beginning of the steam reforming test at 1123 K (850°C) and 21 bar with a GHSV of 3800 h^{-1}, but slow and constant deactivation is observed as the ceria layer diffuses into the bulk, resulting in partial embedding of the Pt particles and deactivation.
Modification of zirconia with 10 wt.% La_2O_3 and a CeO_2 surface layer to disperse Pt particles results in an enhanced stability of the catalytic performance. During 60 h in steam reforming of methane with a steam-to-carbon ration of one at 1123 K (850°C) and 21 bar with a GHSV of 3800 h^{-1}, methane conversions are stabilized at 45% after the ceria surface layer diffused into the bulk. This catalyst is chosen for further kinetic investigations.
The kinetic investigations showed that most catalysts reach the thermodynamic equilibrium of steam reforming of methane with or without addition of 18 vol% CO_2 and with CO_2 reforming with addition of 36-30 vol.% H_2O in the temperature range of 1073-1173 K (800-900°C) at atmospheric pressure with a GHSV between 3600-41000 h^{-1}.
Only the performance data obtained at 1023 K (750°C) show that the Pt-based catalyst does not reach the thermodynamic equilibrium of reforming and that in methane reforming, methane activation is accomplished by steam whereas CO_2 reacts with H_2 by reverse water gas shift reaction, or with methane as well, but in this case at a lower reaction rate than in the case of steam reforming. Indeed, TOFs of methane conversions are always higher than TOFs of CO_2 conversions.
The steam reforming of methane in the presence of CO_2 and H_2O over corundum shows that the impact of the gas-phase is significant first at 1173 K (900°C).

- Ni-based spinels for steam reforming in presence of CO_2

  The molten-salt impregnation of hydrotalcite-like support with a Mg/Al ratio of 1/2 appears to be attractive for the preparation of a catalyst for mixed-steam CO_2 reforming at 1123 K (850°C), 21 bar, and with a GHSV of 3800 h^{-1} due to its high activity and stability.
  The fresh catalyst consists of mixed oxides of (Ni/Mg)O and (Ni/Mg)Al_2O_4 that exhibit a relatively high surface area (42 $m^2.g^{-1}$) after 4 h calcination in air at 1123 K (950°C). In comparison with this benchmark material, the catalyst prepared by precipitation is unattractive due to a low specific surface area (11 $m^2.g^{-1}$) and impurities found after final calcination, like Si and Na, whereas the catalyst prepared by spray drying of a hydrotalcite-like carrier undergoes segregation into the hydrotalcite and the boehmite components in the spray tower, leading to 50% larger crystallites of the mixed oxides.
  The preformation of the catalyst results in the reduction of Ni^{2+} from both mixed oxides, thus leaving "free" MgO from (Mg/Ni)O and γ-Al_2O_3 from (Ni/Mg)Al_2O_4 that can react further to form $MgAl_2O_4$ with traces of MgO. Finally, metallic Ni nanoparticles highly dispersed over $MgAl_2O_4$ are obtained after complete preformation under reducing atmosphere (5 vol.% H_2 in N_2) above 1073 K (800°C). This preforming mechanism is shown to be sensitive to the composition of the reducing atmosphere; indeed, the presence of 10 vol.% H_2O and/or 5 vol.% CO_2 significantly inhibits this mechanism.

The catalytic test of 20 ml of catalyst prepared by molten-salt impregnation with a corundum prebed is performed with the H_2 test protocol, exhibiting after long preformation a high and stable performance under CO_2 reforming with 10 vol.% H_2O for more than 100 h with a H_2/CO ratio of 0.9 and methane and CO_2 conversions of 82 and 74%, respectively. These conversions are about 3-4% below the thermodynamic equilibrium of reforming under CO_2 reforming (CH_4/CO_2=0.9/1) with addition of 10 vol.% of H_2O at 1223 K (950°C) and 21 bar for more than 100 h. In comparison, the use of H_2O test protocol leads to inhibition of catalyst preformation, and only a poor performance with methane conversions below 40% is achieved, especially if 78 ml of catalyst is used instead of 20 ml without corundum prebed.
These observations highlight the necessity of catalyst preformation prior to testing in mixed-steam CO_2 reforming.

- Ni-hexaaluminates in CO_2 reforming

Various Ni hexaaluminates are investigated in CO_2 reforming of methane in a differential reactor at 11 bar and 1123 K (850°C) on a small scale for 10 h.
The Ni hexaaluminates synthesized are relatively pure (>80 wt.%) after mild calcination at 1473 K (1200°C) for 2.5 h in air, allowing to reach high specific surface areas of about 15 $m^2.g^{-1}$. The La,Ni and Sr,Ni hexaaluminates exhibit a magnetoplumbite-like structure as main phase and as side phase $LaAlO_3$ and $SrAl_2O_4$, respectively, whereas Ba,Ni hexaaluminates show a very high content of β"-alumina and only traces of $BaAl_2O_4$. The different side phases identified are not found to be detrimental to the activity or stability of Ni hexaaluminates. The reduction of the various Ni hexaaluminates is suggested to be based on a "coupled electron defect migration reduction", resulting in stabilization of Ni on surface defects, where Ni nuclei display first a strong textural growth of metallic Ni nanoparticles, and then they lose their textural growth. Highly dispersed Ni nanoparticles are achieved over the high specific surface area of the hexaaluminate by using mild calcination at 1473 K (1200°C) for 2.5 h and minimizing the Ni loading to y=0.25 in $ANi_yAl_{12-y}O_{19-\delta}$, where A are the mirror-plane cations La, Sr, or Ba.
Regarding the test performance achieved in the differential reactor, the Sr and Ba mirror-plane cations appear to ensure a high activity in the CO_2 reforming of methane at 11 bar, while the Ni loading should be kept below the threshold of y=0.25 in $SrNi_yAl_{12-y}O_{19-\delta}$ and in $BaNi_yAl_{12-y}O_{19-\delta}$ to maintain a high catalytic stability. Indeed, the excess of Ni in the hexaaluminate lattice leads to complete reduction of Ni^{2+} with subsequent formation of Ni nanoparticles in larger particles, which enhances coke selectivity. The calcination should be, therefore, performed at moderate temperatures to obtain high surface areas and higher densities of surface defects that can be used as anchoring points for the metallic Ni nanoparticles. Contrary to Sr,Ni and Ba,Ni hexaaluminates, the La,Ni hexaaluminates exhibit a high stability but only poor activity for the CO_2 reforming of methane at 1123 K (850°C) and 11 bar.

- Outlook

  The concept used for the synthesis of highly dispersed and stable nanoparticles appears to be efficient to design new catalysts for the mixed-steam CO_2 reforming of methane under high pressure. The use of layered hydroxides, like hydrotalcite and boehmite, in the preparation of Ni-based catalysts exhibits high potential in the formation of highly dispersed and stable Ni nanoparticles, which are less prone to coking at high-severity conditions. Understanding the mechanism of the preformation of Ni-based catalysts allows tuning the catalytic features and designing more efficient catalysts for the target reaction.

  Finally, the research made in quasi-ternary catalytic systems A-Al-Ni(-O), with A=Mg, Ba, La, Sr, can be further investigated with the use of quasi-quaternary systems. For instance, (La/Sr),Ni-hexaaluminates or (Ba/Sr),Ni-hexaaluminates with very low Ni content and calcination at 1473 K (1200°C) for 2.5 h could be synthesized and tested for the target reaction to utilize the high stability of La,Ni hexaaluminates and also the high activity of Sr,Ni and Ba,Ni hexaaluminates, respectively.

Bibliography

The references for this PhD thesis are reported below. In addition, at the end of each reference, the page number, where the reference is used, is quoted.

[1] D. Treacy and J.R.H. Ross, *Preprint Papers - American Chemical Society, Division of Fuel Chemistry* **4**, pp. 126–127 (2004). 2

[2] J. Saget, "Global CO_2 emissions set record in 2010 - IEA" (2011). 2

[3] Z. Khorshidi, M. Soltanieh, Y. Saboohi, and M. Arab, *Energy Procedia* **4**, pp. 1886–1892 (2011). 2

[4] Y. Huang, M. Wang, P. Stephenson, S. Rezvani, D. Mc Ilveen-Wright, A. Minchener, N. Hewitt, A. Dave, and A. Fleche, *Fuel* **101**, pp. 244–253 (2012). 2

[5] http://www.chemeurope.com/en/news/117464/messer-commissions-largest-co2-recovery plant.html, "Messer commissions largest CO_2 recovery plant" (2010). 2

[6] http://www.chemicals-technology.com/news/newssichuan-meifeng-messer-jv-new-chinese-co2 plant, "Sichuan-Messer JV to build new Chinese CO_2 plant" (2013). 2

[7] S. Thibeau and V. Mucha, "Have we overestimated saline aquifer CO_2 storage capacity?", Technical report IFP Energies nouvelles (2009). 2

[8] P.L. Spath and M.K. Mann, "The net energy and global warming potential of biomass power compared to coal-fired electricity with CO_2 sequestration - A life cycle approach", Technical report National Renewable Energy Laboratory (2002). 2

[9] G.E. Sigvaldason, *Journal of Volcanology and Geothermal Research* **39**, pp. 97–107 (1989). 2

[10] V. Subramani, P. Sharma, L. Zhang, K. Liu, and C. Song, *Hydrogen and Syngas Production and Purification Technologies: Hydrocarbon Processing for H_2 Production (Eds. K. Liu, C. Song, V. Subramani)* , pp. 14–126, Wiley, New-York (2010). 2, 3, 7, 8, 10, 14, 22, 25, 26, 27, 42, 58, 83, 90, 91, 119

[11] X.D. Peng, A.W. Wang, B.A. Toseland, and P.J.A. Tijm, *Industrial & Engineering Chemistry Research* **38**, pp. 4381–4388 (1999). 2

[12] W. Boll, E. Supp, G. Hochgesand, C. Higman, P.Kalteier, W.D. Müller, M. Kriebel, H. Schlichting, and H. Tanz, *Ullmann's Encyclopedia of Industrial Chemistry* , pp. 75–127, Wiley-VCH, Weinheim (2007). 2, 9

[13] I. Wender, *Fuel Processing Technology* **48**, pp. 189–297 (1996). 7, 9

[14] A.P.E. York, T. Xiao, M.L.H. Green, and J.B. Claridge, *Catalysis Reviews* **49**, pp. 511–560 (2007). 2, 9, 58

[15] M. Limbach and S.A. Schunk, "Acrylates from alkenes and CO_2, the stuff that dreams are made of", Symposium CO_2 als Wertstoff (2012). 2

[16] H.C. Dibbern, P. Olesen, J.R. Rostrup-Nielsen, P.B. Tottrup, and N.R. Udengaard, *Hydrocarbon Processing* **65**, pp. 71–74 (1986). 3, 20

[17] S. Corthals, T. Witvrouwen, P. Jacobs, and B. Sels, *Catalysis Today* **159**, pp. 12–24 (2011).

[18] S.C. Teuner, P. Neumann, and F. von Linde, *Oil gas* **44**, pp. 44–46 (2001). 15, 16

[19] J.R. Rostrup-Nielsen, *Catalysis Today* **111**, pp. 4–11 (2006). 14, 41

[20] X. Song and Z. Guo, *Energy Conversion and Management* **47**, pp. 560–569 (2006). 3, 15

[21] J.R. Rostrup-Nielsen, J. Sehested, and J.K. NØrskov, *Advances in Catalysis* **47**, pp. 65–139 (2002). 3, 14, 15, 20, 22, 23, 25, 73

[22] L.C.S. Kahle, T. Roussière, L. Maier, K. Herrera Delgado, G. Wasserschaff, S.A. Schunk, and O. Deutschmann, *Industrial & Engineering Chemistry Research* **Accepted** (2013). 3, 38, 57, 76, 87, 88

[23] J.R. Rostrup-Nielsen and L.J. Christiansen, *Concept in Syngas Manufacture* , pp. 143–311, Imperial College Press (2011). 3

[24] A. Slagtern, U. Oblbye, R. Blom, I. M. Dahl, and H. Fjellvag, *Applied Catalysis A: General* **245**, pp. 375–388 (1996). 3

[25] G. Valderrama, M.R. Goldwasser, C.U. de Navarro, J.M. Tatibouet, J. Barrault, C. Batiot-Dupeyrat, and F. Martinez, *Catalysis Today* **107**, pp. 785–791 (2005). 59

[26] Y.H. Hu and E. Ruckenstein, *Catalysis Letters* **36**, pp. 145–149 (1996).

[27] S.C. Tang, J.B. Claridge, and M.L.H. Green, *Catalysis Today* **23**, pp. 3–15 (1995).

[28] L.C.S. Kahle, *Reaktionskinetik der Oxidation und Reformierung von H_2, CO und CH_4 über Platinkatalysatoren*, PhD thesis , Karlsruhe Institute of Technology (Faculty of Chemistry and Biosciences), Karlsruhe (Germany) (2013). 3, 57

[29] F. Pompeo, N.N. Nichio, M.M.V.M. Souza, D.V. Cesar, O.A. Ferretti, and M. Schmal, *Applied Catalysis A: General* **316**, pp. 175–183 (2007). 3, 58

[30] C. E. Gigola, M. S. Moreno, I. Costilla, and M. D. Sánchez, *Applied Surface Science* **254**, pp. 325–329 (2007).

[31] J.F. Múnera, S. Irusta, L.M. Cornaglia, E.A. Lombardo, D.V. Cesar, and M. Schmal, *Journal of Catalysis* **245**, pp. 25–34 (2007). 22

[32] K. Hashimoto, S. Watase, and N. Toukai, *Catalysis Letters* **80**, pp. 147–152 (2002).

[33] K. Nagaoka, K. Seshan, K. Aika, and J.A. Lercher, *Journal of Catalysis* **197**, pp. 34–42 (2001). 90, 91

[34] M.C.J. Bradford and M.A. Vannice, *Catalysis Reviews* **41**, pp. 1–42 (1999). 90

[35] M.M. Barroso Quiroga and A.E. Castro Luna, *Industrial & Engineering Chemistry Research* **46**, pp. 5265–5270 (2007). 3

[36] C.H. Bartholomew, *Applied Catalysis A: General* **212**, pp. 17–60 (2001). 3, 20, 25, 26, 37, 38, 39, 40, 41, 73, 74, 79, 80, 97, 135, 156

[37] Z. Li, X. Hu, L. Zhang, S. Liu, and G. Lu, *Applied Catalysis A: General* **417**, pp. 281–289 (2012). 3, 164, 166

[38] L. Zhang, X. Wang, B. Tan, and U.S. Ozkan, *Journal of Molecular Catalysis A: Chemical* **297**, pp. 26–34 (2009). 3, 57, 58, 147, 164, 166

[39] A. Bhattacharyya and V.W. Chang, *Studies in Surface Science and Catalysis* **88**, pp. 207–213 (1994). 4

[40] W. Chu, W. Yang, and L. Lin, *Applied Catalysis A: General* **235**, pp. 39–45 (2002). 149, 168

[41] V.C.H. Kroll, H.M. Swann, and C. Mirodatos, *Journal of Catalysis* **61**, pp. 409–422 (1996). 4, 147

[42] E. Ruckenstein and Y.H. Hu, *Applied Catalysis A: General* **183**, pp. 85–92 (1999). 4

[43] A. Djaidja, S. Libs, A. Kiennemann, and A. Barama, *Catalysis Today* **113**, pp. 194–200 (2006). 4

[44] S.M. de Lima, A.M. da Silva, L.O.O. da Costa, J.M. Assaf, G. Jacobs, B.H. Davis, L.V. Mattos, and F.B. Noronha, *Applied Catalysis A: General* **377**, pp. 181–190 (2010). 4

[45] A. Jahangiri, H. Pahlavanzadeh, and H. Aghabozorg, *International Journal of Hydrogen Energy* **37**, pp. 9977 – 9984 (2012). 4

[46] T.H. Gardner, *Hexaaluminate catalysts for the partial oxidation of middle distillate fuels*, PhD thesis , West Virginia University (Department of Chemical Engineering), Morgantown (USA) (2007). 4, 59, 147, 149

[47] T.H. Gardner, J.J. Spivey, E.L. Kugler, A. Campos, J.C. Hissam, and A.D. Roy, *Journal of Physical Chemistry* **114**, pp. 7888–7894 (2010). 4, 59, 147, 149, 154, 155, 162, 164

[48] C. Song, *Hydrogen and Syngas Production and Purification Technologies: Hydrocarbon Processing for H_2 Production (Eds. K. Liu, C. Song, V. Subramani)* , pp. 1–13, Wiley, New-York (2010). 6, 7

[49] N. Boehmer, T. Roussière, M. Kuba, and S.A. Schunk, *Combinatorial Chemistry and High Throughput Screening* **15**, pp. 123–135 (2012). 6

[50] N.M. Laurendeau, *Progress in Energy and Combustion Science* **4**, pp. 221–270 (1978). 6

[51] X.T. Li, J.R. Grace, C.J. Lim, A.P. Watkinson, H.P. Chen, and J.R. Kim, *Biomass and Bioenergy* **26**, pp. 171–193 (2004). 6

[52] F. Marschner, H.J. Renner, and W. Boll, *Ullmann's Encyclopedia of Industrial Chemistry* , pp. 21–39, Wiley-WCH, Weinheim (2007). 7, 10

[53] R.F. Aguilera, *Energy* **35**, pp. 3332–3339 (2010). 7

[54] H.H. Rogner, *Annual Review of Energy and Environment* **22**, pp. 217–262 (1997).

[55] D. Moest and H. Perlwitz, *Energy* **34**, pp. 1510–1522 (2009). 7

[56] R.E. Stoll and F. von Linde, *Hydrocarbon Processing* **79**, pp. 42–46 (2000). 8

[57] J.N. Armor, *Applied Catalysis A: General* **176**, pp. 159–176 (1999). 9

[58] S. Sircar and T.C. Golden, *Separation Science and Technology* **35**, pp. 667–687 (2000). 9

[59] E. Kikuchi, *Catalysis Today* **56**, pp. 97–101 (2000). 9, 27

[60] S. Uemiya, N. Sato, H. Ando, T. Matsuda, and E. Kikuchi, *Applied Catalysis* **67**, pp. 223–230 (1991). 9

[61] K. Liu, G.D. Deluga, A. Bitsch-Larsen, L.D. Schmidt, and L. Zhang, *Hydrogen and Syngas Production and Purification Technologies: Hydrocarbon Processing for H_2 Production (Eds. K. Liu, C. Song, V. Subramani)* , pp. 127–155, Wiley, New-York (2010). 9, 10, 90

[62] J.M. Ogden, T.G. Kreutz, M. Steinbugler, A.B. Cox, and J.W. White, "Hydrogen energy systems studies", In *Proceedings of the 1996 U.S. DOE Hydrogen Program Review, Miami* (1996). 9

[63] E. Supp, M. Brejc, and W. Liebner, *Ullmann's Encyclopedia of Industrial Chemistry* , pp. 40–52, Wiley-VCH, Weinheim (2007). 9

[64] L.W. ter Haar, *Industrie Chimique Belge* **33**, pp. 655–668 (1968). 9

[65] R. Schwiedernoch, S. Tischer, C. Correa, and O. Deutschmann, *Chemical Engineering Science* **58**, pp. 633–642 (2003). 9

[66] T. Kaltschmitt and O. Deutschmann, "Advances in Chemical Engineering - Fuel Processing for Fuel Cells (Ed. K. Sunmacher)", In *Fuel Cell Engineering* , pp. 1–64. Academic Press, Burlington (2012). 9

[67] R. Farrauto, S. Hwang, L. Shore, W. Ruettinger, J. Lampert, T. Giroux, Y. Liu, and O. Ilinich, *Annual Review of Materials Research* **33**, pp. 1–27 (2003). 10

[68] T. Giroux, S. Hwang, Y. Liu, W. Ruettinger, and L. Shore, *Applied Catalysis B: Environmental* **56**, pp. 95–110 (2005). 10

[69] *Medium-Term Coal Market Report 2012*, International Energy Agency http://www.iea.org/W/bookshop/add.aspx?id=436 (2012). 11

[70] K. Liu, Z. Cui, and T Fletcher, *Hydrogen and Syngas Production and Purification Technologies: Hydrocarbon Processing for H_2 Production (Eds. K. Liu, C. Song, V. Subramani)* , pp. 156–218, Wiley, New-York (2010). 11, 12, 13

[71] R. Reimert and G. Schaub, *Ullmann's Encyclopedia of Industrial Chemistry* , pp. 52–77, Wiley-VCH, Weinheim (2007). 11, 12, 13

[72] James G. Speight, *The Chemistry and Technology of Coal, 3^{rd} Edition* , pp. 635–662, CRC Press, Laramie (2012). 12

[73] J. Phillips, "Different types of gasifiers and their integration with gas turbines", Technical report EPRI / Advanced Coal Generation, http://www.netl.doe.gov/technologies/coalpower/turbines/refshelf/handbook/1.2.1.pdf. 12

[74] F. Chejne and J.P. Hernandez, *Fuel* **81**, pp. 1687–1702 (2002). 12

[75] A. van der Drift, H. Boerrigter, B. Coda, M.K. Cieplik, and K. Hemmes, "Entrained flow gasification of biomass - ash behaviour, feeding issues, and system analyses", Technical report ECN (2004). 12

[76] H.S. Bengaard, J.K. NØrskov, J. Sehested, B.S. Clausen, L.P. Nielsen, A.M. Molenbroek, and J.R. Rostrup-Nielsen, *Journal of Catalysis* **209**, pp. 365–384 (2002). 14

[77] J.R. Rostrup-Nielsen, *Journal of Catalysis* **85**, pp. 31–43 (1984). 14, 20

[78] N.R. Udengaard, J.H.B. Hansen, D.C. Hanson, and J.A. Stal, *Oil & Gas Journal* **90**, pp. 62–67 (1992). 15

[79] H. Tops∅e and J.R. Rostrup-Nielsen, *Scandinavian Journal of Metallurgy* **8**, pp. 168–172 (1979). 15

[80] O. Deutschmann, S. Tischer, S. Kleditzsch, V.M. Janardhanan, C. Correa, D. Chatterjee, N. Mladenov, and H.D. Mihn, "Detchem products", http://www.detchem.com/software/software.html (2010). 16

[81] L. Basini and L. Piovesan, *Industrial & Engineering Chemistry Research* **37**, pp. 258–266 (1998). 20, 27

[82] J.R. Rostrup-Nielsen, *Catalytic Steam Reforming (Eds. J. R. Andersen, M. Boudart)* , pp. 1–118, Springer, Berlin (1984). 20, 42, 83

[83] J.R. Rostrup-Nielsen, J.H. Bak Hansen, and L.M. Aparicio, *Journal of Japanese Petroleum Institute* **40**, pp. 366–377 (1997). 20

[84] J.R. Rostrup-Nielsen and J.H. Bak Hansen, *Journal of Catalysis* **144**, pp. 38–49 (1993). 20

[85] M.V. Twigg, *Catalyst Handbook, 2nd Edition (Ed. M.V. Twigg)*, Wolfe Publishing Ltd., London (1989). 22

[86] J. Xu and G.F. Froment, *AIChE Journal* **35**, pp. 88–96 (1989). 22, 23, 24, 25

[87] M.A. Soria, C. Mateos-Pedrero, P. Marin, S. Ordonez, A. Guerrero-Ruiz, and I. Rodriguez-Ramos, *Applied Catalysis A: General* **413**, pp. 366–374 (2012). 22

[88] S. Asleshirin, M. Bahmani, A. Fazlali, and O. Fadavi, *Petroleum Science and Technology* **30**, pp. 1882–1892 (2012).

[89] D. Chen, R. Lodeng, H. Svendsen, and A. Holmen, *Industrial & Engineering Chemistry Research* **50**, pp. 2600–2612 (2011).

[90] M. Zeppieri, P.L. Villa, N. Verdone, M. Scarsella, and P. De Filippis, *Applied Catalysis A: General* **387**, pp. 147–154 (2010).

[91] K. Hou and R. Hughes, *Chemical Engineering Journal* **82**, pp. 311–328 (2001).

[92] E. Achenbach and E. Riensche, *Journal of Power Sources* **52**, pp. 283–288 (1994).

[93] A. Berman, R.K. Karn, and M. Epstein, *Applied Catalysis A: General* **282**, pp. 73–83 (2005).

[94] N. Laosiripojana, W. Sutthisripok, and S. Assabumrungrat, *Chemical Engineering Journal* **112**, pp. 13–22 (2005). 22

[95] N. Gokon, Y. Osawa, D. Nakazawa, and T. Kodama, *International Journal of Hydrogen Energy* **34**, pp. 1787–1800 (2009). 22, 23

[96] M.F. Mark, F. Mark, and W.F. Maier, *Chemical Engineering & Technology* **20**, pp. 361–370 (1997).

[97] J.G. Jakobsen, T.L. Jorgensen, I. Chorkendorff, and J. Sehested, *Applied Catalysis A: General* **377**, pp. 158–166 (2010).

[98] M.V. Iyer, L.P. Norcio, E.L. Kugler, and D.B. Dadyburjor, *Industrial & Engineering Chemistry Research* **42**, pp. 2712–2721 (2003).

[99] A.R.S. Darujati and W.J. Thomson, *Chemical Engineering Science* **61**, pp. 4309–4315 (2006). 22

[100] C.S. Song and P. Wei, *Catalysis Today* **98**, pp. 463–484 (2004). 22

[101] G.F. Froment, *Journal of Molecular Catalysis A: Chemical* **163**, pp. 147–156 (2000). 22

[102] D.L. Trimm and Z.I. Önsan, *Catalysis Reviews: Science and Engineering* **43**, pp. 31–84 (2001). 22, 23

[103] J.M. Wei and E. Iglesia, *Physical Chemistry Chemical Physics* **6**, pp. 3754–3759 (2004). 23, 25

[104] J.M. Wei and E. Iglesia, *Journal of Catalysis* **225**, pp. 116–127 (2004).

[105] J.M. Wei and E. Iglesia, *Journal of Physical Chemistry B* **108**, pp. 4094–4103 (2004). 91

[106] J.M. Wei and E. Iglesia, *Journal of Physical Chemistry B* **108**, pp. 7253–7262 (2004).

[107] J.M. Wei and E. Iglesia, *Journal of Catalysis* **224**, pp. 370–383 (2004). 23, 25, 91, 119

[108] J. Xu and G.F. Froment, *AIChE Journal* **35**, pp. 97–103 (1989). 25

[109] P. Forzatti and L. Lietti, *Catalysis Today* **52**, pp. 165–181 (1999). 25, 39

[110] J.W. Snoeck, G.F. Froment, and M. Fowles, *Journal of Catalysis* **169**, pp. 250–262 (1997). 25

[111] J.I. Villacampa, C. Royo, E. Romeo, J.A. Montoya, P. Del Angel, and A. Monzón, *Applied Catalysis A: General* **252**, pp. 363–383 (2003). 25

[112] Y.H. Wang, H. Wang, Y. Li, Q.M. Zhu, and B.Q. Xu, *Topics in Catalysis* **32**, pp. 109–116 (2005). 26, 156

[113] O. Deutschmann, H. Knözinger, K. Kochloefl, and T. Turek, *Ullmann's Encyclopedia of Industrial Chemistry* , pp. 483–549, Wiley-VCH, Weinheim (2012). 26, 37, 41, 51

[114] S.M. Walas, *Perry's Chemical Engineers Handbook - 7^{th} Edition, (Eds. R.H. Perry and D.W. Green and J.O. Maloney)*, McGraw-Hill (1997). 26

[115] G. Eigenberger, J.Werther, and H. Schoenfelder, *Handbook of Heterogeneous Catalysis (Eds. G. Ertl, H. Knözinger, J. Weitkamp)* , pp. 1399–1444, Wiley-VCH, Weinheim (1997). 26

[116] W.L. Luyben, *Chemical Reactor Design and Control* , pp. 1–30, Wiley, New-York (2007). 26

[117] J. Hagen, *Industrial Catalysis: A Practical Approach* , pp. 403–424, Wiley-VCH, Weinheim (2006). 26

[118] P.K. Seelam, S. Liguori, A. Iulianelli, P. Pinacci, V. Calabra, M. Huuhtanen, R. Keiski, V. Piemonte, S. Tosti, M. De Falco, and A. Basile, *Catalysis Today* **193**, pp. 42–48 (2012). 27

[119] S. Tosti, *International Journal of Hydrogen Energy* **35**, pp. 12650–12659 (2010). 27

[120] T. Tsuru, K. Yamaguchi, T. Yoshioka, and M. Asaeda, *AIChE Journal* **50**, pp. 2794–2805 (2004). 27

[121] J.R. Rostrup-Nielsen and J. Sehested, *Fuel Chemistry Preprints* **48**, pp. 218–219 (2003). 27

[122] Y. Lim, C.J. Lee, Y.S. Jeong, I.H. Song, C.J. Lee, and C. Han, *Industrial and Engineering Chemistry Research* **51**, pp. 4982–4989 (2012). 27

[123] A.J. Jorpes and B. Steele, *Berzelius: His life and Work*, University of California Press (1971). 28

[124] W. Ostwald, *Zeitschrift für Physikalische Chemie* **3**, pp. 313 (1902). 28

[125] J. Hagen, *Industrial Catalysis: A Practical Approach* , pp. 99–221, Wiley-VCH, Weinheim (2006). 29, 34, 35, 36, 37, 41

[126] P. Wasserscheid, "Kinetics I", Presentation in Catalysis Course in the University of Ulm (2010). 31, 32

[127] N. Brem, *Entwicklung und Optimierung neuartiger Katalysatorsysteme für die partielle Oxidation von o-Xylol mittels Hochdurchsatzmethoden*, PhD thesis , Heidelberg University (Department of Natural Sciences, Mathematics and Computer Sciences), Heidelberg (Germany) (2009). 32

[128] S.A. Schunk, O. Busch, D.G. Demuth, O. Gerlach, A. Hass, J. Klein, and T. Zech, *Surface and Nanomolecular Catalysis (Ed. R. Richards)* , pp. 373–424, Taylor & Francis, Colorado (2006). 32

[129] I. Chorkendorff and J.W. Niemantsverdriet, *Concepts of Modern Catalysis and Kinetics* , pp. 215–263, Wiley-VCH, Weinheim (2003). 33

[130] G. Scacchi, M. Bouchy, J.F. Foucaut, and O. Zahraa, *Cinétique et catalyse* , pp. 339–422, Lavoisier - Tec & Doc (1996). 35, 36, 37, 51

[131] J. Hagen, *Technische Katalyse - Eine Einführung*, Wiley-VCH, Weinheim (1996). 36, 37

[132] D.L. Trimm, *Handbook of Heterogeneous Catalysis (Eds. G. Ertl, H. Knözinger, J. Weitkamp)* , pp. 1263–1282, Wiley-VCH, Weinheim (1997). 37, 38, 40, 74, 97, 135

[133] J.M. Thomas and W.J. Thomas, *Principles and Practice of Heterogeneous Catalysis*, Wiley-VCH, Weinheim (1997). 37

[134] C.H. Bartholomew, *Chemical Engineering* **23**, pp. 96–112 (1984). 38, 39, 58

[135] S. Helveg, J. Sehested, and J.R. Rostrup-Nielsen, *Catalysis Today* **178**, pp. 42–46 (2011). 38

[136] B. Munch, P. Elholm, and M. Stenseng, "From science to proven technology development of new Tops∅e prereforming catalyst AR-401", Technical report Haldor Topsoe (2007). 38

[137] J. Lahiri, T. Miller, L. Adamska, I.I. Oleynik, and M. Batzill, *Nano Letters* **11**, pp. 518–522 (2011). 38

[138] F.G. Billaud and F. Baronnet, *Industrial & Engineering Chemistry Research* **32**, pp. 1549–1554 (1993). 38, 39, 73, 74, 83, 86

[139] K. Norinaga and O. Deutschmann, *Industrial & Engineering Chemistry Research* **46**, pp. 3547–3557 (2007). 38, 39, 73, 74

[140] D.L. Trimm, *Catalysis in Petroleum Refining (Eds. D.L. Trimm, S. Akashah, M. Absi-Halabi, A. Bishara)* , p. 41, Elsevier, Amsterdam (1990). 39

[141] J. Weitkamp and Y. Traa, "Catalyst Deactivation", Presentation in Catalysis Course in the University of Ulm (2011). 39

[142] J.A. Moulijn, A.E. van Diepen, and F. Kapteijn, *Applied Catalysis A: General* **212**, pp. 3–16 (2001). 40

[143] D.L. Trimm, *Studies in Surface Science and Catalysis* **68**, pp. 29–51 (1991). 40

[144] R.T. Baker, C.H. Bartholomew, and D.B. Dadyburjor, "Stability of supported catalyst: Sintering and redispersion", Technical report Royal Society of Chemistry (1991). 40

[145] H. Schaper, E.B.M. Doesburg, and L.L. Van Reijen, *Applied Catalysis* **7**, pp. 211–220 (1983). 40

[146] J.S. Church, N.W. Cant, and D.L. Trimm, *Applied Catalysis A: General* **101**, pp. 105–116 (1993). 40

[147] S.E. Wanke and P.C. Flynn, *Catalysis Reviews: Science and Engineering* **12**, pp. 93–135 (1975). 40

[148] H.H. Lee, *Journal of Catalysis* **63**, pp. 129–137 (1980).

[149] G.C. Chinchen, *Selected developments in catalysis, Report on applied chemistry - Volume 12 (Ed. J.R. Jennings)*, Blackwell Scientific, London (1985). 40

[150] G.A. Fuentes, *Applied Catalysis A: General* **15**, pp. 33–40 (1985). 40

[151] C.H. Bartholomew, *Catalysis* **10** (1992). 40

[152] C. H. Bartholomew, *Studies in Surface Science and Catalysis* **88**, pp. 1–18 (1994). 40

[153] C.H. Bartholomew, P. Agrawal, and J. Katzer, *Advances in Catalysis* **31**, pp. 135–242 (1982). 41

[154] I. Alstrup, B.S. Clausen, C. Olsen, R.H.H. Smits, and J.R. Rostrup-Nielsen, *Studies in Surface Science and Catalysis* **119**, pp. 5–14 (1998). 42

[155] J.S. Lisboa, D.C.R.M. Santos, F.B. Passos, and F.B. Noronha, *Catalysis Today* **101**, pp. 15–21 (2005). 42

[156] M.A. Vicerich, C. Especel, V.M. Benitez, F. Epron, and C.L. Pieck, *Applied Catalysis A: General* **407**, pp. 49–55 (2011). 42

[157] J. Xiao and R.J. Puddephatt, *Coordination Chemistry Reviews* **143**, pp. 457–500 (1995). 42

[158] Y.G. Chen, K. Tomishige, K. Yokoyama, and K. Fujimoto, *Applied Catalysis A: General* **165**, pp. 335–347 (1997). 42

[159] C. Crisafulli, S. Scire, R. Maggiore, S. Minico, and S. Galvagno, *Catalysis Letters* **59**, pp. 21–26 (1999).

[160] B.C. Enger, R. Lodeng, and A. Holmen, *Catalysis Letters* **134**, pp. 13–23 (2010). 42

[161] S. Li, H. Liu, L. Yan, and X. Wang, *Catalysis Communications* **8**, pp. 237–240 (2007). 42

[162] J. Zhang, H. Wang, and A.K. Dalai, *Journal of Catalysis* **249**, pp. 300–310 (2007).

[163] A.K. Avci, D.L. Trimm, A.E. Aksoylu, and Z. Onsan, *Applied Catalysis A: General* **258**, pp. 235–240 (2004).

[164] B. Li, S. Kado, Y. Mukainakano, M. Nurunnabi, T. Miyao, S. Naito, K. Kunimori, and K. Tomishige, *Applied Catalysis A: General* **304**, pp. 62–71 (2006).

[165] B. Pawelec, S. Damyanova, K. Arishtirova, J.L.G. Fierro, and L. Petrov, *Applied Catalysis A: General* **323**, pp. 188–201 (2007).

[166] K. Tomishige, S. Kanazawa, M. Sato, K. Ikushima, and K. Kunimori, *Catalysis Letters* **84**, pp. 69–74 (2002). 42

[167] D. San-José-Alonso, J. Juan-Juan, M.J. Illán-Gomez, and M.C. Román-Martínez, *Applied Catalysis A: General* **371**, pp. 54–59 (2009). 42

[168] S.M. de Lima and J.M. Assaf, *Quimica Nova* **30**, pp. 298–303 (2007).

[169] J.X. Wang, Y. Liu, T.X. Cheng, W.X. Li, Y.L. Bi, and K.J. Zhen, *Applied Catalysis A: General* **250**, pp. 13–23 (2003). 149

[170] A.W. Budiman, S.H. Song, T.S. Chang, C.H. Shin, and M.J. Choi, *Catalysis Surveys from Asia* **16**, pp. 183–197 (2012).

[171] I.G. Črnivec, P. Djinović, B. Erjavec, and A. Pintar, *Chemical Engineering Journal* **207**, pp. 299–307 (2012). 42

[172] R. da Paz Fiuza, M.A. da Silva, and J.S. Boaventura, *International Journal of Hydrogen Energy* **35**, pp. 11216–11228 (2010). 42

[173] V.A. Mazzieri, J.M. Grau, C.R. Vera, J.C. Yori, J.M. Parera, and C.L. Pieck, *Applied Catalysis A: General* **296**, pp. 216–221 (2005). 42

[174] C. Carnevillier, F. Epron, and P. Marecot, *Applied Catalysis A: General* **275**, pp. 25–33 (2004). 42

[175] F. Schüth, M. Hesse, and K.K. Unger, *Handbook of Heterogeneous Catalysis (Eds. G. Ertl, H. Knözinger, F. Schüth, J. Weitkamp)* , pp. 100–119, Wiley-VCH, Weinheim (2008). 43, 44, 45

[176] D. Horn and J. Rieger, *Angewandte Chemie International Edition* **40**, pp. 4330–4361 (2001). 44

[177] S. Auer and D. Frenkel, *Advances in Polymer Science* **173**, pp. 149–208 (2005). 44

[178] E. Marceau, X. Carrier, M. Che, O. Clause, and C. Marcilly, *Handbook of Heterogeneous Catalysis (Eds. G. Ertl, H. Knözinger, F. Schüth, J. Weitkamp)* , pp. 467–484, Wiley-VCH, Weinheim (2008). 45, 46

[179] *Acidity and Basicity of Solids: Theory, Assessment and Utility (Eds. J. Fraissard, L. Petrakis* , pp. 415–444. 46

[180] C.F. Baes and R.E. Messer, *The Hydrolysis of Cations*, Wiley, New-York (1976). 46

[181] J.F. Lambert and M. Che, *Journal of Molecular Catalysis A: Chemical* **162**, pp. 5–18 (2000). 46

[182] B. Delmon, *Handbook of Heterogeneous Catalysis (Eds. G. Ertl, H. Knözinger, F. Schüth, J. Weitkamp)* , pp. 655–676, Wiley-VCH, Weinheim (2008). 47

[183] H. Knözinger, *Handbook of Heterogeneous Catalysis (Eds. G. Ertl, H. Knözinger, F. Schüth, J. Weitkamp)* , pp. 1080–1095, Wiley-VCH, Weinheim (2008). 47, 48, 52, 53, 154

[184] J. Haber, *Journal of the Less Common Metals* **54**, pp. 243–261 (1977). 47

[185] J.L. Lemaitre, *Characterization of Heterogeneous Catalysts (Ed. F. Delanay)*, M. Dekker (1984). 48

[186] S.A. Schunk, N. Böhmer, C. Futter, A. Kuschel, E. Prasetyo, and T. Roussière, *Catalysis (Eds. J.J. Spivey, Y.-F. Han, K.M. Dooley)* , pp. 172–215, Royal Society of Chemistry, London (2012). 48

[187] D. Herein, *Handbook of Heterogeneous Catalysis (Eds. G. Ertl, H. Knözinger, F. Schüth, J. Weitkamp)* , pp. 765–774, Wiley-VCH, Weinheim (2008). 48

[188] J.R. Connolly, "Introduction to Quantitative X-Ray Diffraction Methods", http://epswww.unm.edu/xrd/xrdclass/09-quant-intro.pdf (2012). 48, 49

[189] G. Bergeret and P. Gazellot, *Handbook of Heterogeneous Catalysis (Eds. G. Ertl, H. Knözinger, F. Schüth, J. Weitkamp)* , pp. 738–765, Wiley-VCH, Weinheim (2008). 49, 51, 52

[190] P. Scherrer, *Königliche Gesellschaft der Wissenschaften zu Göttingen* **2**, pp. 98–100 (1918). 49

[191] J.I. Langford and A.J.C. Wilson, *Journal of Applied Crystallography* **11**, pp. 102–113 (1978). 49

[192] J. Hagen, *Industrial Catalysis: A Practical Approach* , pp. 207–222, Wiley-VCH, Weinheim (2006). 50, 51

[193] A.V. Neimark, K.S.W. Sing, and M. Thommes, *Handbook of Heterogeneous Catalysis (Eds. G. Ertl, H. Knözinger, F. Schüth, J. Weitkamp)* , pp. 721–738, Wiley-VCH, Weinheim (2008). 51

[194] S. Brunauer, P.H. Emmett, and E. Teller, *Journal of the American Chemical Society* **60**, pp. 309–319 (1938). 51

[195] *Determination of the specific surface area of powders. recommendation for methods of determination of metal surface area using gas adsorption techniques*, British Standards 4359-4 (1995). 51

[196] J.A. Anderson, M. Fernandez-Garcia, and A. Martinez-Arias, *Supported Metals in Catalysis (Eds. J.A. Anderson, M. Fernandez-Garcia)* , p. 123, Imperial College Press, London (2005). 51

[197] M.S. Chen, Y. Cai, Z. Yan, K.K. Gath, S. Axnanda, and D. Wayne Goodman, *Surface Science* **601**, pp. 5326–5331 (2007). 51

[198] H.J. Freund, *Handbook of Heterogeneous Catalysis (Eds. G. Ertl, H. Knözinger, F. Schüth, J. Weitkamp)* , pp. 1375–1415, Wiley-VCH, Weinheim (2008). 51

[199] Z. Paal and P.G. Menon, *Hydrogen Effects in Catalysis: Fundamentals and Practical Applications (Eds. Z. Paal, P.G. Menon)* , pp. 117–138, Marcel Dekker Inc (1987). 51

[200] C. Karakaya and O. Deutschmann, *Applied Catalysis A: General* **445**, pp. 221–230 (2012). 51, 94

[201] J.J.F. Scholten, A.P. Pijpers, and A.M.L Hustings, *Catalysis Reviews - Science and Engineering* **27**, pp. 151–206 (1985). 52

[202] P.D. Garn, *Thermoanalytical Methods of Investigation*, Academic Press, New York (1965). 52

[203] R.C. Mackenzie, *Differential Thermal Analysis: Applications*, Academic Press, London (1972). 52

[204] A.K. Datye, P.L. Hansen, and S. Helveg, *Handbook of Heterogeneous Catalysis (Eds. G. Ertl, H. Knözinger, F. Schüth, J. Weitkamp)* , pp. 803–833, Wiley-VCH, Weinheim (2008). 53, 54, 55

[205] J.H. Block, A.M. Bradshaw, P.C. Gravelle, J. Haber, R.S. Hansen, M.W. Roberts, N. Sheppard, and K. Tamaru, *Pure and Applied Chemistry* **62**, pp. 2297–2322 (1990). 53

[206] J. Haber, J.H. Block, and B. Delmon, *Pure and Applied Chemistry* **67**, pp. 1257–1306 (1995), 1257-1306. 53, 54, 55

[207] M. Karlik, *Materials and Structures* **8**, pp. 3–15 (2001). 54

[208] J. Liu, *Journal of Electron Microscopy* **54**, pp. 251–278 (2005). 55

[209] M.T. Bore, H.N. Pham, E.E. Switzer, T.L. Ward, A. Fukuoka, and A.K. Datye, *The Journal of Physical Chemistry B* **109**, pp. 2873–2880 (2005). 55

[210] S.J. Pennycook, A.R. Lupini, M. Varela, A. Borisevich, Y. Peng, M.P. Oxley, K. Benthem, and M.F. Chisholm, *Scanning Transmission Electron Microscopy for Nanostructure Characterization (Eds. W. Zhou, Z.L. Wang)* , pp. 152–191, Springer, New York (2007). 55

[211] O. Deutschmann, *Catalysis (Eds. M. Beller, A. Renken, R.A. van Santen)* , pp. 365–389, Wiley-VCH, Weinheim (2011). 57

[212] O. Deutschmann, *Chemie Ingenieur Technik* **83**, pp. 1954–1964 (2011).

[213] L. Maier, M. Hartmann, S. Tischer, and O. Deutschmann, *Combustion and Flame* **158**, pp. 796–808 (2011). 57

[214] K. Herrera Delgado, L. Maier, and O. Deutschmann, "Surface reaction kinetics of steam and CO_2 reforming as well as oxidation of methane over Ni", Presentation at the 46^{th} Jahrestreffen Deutscher Katalytiker (2013). 57, 144

[215] H.S. Roh, K.Y. Koo, J. Jeong, Y. Seo, D. Seo, Y.S. Seo, W.L. Yoon, and S. Park, *Catalysis Letters* **117**, pp. 85–90 (2007). 57, 58, 119

[216] M. Shelef and R.W. McCabe, *Catalysis Today* **62**, pp. 35–50 (2000). 58

[217] T. Li, P.A.J. Bagot, E.A. Marquis, S.C.E. Tsang, and G.D.W. Smith, *The Journal of Physical Chemistry C* **116**, pp. 4760–4766 (2012). 58

[218] S. Guo and E. Wang, *Nano Today* **6**, pp. 240–264 (2011). 58

[219] W. Chen, *Progress in Chemistry* **24**, pp. 246–252 (2012). 58

[220] H. Hua, S. Sergey, and Y.K. Vohra, *Physical Review B: Condensed Matter and Materials Physics* **54**, pp. 6200–6209 (1996). 58

[221] N. Iyi, S. Takekawa, and S. Kimura, *Journal of Solid State Chemistry* **83**, pp. 8–19 (1989). 58, 147

[222] K.Y. Koo, H.S. Roh, Y.T. Seo, D.J. Seo, W.L. Yoon, and S.B. Park, *Applied Catalysis A: General* **340**, pp. 183–190 (2008). 58, 119

[223] K.Y. Koo, H.S. Roh, Y.T. Seo, D.J. Seo, W.L. Yoon, and S.B. Park, *International Journal of Hydrogen Energy* **33**, pp. 2036–2043 (2008). 58, 119

[224] Z.W. Liu, H.S. Roh, and K.W. Jun, *Journal of Industrial and Engineering Chemistry* **9**, pp. 753–761 (2003). 59, 119

[225] J.W. Bae, A.R. Kim, S.C. Baek, and K.W. Jun, *Reaction Kinetics Mechanisms and Catalysis* **104**, pp. 377–388 (2011). 59, 119

[226] K.W. Jun, S.C. Baek, J.W. Bae, K.S. Min, S.L. Song, T.Y. Oh (Hyundai Heavy Industries Corporation and Korea Research Institute of Chemical Technology), "Patent EP 2308594 A2" (2009). 58, 59, 119

[227] A. Ersson, *Materials for High-Temperature Catalytic Combustion*, PhD thesis , Kungliga Tekniska Högskolan (Department of Chemical Engineering and Technology), Stockholm (Sweden) (2003). 58

[228] R. Kikuchi, Y. Iwasa, T. Takeguchi, and K. Eguchi, *Applied Catalysis A: General* **281**, pp. 61–67 (2005). 58, 149

[229] O. Yamamoto, Y. Takeda, R. Kanno, and M. Noda, *Solid State Ionics* **22**, pp. 241–246 (1987). 58

[230] M.E.S. Hegarty, A.M. O'Connor, and J.R.H. Ross, *Catalysis Today* **42**, pp. 225–232 (1998). 58

[231] A.P.E. York, J.B. Claridge, C. Marquez-Alvarez, A.J. Brungs, S.C. Tsang, and M.L.H. Green, *Studies in Surface Science and Catalysis* **110**, pp. 711–720 (1997). 58, 60

[232] A.J. Brungs, A.P.E. York, and M.L.H. Green, *Catalysis Letters* **57**, pp. 65–69 (1999). 60

[233] A.J. Brungs, A.P.E. York, J.B. Claridge, C. Marquez-Alvarez, and M.L.H. Green, *Catalysis Letters* **70**, pp. 117–122 (2000). 60

[234] J.B. Claridge, A.P.E York, A.J. Brungs, C. Marquez-Alvarez, J. Sloan, S.C. Tsang, and M.L.H. Green, *Journal of Catalysis* **180**, pp. 85–100 (1998). 60

[235] A.P.E. York, T. Suhartanto, and M.L.H. Green, *Studies in Surface Science and Catalysis* **119**, pp. 777–782 (1998). 58, 60

[236] T.V. Choudhary, S. Banerjee, and V.R. Choudhary, *Applied Catalysis A: General* **234**, pp. 1–23 (2002). 59

[237] P. Forzatti and G. Groppi, *Catalysis Today* **54**, pp. 165–180 (1999).

[238] B.W.L. Jang, R.M. Nelson, J.J. Spivey, M. Ocal, R. Oukaci, and G. Marcelin, *Catalysis Today* **47**, pp. 103–113 (1999).

[239] P. Artizzu-Duart, J.M. Millet, N. Guilhaume, E. Garbowski, and M. Primet, *Catalysis Today* **59**, pp. 163–177 (2000). 59

[240] T. Roussière, K.M. Schelkle, S. Titlbach, G. Wasserschaff, A. Milanov, E. Schwab, O. Deutschmann, S. Schulz, A. Jentys, J. A. Lercher, and S.A. Schunk, *In preparation* (2013). 59, 146, 147, 148, 150, 155, 156, 158, 160, 161, 162, 163, 164, 165

[241] T. Roussière, S. Schulz, K.M. Schelkle, G. Wasserschaff, A. Jentys, J. A. Lercher, O. Deutschmann, A. Milanov, E. Schwab, and S.A. Schunk, *In preparation* (2013). 59, 66, 67, 146, 147, 153, 156, 159, 161, 163, 167

[242] T.H. Gardner, D. Shekhawat, D.A. Berry, M.W. Smith, M. Salazar, and E.L. Kugler, *Applied Catalysis A: General* **323**, pp. 1–8 (2007). 59, 147, 149

[243] N.E. Mc Guire, N.P. Sullivan, O. Deutschmann, H. Zhu, and R.J. Kee, *Applied Catalysis A: General* **394**, pp. 257–265 (2011). 59, 149

[244] K. Ikkour, D. Sellam, A. Kiennemann, S. Tezkratt, and O. Cherifi, *Catalysis Letters* **132**, pp. 213–217 (2009).

[245] Z.L. Xu, M. Zhen, Y.L. Bi, and K.J. Zhen, *Applied Catalysis A: General* **198**, pp. 267–273 (2000). 149

[246] Z.L. Xu, M. Zhen, Y.L. Bi, and K.J. Zhen, *Catalysis Letters* **64**, pp. 157–161 (2000). 59, 149, 154

[247] Y. Liu, T. Cheng, D. Li, P. Jiang, J. Wang, W. Li, Y. Bi, and K. Zhen, *Catalysis Letters* **85**, pp. 101–107 (2003). 59, 149

[248] G. Sierra Gallego, C. Batiot-Dupeyrat, J. Barrault, E. Florez, and F. Mondragon, *Applied Catalysis A: General* **334**, pp. 251–258 (2008). 59

[249] G. Valderrama, A. Kiennemann, and M.R. Goldwasser, *Catalysis Today* **133**, pp. 142–148 (2008). 59

[250] G. Valderrama, A. Kiennemann, and M.R. Goldwasser, *Journal of Power Sources* **195**, pp. 1765–1771 (2010). 59

[251] G. Sierra Gallego, J. Gallego Marin, C. Batiot-Dupeyrat, J. Barrault, and F. Mondragon, *Applied Catalysis A: General* **369**, pp. 97–103 (2009). 59

[252] G.S. Gallego, C. Batiot-Dupeyrat, J. Barrault, and F. Mondragon, *Industrial & Engineering Chemistry Research* **47**, pp. 9272–9278 (2008). 59

[253] T. Hayakawa, S. Suzuki, J. Nakamura, T. Uchijima, S. Hamakawa, K. Suzuki, T. Shishido, and K. Takehira, *Applied Catalysis A: General* **183**, pp. 273–285 (1999). 59

[254] S. Pavlova, L. Kapokova, R. Bunina, G. Alikina, N. Sazonova, T. Krieger, A. Ishchenko, V. Rogov, R. Gulyaev, V. Sadykovab, and C. Mirodatosc, *Catalysis Science & Technology* **2**, pp. 2099–2108 (2012). 59

[255] V.R. Choudhary, K.C. Mondal, A.S. Mamman, and U.A. Joshi, *Catalysis Letters* **100**, pp. 271–276 (2005). 59, 60

[256] V.R. Choudhary and K.C. Mondal, *Applied Energy* **83**, pp. 1024–1032 (2006). 59

[257] A. Zhang, A. Zhu, B. Chen, S. Zhang, C. Au, and C. Shi, *Catalysis Communications* **12**, pp. 803–807 (2011). 60

[258] A. Lange de Oliveira, M. Dejmek, O. Koechel, J. Bechtel (hte AG), "Patent WO 12052149 a" (2012). 65

[259] J.M. Ginsburg, J. Pina, T. El Solh, and H.I. de Lasa, *Industrial & Engineering Chemistry Research* **44**(14), pp. 4846–4854 (2005). 73

[260] T. Kaltschmitt, L. Maier, M. Hartmann, C. Hauck, and O. Deutschmann, *Proceedings of the Combustion Institute* **33**, pp. 3177–3183 (2011). 73

[261] Q. Chen, J.H.B.J Hoebink, and G.B. Marin, *Industrial & Engineering Chemistry Research* **30**, pp. 2088–2097 (1991). 73

[262] H. Zanthoff and M. Baerns, *Industrial & Engineering Chemistry Research* **29**, pp. 2–10 (1990). 73

[263] K. Norinaga, O. Deutschmann, N. Saegusa, and J.I. Hayashi, *Journal of Analytical and Applied Pyrolysis* **86**, pp. 148–160 (2009). 73, 74, 83

[264] A. Becker and K.J. Hüttinger, *Carbon* **36**, pp. 213–224 (1998). 73, 74, 76, 78, 80

[265] I. Naydenova, M. Nullmeier, J. Warnatz, and A. Vlasov, *Combustion Science and Technology* **176**, pp. 1667–1703 (2004). 74

[266] K. Norinaga and K.J. Hüttinger, *Carbon* **41**, pp. 1509–1514 (2003). 74

[267] D.A. Dowden, *Catalysis*, Specialist Periodical Report Chemical Society (1978). 74

[268] J.H. Sinfelt, *AIChE Journal* **25**, pp. 734–734 (1979). 74, 80

[269] A. Becker, Z. Hu, and K.J. Hüttinger, *Fuel* **79**, pp. 1573–1580 (2000). 74, 76, 78, 80

[270] A. Li, K. Norinaga, W. Zhang, and O. Deutschmann, *Composites Science and Technology* **68**, pp. 1097–1104 (2008). 76, 78

[271] U. Olsbye, O. Moen, A. Slagtern, and I.M. Dahl, *Applied Catalysis A: General* **228**, pp. 289–303 (2002). 79

[272] C. Naccache, *Deactivation and poisonong catalysts (Eds. J. Oudar, H. Wise)* , pp. 185–201, Marcel Dekker (1985). 80

[273] E.A. Blekkan, R. Myrstad, O. Olsvik, and O.A. Rokstad, *Carbon* **30**, pp. 665–673 (1992). 83

[274] A. Holmen, O. Olsvik, and O.A. Rokstad, *Fuel Processing Technology* **42**, pp. 249–267 (1995). 83

[275] F.G. Billaud, C.P. Gueret, and F. Baronnet, *Industrial & Engineering Chemistry Research* **31**, pp. 2748–2753 (1992). 86

[276] J.H. Bitter, *Platinum bifunctional catalysts for carbon dioxide reforming of methane*, PhD thesis , University of Twente (Faculty of Science and Technology), Twente (Netherlands) (1997). 90, 91

[277] M.L. Kastens and R. Sutherland, *Industrial & Engineering Chemistry* **42**, pp. 582–593 (1950). 90

[278] J.F. Snuggs, J.A. Bock, J.E. Wolf (Standard Oil Company), "Patent US 2773014" (1956).

[279] V. Haensel (Universal Oil Products Company), "Patent US 2479110" (1949).

[280] V.B. Mortola, S. Damyanova, D. Zanchet, and J.M.C. Bueno, *Applied Catalysis B: Environmental* **107**, pp. 221–236 (2011). 90

[281] K. Kusakabe, K.I. Sotowa, T. Eda, and Y. Iwamoto, *Fuel Processing Technology* **86**, pp. 319–326 (2004). 90

[282] A. Ballarini, F. Basile, P. Benito, I. Bersani, G. Fornasari, S. de Miguel, S.C.P. Maina, J. Vilella, A. Vaccari, and O.A. Scelza, *Applied Catalysis A: General* **433**, pp. 1–11 (2012). 90

[283] Y. Takahashi and T. Yamazaki, *Fuel* **102**, pp. 239–246 (2012). 90

[284] A.N.J. van Keulen, M.E.S. Hegarty, J.R.H. Ross, and P.F. van den Oosterkamp, *Studies in Surface Science and Catalysis* **107**, pp. 537–546 (1997). 90

[285] K. Tao, Y. Zhang, S. Terao, and N. Tsubaki, *Catalysis Today* **153**, pp. 150–155 (2010). 91

[286] S.M. Stagg-Williams, F.B. Noronha, G. Fendley, and D.E. Resasco, *Journal of Catalysis* **194**, pp. 240–249 (2000). 91, 104

[287] A.M. O'Connor, Y. Schuurman, J. R.H. Ross, and C. Mirodatos, *Catalysis Today* **115**, pp. 191–198 (2006). 90

[288] L.V. Mattos, E. Rodino, D.E. Resasco, F.B. Passos, and F.B. Noronha, *Fuel Processing Technology* **83**, pp. 147 – 161 (2003). 90, 91

[289] J.H. Bitter, K. Seshan, and J.A. Lercher, *Journal of Catalysis* **171**, pp. 279–286 (1997). 91, 92, 99

[290] J.H. Bitter, K. Seshan, and J.A. Lercher, *Journal of Catalysis* **183**, pp. 336–343 (1999). 90, 91, 92, 96

[291] J.H. Bitter, W. Hally, K. Seshan, J.G. van Ommen, and J.A. Lercher, *Catalysis Today* **29**, pp. 349–353 (1996). 90

[292] G.K. Reddy, S. Loridant, A. Takahashi, P. Delichère, and B.M. Reddy, *Applied Catalysis A: General* **389**, pp. 92–100 (2010). 91, 97, 99, 103

[293] Y.Z. Chen, B.J. Liaw, and W.H. Lai, *Applied Catalysis A: General* **230**, pp. 73–83 (2002). 90, 91, 97

[294] M.M.V.M. Souza, D.A.G. Aranda, and M. Schmal, *Journal of Catalysis* **204**, pp. 498–511 (2001). 90, 91

[295] S. Fokkema, *International Tables for Cristallography - Volume A - Space Group symmetry, 5^{th} Edition (Ed. T. Hahn)* , pp. 111–718, Springer, Dordrecht (2005). 90, 117, 147

[296] A.F. Holleman, E. Wiberg, and N. Wiberg, *Lehrbuch der Anorganischen Chemie* , pp. 1533–1541, W. de Gruyter, Berlin (2007). 90

[297] F. Gallino, C. Di Valentin, and G. Pacchioni, *Physical Chemistry Chemical Physics* **13**, pp. 17667–17675 (2011). 90

[298] K. Momma and F. Izumi, *Journal of Applied Crystallography* **44**, pp. 1272–1276 (2011). 90, 117, 119, 120, 148

[299] M. Winterer, R. Delaplane, and R. Mc Greevy, *Journal of Applied Crystallography* **35**, pp. 434–442 (2002). 90

[300] J.E. Jaffe, R.A. Bachorz, and M. Gutowski, *Physical Review B: Condensed Matter and Materials Physics* **72**, pp. 144107–144116 (2005). 90

[301] P. Bouvier, E. Djurado, G. Lucazeau, and T. Le Bihan, *Physical Review B: Condensed Matter and Materials Physics* **62**, pp. 8731–8737 (200). 90

[302] S. Damyanova, B. Pawelec, K. Arishtirova, M.V. Martinez Huerta, and J.L.G. Fierro, *Applied Catalysis B: Environmental* **89**, pp. 149–159 (2009). 91

[303] J.R. Kim, W.J. Myeong, and S.K. Ihm, *Applied Catalysis B: Environmental* **71**, pp. 57–63 (2007). 91

[304] P.D.L. Mercera, J.G. van Ommen, E.B.M. Doesburg, A.J. Burggraaf, and J.R.H. Ross, *Applied Catalysis* **71**, pp. 363–391 (1991). 91

[305] P.D.L. Mercera, J.G. van Ommen, E.B.M. Doesburg, A.J. Burggraaf, and J.R.H. Roes, *Applied Catalysis* **78**, pp. 79–96 (1991). 91

[306] S.M. Stagg, E. Romeo, C. Padro, and D.E. Resasco, *Journal of Catalysis* **178**, pp. 137–145 (1998). 91

[307] K. Takanabe, K.I. Aika, K. Inazu, T. Baba, K. Seshan, and L. Lefferts, *Journal of Catalysis* **243**, pp. 263–269 (2006). 91, 97, 103

[308] R. Pellegrini, G. Leofanti, G. Agostini, L. Bertinetti, S. Bertarione, E. Groppo, A. Zecchina, and C. Lamberti, *Journal of Catalysis* **267**, pp. 40–49 (2009). 99, 103

[309] M.Y. Kim, J.S. Choi, T.J. Toops, E.S. Jeong, S.W. Han, V. Schwartz, and J. Chen, *Catalysts* **3**, pp. 88–103 (2013). 99

[310] J.R. Rostrup-Nielsen (Haldor Tops∅e), "Patent UK 1,182,829" (1967). 117

[311] J. N. Rostrup (Haldor Tops∅e), "Patent US 3791993" (1968).

[312] H.F.A. Tops∅e (Haldor Tops∅e), "Patent UK 1058757" (1963). 117

[313] A.F. Holleman, E. Wiberg, and N. Wiberg, *Lehrbuch der Anorganischen Chemie* , pp. 1137–1178, W. de Gruyter, Berlin (2007). 117, 118

[314] A. Bhattacharyya, V.W. Chang, and D.J. Schumacher, *Applied Clay Science* **13**, pp. 317–328 (1998). 118, 119, 138

[315] A. Bhattacharyya (Amoco Corporation), "Patent US 5246899" (1993).

[316] A. Bhattacharyya, W.D. Chang, M.S. Kleefisch, C.A. Udovich (Amoco Corporation), "Patent US 5399537" (1995).

[317] A. Bhattacharyya, W.D. Chang, M.S. Kleefisch, C.A. Udovich (Amoco Corporation), "Patent US 5591238" (1997).

[318] A. Bhattacharyya, W.D. Chang, M.S. Kleefisch, C.A. Udovich (Amoco Corporation), "Patent US 5653774" (1997). 118

[319] K. Takehira, T. Kawabata, T. Shishido, K. Murakami, T. Ohi, D. Shoro, M. Honda, and K. Takaki, *Journal of Catalysis* **231**, pp. 92–104 (2005). 118

[320] K. Takehira, T. Shishido, D. Shouro, K. Murakami, M. Honda, T. Kawabata, and K. Takaki, *Applied Catalysis A: General* **279**, pp. 41–51 (2005).

[321] K. Takehira, T. Shishido, P. Wang, T. Kosaka, and K. Takaki, *Journal of Catalysis* **221**, pp. 43–54 (2004).

[322] K. Takehira, T. Shishido, D. Shoro, K. Murakami, M. Honda, T. Kawabata, and K. Takaki, *Catalysis Communications* **5**, pp. 209–213 (2004). 118

[323] A. Serrano-Lotina, L. Rodriguez, G. Munoz, A.J. Martin, M.A. Folgado, and L. Daza, *Catalysis Communications* **12**, pp. 961–967 (2011).

[324] C. Resini, T. Montanari, L. Barattini, G. Ramis, G. Busca, S. Presto, P. Riani, R. Marazza, M. Sisani, F. Marmottini, and U. Costantino, *Applied Catalysis A: General* **355**, pp. 83–93 (2009).

[325] K. Nagaoka, A. Jentys, and J.A. Lercher, *Journal of Catalysis* **229**, pp. 185–196 (2005).

[326] M. Li, X. Wang, S. Li, S. Wang, and X. Ma, *International Journal of Hydrogen Energy* **35**, pp. 6699–6708 (2010).

[327] D. Li, L. Wang, M. Koike, Y. Nakagawa, and K. Tomishige, *Applied Catalysis B: Environmental* **102**, pp. 528–538 (2011).

[328] R. Guil-Lopez, V. La Parola, M.A. Pena, and J.L.G. Fierro, *International Journal of Hydrogen Energy* **37**, pp. 7042–7055 (2012).

[329] C.E. Daza, C.R. Cabrera, S. Moreno, and R. Molina, *Applied Catalysis A: General* **378**, pp. 125–133 (2010). 118

[330] L.J.I. Coleman, W. Epling, R.R. Hudgins, and E. Croiset, *Applied Catalysis A: General* **363**, pp. 52–63 (2009). 129, 136

[331] F. Basile, P. Benito, G. Fornasari, and A. Vaccari, *Applied Clay Science* **48**, pp. 250–259 (2010). 118

[332] O.W. Perez-Lopez, A. Senger, N.R. Marcilio, and M.A. Lansarin, *Applied Catalysis A: General* **303**, pp. 234–244 (2006). 118

[333] F. Cavani, F. Trifirò, and A. Vaccari, *Catalysis Today* **11**, pp. 173–301 (1991). 118

[334] S. Miyata and A. Okada, *Clays and Clay Minerals* **25**, pp. 14–18 (1977). 119

[335] T. Hibino and A. Tsunashima, *Clays and Clay Minerals* **45**, pp. 842–853 (1997). 118

[336] L. Ingram and H.F.W. Taylor, *Mineralogical Magazine* **36**, pp. 465–479 (1967). 118

[337] R. Allmann, *Acta Crystallographica* **B24**, pp. 972–977 (1968). 118

[338] S. Miyata, *Clays and Clay Minerals* **28**, pp. 50–56 (1980). 118

[339] G. Fornasari, M. Gazzano, D. Matteuzzi, F. Trifiro, and A. Vaccari, *Applied Clay Science* **10**, pp. 69–82 (1995). 118, 127

[340] Sasol, "PURAL MG 30, 70 (Product information)", http://www.sasoltechdata.com/tds/PURAL-MG.pdf (2007). 120

[341] K.Y. Koo, H.S. Roh, U.H. Jung, Y.T. Seo, D.J. Seo, and W.L. Yoon, *Catalysis Today* **146**, pp. 166–171 (2009). 127, 129

[342] C.L. Huang, C.Y. Tai, C.Y. Huang, and Y.H. Chien, *Journal of The American Ceramic Society* **93**, pp. 1999–2003 (2010). 127

[343] L. Xu, H. Song, and L. Chou, *Applied Catalysis B: Environmental* **108**, pp. 177–190 (2011). 136

[344] K. Herrera Delgado, L. Maier, and O. Deutschmann, "Surface reaction kinetics of steam and CO_2 reforming as well as oxidation of methane over Ni", Presentation at the 23^{rd} North American Catalysis Society Meeting (2013). 144

[345] M. Machida, T. Shiomitsu, K. Eguchi, H. Arai, and Y. Shimizu, *Journal of Solid State Chemistry* **95**, pp. 220–223 (1991). 147, 148, 164

[346] M. Machida, K. Eguchi, and H. Arai, *Journal of Catalysis* **120**, pp. 377–386 (1989). 148, 164

[347] M. Machida, K. Eguchi, and H. Arai, *Journal of the American Ceramic Society* **71**, pp. 1142–1147 (1988). 147

[348] M. Machida, K. Eguchi, and K. Arai, *Journal of Catalysis* **103**, pp. 385–393 (1987). 147

[349] M. Santiago and J. Pérez-Ramírez, *Environmental Science and Technology* **41**, pp. 1704–1709 (2007). 162

[350] M.F.M. Zwinkels, S.G. Jaras, P.G. Menon, and T.A. Griffin, *Catalysis Reviews: Science and Engineering* **35**, pp. 319–358 (1993). 147, 155

[351] G. Groppi, M. Bellotto, C. Cristiani, P. Forzatti, and P.L. Villa, *Applied Catalysis A: General* **104**, pp. 101–108 (1993). 147, 149

[352] L. Lietti, C. Cristiani, , G. Groppi, and P. Forzatti, *Catalysis Today* **59**, pp. 191–204 (2000). 147, 149, 155, 162

[353] K. Kato and H. Saalfeld, *Neues Jahrbuch für Mineralogie, Abhandlungen* **109**, pp. 192–200 (1968). 147

[354] A. Utsunomiya, K. Tanaka, H. Morikawa, F. Marumo, and H. Kojima, *Journal Solid State Chemistry* **75**, pp. 197–200 (1988). 147

[355] A.J. Lindop, C. Matthews, and D.W. Goodwin, *Acta Crystallographica Section B* **31**, pp. 2940–2941 (1975). 147

[356] M. Gasperin, M.C. Saine, A. Kahn, F. Laville, and A.M. Lejus, *Journal of Solid State Chemistry* **54**, pp. 61–69 (1984). 147

[357] N. Iyi, Z. Inoue, S. Takekawa, and S. Kimura, *Journal of Solid State Chemistry* **54**, pp. 70–77 (1984). 147

[358] N. Iyi, *Crystal structure and defects of β-alumina-related hexagonal aluminates*, PhD thesis , Osaka University, Osaka (Japan) (1986). 148

[359] W. Chu, W. Yang, and L. Lin, *Catalysis Letters* **74**, pp. 139–144 (2001). 148, 149

[360] T.H. Gardner, J.J. Spivey, E.L. Kluger, and D. Pakhare, *Applied Catalysis A: General* **455**, pp. 129–136 (2013). 148, 149, 168

[361] O. Yokota, T. Tanaka, Z. Hou, and T. Yashima, *Studies in Surface Science and Catalysis* **153**, pp. 141–144 (2004). 149

[362] M. Machida, A. Sato, T. Kijima, H. Inoue, K. Eguchi, and H. Arai, *Catalysis Today* **26**, pp. 239–245 (1995). 149, 165

[363] J. Li, D. Wang, G. Zhou, Y. Xue, C. Li, and T. Cheng, *Industrial & Engineering Chemistry Research* **50**, pp. 10955–10961 (2011). 149

[364] J.X. Wang, D.W. Meng, X.L. Wu, J.H. Hong, D.Z. An, and K.J. Zhen, *Reaction Kinetics and Catalysis Letters* **96**, pp. 65–73 (2009). 149

[365] S.A. Schunk, A. Milanov, A. Strasser, G. Wasserschaff, and T. Roussière, "Verfahren zur Herstellung eines Katalysators zur Reformierung von Kohlenwasserstoffen sowie ein Verfahren zu Reformierung (not published yet)" (2012). 149

[366] Y. Liu, Z.L. Xu, T.X. Cheng, G.D. Zhou, J.X. Wang, W.X. Li, Y.L. Bi, and K.J. Zhen, *Kinetics and Catalysis* **43**, pp. 522–527 (2002). 149

[367] K.M. Schelkle, Thomas Roussière, S.A. Schunk, G. Wasserschaff, A. Milanov, E. Schwab, G. Cox, O. Deutschmann, L. Schulz, A. Jentys, and J.A. Lercher, "Understanding the reduction mechanism of Ni-hexaaluminates - A mechanistic proposal", Poster at the 46^{th} Jahrestreffen Deutscher Katalytiker (Weimar). 150, 164, 165, 166

[368] K.M. Schelkle, ", Complex Oxides of the Iron Group - Complex Oxides with Hexaaluminate and Garnet Structure", Master's thesis , Technische Universität München (German Institute of Science and Technology), München (Germany) (2012). 150, 164

[369] H. Putz and K. Brandenburg, "Match!: Phase Identification from Powder Diffraction, Crystal Impact 2003-2012.", http://crystalimpact.com/match/Default.htm. 152

[370] T.J.B. Holland and S.A.T. Redfern, *Mineralogical Magazine* **61**, pp. 65–77 (1997). 152

[371] G. Groppi, C. Cristiani, P. Forzatti, and M. Bellotto, *Journal of Materials Science* **29**, pp. 3441–3450 (1994). 155

[372] G. Bergerhoff and I.D. Brown, *Crystallographic Databases*, International Union of Crystallography (1987). 155, 158, 160, 162

[373] I.N. Stranski, *Zeitschrift für Physikalische Chemie* **136**, pp. 259–278 (1928). 156, 165

[374] W. Kossel, *Annalen der Physik* **21**, pp. 455 (1934).

[375] W. Kossel, *Annalen der Physik* **33**, pp. 651 (1938).

[376] S.A. Schunk, *Entwicklung neuer Methoden zur Beobachtung früher Stadien der Kristallisation in Lösung*, PhD thesis , University of Frankfurt (Department of Inorganic Chemistry), Frankfurt (Germany) (1998). 156, 165

[377] R.F Strickland-Constable, *Kinetics and Mechanism of Crystallization*, Academic Press, New York (1968). 158

[378] M.V. Bukhtiyarova, A.S. Ivanova, E.M. Slavinskaya, P.A. Kuznetsov, L.M. Plyasova, O.A. Stonkus, V.A. Rogov, V.V. Kaichev, and A.S. Noskov, *Catalysis for Sustainable Energy* **1**, pp. 11–21 (2012). 159

[379] M. Ji, Y.L. Bi, K.J. Zhen, and Y. Wu, *Journal of Natural Gas Chemistry* **7**, pp. 291–296 (1998). 159

[380] F. Yin, S. Ji, P. Wu, F. Zhao, and C. Li, *Journal of Molecular Catalysis A: Chemical* **294**, pp. 27–36 (2008). 164

[381] H. Putz and K. Brandenburg, "Diamond: Crystal and Molecular Structure Visualization, Crystal Impact 2003-2012.", http://www.crystalimpact.com/diamond. 165

Appendix

A - Gas-phase reactions over "inert" materials

- Isotherm measurements

Measurement at 850°C	
Height from the bottom [cm]	**Temperature [°C]**
8	242
10	273
12	314
14	366
16	418
18	478
20	560
22	656
24	723
26	756
28	781
30	792
32	798
34	802
36	805
38	807
40	813
42	820
44	827
46	830
48	835
50	838
52	840
54	843
56	846
58	849
60	851
62	852
64	853
66	853
68	852
70	852
72	852
74	853
76	853
78	852
80	851
82	848
84	845
86	843
88	840
90	838
92	835
94	832
96	829
98	825
100	822
102	819
104	816
106	813
108	810
110	805
112	799
114	792
116	775
118	742
123	543
128	329

Measurement at 950°C	
Height from the bottom [cm]	Temperature [°C]
6	299
11	390
18	778
20	835
22	865
24	881
26	891
28	897
30	901
32	905
34	909
36	915
38	921
40	926
42	931
44	934
46	937
48	939
50	942
52	945
54	949
56	950
58	951
60	951
62	951
64	951
66	951
68	952
70	952
72	951
74	949
76	946
78	943
80	941
82	939
84	937
86	934
88	931
90	928
92	924
94	920
96	917
98	914
100	910
102	906
104	900
106	891
124	800
126	650
128	400

- Pressure increase (green line) observed during coking in screening setup during the hydrogen test protocol

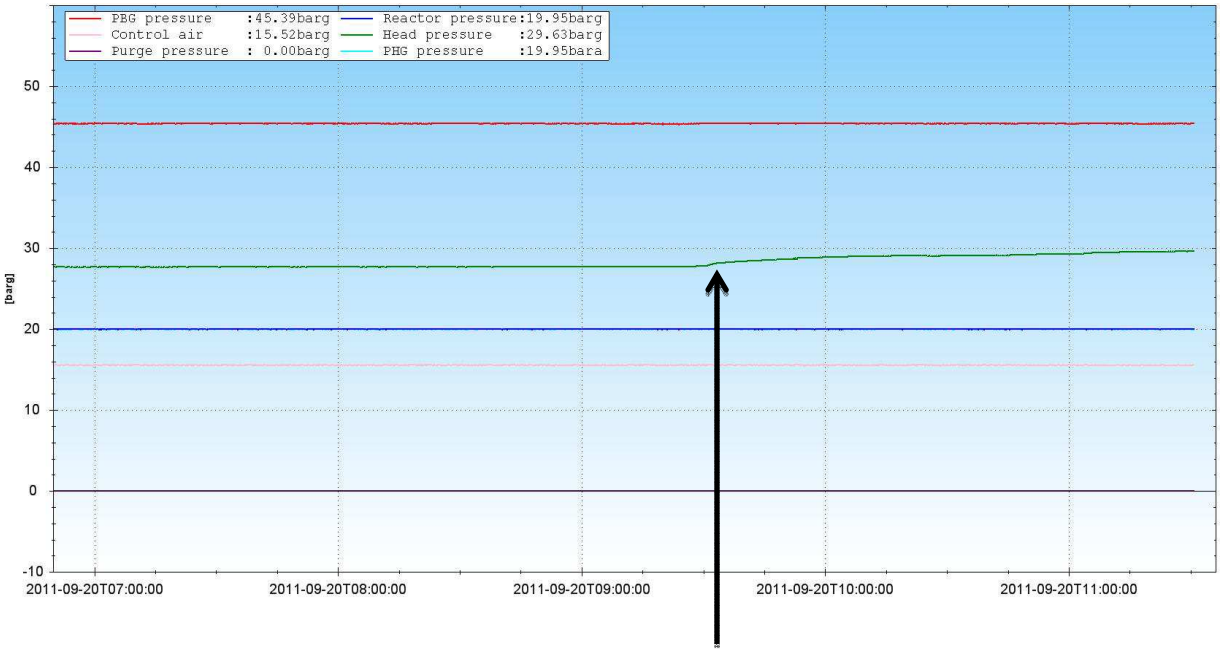

Pressure increase observed under CO_2 reforming without additional H_2

B - Pt-based catalysts for CH_4 reforming in the presence of H_2O and CO_2 - A kinetic study

- Catalyst preparation

	Pt nitrate solution	Pt-EA solution	Ce nitrate hexahydrate	XZO 880 - shaped	SZ 31107	SZ 61156	H_2O for impregnation
	Umicore	Umicore	Sigma Aldrich	Split-500-1000µm	Saint Gobain NorPro	Saint Gobain NorPro	
Specification	30.628 wt.% Pt	9.570 wt.% Pt	Purity >99%				
	[g]	[g]	[g]	[g]	[g]	[g]	[g]
PtZ	5.865	-		193.98	-	-	400
PtSZ	-	6.77			67.2		120
PtCSZ	-	7.21	12.3		64.04		120
PtCLZ	-	6.479	11.18	-	-	58.02	120

- XRD patterns of PtZ before and after steam reforming at 850°C, 21 bar, S/C=1, GHSV=3800 h^{-1}

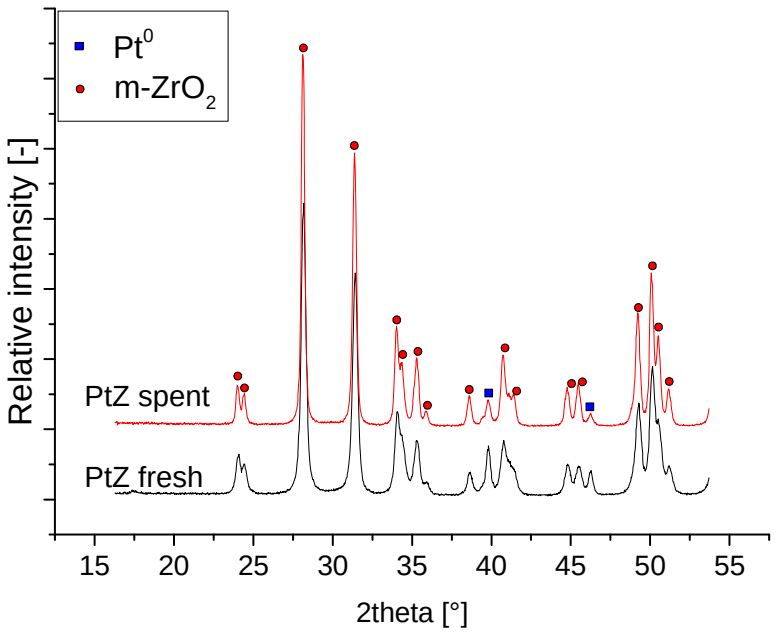

- XRD patterns of PtSZ before and after steam reforming at 850°C, 21 bar, S/C=1, GHSV=3800 h^{-1}

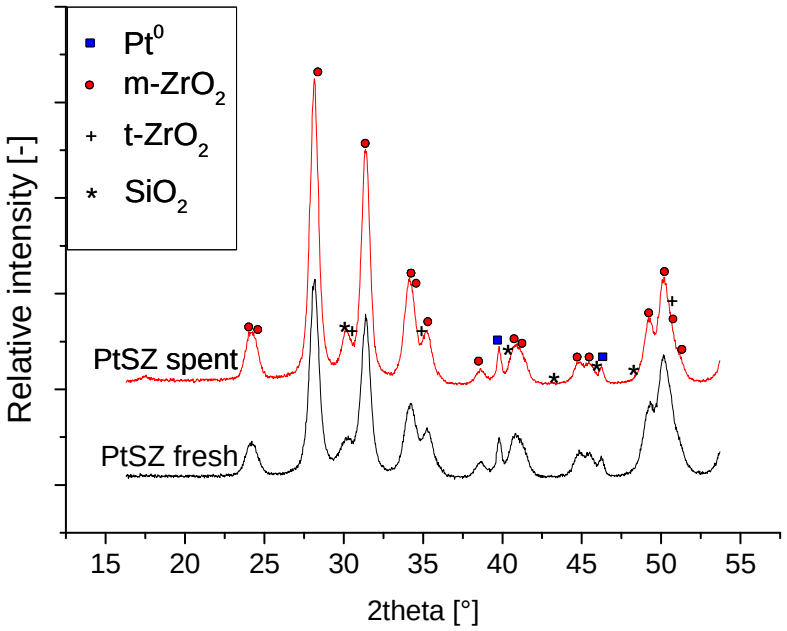

- XRD patterns of PtCSZ before and after steam reforming at 850°C, 21 bar, S/C=1, GHSV=3800 h^{-1}

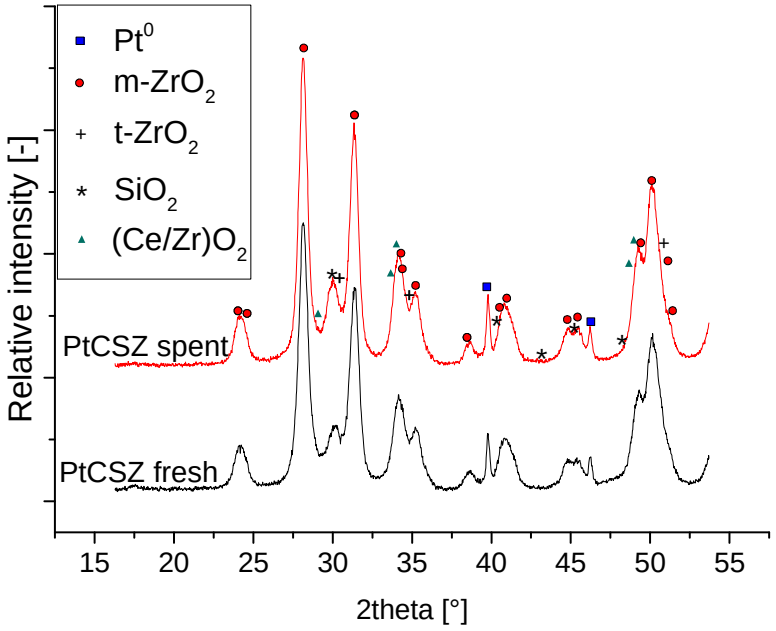

- XRD patterns of PtCLZ before and after steam reforming at 850°C, 21 bar, S/C=1, GHSV=3800 h^{-1}

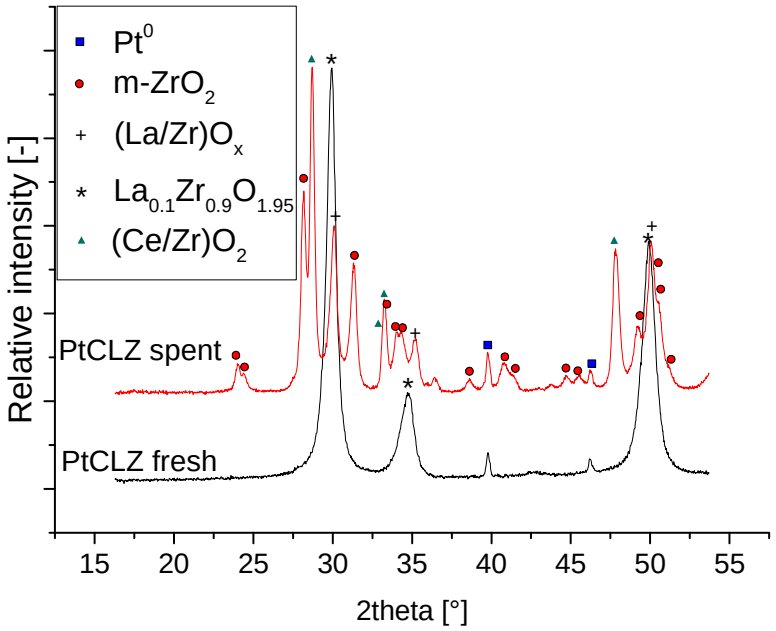

- Plate design for kinetic investigations with PtCLZ as catalyst or corundum

#	Filling material	Filling volume [ml]	Filling mass [g]	Gas factor distribution	GHSV [1/h]
Reactor 1	PtCLZ	1.021	1.5506	0.96	3604.3
Reactor 2	PtCLZ	0.118	0.1937	0.98	33559
Reactor 3	PtCLZ	0.236	0.3876	0.98	17288
Reactor 4	Corundum	1.0	2.253	0.98	-
Reactor 5	PtCLZ	1.021	1.55	1	4035.3
Reactor 6	PtCLZ	0.098	0.1938	1	41225
Reactor 7	PtCLZ	0.255	0.3871	1	15686
Reactor 8	Corundum	1.0	2.253	1.05	-
Reactor 9	PtCLZ	1.021	1.5503	1	3956.9
Reactor 10	PtCLZ	0.118	0.1934	1	33898
Reactor 11	PtCLZ	0.255	0.3876	1	15686
Reactor 12	Corundum	1.0	2.253	1.02	-
Reactor 13	PtCLZ	0.982	1.5505	1	4073.3
Reactor 14	PtCLZ	0.098	0.1938	1.01	41225
Reactor 15	PtCLZ	0.236	0.3877	1.01	15593
Reactor 16	Corundum	1.0	2.253	1.01	-

C - Ni-based spinels for steam reforming in presence of CO_2

- Catalyst preparation
  - By impregnation

Short name	Sasol	Merck
	Pural MG 30	Ni nitrate hexahydrate (Purity >99%)
	[g]	[g]
MSI	400	261.67
SD	400	261.57

  - By precipitation:

	Al nitrate solution	Ni nitrate solution	Mg nitrate solution
	1 mol/L	1 mol/L	1 mol/L
	[mL]	[mL]	[mL]
PRC	1660	420	840

- XRD patterns after reduction

  - Under 5vol.% H_2/N_2:

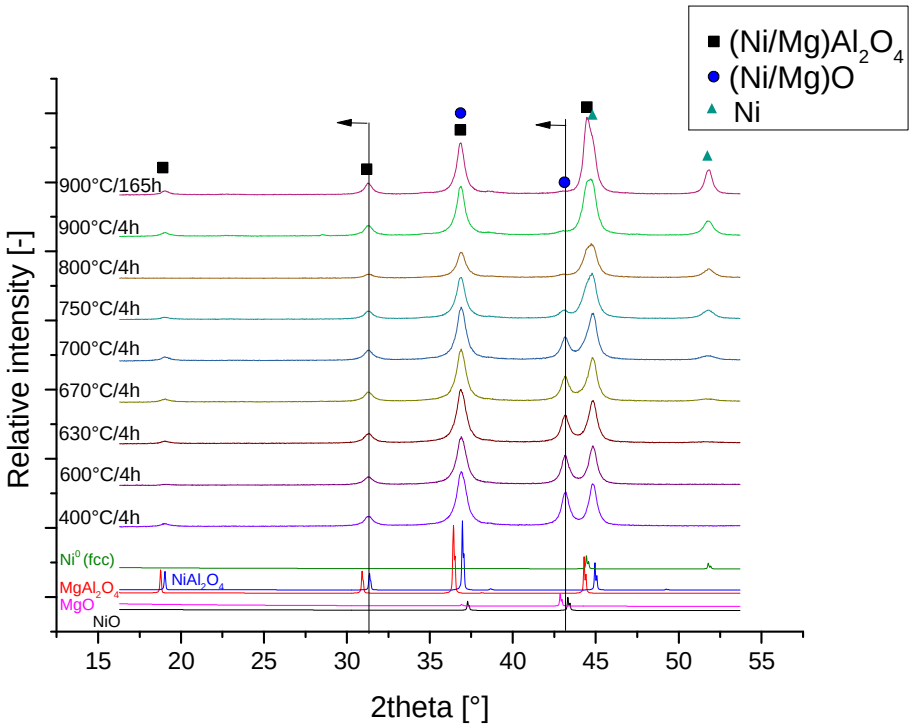

  - Under 5 vol.% H_2 + 10 vol.% H_2O/N_2:

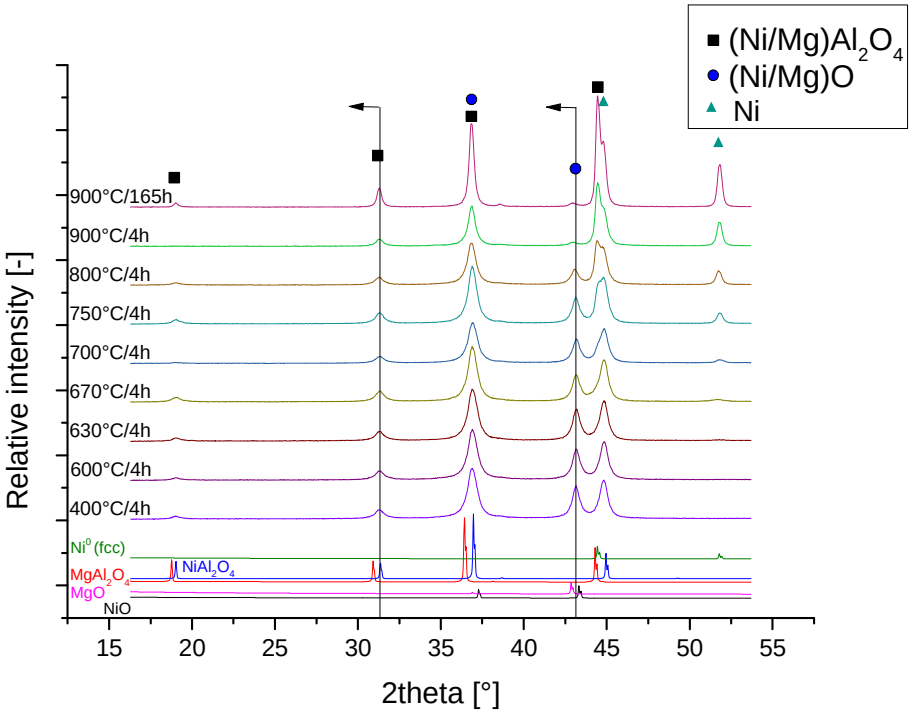

- Under 5 vol.% H_2 + 5 vol.% CO_2/N_2:

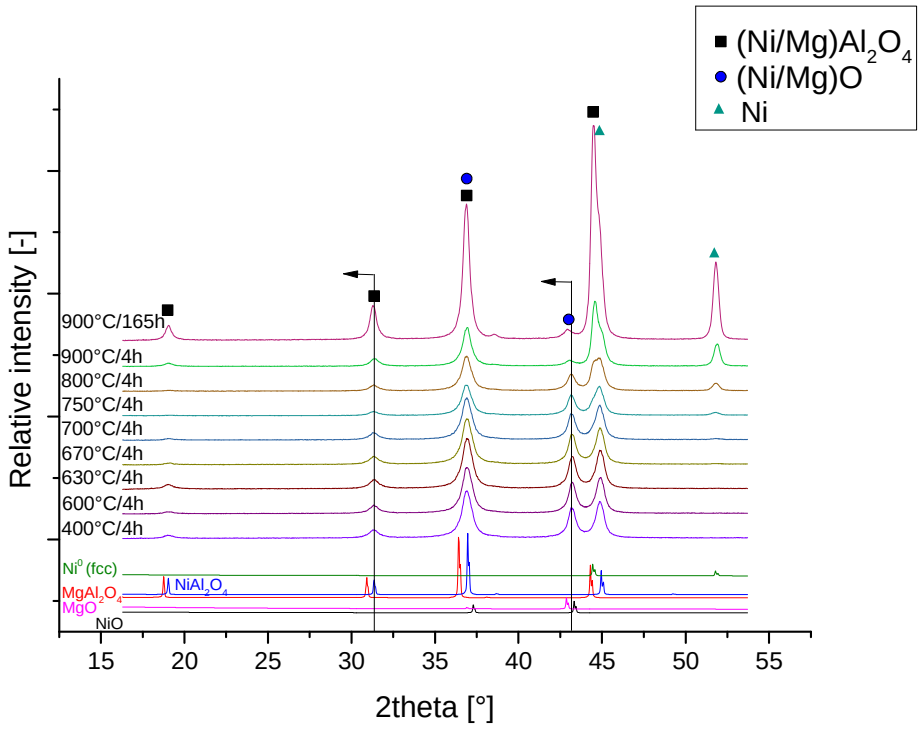

- Under 5 vol.% H_2 + 10 vol.% H_2O + 5 vol.% CO_2/N_2:

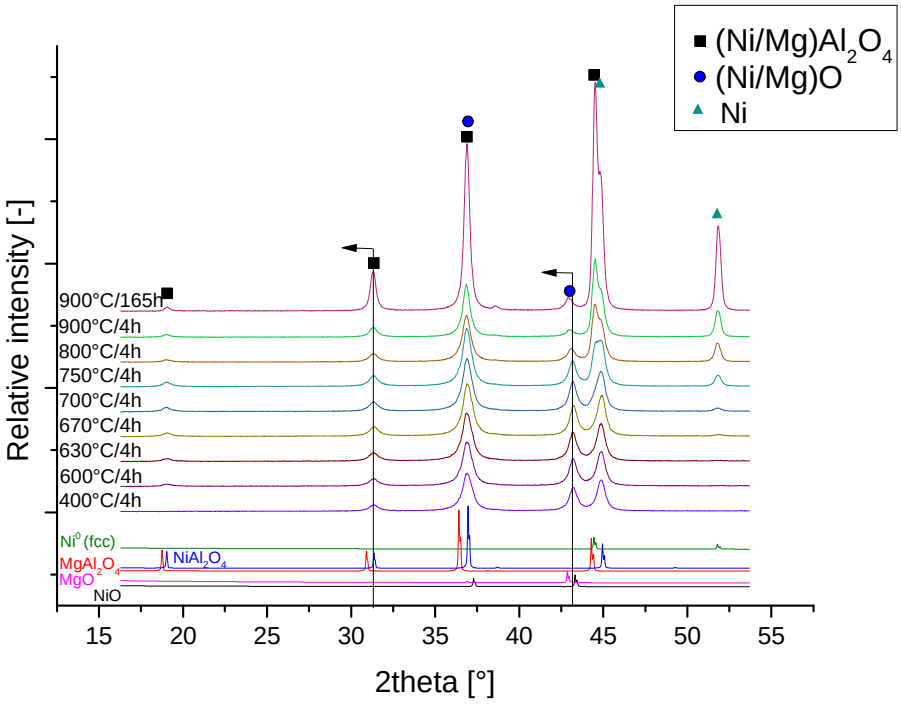

D - Ni-based hexaaluminates as catalysts in reforming reactions in the presence of CO_2

- Catalyst preparation

	Disperal	Ni nitrate hexahydrate	La nitrate hexahydrate	Sr nitrate	Ba Nitrate
	Sasol	Merck	ChemPur	Sigma Aldrich	Sigma Aldrich
		Purity >99%	Purity >99%	Purity >99%	Purity >99%
	[g]	[g]	[g]	[g]	[g]
LaNi0.25-1600	36.53	3.46	19.58	-	-
LaNi0.5-1600	35.76	6.91	19.58	-	-
LaNi0.75-1600	34.98	10.37	19.58	-	-
LaNi1-1600	34.20	13.83	19.58	-	-
LaNi0.25-1200	36.53	3.46	19.58	-	-
LaNi0.5-1200	35.76	6.91	19.58	-	-
LaNi0.75-1200	34.98	10.37	19.58	-	-
LaNi1-1200	34.20	13.83	19.58	-	-
SrNi0.25-1200	36.53	3.46	-	9.960	-
SrNi0.5-1200	35.76	6.91	-	9.960	-
SrNi0.75-1200	34.98	10.37	-	9.960	-
SrNi1-1200	34.20	13.83	-	9.960	-
BaNi0.25-1200	36.53	3.46	-	-	12.42
BaNi0.5-1200	35.76	6.91	-	-	12.42
BaNi0.75-1200	34.98	10.37	-	-	12.42
BaNi1-1200	34.20	13.83	-	-	12.42

- XRD patterns
  - La,Ni hexaaluminates ($LaNi_yAl_{12-y}O_{19-\delta}$) calcined at 1600°C
    - Before reduction

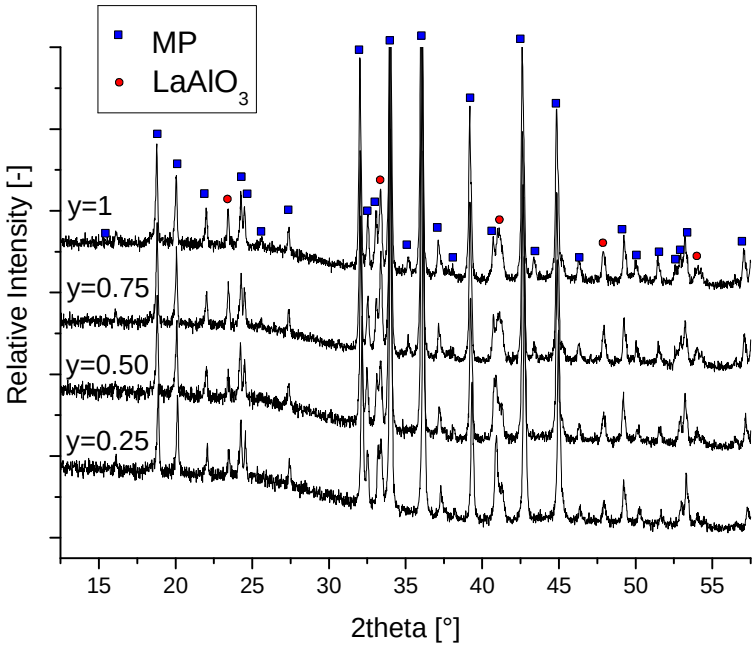

    - Difference before reduction (grey) and after reduction (black)

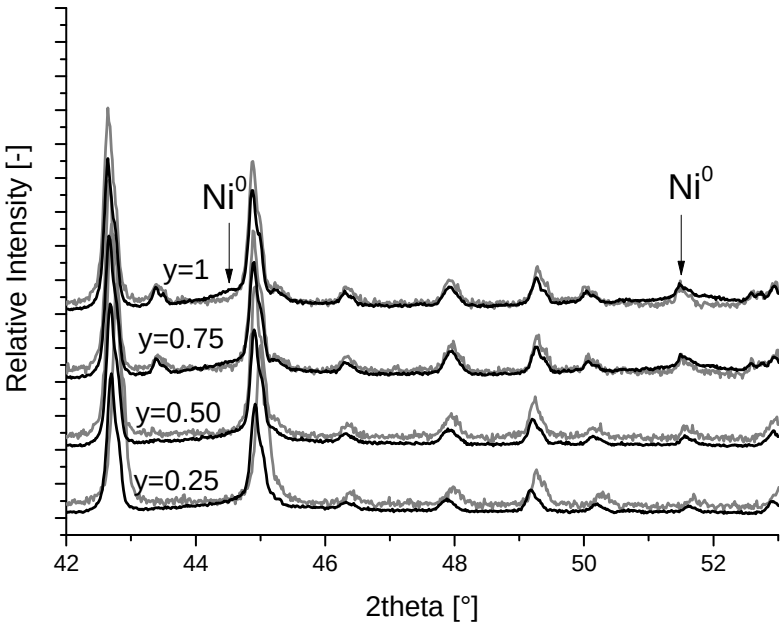

- La,Ni hexaaluminates ($LaNi_yAl_{12-y}O_{19-\delta}$) calcined at 1200°C

  - Before reduction

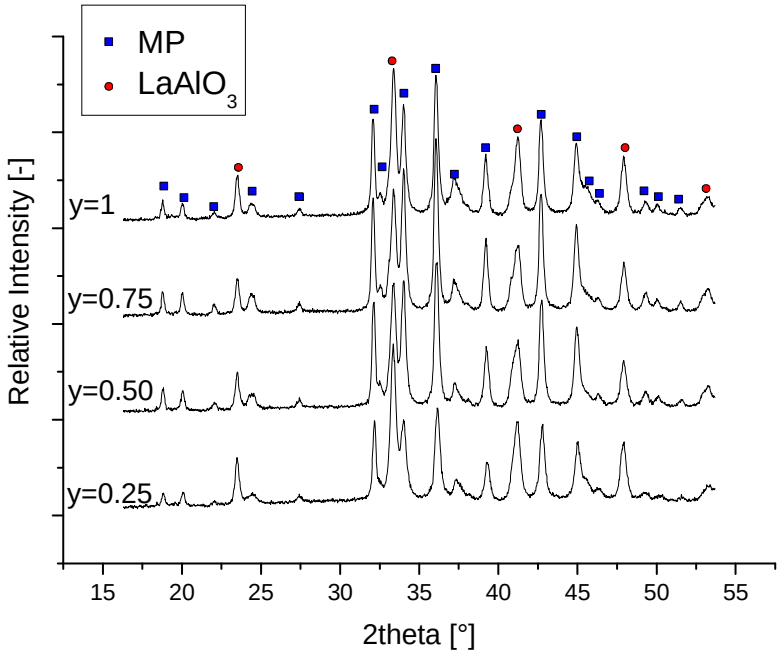

  - Difference before reduction (grey) and after reduction (black)

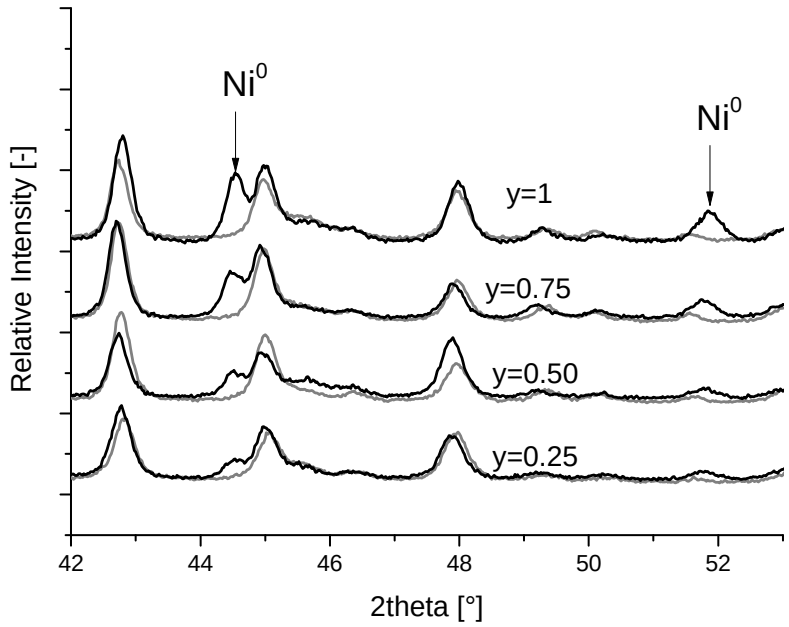

- Sr,Ni hexaaluminates calcined ($SrNi_yAl_{12-y}O_{19-\delta}$) at 1200°C

  - Before reduction

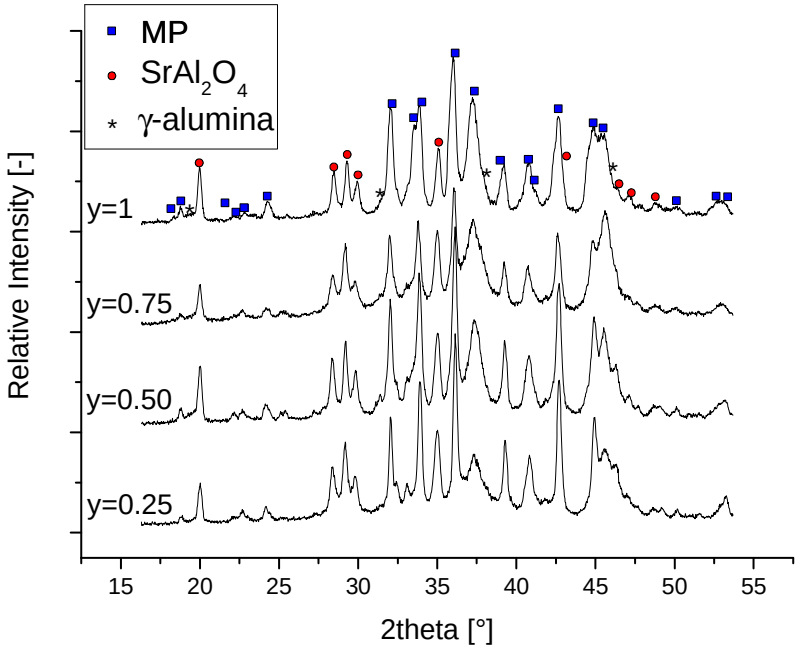

  - Difference before reduction (grey) and after reduction (black)

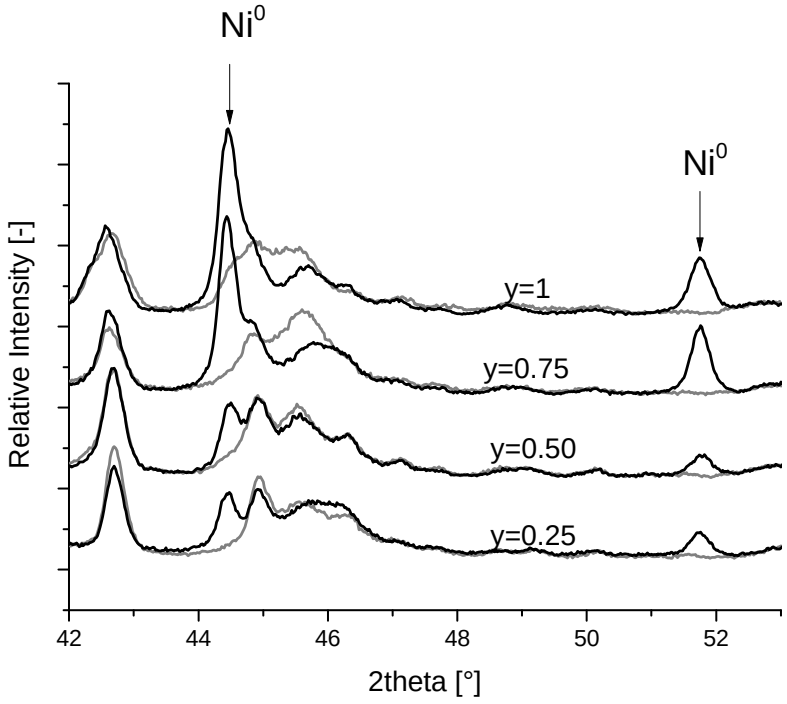

- Ba,Ni hexaaluminates ($BaNi_yAl_{12-y}O_{19-\delta}$) calcined at 1200°C

  - Before reduction

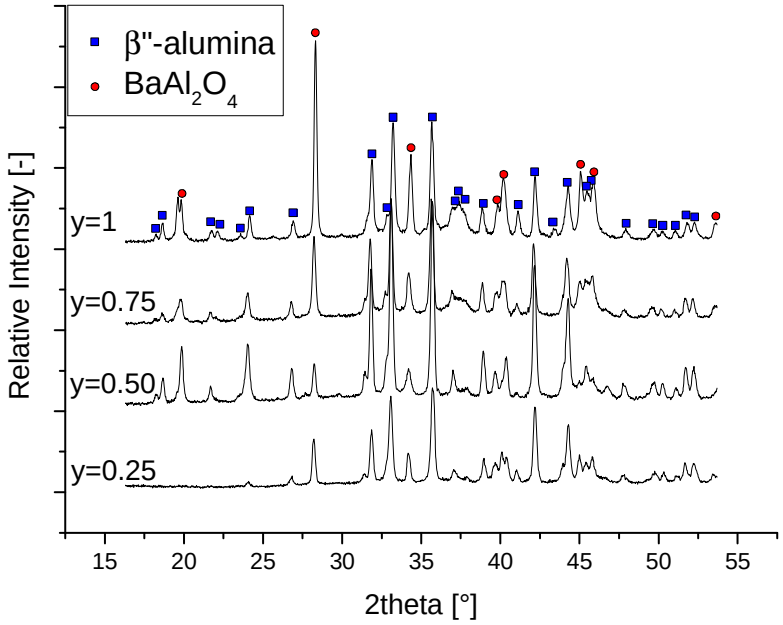

  - Difference before reduction (grey) and after reduction (black)

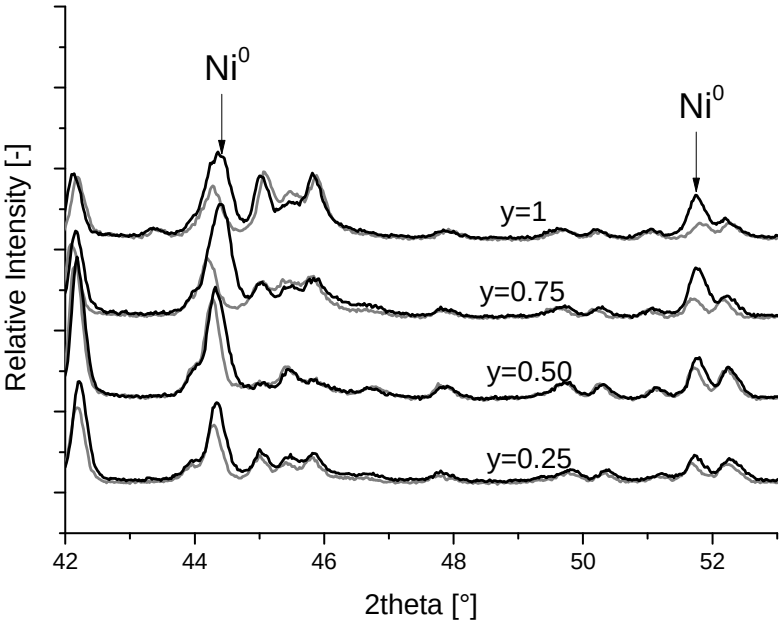

Publications

Articles

1 T. Roussière, L. Schulz, K. Schelkle, G. Wasserschaff, A. Milanov, E. Schwab, O. Deutschmann, A. Jentys, J.A. Lercher, S.A. Schunk, 2013, In Preparation, Maximizing activity and stability of hexaaluminate based catalysts in dry reforming of methane.

2 T. Roussière, K. Schelkle, S. Titlbach, G. Wasserschaff, A. Milanov, G. Cox, E. Schwab, O. Deutschmann, L. Schulz, A, Jentys, J.A. Lercher, S.A. Schunk, 2013, In Preparation, Synthesis and characterization of Ni-Hexaaluminates - Controlling Ni-particle growth.

3 L.C.S. Kahle, T. Roussière, L. Maier, K. Herrera Delgado, G. Wasserschaff, S.A. Schunk, O. Deutschmann, Industrial & Engineering Chemistry Research, 2013, Accepted.

4 N. Böhmer, T. Roussière, M. Kuba, S.A. Schunk, Combinatorial Chemistry & High Throughput Screening 15, 2012, 123-135.

Books (Chapter)

1 S.A. Schunk, C. Futter, N. Böhmer, A Kuschel, E. Prasetyo, T. Roussière, Catalysis 25, 2012, Chapter 10.

Patents

1 Verfahren zur Herstellung eines Methanisierungskatalysators sowie ein Verfahren zur Methanisierung von Synthesegas, C. Querner, A. Milanov, S.A. Schunk, S. Strasser, G. Wasserschaff, T. Roussière, 2011.

2 Verfahren zur Herstellung eines Methanisierungskatalysators sowie die Reformierung von Methan, E. Schwab, A. Milanov, S.A. Schunk, T. Roussière, S. Strasser, G. Wasserschaff, 2011.

3 Hexaaluminat-haltiger Katalysator zur Refomierung von Kohlenwasserstoffen sowie ein Verfahren zur Reformierung, S.A. Schunk, A. Milanov, A. Strasser, G. Wasserschaff, T. Roussière, 2012.

4 Nickelhexaaluminathaltiger Katalysator zur Reformierung von Kohlenwasserstoffen in Gegenwart von Kohlendioxid, S.A. Schunk, E. Schwab, A. Milanov, T. Roussière, G. Wasserschaff, G. Cox, B. Hinrichsen, U. Floerchinger, 2013.

Posters

1 Dry Reforming, March 2011, 44. Jahrestreffen Deutscher Katalytiker, Weimar

2 Dry Reforming with Pt-based Catalysts, March 2012, 45. Jahrestreffen Deutscher Katalytiker, Weimar

3 Understanding Structure-Property Relationships for Ni-containing Hexaaluminates in the Dry Reforming of Methane, March 2013, 46. Jahrestreffen Deutscher Katalytiker, Weimar

Erklärung

Hiermit versichere ich, dass ich diese Arbeit selbständig verfasst und keine anderen als die angegebenen Quellen und Hilfsmittel verwendet habe sowie die wörtlich oder inhaltlich übernommenen Stellen als solche kenntlich gemacht, und die Satzung der Universität Karlsruhe (TH) zur Sicherung guter wissenschaftlicher Praxis beachtet habe.

Mannheim, den 21. August 2013